Universität Augsburg
Lehrstuhl für
Experimentalphysik I

Acousto-Optoelectric Spectroscopy on Semiconductor Nanowires and Their Heterostructures

Dissertation
zur Erlangung des akademischen Grades
Dr. rer. nat.

Eingereicht an der
Mathematisch Naturwissenschaftlich Technischen Fakultät
der Universität Augsburg

von

Maximilian M. Sonner

Augsburg, Dezember 2021

nanosystems initiative munich

Deutsche
Forschungsgemeinschaft
German Research Foundation

First referee: Prof. Dr. Hubert J. Krenner
Second referee: PD Dr. Gregor Koblmüller
Date of oral exam: 25.03.2022

Die Geschichte vom Blumentopf und dem Bier

Ein Professor stand vor seiner Philosophie-Klasse und hatte einige Gegenstände vor sich. Als der Unterricht begann, nahm er wortlos einen sehr großen Blumentopf und begann, diesen mit Golfbällen zu füllen. Er fragte die Studenten, ob der Topf nun voll sei. Sie bejahten es.
Dann nahm der Professor ein Behältnis mit Kieselsteinen und schüttete diese in den Topf. Er bewegte den Topf sachte, und die Kieselsteine rollten in die Leerräume zwischen den Golfbällen. Dann fragte er die Studenten wiederum, ob der Topf nun voll sei. Sie stimmten zu.
Der Professor nahm als nächstes eine Dose mit Sand und schüttete diesen in den Topf. Natürlich füllte der Sand den kleinsten verbliebenen Freiraum. Er fragte wiederum, ob der Topf nun voll sei. Die Studenten antworteten einstimmig mit "Ja".
Nun holte der Professor zwei Flaschen Bier unter dem Tisch hervor und schüttete den ganzen Inhalt in den Topf und füllte somit den letzten Raum zwischen den Sandkörnern aus. Die Studenten lachten.

"Nun", sagte der Professor, als das Lachen langsam nachließ, "ich möchte, dass Sie diesen Topf als die Repräsentation Ihres Lebens ansehen. Die Golfbälle sind die wichtigen Dinge in Ihrem Leben: Ihre Familie, Ihre Kinder, Ihre Gesundheit, Ihre Freunde; die bevorzugten, ja leidenschaftlichen Aspekte Ihres Lebens, welche, falls in Ihrem Leben alles verloren ginge und nur noch diese verbleiben würden, Ihr Leben trotzdem noch erfüllend wäre.
Die Kieselsteine symbolisieren andere Dinge im Leben wie Ihre Arbeit, Ihr Haus, Ihr Auto. Der Sand ist alles andere, die Kleinigkeiten.
Falls Sie den Sand zuerst in den Topf geben", fuhr der Professor fort, "hat es weder Platz für die Kieselsteine noch für die Golfbälle. Dasselbe gilt für Ihr Leben. Wenn Sie all Ihre Zeit und Energie in Kleinigkeiten investieren, werden Sie nie Platz haben für die wichtigen Dinge. Achten Sie auf die Dinge, welche Ihr Glück gefährden.
Spielen Sie mit den Kindern. Nehmen Sie sich Zeit für eine medizinische Untersuchung. Führen Sie Ihren Partner zum Essen aus. Es wird immer noch Zeit bleiben, um das Haus zu reinigen oder Pflichten zu erledigen. Achten Sie zuerst auf die Golfbälle, die Dinge, die wirklich wichtig sind. Setzen Sie Ihre Prioritäten. Der Rest ist nur Sand."

Einer der Studenten erhob die Hand und wollte wissen, was denn das Bier repräsentieren soll.
Der Professor schmunzelte: "Ich bin froh, dass Sie das fragen. Es ist dafür da, Ihnen zu zeigen, dass, egal wie schwierig Ihr Leben auch sein mag, es immer noch Platz hat für ein oder zwei Bierchen."

Autor unbekannt

Abstract

Over the last decades, III-V semiconductor nanowires have gained much interest in research and industry as they are very promising candidates for future high-performance nanoelectronic and nanophotonic devices and enable fundamental research in low-dimensional systems. In particular, they allow the integration of the superior electronic and optical properties of III-V semiconductors onto the well-established silicon platform and the controlled integration of functional heterostructures which can be arranged axially and radially within nanowire heterostructures. Hence, novel device concepts are realized such as high-performance nanowire lasers, light-emitting diodes and nanowire-based photodetectors, as well as novel transistors and device platforms for quantum transport investigations. Hereby, the understanding and the control of charge carrier dynamics within nanowire systems is crucial for the improvement and design of such devices.

In this thesis, we investigate the coupled charge carrier dynamics within radial and axial GaAs-(In)GaAlAs core-shell nanowire heterostructures by acousto-optoelectric spectroscopy. With this technique, we control and manipulate the optical properties of such nanowires via the acousto-electric coupling of charge carriers and the electric field of a piezoelectric surface acoustic wave. These waves are mechanical waves which propagate along the surface of a crystal and are accompanied by a gyrating electric field. This electric field, in turn, ionizes excitons and induces spatio-temporal dynamics of the dissociated electrons and holes which can be observed in a photoluminescence experiment.

The first part of this thesis focuses on the charge carrier dynamics driven in a radial quantum well system which is embedded in a GaAs-$\mathrm{Al}_{0.3}\mathrm{Ga}_{0.7}\mathrm{As}$ core-shell nanowire heterostructure. Such radial heterostructure quantum wells are well-known to exhibit pronounced thickness fluctuations which strongly affect the localization of the charge carrier distribution within radial quantum wells. Hereby, theoretical modeling shows that only moderate deviations from the ideal symmetric hexagonal geometry result in the localization of charge carriers fully at the thickest side facets and, thus, lead to clear spectral shifts and multipeak structures which are observed in the photoluminescence spectrum of radial quantum wells. In addition, these fluctuations of the quantum well width which are observed in transmission microscopy measurements induce the formation of spatially separated but interconnected quantum well systems for which surface acoustic wave-induced coupling and reversible carrier exchange are observed on subnanosecond time scales. Hereby, we detect the counterclockwise motion of ultrafast electron cycloids between two quantum well segments which are located on neighboring sidewall facets of a nanowire heterostructure. These dynamics give direct insights into the transverse spin properties of surface acoustic waves which are strikingly similar to spin-momentum locking. The observed spin-momentum locking itself is a universal wave phenomenon in which the direction of spin is locked to the propagation direction of the surface acoustic wave.

In the second part, we report on a combined structural, optical and acousto-optoelectric study of different types of polytypic GaAs nanowires. Hereby, transmission electron microscopy and scanning photoluminescence spectroscopy analysis reveal two types of polytypic nanowires which differ in their crystal structure along the nanowire axis. This polytypism gives rise to three characteristic coupled decay channels within each nanowire which are attributed to different types of spatially direct and spatially indirect recombination. These decay channels correspond to distinct transitions in the type-II band edge modulation induced by crystal-phase mixing, and, thus, to the transition of electrons and holes located either within the same crystal phase segment or in different segments. In our acousto-optoelectric experiments, we resolve the spatio-temporal charge carrier dynamics between these different, coupled recombination channels within each nanowire which are driven by the electric field of a surface acoustic wave. In particular, we find unambiguous fingerprints in the observed suppression of the nanowire emission and its dynamic temporal modulation due to the local band edge variations induced by the crystal phase mixing. A nanowire, which exhibits a change of the crystal structure from a near-pristine zincblende phase to a highly polytypic crystal structure with extended wurtzite and zincblende segments, shows a clear dependence on the propagation direction of the acoustic wave. In contrast, no pronounced directionality is found for more homogeneous nanowires which exhibit only extended near-pristine zincblende segments. We corroborate our measurements by numerically solving the surface acoustic wave induced drift and diffusion equations of electrons and holes and reproduce key characteristics of our experimental observations of the charge carrier dynamics by assuming basic models of both types of nanowires. Finally, we determine the second- and third-order correlation functions from the recorded time-correlated single-photon-counting data allowing to probe the correlations of surface acoustic wave-driven, coupled carrier dynamics between three decay channels of each nanowire.

Zusammenfassung

In den letzten Jahrzehnten haben III-V Halbleiter Nanodrähte großes Interesse in vielen Bereichen der Forschung und Industrie geweckt, da sie sehr vielversprechende Materialsysteme für zukünftige hochleistungsfähige, nanoelektronische und nanophotonische Bauelemente sind sowie Grundlagenforschung in niederdimensionalen Systemen ermöglichen. Insbesondere erlauben sie die Integration der überlegenen elektronischen und optischen Eigenschaften von III-V Halbleitern auf die bereits etablierte Silizium-Technologie sowie die kontrollierte Realisierung von funktionellen Heterostrukturen, die sowohl axial als auch radial innerhalb einer Nanodraht Heterostruktur angeordnet werden können. So wurden neuartige Konzepte, wie Hochleistungsnanodrahtlaser, Leuchtdioden und Nanodraht-basierende Photodetektoren sowie neuartige Transistoren und Prototypen für Quantentransportuntersuchungen realisiert. Dabei ist das Verständnis und die Steuerung der Ladungsträgerdynamik innerhalb solcher Nanodrahtsysteme entscheidend für die Verbesserung und das Design solch neuer Technologien.

In dieser Arbeit werden die gekoppelten Ladungsträgerdynamiken in verschiedenen GaAs-(In)GaAlAs Kern-Mantel Nanodraht-Heterostrukturen mittels akusto-optoelektrischer Spektroskopie untersucht. Mit dieser Technik werden die optischen Eigenschaften solcher Nanodrähte über die akusto-elektrische Kopplung von Ladungsträgern und dem elektrischem Feld einer piezoelektrischen, akustischen Oberflächenwelle manipuliert. Bei akustischen Oberflächenwellen handelt es sich um mechanische Wellen, die sich entlang der Oberfläche eines Kristalls ausbreiten und von einem gyrierenden, elektrischen Feld begleitet werden. Dieses elektrische Feld wiederum ionisiert Exzitonen und induziert raumzeitliche Dynamik der dissoziierten Elektronen und Löcher, die in einem Photolumineszenzexperiment beobachtet werden können.

Der erste Teil der Arbeit konzentriert sich auf die Ladungsträgerdynamiken, die in radialen Quantentöpfen induziert werden, welche wiederum in eine GaAs-$\mathrm{Al}_{0.3}\mathrm{Ga}_{0.7}\mathrm{As}$ Kern-Mantel Nanodraht Heterostruktur eingebettet sind. Solche radialen Quantentöpfe weisen bekanntermaßen ausgeprägte Dickenschwankungen auf, die die Lokalisation der Ladungsträgerverteilung innerhalb des radialen Quantentopfes stark beeinflussen. Theoretische Modellierungen zeigen, dass nur moderate Abweichungen von der idealen symmetrischen, hexagonalen Geometrie zu einer vollständigen Lokalisierung von Ladungsträgern an den dicksten Seitenfacetten führen und somit in deutlichen spektralen Verbreiterungen und Multipeakstrukturen resultieren, die wiederum im Photolumineszenzspektrum des radialen Quantentopfes beobachtet werden können. Darüber hinaus induzieren diese Dickenfluktuationen der Quantentopfbreite, die in Transmissionselektronenmikroskopie Messungen beobachtet wurden, die Bildung von räumlich getrennten, aber miteinander verbundenen Quantentopfsystemen. Für diese wiederum wird eine durch eine akustische Welle induzierte Kopplung und ein reversibler Ladungsträgeraustausch auf Subnanosekunden-Zeitskalen beobachtet. Dabei wird die Bewegung ultraschneller Elektronenzykloiden zwischen zwei Quantentopfsegmenten, die sich auf benachbarten Seitenwandfacetten befinden, gegen den Uhrzeigersinn detektiert. Diese geben direkte Einblicke in die Eigenschaften des transversen Spins einer akustischer Oberflächenwelle, die den sogenannten "spin-momentum locking" Eigenschaften auffallend ähnlich sind. Das beobachtete "spin-momentum locking" selbst ist ein universelles Wellenphänomen, bei dem die Spinrichtung an die Ausbreitungsrichtung der akustischen Oberflächenwelle gebunden ist.

Im zweiten Teil berichten wir über eine kombinierte strukturelle, optische und akusto-optoelektrische Untersuchung verschiedener Arten von polytypischen GaAs-Nanodrähten. Dabei werden mittels Transmissionselektronenmikroskopie und Rasterphotolumineszenzspektroskopie zwei unterschiedliche Arten von polytypischen Nanodrähten gefunden, die sich stark in ihrer Kristallstruktur entlang der Nanodrahtachse unterscheiden. Aufgrund der jeweiligen Kristallstruktur entstehen drei charakteristische, gekoppelte Zerfallskanäle innerhalb jedes Nanodrahtes, die verschiedenen Arten von räumlich direkter und räumlich indirekter Rekombination zugeschrieben werden. Diese Zerfallskanäle entsprechen unterschiedlichen Übergängen in der Typ-II-Bandkantenmodulation, die durch die Kristallphasenmischung induziert wird, und damit dem Übergang von Elektronen und Löchern, die sich entweder innerhalb desselben Kristallphasensegments oder in verschiedenen Segmenten befinden. In unseren akusto-optoelektrischen Experimenten werden die raumzeitliche Ladungsträgerdynamik, die durch das elektrische Feld einer akustischen Oberflächenwelle zwischen den verschiedenen, gekoppelten Rekombinationskanälen innerhalb jedes Nanodrahtes angetrieben werden, aufgezeigt. Insbesondere finden wir eindeutige Fingerabdrücke in der beobachteten Unterdrückung der Nanodrahtemission und ihrer zeitlich dynamischen Modulation aufgrund der lokalen Bandkantenvariationen, die aus der Kristallstruktur entlang des Nanodrahtes resultieren. Hierbei zeigt ein Nanodraht, der eine Veränderung der Kristallstruktur von einer nahezu reinen Zinkblendenphase zu einer hochpolytypischen Kristallstruktur mit ausgedehnten Wurtzit- und Zinkblendesegmenten aufweist, eine deutliche Abhängigkeit von der Ausbreitungsrichtung der akustischen Welle. Im Gegensatz dazu findet sich für homogenere Nanodrähte, welche nur ausgedehnte pristine Zinkblendesegmente aufweisen, keine ausgeprägte Richtungsabhängigkeit. Unter anderem werden die experimentell beobachteten Ladungsträgerdynamiken durch numerisches Lösen der durch die akustischen Wellen induzierten Drift- und Diffusionsgleichungen von Elektronen und Löchern reproduziert, indem ein grundlegendes Modell beider Arten von Nanodrähten angenohmen wird. Schließlich werden die Korrelationsfunktionen zweiter und dritter Ordnung aus den aufgezeichneten zeitkorrelierten Einzelphotonenzähldaten bestimmt, welche es ermöglichen, die Korrelationen der akustischen, gekoppelten Ladungsträgerdynamik zwischen drei Zerfallskanälen jedes Nanodrahtes zu untersuchen.

Contents

Chapter 1

Introduction

In our digitalized world, consumer electronics have become increasingly smaller, faster and more efficient over the past decades by the advancing miniaturization of integrated circuits. This trend of miniaturization is still well described by Moore's law [1]. However, further down-scaling of the size of such electronic circuits will eventually reach physical and economic limits and, thus, requires the development of novel device concepts. In particular, semiconductor nanowires (NWs) can be considered as extremely promising candidates for future high performance nanoelectronic and nanophotonic devices [2–6]. This, in turn, has led to a great interest of nanowires in research and industry due to their unique material properties.

The most unique feature of nanowire structures is that they allow the combination of heavily lattice mismatched materials such as silicon and III-V semiconductors. In conventional heteroepitaxy, a large lattice mismatch results regularly in interfacial dislocations if the layer thicknesses exceed a certain critical thickness and, thus, detrimentally affect the crystal quality. For nanowire structures, however, the specific, one-dimensional-like geometry with a small footprint facilitates the efficient lateral strain relaxation at interfaces and, thus, enables the integration of III-V semiconductors onto the well-established silicon platform. Consequently, the superior optical properties (direct bandgap) and also the superior electrical properties (higher carrier mobilities) of group III-V semiconductors can be combined with the advanced, less expensive silicon technology.

Besides the integration of III-V semiconductors on silicon, the unique nanowire geometry additionally allows the controlled integration of functional heterostructures which can be arranged in axial and radial direction within nanowire heterostructures. Consequently, the paradigm of band structure engineering [7] and the exploitation of quantum-confined systems have been transferred in the recent years from planar heterostructured semiconductors onto the one-dimensional platform of nanowires [8–12] and thereby allow the realization of new device concepts. After first hallmark experiments [8, 9], the realization of fully fledged quantum confined heterostructures such as two-dimensional quantum wells (QW), one-dimensional quantum wires and zero-dimensional quantum dots within the nanowire geometry is continuously growing and, yet, much more demanding than in conventional planar epitaxy [13].

In addition, another property of III-V semiconductors nanowires has attracted increasing attention. While most bulk arsenide-based semiconductor materials crystallize in a zincblende phase, nanowires are often found to be also thermally stable in the form of a wurtzite crystal [14, 15]. Commonly, nanowires have a polytypic nature with a mixed wurtzite/zincblende crystal structure and a high density of stacking faults along their axis.

This crystal phase mixing within nanowires strongly influences the electronic and optical properties due to the underlying type-II alignment of the electronic band structure [16–29]. This, in turn, induces the localization of electrons and holes within different regions and scattering centers along the nanowire axis which certainly lead to new recombination channels and affect carrier transport along the nanowires. Thus, the realization of high performance nanoelectronic and nanophotonic devices requires a great degree of control of the crystal structure.

In particular, these unique properties and the advantages of bottom-up fabrication have been driving forces towards the development of prototypical devices, such as nanowire lasers [6, 30, 31], high-performance avalanche photo-detectors [32, 33] and highly efficient solar-cells [5, 34, 35] as well as tunneling diodes [36, 37] and high-performance wrap-gate transistors [4]. For all these devices, the behavior of electrons and holes within nanowire structures is essential defining the properties of device performance and operation range. Hereby, the charge carrier diffusion length and lifetime as well as the mobilities of electrons and holes have major impact for the optimization of these devices. Consequently, the understanding and the control of charge carrier dynamics within nanowire systems are important for the improvement and design of novel nanoelectronic and nanophotonic devices.

Hereby, acousto-optoelectric spectroscopy is routinely employed to sense and manipulate semiconductor nanowires and, thus, gives direct insights into the charge carrier dynamics by utilizing the acousto-electric coupling between charge carriers and the piezoelectric field of a surface acoustic wave (SAW) [28, 38, 39]. In particular, surface acoustic waves on the nanoscale are known to universally couple to literally any type of system [40]. These Rayleigh surface acoustic waves consist of a transversal and a longitudinal wave component with an elliptical movement of the particles. When these waves [41] propagate on a piezoelectric material, strain induces a gyrating electric electric field. In particular, both, the elliptical motion of the particles and the gyrating electric field occur in the sagittal plane of the wave and correspond to a non zero transverse spin angular momentum and, thus, are remarkably similar to spin-momentum locking [42]. Moreover, in acousto-optoelectric spectroscopy, the electric field efficiently dissociates weakly bound excitons [43, 44] and induces the spatio-temporal dynamics of such dissociated electrons and holes in semiconductor nanowires [28, 45]. This allows to dynamically control the overlap of electrons and holes and, consequently, the radiative emission of nanowires which is modulated in the time domain.

This acousto-optoelectric technique has been performed recently on various semiconductor nanowire heterostructures by transferring such nanowire structures onto piezoelectric $LiNbO_3$ surface acoustic wave chips. In first experiments, the directional and dynamic modulation of the optical emission properties of individual nanowires are driven by radio frequency surface acoustic waves [38]. In addition, by the remote carrier control, charge carriers are accelerated along the axis of nanowire cores and are injected into single quantum dots and defects allowing the triggered photon emission via surface acoustic waves [46, 47]. Moreover, single nanowire quantum dots and optically active dot-like emission centers are dynamically controlled by surface acoustic waves [39, 48, 49]. Finally, by comparing experiments and numerical calculations of the underlying charge carrier dynamics, transport mobilities of electrons and holes, as well as the impact of local potential modulations of individual GaAs/AlGaAs core/shell and halide perovskite nanowires have been studied in the fundamental, native material limit of low carrier density [28, 50].

Within the scope of this thesis, the coupled dynamics of charge carriers within different types of GaAs/(In)GaAlAs nanowire heterostructure systems are investigated by acousto-optoelectric spectroscopy. These results might pave the way for the optimization of future nanoelectronic and nanophotonic devices.

The results of this thesis are organized as follows:

Chapter 2 summarizes the fundamental properties of GaAs/(In)GaAlAs nanowire heterostructures. It describes the crystal structure, the associated properties of the band structure and the resulting optical properties of GaAs nanowires. Moreover, it focuses on the growth of self-catalyzed GaAs nanowires on Si(111) substrates and the realization of nanowire heterostructures using molecular beam epitaxy. Finally, it demonstrates the impact of the structural properties on the optical recombination dynamics and electrical transport properties of radial GaAs-$Al_{0.3}Ga_{0.7}As$ nanowire-quantum well heterostructures by emphasizing the role of the commonly observed variations of the quantum well thickness at different facets.

Chapter 3 introduces the basics of propagating surface acoustic waves and gives an overview of the most important mechanical and electrical characteristics of surface acoustic waves. This includes the solution of the corresponding equations of motion by numerical calculations and finite element modeling for the YZ-cut $LiNbO_3$ material system. In addition, it illustrates the generation of surface acoustic waves on a piezoelectric substrate using so-called interdigital transducers and treats the design and fabrication of samples that allow to optically probe the dynamics of electrons and holes in single semiconductor nanowires. Afterwards, we present the interaction of the electric field of the surface acoustic wave with the optically excited charge carriers and the resulting dynamics.

Chapter 4 is dedicated to acousto-optoelectric spectroscopy. It specifies the basic implementation of the setup and, in particular, addresses the excitation conditions within a surface acoustic wave cycle programming the dynamics of the photo-excited charge carriers. Moreover, it gives a short overview of the state of the art of the major characteristic fingerprints which result from the surface acoustic wave driven charge carriers in almost pristine zincblende nanowires with low rational twin density.

Chapter 5 reports on the transverse spin properties of a Rayleigh-type surface acoustic wave. This manifestation of acoustic spin is strikingly similar to spin-momentum locking, a universal phenomenon arising from evanescent waves. It discusses the observation of the full spin dynamics by detecting ultrafast electron cycloids which are driven by the gyrating electric field of a surface acoustic wave propagating on the surface of a YZ-cut $LiNbO_3$

chip. Hereby, a tubular quantum well embedded within a GaAs-$Al_{0.3}Ga_{0.7}As$ core-shell nanowire heterostructure serves as an ultrafast sensor tracking the full cyclic motion of electrons.

Chapter 6 first presents the implementation of a high-dimensional acousto-optoelectric correlation spectroscopy setup which allows to monitor the time-dependent surface acoustic wave-modulated emission of up to three spectrally isolated decay channels in polytypic GaAs-(Al)GaAs core-shell nanowires. After that, the structural and optical properties of two different types of typical, polytypic nanowires are discussed, which clearly differ in the crystal structure along their axes. Both exhibit characteristic recombination channels which are assigned to different types of spatially direct and spatially indirect transitions. Moreover, it reveals the spatio-temporal charge carrier dynamics between these different recombination channels induced by a piezoelectric surface acoustic wave. Hereby, the observed suppression of the emission and its dynamic temporal modulation show unambiguous fingerprints of the local band edge variations induced by the crystal phase mixing. We corroborate the experimental observations by solving the drift and diffusion equations of electrons and holes which are induced by the surface acoustic wave and demonstrate that the experimental observed fingerprints are well reproduced in the numerical calculations. Finally, second- and third-order correlations are investigated resolving coupled carrier dynamics which reveal an exchange between the recombination channels of both nanowires.

Chapter 7 summarizes this thesis and presents first experiments on a biaxial tensile strained GaAs core which is surrounded by a quaternary $In_{0.3}Al_{0.3}Ga_{0.4}As$ buffer layer. These measurements might indicate a transition of the heavy hole-light hole ground state and similar mobilities of both charge carrier species.

Chapter 2

Semiconductor nanowires: properties and growth

First, epitaxial growth of semiconductor nanowires was studied by R. S.Wagner and W. C. Ellis reporting on the vapor-liquid-solid synthesis mechanism of silicon nano-whiskers [51]. By using gold droplets on a silicon substrate as a catalyst, they realized the self-assembled growth of several micrometer long silicon nanowires with diameters on the order of 100 nm and, thus, founded this very active research area. From this point, this bottom-up approach of one-dimensional growth have gained much interest and was expanded to the III-V materials over the past decades triggering research activities mainly focusing on the fabrication, characterization and application of semiconductor nanowires nowadays [15, 52]. However, using gold droplets as catalysts often results in an unintentional incorporation of impurities which can introduce deep level traps and, thus, compromises the electrical and optical properties of semiconductor nanowires [53–56]. Alternatively, GaAs nanowires can be grown in a self-catalyzed manner by using a gallium droplet as a catalyst [57–61]. Hence, unintentional impurities can be avoided. Moreover, the self-assembled growth of nanowires enables the controlled integration of functional heterostructures within the nanowire geometry which can be arranged in axial direction along the nanowire axis [8, 11, 12] as well as in radial direction by elegantly wrapping complex quantum well-based and multidimensional quantum heterostructures around a typical bulk-like (3D) nanowire core [9, 10]. Consequently, this unique architecture allows both, electronic and optical, confinement along the axis and in the radial direction with respect to their electronic and nanophotonic functionalities. In this sense, contact-free methods, such as photoluminescence spectroscopy, are paramount for characterizing the electronic and optical properties of such nanowire heterostructures.

This chapter gives first a short introduction of the fundamental properties of GaAs nanowires, in particular of the crystal structure, the band structure and the resulting optical properties of GaAs nanowire heterostructures. Subsequently, the self-assembled growth of GaAs-based nanowire heterostructures on silicon substrates by a Ga-assisted vapor-liquid-solid growth using molecular beam epitaxy will be described. Finally, we discuss the impact of commonly observed thickness inhomogeneities of radial quantum well systems in GaAs-$Al_{0.3}Ga_{0.7}As$ core-shell nanowire heterostructures on the optical and electronic properties.

2.1 Crystal structures within semiconductor nanowires

GaAs is nowadays one of the most important materials for nanoelectronic and nanophotonic devices. Like other Group III-arsenides, it mainly crystallizes in a zincblende (ZB) phase in its bulk form which is depicted in Figure 2.1 (a). Zincblende is a cubic structure and is described by two face-centered cubic lattices with a 2-atomic basis. Hereby, one basis consists of Ga atoms, while the other is formed by As atoms, which are shifted by $(\frac{1}{4}a, \frac{1}{4}a, \frac{1}{4}a)$ with respect to each other. Consequently, the atomic layers follow an ABC stacking along the [111] direction (lower panel of Figure 2.1 (a)). In nanowires, however, GaAs is also found to be thermally stable in the form of a hexagonal wurtzite (WZ) crystal structure exhibiting an AB layer stacking in the [0001] direction as shown in Figure 2.1 (b) [18, 62, 63]. Hence, differences of atomic arrangement between zincblende and wurtzite phase occur only at the third-nearest layer. In general, the wurtzite phase formation in nanowires is found to stabilize due to a lower effective surface energy of the accord-

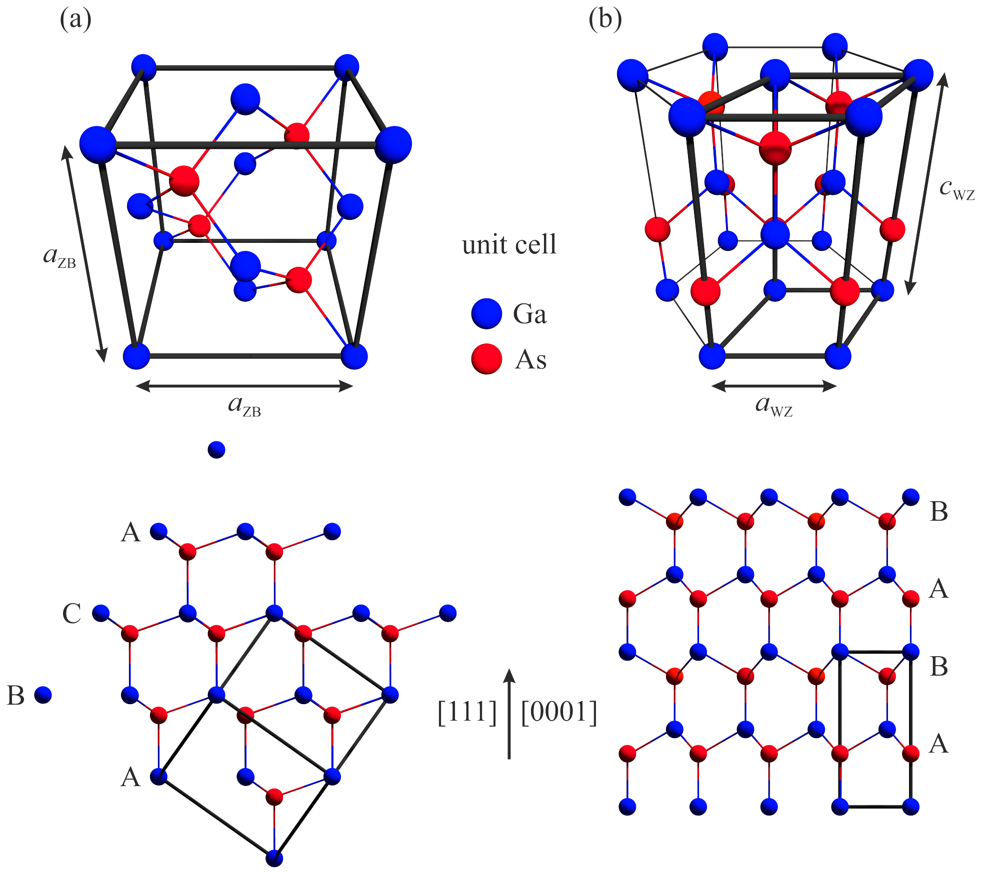

Figure 2.1: Two different types of crystal structures typically occur in GaAs nanowires. (a) The zincblende crystal structure consists of a cubic unit cell. (b) The wurtzite crystal structure shows clearly a hexagonal symmetry. The upper panels show the unit cell of the two crystal structures. The lower panels show the stacking sequences in nanowire growth direction: [111] for zincblende and [0001] for wurtzite phase.

ing wurtzite sidewalls compensating the bulk energy difference between the wurtzite and zincblende phase [64].
As a consequence of two stable crystal structures, nanowires often crystallize in a polytypic nature with an intermixing of both structures and a high density of stacking faults which results in a highly disordered arrangement of layers. In the zincblende phase, the rotation of a single layer by 60° creates a twin plane and the original crystal structure maintains, yet is rotated by 60°. Moreover, a sequence of two consecutive twin planes will result in a transition from zincblende to wurtzite phase [63]. As both structures are similar, a stacking fault in one crystal structure can be regarded as a single segment of the other structure. In particular, several energetic and kinetic factors have significant impact on the stacking sequences along the axis of a nanowire and, thus, the formation of a specific crystal phase during the nucleation of an atomic layer. Thereby, the supersaturation within the droplet, the nucleation site of each layer and the interfacial energies between the different boundaries play an important role [65–68].

Moreover, zincblende and wurtzite semiconductors are known to have different band structures [69]. Consequently, crystal phase mixing along the axis of a nanowire causes a modulation of the band structure which affects the electronic and optical properties of nanowires which are discussed in the following sections.

2.2 Band structure and optical properties of GaAs

The electronic band structure of zincblende GaAs near the fundamental bandgap is schematically depicted in Figure 2.2 (a). For semiconductors, the highest band, which is completely occupied by electrons at $T = 0$ K, is called valence band (VB), while the next allowed band, the conduction band (CB), which is separated by an energy gap E_g, is completely unoccupied at $T = 0$ K. For GaAs, the valence band maximum is located at Γ-Point exhibiting there three sub-bands. Two of these sub-bands are degenerated, yet having different curvatures and, thus, different effective masses m^*. For this reason, the more weakly curved band is referred to as the heavy-hole (HH) band, whereas the more curved as the light-hole (LH) band. Furthermore, the third sub-band is energetically separated by Δ_{SO} due to spin-orbit-coupling and forms the so-called split-off (SO) band. The splitting at the top of the valance band arises from primarily p-type states having an orbital angular momentum of $\hbar$ leading to a strong interaction of the electron spin and the orbital motion and, thus, the splitting of the valance band into sub-bands. The conduction band of GaAs exhibits three local minima at the high symmetry X-, Γ- and L-point of the reciprocal space with the global minimum being located at the Γ-point. As both valance band maximum and conduction band minimum are at the Γ-point, zincblende GaAs is a so-called direct semiconductor with a bandgap E_g. The band structure of wurtzite GaAs is more complicated than that of zincblende. In particular, a lower symmetry of the wurtzite lattice leads to crystal fields which additionally split the valance band at the Γ-point [69–71]. Consequently, the degeneracy of the heavy-hole and light hole bands at the Γ-point is

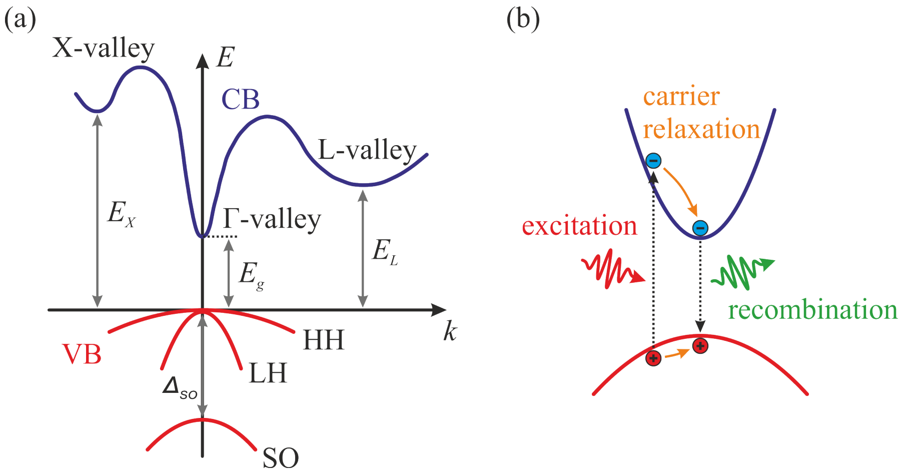

Figure 2.2: (a) Schematic of the zincblende GaAs band structure with a direct bandgap at the Γ-point. (b) Schematic illustration of photoluminescence. Electron-hole pairs are excited above the bandgap by absorbing photons with an energy larger than the bandgap. Charge carriers relax by emitting phonons and reach the lowest energetic states in the conduction and valance band, respectively. Electron-hole pairs can recombine by emitting a photon. The emitted light provides information about distribution of carriers and quantized energy levels of the nanostructure.

lifted by the influence of the crystal field and the spin-orbit interaction. Moreover, GaAs in the wurtzite phase still is a direct bandgaps semiconductor [69–71]. However, the exact bandgap energy of wurtzite GaAs is still controversially discussed in literature [20, 21, 69, 72–81].

In semiconductors, the band structure near the conduction band minimum and the valance band maximum can be approximately described by parabolic dispersion relations:

$$E(k) = E_0 + \frac{\hbar^2 k^2}{2m^*} \tag{2.1}$$

where m^* is the effective mass being related to the curvature of the dispersion relations $E(k)$:

$$m^* = \hbar^2 \left(\frac{\mathrm{d}^2 E(k)}{\mathrm{d}k^2} \right)^{-1} . \tag{2.2}$$

This approach of an effective mass allows to treat the motion of charge carriers in the conduction and valance band as the motion of free charge particles, yet considering the interaction with the periodic potential of the crystal lattice.

Moreover, information on the band structure as well as the charge carrier dynamics in semiconductors can be examined by photoluminescence (PL) spectroscopy being one of the fundamental optical spectroscopy techniques. The principle of the photoluminescence process is depicted in Figure 2.2 (b). First, electrons in the valance band are excited to the conduction band by absorbing a photon with an excitation energy $\hbar\omega$ which is larger than the bandgap E_g. This leaves the initial states of the electrons in the valance band unoccupied and the missing electrons can be regarded as positive charged quasi-particles, so-called holes. After separation, both types of charge carriers rapidly relax to their respective band edges minimizing their energy by emitting phonons. If an electron in the conduction band and a hole in the valance band are located at the same position in the real and reciprocal space of the crystal, both charge carriers can spontaneously recombine by emitting a photon with the energy E_g. Such radiative recombination in GaAs usually occurs on the timescale of nanoseconds and is much slower than the phononic relaxation which is in the 100 fs range [82].

The absorption and emission of photons can be theoretically described by the time-dependent perturbation theory with a weak perturbation which is associated with the light wave. According to Fermi's golden rule, the transition rate between the state $|i\rangle$ and the state $\langle f|$ which are separated by an energy difference $\hbar\omega$, is given by [82, 83]

$$\Gamma_{i\to f} = \frac{2\pi}{\hbar} \left|\langle f \left| H' \right| i\rangle\right|^2 g(\hbar\omega) \tag{2.3}$$

which depends on the transition matrix element $|\langle f \left| H' \right| i\rangle|$ and the joint density of states $g(\hbar\omega)$. The transition matrix element describes the effect of the perturbation H' which is caused by an electromagnetic wave on the band electrons. In particular, the corresponding Hamiltonian can be approximated the electric dipole interaction:

$$H' = \mathbf{p}_e \cdot \mathbf{E}_0 \tag{2.4}$$

where $\mathbf{p}_e = -e\mathbf{r}$ and $\mathbf{E}_0$ are the electric dipole moment of an electron and the electric field amplitude, respectively. Moreover, the joint density of states is the total number of states in the conduction and valence bands which are connected by a vertical optical transition, and considers the fact that the initial and final states lie within continuous bands. The 3D joint density of states of the electron-hole system with a reduced effective mass $\mu = \left(\frac{1}{m_e^*} + \frac{1}{m_h^*}\right)^{-1}$ is given by:

$$g_{3D}(\hbar\omega) = \frac{1}{2\pi^2} \left(\frac{2\mu^*}{\hbar^2}\right)^{3/2} \sqrt{\hbar\omega - E_g} \tag{2.5}$$

Taken together, this results in a constant transition rate of an excited state and, consequently, the excited state X exponentially decays with the rate $1/\tau$:

$$X(t) = X_0 \cdot exp\left(-\frac{t}{\tau}\right) \tag{2.6}$$

where X_0 describes the initial occupation. Hence, if the expanding wave functions of electron and hole overlap in the real and reciprocal space, both charge carriers recombine with a radiative lifetime τ_r.

At low temperatures, the excited electron and the corresponding hole often form due to the attractive Coulomb interaction a bound quasi-particle, a so-called exciton. It cannot move independently through the crystal and is in first approximation not affected by an external electric field as a consequence of its neutral character. However, by applying large electric fields, excitons can be efficiently dissociated resulting in the spatial separation of electrons and holes. The energy of the excitonic transition is lowered by its binding energy which is given in analogy to a hydrogen atom by:

$$E_X = \frac{e^4}{32\pi^2\hbar^2}\frac{\mu}{\epsilon^2} \approx 4.6 \text{ meV} \tag{2.7}$$

where μ is again the reduced effective mass ($1/\mu = 1/m_e^* + 1/m_h^*$) and ϵ the dielectric constant of the material ($\epsilon = 12.9 \cdot \epsilon_0$ for GaAs), respectively. Moreover, the calculated exciton energy E_X is in good agreement with experimentally observed values for bulk GaAs ($E_X = 4.2$ meV [84]). The size of an exciton is determined by the Bohr radius:

$$r_X = \frac{4\pi\hbar^2}{e^2}\frac{\epsilon}{\mu} \approx 12.2 \text{ nm} \tag{2.8}$$

and, thus, is larger than the lattice spacing of the crystal.

2.3 Engineering the bandgap of semiconductor nanowires

To achieve the design of new semiconductor materials and devices, the electrical and optical properties of a semiconductor system can be tuned by the concept of bandgap engineering, which is the spatial tailoring of the band structure allowing arbitrary and continuous bandgap variations [7]. For GaAs nanowires, two basic bandgap engineering methods can be considered.

In the first case, the local band structure is determined by the composition profile of ternary semiconductors, such as $\mathrm{Al}_x\mathrm{Ga}_{1-x}\mathrm{As}$. In particular, $\mathrm{Al}_x\mathrm{Ga}_{1-x}\mathrm{As}$ is technologically important since GaAs and $\mathrm{Al}_x\mathrm{Ga}_{1-x}\mathrm{As}$ form over the entire ($0 \leq x \leq 1$) composition range a heterostructure with very little variation of lattice constant of well below 1%. Hence, this allows the growth of multilayers with a very high quality. Thereby, the bandgab can be tuned by the Al content in $\mathrm{Al}_x\mathrm{Ga}_{1-x}\mathrm{As}$ between $E_g = 1.519\,\mathrm{eV}$, for the case of pure GaAs ($x = 0$), and $E_g = 3.099\,\mathrm{eV}$ for pure AlAs ($x = 1$) at low temperatures ($T = 8\,\mathrm{K}$). Note, a reversal of the band ordering of $\mathrm{Al}_x\mathrm{Ga}_{1-x}\mathrm{As}$ occurs at around $x = 0.4$ which results in a transition from a direct to an indirect bandgap semiconductor. Thus, a variable direct bandgap is obtained for the range $x < 0.4$ while for $x > 0.4$ the bandgap is indirect.

This controlled adjustment of the bandgap and the epitaxial deposition of different material layers with high quality can be used for the realization of different types of potential profiles in semiconductor heterostructures. In the case of the GaAs - $\mathrm{Al}_x\mathrm{Ga}_{1-x}\mathrm{As}$ heterointerfaces, a so-called type-I band alignment can be realized. As shown in Figure 2.3 (a),

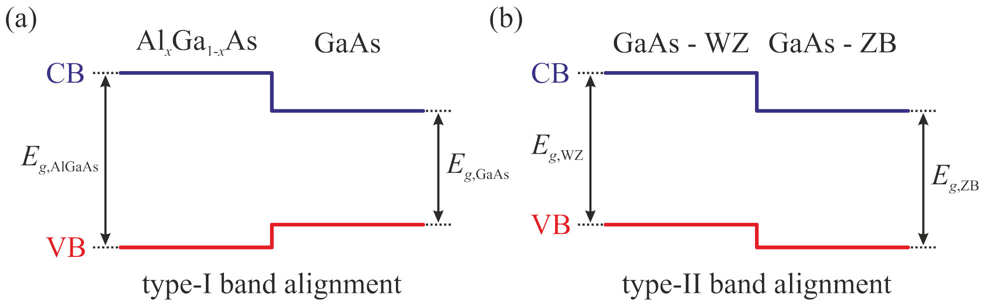

Figure 2.3: Band offsets and alignments typically occurring in epitaxial grown GaAs semiconductor nanowires. (a) In type-I heterostructures, the narrow gap material, such as GaAs, is completely enclosed by the wider gap material like Al$_x$Ga$_{1-x}$As. Electrons and holes are trapped in the narrow bandgap material. (b) In type-II systems, the lowest conduction band edge is in one material (GaAs - ZB) while the highest valence band edge is in the other material (GaAs - WZ). The lower conduction band exceeds the higher valence band. Electrons and holes are located in different materials and, thus, spatially separated.

the conduction and valance band edges of the smaller bandgap material GaAs are in the bandgap region of the larger bandgap material Al$_x$Ga$_{1-x}$As. Consequently, both electrons and holes are trapped in the narrow bandgap GaAs layer. By enclosing the narrow gap material completely by the wider gap material, it is possible to confine the electronic states in semiconductors and realize lower dimensional systems which are discussed in the following section (see Section 2.4). In nanowires, this is usually realized by wrapping multishell heterostructures in radial direction around the nanowire core [9, 10].

Secondly, the band structure of GaAs nanowires can be varied due to the polytypic nature of the crystal structure. Since the zincblende and wurtzite phase differ from each other in their bandgap, the switching between both allows to modulate the bandgap along the nanowire axis resulting in heterostructures with complex optical properties. In particular, the value of the bandgap energy of wurtzite GaAs is controversially discussed. On the one hand, theoretical and experimental investigations suggest that the bandgap of wurtzite GaAs is increased by 30 to 55 meV compared to the one of zincblende GaAs [21, 72–77]. On the other hand, it is reported that the bandgap of wurtzite GaAs is slightly smaller or similar to the bandgap of zincblende GaAs [20, 69, 78–81]. However, most agree that the wurtzite-zincblende interface in GaAs nanowires forms a type-II band alignment. As depicted in Figure 2.3 (b), the valence and conduction band of the wurtzite phase are energetically raised compared to the zincblende structure. As a consequence of the type-II band alignment, electrons are accumulated in the conduction band of the zincblende phase, whereas the holes are trapped in the valence band of the wurtzite phase. Hence, electrons and holes are spatially separated and electron-hole pairs located at the wurtzite/zincblende interface give rise to a spatially indirect recombination. This spatially indirect recombination is consequently at lower energies and occurs on longer timescales than the transition in pure zincblende GaAs [18].

2.4 Low-dimensional semiconductor systems

Low-dimensional quantum structures can be realized by embedding a smaller bandgap semiconductor in a higher bandgap matrix such as it is formed by an AlGaAs-GaAs-AlGaAs structure. Thereby, the quantum mechanical confinement becomes important, when charge carriers (electrons and holes) are localized in structured regions of nanometer length scales influencing the energy states and, thus, the optical properties of the semiconductor heterostructures. In Figure 2.4, the band diagram as well as the photoluminescence process of a quantum well are schematically shown. The one-dimensional confinement of the quantum well results in a number of bound electron states and bound hole states (for both heavy and light hole valence bands) which are depicted by black dotted lines. These states can derived from the Schrödinger equation:

$$\left[-\frac{\hbar^2}{2m^*}\nabla^2 + V(z)\right]\Psi = E\Psi \tag{2.9}$$

where the confinement potential $V(z)$ in the z-direction (growth direction) can be approximately described by an infinite potential barrier of width d:

$$V(z) = \begin{cases} 0 & \text{for } -\frac{d}{2} \leq z \leq \frac{d}{2} \\ \infty & \text{for } z > |\frac{d}{2}| \end{cases} \tag{2.10}$$

The solutions for this well known problem are discrete energy levels $E_z^{e,h}$ in the direction of confinement with an energies spacing:

$$E_z^{e,h} = \frac{\pi^2\hbar^2}{2m^*_{e,h}}\frac{n_z^2}{d^2} \tag{2.11}$$

which increases with the quantum number $n_z = 1,\, 2,\, 3, \ldots$ and with decreasing width d. Since no further confinements exist in the x- and z-direction, particle motion in x- and y-

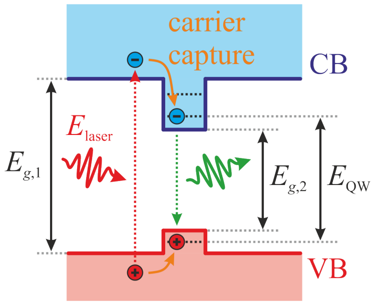

Figure 2.4: Band structure and photoluminescence process of a quantum well: The optically excited charge carriers relax to their lowest energetic states and are captured into the quantum well. Electrons and holes can radiatively recombine through photon emission.

direction is still continuous and the quantum well still has continuous energy bands which are split into subbands. Moreover, for real semiconductor quantum wells the potential barrier is not infinite and, thus, the wavefunction decays exponentially into the higher bandgap material.

The energy states of a semiconductor quantum well can be probed by photoluminescence spectroscopy as shown in Figure 2.4. An above bandgap laser excites electron hole pairs in the bulk material. Both charge carriers relax to their respective energetically lowest energetic state and are captured into quantum well on a timescale below 100 ps. Finally, both electrons and holes can recombine within the characteristic decay time by emitting a photon which is than detected.

2.5 Epitaxial growth of semiconductor nanowire heterostructures

Molecular beam epitaxy is frequently used for the growth of a great variety of high purity semiconductor nanostructures, such as thin film heterostuctures, quantum dots and nanowires. In particular, its slow growth rates and ultra-high vacuum conditions allow a high control of layer thickness and result in ultra pure materials. Moreover, growth can be monitored by in-situ analysis techniques such as reflection high energy electron diffraction allowing the excellent control of nanowire nucleation and growth rate with sub monolayer precision being essential for nanowire growth. The basic principles concerning nanowire growth and growth substrate preparation are presented in the following sections.

The nanowires used in this thesis were grown by Daniel Rudolph, Bernhard Loitsch and Paul Schmiedeke in the research group of Gregor Koblmüller at the Walter Schottky Institute (WSI, TU Munich).

2.5.1 Self-catalyzed growth of GaAs nanowires

The nanowires characterized in this thesis are grown by molecular beam epitaxy on a silicon wafer which is covered with a silicon oxide mask. The Veeco GEN II MBE system being used is equipped with solid effusion cells for Al, Ga and In supply and a valve cracker cell for As_4 supply. The background pressure is in the low 10^{-11} mbar range. Before the growth of nanowires, appropriate substrates have to be prepared and the definition of specific nucleation sites is essential. Therefore, commercially available Si(111) wafers were single-side polished and covered by a uniform, thermally grown silicon dioxide (SiO_2) film with a thickness of about 20 nm. Subsequently, the SiO_2 film on top of these wafers is thinned down to a thickness of 1-2 nm in a wet-chemical etching step using a buffered hydrofluoric acid solution. This self-assembled process will open nanometer size pinholes in the porous oxide layer which act as nanowire nucleation sites. Growth was initiated by a 5 min pre-exposure to As_4, followed by Ga atoms supply. At high growth temperatures of about 630°C, the vapor pressure of As is increased with respect to Ga and leads to the

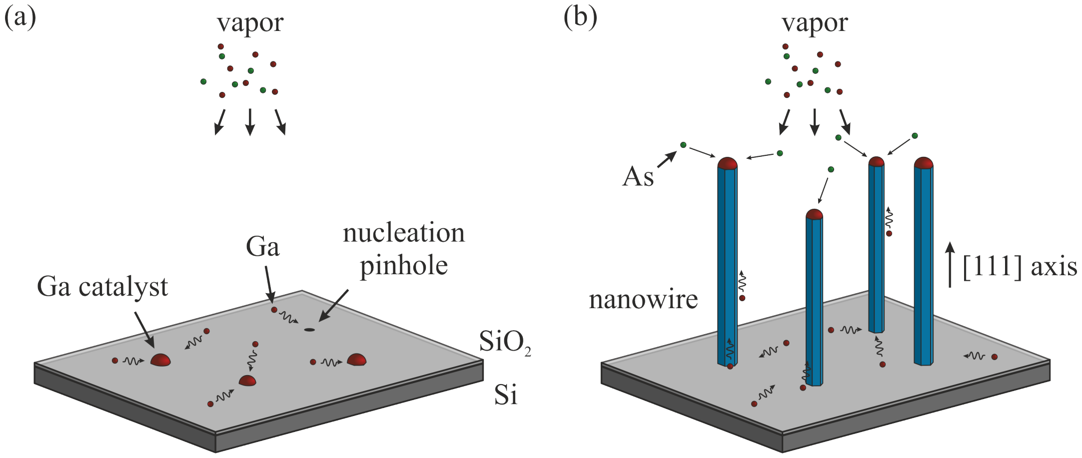

Figure 2.5: Schematic of the vapor-liquid-solid-type axial growth process of GaAs nanowires. (a) Nanometer-sized pinholes in the SiO_2 act as nucleation sites for self-catalyzed nanowire growth by collecting Ga atoms diffusing on the SiO_2 surface into Ga droplets. (b) As atoms are absorbed by the Ga droplet from the vapor forming crystalline GaAs at the solid–liquid interface at the bottom of the droplet. This leads to the epitaxial growth of GaAs nanowires. Ga atoms diffusing on the SiO_2 surface and along the nanowire sidewalls enrich the Ga droplets.

desorption of the As_4 molecules impinging on the SiO_2 surface. Consequently, the SiO_2 surface becomes enriched by Ga atoms and Ga droplets are formed at the nanometer size pinholes due to the enhanced diffusion length of the Ga atoms as shown in Figure 2.5 (a). Subsequently, the As atoms are absorbed by the Ga droplets and alloy with Ga atoms, thereby forming GaAs. As soon as the droplet becomes supersaturated, the III-V material precipitates at the liquid-solid interface due to its higher melting point. As a consequence, the nanowires start to grow containing the droplet on its tip as shown in Figure 2.5 (b) [57]. During growth, the Ga droplets are constantly enriched by Ga atoms diffusing on the SiO_2 surface and along the nanowire sidewalls. Due to the orientation of the underlying silicon substrate, the vertically aligned nanowires grow along the [111] growth direction. Moreover, they exhibit a hexagonal cross-section with six sidewall facets related to either the {110} or {112} family of planes.

Importantly, the nanowire growth is mainly controlled by the following three parameters: the growth temperature, the V/III flux ratio and the growth time. The exact growth temperatures, material fluxes and growth times of the nanowires measured in this thesis can be found in the Appendix. Further details on the synthesis and the influence of the parameters on the morphology can be found elsewhere [61, 85–87]. As shown by the high resolution transmission electron microscopy images of Figure 2.6 (a,b), the crystal structure of self-catalyzed GaAs nanowires can vary from a near-pristine zincblende phase (with ABC stacking sequences) with individual rational twin defects (marked by alternating ZB-A and ZB-B segments in (a)) to a highly polytypic crystal structure with short zincblende and wurtzite segments (with AB layer stacking in (b)). Moreover, the structure changes from nanowire to nanowire leading to differences in the sequences of wurtzite and zincblende phases along the nanowires. In particular, it has been shown that

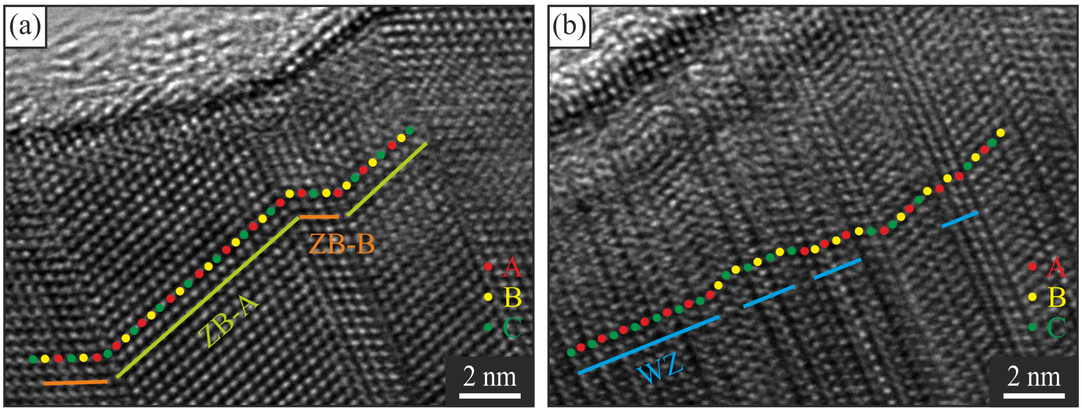

Figure 2.6: High resolution transmission electron microscopy images of characteristic layer stacking usually occurring in as-grown GaAs nanowires. (a) This region of a representative nanowire exhibits a zincblende crystal structure and individual rotational twinning defects (marked by alternating ZB-A and ZB-B segments). (b) The transmission electron microscopy image corresponds to a region with several twin defects and extended wurtzite segments. The layer stacking (A, B and C) is marked by red, yellow and green dots.

the V/III ratio has a great impact on the growth rate and the crystal structure of the self-catalyzed GaAs nanowires [18, 57, 60, 61, 88]. A low V/III ratio induces the growth of nanowires with a high density of stacking faults and an unordered crystal structure with short zincblende and wurtzite segments along the nanowire axis. In contrast, a high V/III ratio will result in predominantly zincblende phase nanowires with only few rotational twinning defects and continuously increases the nanowire growth rate. However, there exist only few studies on the influence of growth temperature on crystal structure of self-catalyzed GaAs nanowires [60, 88, 89]. For vapor-liquid-solid grown nanowires, the formation of a specific crystal structure is related to the nucleation at the triple-phase-line between the vapor, the droplet and the Si substrate and depends on supersaturation within the droplet, and, consequently, on the V/III ratio [65–68].

Additionally, the underlying substrate plays a crucial role on the growth kinetics of nanowires. As a spontaneous growth without any additional prepatterning of the substrate has been employed in this thesis, the nanowire growth mainly results in a random, non-periodic distribution of nanowires on the silicon substrate. Typical scanning electron microscopy micrographs of such random grown nanowires are depicted in Figure 2.7 (a,b). They clearly show variations in the interwire distance and a broad size distribution for the nanowire length and diameter as well as a slight tilt from the perfect vertical alignment. On the one hand, for short nanowire distances, growth is limited by material competition as illustrated in Figure 2.7 (c) [90, 91]. Hereby, neighboring nanowires compete for Ga adatoms diffusing on the SiO_2 surface and the collection of Ga atoms impinging on the nanowire sidewall facets. As a consequence, subsequent diffusion along the facets to the Ga droplet is shadowed by neighboring nanowires and, thus, these two mechanisms lead to a decrease in both vertical and radial growth rate. For large interwire distances, nanowire growth is no longer limited by material competition and occurs in

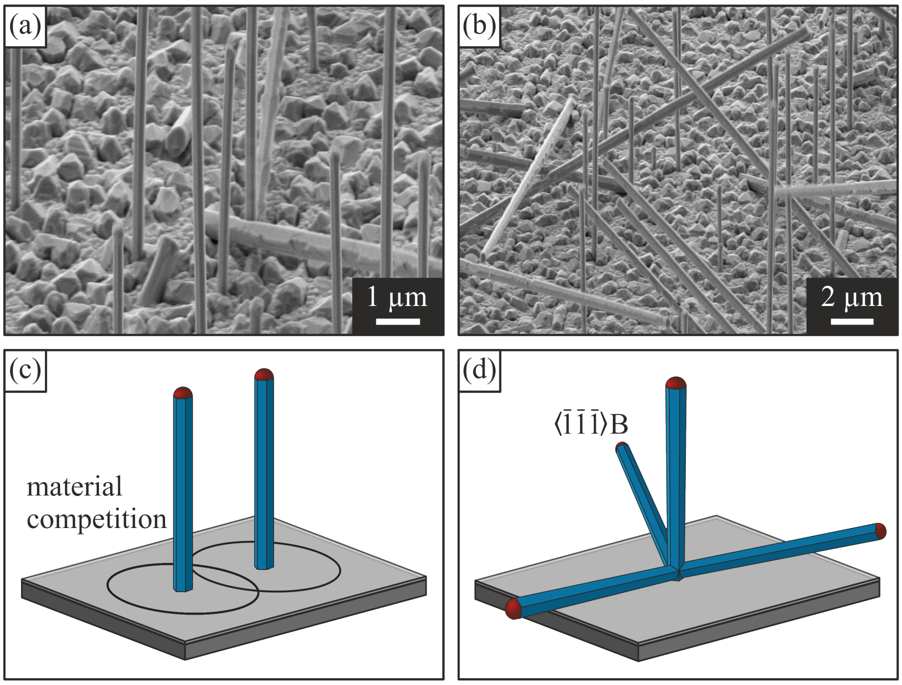

Figure 2.7: (a,b) Scanning electron microscopy images of GaAs-$Al_{0.3}Ga_{0.7}As$ nanowires randomly grown by molecular beam epitaxy on the same Si(111) substrate. (c) The schematic illustrates nanowire growth in the competitive regime leading to distinct growth rate anisotropies. The black lines indicate the available surface collection area of the corresponding nanowires. (d) Schematic of the expected nanowire growth directions on a Si(111) substrate. It shows three equivalent ⟨111⟩ growth directions forming an angle of 19.6° with respect to the surface of the substrate and having an angle of 120° from each other as well as the coexisting, vertically aligned [111] growth direction. Both effects lead to the commonly observed characteristic inhomogeneities of the axial and radial growth of nanowires.

diffusion-limited regime [90, 91]. In order to avoid inherently random interwire spacing, the nucleation sites can be prepatterned by using specific lithography, most notably electron beam lithography and nanoimprint lithography. On the other hand, such bottom-up synthesized nanowires often exhibit a slight tilt from the perfect vertical alignment as predominantly displayed in the scanning electron microscopy image of Figure 2.7 (b). In general, nanowire growth was induced on a (111)-orientated Si substrate and, thus, is expected to occur along the four equivalent ⟨111⟩B directions of the Si substrate due to the non-polarity of Si (see Figure 2.7 (d)) [92–94]. The main direction is oriented perpendicular to the surface, while the other three orientations form an angle of 19.6° with respect to the surface of the substrate having an in-plane angle of 120° from each other. The combination of these effects, variation of the interwire distance and the tilt from the perfect vertical alignment, typically leads to the commonly observed characteristic inhomogeneities of the axial and radial growth of nanowires.

Beside the synthesis of pure GaAs nanowires, the vapor-liquid-solid growth mechanism allows to partially substitute ternary partner during axial growth. By using a source for another atomic group-III element, such as indium, it is possible to incorporate indium into the Ga droplet and, thus, self-catalyzed growth of $In_xGa_{1-x}As$ segments can be realized. However, the incorporation of In into the Ga droplet is significantly delayed and limited to less than 5% during growth, complicating the formation of sharp axial material boundaries of nanowire heterostructures [95]. Instead, higher In contents can be achieved by the arsenic-rich non-vapor-liquid-solid growth regime based on the direct nucleation of the wire without the formation of a droplet [96–100].

In contrast to vapor-liquid-solid growth regime, in the catalyst-free or non-vapor-liquid-solid growth nanowires are directly synthesized from the gas phase by changing the V/III ratio to As-rich conditions. Thereby, growth is mainly governed by the highly anisotropic growth rates of the different facets. In particular, the growth rate along the axial {111} facets is much higher compared to the {110} sidewall facets [96, 101, 102].

2.5.2 Properties of nanowire heterostructures

The geometry of nanowires allows the growth of functional, radial core-shell nanowire heterostructures by the radial overgrowth of the nanowire core opening up new possibilities to tailor the optical and electronic properties of nanowires [9]. In particular, it is possible to implement fully fledged quantum confined heterostructures such as two-dimensional quantum wells, one-dimensional quantum wires and zero-dimensional quantum dots within the nanowire geometry. Hence, several different nanowire heterostructures with different degrees of quantum-confinement can be realized. Three different configurations of nanowire heterostructures are schematically depicted in Figure 2.8.

In contrast to the vapor-liquid-solid core growth, the radial growth of the shell occurs in the non-vapor-liquid-solid growth regime. After the growth of the GaAs nanowire core is completed, the substrate temperature is reduced to a shell growth temperature of $T = 420 - 490°C$ while the As_4 flux is increased to As-rich conditions. This results in the crystallization of the Ga droplet and prepares the subsequent radial shell growth along the {110}-oriented sidewall facets. Afterwards, growth of a radial $Al_{0.3}Ga_{0.7}As$ shell is initiated by simultaneously opening the Al and Ga shutters. Note that the shell overgrowth also induces an axially growth along the [111] direction on top of the nanowire core and leads to Al-rich stripes which evolve along the [112] directions across the entire shell thickness being characteristic for a nonplanar overgrowth with facet-dependent differences of the surface free energy [85]. Moreover, shadowing effects and material competition during shell overgrowth give rise to distinct growth rate anisotropies and, hence, to fluctuations of the layer thicknesses on different sidewall facets, resulting in deviations of the perfectly symmetric hexagonal cross-section.

The overgrowth of a $Al_{0.3}Ga_{0.7}As$ shell allows to improve the electronic and optical properties of nanowires. In nanowires, surface states act as non-radiative recombination centers for free carriers and considerably influence the intrinsic properties, in particular, due to their large surface to volume ratio [103–105]. Consequently, the surface passivation of a 3D-bulk like core by the higher bandgap material AlGaAs (as shown in the left panel of Figure 2.8) plays an important role and is an efficient method to increase the radiative

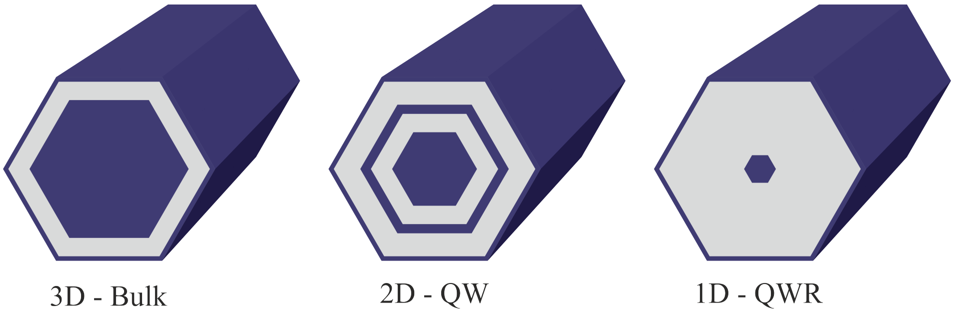

Figure 2.8: Schematics of different core–shell GaAs–AlGaAs nanowire heterostructures (GaAs: blue; AlGaAs: grey) with different degrees of quantum-confinement. The dimensionality reduces from a classical 3D-bulk like structure to a radial quantum well heterostructure (2D) and a quantum wire heterostructure (1D).

efficiency of electronic and optical nanowire devices [85, 106–108]. Moreover, the possibility to epitaxially overgrow nanowires and the ability to form abrupt interfaces in radial direction enable more advanced heterostructures such as multi-shell or radial quantum well nanowires (see center panel of Figure 2.8). By embedding GaAs quantum wells in an AlGaAs shell barrier, optically highly active structures can be integrated into the nanowire based systems enabling spectral tuning of the emission wavelength and increasing their efficiency. Nanowires with 1D-electronic structure (right panel of Figure 2.8) can be realized by reverse-reaction growth step [87, 109–111]. After the self-catalyzed vapor-liquid-solid growth of the nanowire core, the nanowires are thinned down by the subsequent thermal decomposition of the {110} sidewall surfaces at higher temperature. This realizes ultrathin GaAs nanowires with diameters below 10 nm. Afterwards, these ultrathin nanowires are passivated by an AlGaAs shell.

Finally, all GaAs-AlGaAs core-shell heterostructures were further overgrown by a GaAs cap layer to prevent oxidation of the AlGaAs after transfer to air.

2.6 Breakdown of corner states and carrier localization in nanowire quantum wells [1]

Radial core-multishell heterostructures play an important role for the realization of high-performance nanoelectronic and nanophotonic devices [3–6, 31]. In particular, complex quantum well based and multi-dimensional quantum heterostructures can be wrapped around a typical bulk-like nanowire core [112–114] being quite useful for high-performance nanowire lasers [31, 115, 116] and light-emitting diodes [3], nanowire photodetectors [117], as well as novel transistors [4, 27] and platforms for quantum transport investigations [118]. Therefore, a perfection down to the monolayer accuracy is required. However, in nanowires and nanowire based heterostructures, the less favorable growth conditions on the {110}

---

[1] mainly published and with permission from [13]. Copyright 2019 American Chemical Society (ACS AuthorChoice and Creative Commons).

side facets of the nanowire often result in pronounced structural and compositional variations within ternary compounds and at interfaces of such heterostructures [39, 85, 118–121]. In addition, pronounced thickness fluctuations [113, 122] and deviations from a perfect hexagonal cross-section of the nanowire core [113, 115, 123–125], which are directly transferred to the radial shell, frequently occur in such radial heterostructure quantum well systems. This even leads in the limit of thin quantum wells with thicknesses below 4 nm to the formation of unintentional quantum dots [48, 126, 127]. Moreover, facet-dependent growth anisotropies result in the emergence of nontrivial extended shapes [122] or the formation of nanoscale islands [128]. Despite these clear evidences, most theoretical work has focused on symmetric hexagonal shapes of quantum wells embedded in nanowire heterostructures [113, 124, 125, 129–131] and only few descriptions exist for realistic, asymmetric radial quantum well structures [132–134]. As known from planar quantum well based heterostructures, these commonly observed imperfections are expected to influence on the optical [135–137] and electrical properties [138] of nanowire heterostructures.

In this section, we demonstrate that commonly observed imperfections of a realistic, asymmetric ring cross-section of radial GaAs-$Al_{0.3}Ga_{0.7}As$ quantum wells have major impact on the optical and electrical characteristics of nanowire-based heterostructures. We show, that typical well width fluctuations of radial quantum wells result in spatially separated, yet interconnected quantum well systems exhibiting line broadening and a multi-peak structure of the emission. Moreover, theoretical calculations predict that even minute deviations of the perfect hexagonal shape of a quantum well will lead to the localization of electrons and holes on the thickest sidewall facet of the quantum well in contrast to a symmetric hexagonal quantum well where electrons and holes are delocalized between all corners.

The main results of this section were published in Nano Letters under the title "Breakdown of Corner States and Carrier Localization by Monolayer Fluctuations in Radial Nanowire Quantum Wells" [13]. The theoretical calculations were performed in collaboration by Anna Sitek at Reykjavik University, Iceland and Wrocław University, Poland. Moreover, transmission electron microscopy measurements were conducted by Markus Döblinger at Ludwig-Maximilians-Universität in Germany.

2.6.1 Asymmetric nanowires and their optical properties

The studied core-multishell nanowires consist of a GaAs core with a length exceeding 10 µm and a diameter of 60 nm which is surrounded by a 30 nm thick $Al_xGa_{1-x}As$ shell with a nominal Al-content of 30%, followed by a 5 nm thick radial GaAs quantum well and a 70 nm thick $Al_xGa_{1-x}As$ layer. This results in a tubular GaAs quantum well embedded between two $Al_{0.3}Ga_{0.7}As$ barriers. For passivation, a GaAs capping layer of 5 nm has been added to prevent the oxidation of the outer $Al_{0.3}Ga_{0.7}As$ shell. The resulting heterostructure is similar to the schematic shown in the center panel of Figure 2.8. Moreover, the growth conditions predominantly give rise to a zincblende crystal phase with few rational twin defects. As already mentioned and shown in scanning electron microscopy images of Figure 2.7 (a,b), we employed spontaneous nucleation on the growth substrate without any additional prepatterning. This straightforward bottom-up approach typically results in the random nucleation of nanowires and, thus, in variations in the interwire distances and a slight tilt from the perfect vertical alignment [114, 139–141]. Both effects typically result in the commonly observed inhomogeneities of the axial and radial growth of nanowires. In particular, nearby nanowires (due to variations in interwire distance) [90, 91, 142, 143] or the slight mis-orientation from exact vertical growth [144] may partially shadow the radial growth of certain side facets. In contrast, other facets are exposed to comparatively more growth species which give rise to distinct growth rate anisotropies, and hence fluctuations of the layer thicknesses on different sidewall facets. Finally, this leads to deviations of the perfectly symmetric hexagonal cross-section of the quantum well embedded in a nanowire.

In order to get a deeper understanding of size and the microstructure of the asymmetric nanowire heterostructure, cross-sectional scanning transmission electron microscopy in high-angle annular dark field mode (STEM-HAADF) was performed on three representative nanowires, referred to NW1, NW2 and NW3, along the [111] zone axis. The cross-sectional scanning transmission electron microscopy images are depicted in Figure 2.9. Due to atomic number sensitive contrast of STEM-HAADF images, the GaAs quantum well appears brighter than the $Al_{0.3}Ga_{0.7}As$ shell. In addition, the AlGaAs shell exhibits six dark stripes which range from the six corners of the nanowire core across the AlGaAs shell and result from regions with high Al-content. The cross-sectional images of the nanowires confirm a clear distortion of the perfect hexagonal quantum well system and the core as well as pronounced variations of the quantum well thickness on the six sidewall facets. The obtained values of the thickness variations are depicted in Table 2.1. We found an extracted average thickness of the radial quantum well to be $\langle d \rangle = 5.5\,\text{nm}$ for NW1 and NW2 and 5.3 nm for NW3 which are slightly increased to the nominal value of 5 nm. In addition, the thicknesses of the quantum wells on the different sidewall facets clearly fluctuate for all three nanowires. The width of the different facets varies between 3.5 nm and 7.1 nm for the NW1, while the quantum well thickness of NW2 and NW3 ranges from 4.2 nm to 6.4 nm and from 4.3 nm to 6.2 nm, respectively. Moreover, the two thickest quantum wells

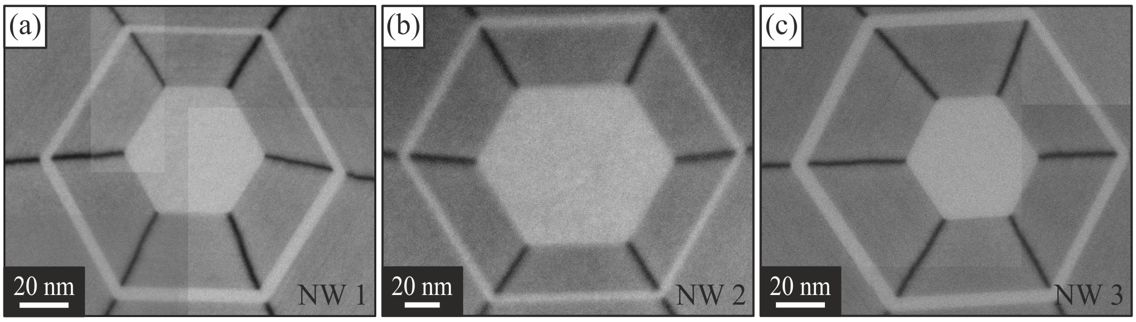

Figure 2.9: (a-c) STEM-HAADF cross-sectional images of the three representative GaAs-$Al_{0.3}Ga_{0.7}As$ nanowire heterostructures with a radial quantum well embedded. Due to the atomic number sensitive contrast of STEM-HAADF images, the GaAs appears brighter than the $Al_{0.3}Ga_{0.7}As$. All three nanowires show clear distortion from the perfect hexagonal shape and pronounced variations of the quantum well thickness on different sidefacets.

	$d\,(\mathrm{nm})$	$\sigma\,(\mathrm{nm})$	$d_{\max} - d\,(\mathrm{nm})$	$d_{\min} - d\,(\mathrm{nm})$
NW 1	5.5	1.4	+1.6	−2.0
NW 2	5.5	0.8	+0.9	−1.3
NW 3	5.3	0.8	+0.9	−1.0

Table 2.1: Quantum well thicknesses of the asymmetric radial quantum well structure of the three selected nanowires in Figure 2.9. Average thickness d of the radial quantum well is significantly larger compared to the nominal value of 5 nm. The pronounced inhomogeneities of the nanowires' cross-section are confirmed by the increased standard deviation σ and the difference between mean thickness and thickness of thickest/ thinnest quantum well facet.

of all three nanowires are located next to each other whereas the thinnest quantum well is separated either by one or two facets from the thickest quantum well. The external radii of the tubular hexagonal quantum wells are found to be $80.3 \pm 0.4\,\mathrm{nm}$ for NW1, $98.6 \pm 1.2\,\mathrm{nm}$ for NW2 and $70.1 \pm 1.0\,\mathrm{nm}$ for NW3. In general, such inhomogeneity of the quantum well width gives rise to distinct differences in the confinement energy and, thus, have a significant impact on the emission of the nanowire quantum wells. This detailed structural information is later used to derive realistic geometries to perform calculations of the electronic properties.

To directly probe the influence of the fluctuations on the radial quantum confinement of the quantum wells, we studied the optical properties of three different nanowires from the same growth sample, referred to NW4, NW5, NW6. Therefore, we performed low temperatures ($T = 8\,\mathrm{K}$) photoluminescence spectroscopy on single nanowires which were mechanically transferred onto a $\mathrm{LiNbO_3}$ substrate in order to address individual nanowires in a lying geometry. The nanowires were excited by an externally triggered diode laser, emitting $\tau_{\mathrm{Laser}} = 90\,\mathrm{ps}$ long pulses at a wavelength of $\lambda_{\mathrm{Laser}} = 660\,\mathrm{nm}$, which was focused to a diffraction limited spot size of $d_{\mathrm{Laser}} = 1.5\,\mu\mathrm{m}$ by a x50 microscope objective mounted to a closed loop piezo-stage for fine position control. The emission of the nanowires was collected through the same objective and was analyzed in a spectrometer equipped with a charge coupled device (CCD) detector. For the temporally resolved photoluminescence spectroscopy, the individual emission bands were filtered using an imaging grating monochromator and the resulting signal was detected in the time domain using a silicon single photon counting detector with a time resolution of $\tau_{\mathrm{SPAD}} \leq 350\,\mathrm{ps}$.
The micro-photoluminescence spectral scans of the three nanowires, which are recorded along their axis at low optical pump power density of about $\sim 3\frac{\mathrm{W}}{\mathrm{cm}^2}$, are shown in the false color plot of Figure 2.10 (a-c). For all three nanowires, we observe an emission centered around the energy of 1.52 eV which is attributed to the recombination of free excitons in the GaAs core with a predominant zincblende crystal phase with only very few individual twin defects [85]. However, the emission of the radial GaAs quantum wells show clear inhomogeneities for all three nanowires. More precisely, the quantum well emission of NW4 features a single, broad emission peak at an energy of about 1.575 eV which occurs along the entire nanowire. In strong contrast, NW5 and NW6 exhibit several distinct emission bands (marked by dashed ellipses) at different energies ranging between 1.556 eV

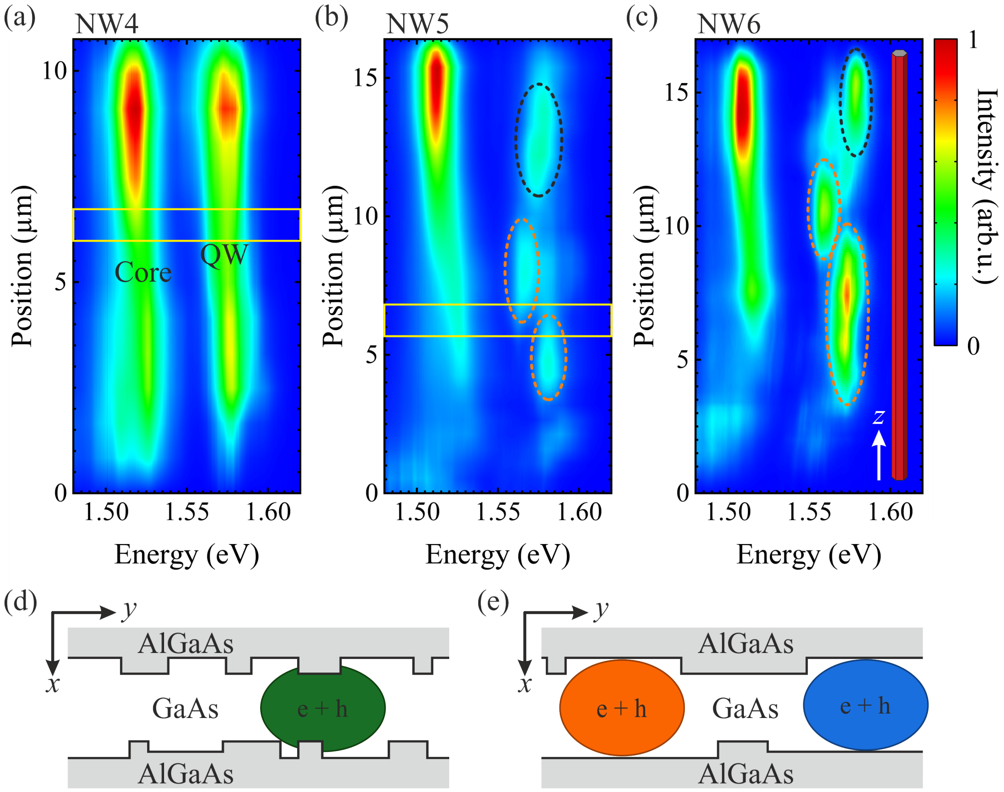

Figure 2.10: (a-c) Spatial resolved photoluminescence maps along the axis of three representative radial GaAs-$Al_{0.3}Ga_{0.7}As$ nanowire-quantum well heterostructures. NW4 (a) exhibits one broad emission peak occurring from the quantum well along the nanowire, whereas NW5 (b) and NW6 (c) show several distinct emission regions of the GaAs quantum well at different energies (highlighted by black and orange dashed ellipses). The emission regions are spatially offset along the axis of nanowires with small spatial overlapped areas. Orange dashed ellipses and yellow boxes indicate the two corresponding quantum well emission centers in the signal and the excitation positions for the following acousto-optoelectric measurements, respectively. (d,e) Schematic illustration of the heterointerfaces of a quantum well with a crystallographic structure of the interfaces for quantum well island sizes (d) smaller and (e) larger than the two-dimensional exciton diameter (illustrated by green, blue and orange circles), respectively. The structural disorder on the atomic scale results in an extent of excitons over several small quantum well islands or the localization of electrons and holes at distinct regions.

and 1.598 eV. In addition, these emission bands are spatially offset along the nanowire with small spatial overlapped regions. As known from previous work on planar GaAs-AlGaAs quantum wells, (110) planar surfaces frequently exhibit instabilities of the surface morphology leading to the formation of islands and valleys and, thus, reducing the optical and electrical properties [145]. Figure 2.10 (d) and (e) schematically show the crystallographic structure of the interfaces of a GaAs quantum well for quantum well island sizes smaller and larger than the two-dimensional exciton diameter, respectively. When the island size at the heterojunction interface becomes much smaller than the exciton size, interface roughness is dominating and, therefore, the energy levels of the exciton are statistically smeared out showing no distinct emission bands [135, 146–148]. Hence, the photoluminescence emission is broadened due to statistical effects caused by interface roughness. In contrast, for island size larger than the exciton size, the excitons will thermalize to quantum well islands with the largest width, leaving higher energy levels, caused by well islands of a smaller width, unoccupied [135, 146, 147]. Consequently, distinct emission centers at different energies will arise. Hence, these thickness fluctuations of the radial nanowire quantum wells will result in the observed line broadening and the local emission centers [149–151].

2.6.2 Electronic structure of radial quantum wells with realistic geometry

In order to understand the nature of the emission from a radial quantum well in more detail, the exciton energy levels and the exciton localization are theoretical calculated by using an approach established in previous works for polygonal quantum rings and prismatic shells [130, 131, 133, 134] and by focusing our calculations to the cross-sectional plane of a radial quantum well at a defined position along the nanowire axis. In a first step, the single-particle states are calculated with a discretization method based on a polar grid which is adapted to hexagonal cross-section obtained from the scanning transmission electron microscopy images of the nanowires [see Figure 2.9 and Table 2.1]. The single-particle Hamiltonian for electrons in the valence and holes the conduction band is

$$H_i = \frac{(-i\hbar\nabla + e\mathbf{A})^2}{2m_i^*} + \delta_{c,i}E_b \tag{2.12}$$

where the subscript $i = e, h$ is associated to one of the two bands; m_i^* is the effective mass of the electrons and holes and E_b is the (bulk) semiconductor bandgap. The single-particle eigenvalues

$$H_i \left|\Psi_i\right\rangle = E_i \left|\Psi_i\right\rangle \tag{2.13}$$

are calculated with the discretization method associated with a polar lattice which is spanned by the polar basis $|kj\sigma\rangle$, where k and j are the discretized radial (r_k) and angular (ϕ_j) coordinates and σ is the spin. Therefore, a circular disk is defined in a first step on which lateral boundary conditions enclosing the hexagonal ring are superimposed. Subsequently, the grid is reduced to the sites situated between the boundaries of the hexagonal quantum well ring as shown in Figure 2.11. Note, the lateral boundary conditions correspond to infinite potential barriers. Next, we use these eigenstates to construct the electron-hole Hamiltonian with the Coulomb interaction included which is given by:

$$H_{e-h} = H_e + H_h - \frac{1}{2}V \tag{2.14}$$

where H_e and H_h are the electronic Hamiltonians which describe an electron in the conduction band and a hole in the valence band, respectively, and V represents the attractive interaction between the electron and the hole. The detailed description of the calculation methods can be found in literature [131].

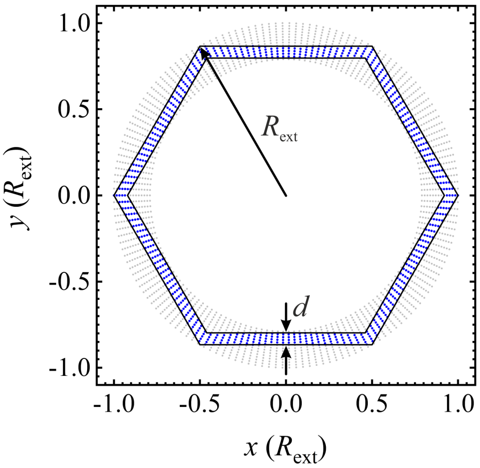

Figure 2.11: The discretization method is based on a polar grid by defining a circular disk. The grid is reduced to the site points situated between the boundaries of a hexagonal quantum well ring with an external radius R_{ext} and side thickness d (blue points). The number of site points is reduced for visibility. Adopted from [131].

For the calculation of exciton energy levels and localization of realistic, radial quantum wells with pronounced thickness fluctuations, we start with an ideal nanowire geometry with a perfectly symmetric hexagonal cross-section of the radial quantum well. Here, the mean quantum well thickness ($\langle d \rangle$) and the external radius (R_{ext}) is set to 5.5 nm and 80 nm, respectively. In a next step, the thickness of the different sidewall facets of the radial quantum well is varied in two ways as depicted in Figure 2.12 (a) and in Table 2.2. Hereby, we restrict ourselves to the two cases of minimal deformation and a linearly graded thickness variation instead of calculating the complex combination of thickness fluctuations and deformation of the perfect hexagonal shape observed by scanning transmission electron microscopy. For Geometry 1, the thickest facet (d_5) is situated next to two equally narrow, yet still thick facets and opposite to the thinnest one, thus preserving a mirror symmetry. In the case of Geometry 2, the mirror symmetry is lifted, and the thickest facet is neighbored by two facets of different width. Additionally, the thickest and thinnest facets are separated by two facets on each side for Geometry 1 and one facet for Geometry 2. Hence, the side thickness monotonically changes around the circumference

Geometry	Facet 1	Facet 2	Facet 3	Facet 4	Facet 5	Facet 6
1	$d - 0.5v$	$d - v$	$d - 0.5v$	$d + 0.5v$	$d + v$	$d + 0.5v$
2	d	$d - 0.5v$	$d - v$	d	$d + v$	$d + 0.5v$

Table 2.2: Two radial quantum well geometries are used for our calculations which are based on scanning transmission electron microscopy analysis. Geometry 1 describes a mirror symmetric system consisting of two quantum wells of reduced width next to the thickest one, whereas Geometry 2 represents an asymmetric system with two differently thick quantum wells next to the thickest one. Here, d and v are the mean width of the side facets and thickness variation parameter, respectively.

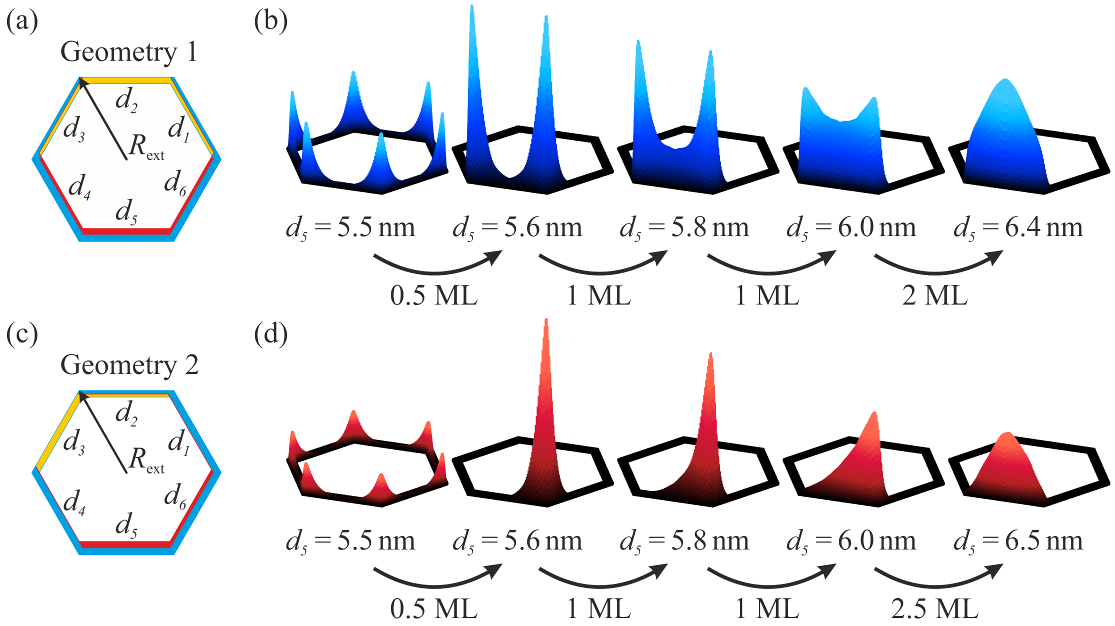

Figure 2.12: (a) Sample models: Geometry 1 describes the symmetric deformation of a perfectly symmetric hexagonal cross-section of the radial quantum well, whereas Geometry 2 represents the asymmetric deformation. The blue colored hexagon depicts the perfectly symmetric hexagonal shape with $d = 5.5\,\mathrm{nm}$ and $R_{\mathrm{ext}} = 80\,\mathrm{nm}$, the red region indicates the overgrowth with respect to the symmetric sample, while the yellow regions are subtracted from the symmetric hexagon due to the increase of the thickness variation parameter v. The radial quantum well geometries used for simulations are listed in Table 2.2. (b) Ground state localization for increasing width of the thickest sidewall facet ($d_5 = \langle d \rangle + v$). As the thickness variation parameter v is increased, the 6-fold corner states-like symmetry is lifted and a transition from corner to side states occurs.

reflecting the geometries observed by scanning transmission electron microscopy. These deviations are quantified by introducing the thickness variation parameter v which is defined as $v = d_{max} - \langle d \rangle$. The thicknesses of the six quantum well facets for both geometries are depicted in Table 2.2. Note, an increase of v increases, on the one hand, the thickness of quantum wells on one side of the hexagon, while it reduces, on the other hand, the quantum well thickness on the other side of the hexagon.

The probability distributions of electrons corresponding to the ground state are shown in Figure 2.12 (b) for both geometries and different thicknesses of the widest facet, i.e., for $d_5 = \langle d \rangle + v$. The corresponding probability distributions of holes are qualitatively similar. For the undeformed, perfect hexagonal quantum well ring structure, the ground state exhibits a 6-fold symmetry, and the wave function is equally delocalized between all six corners of the hexagonal cross-section which is also predicted in previous theoretical works [113, 124, 125, 129–132, 152]. Introducing a finite asymmetry to the hexagonal ring structure results in a strong impact on the probability distribution in the quantum well: increasing d_5 by only $v = 0.1\,\mathrm{nm}$ corresponding to 0.5 monolayers (MLs) results in the lifting of the 6-fold symmetry of the charge carrier distributions. This minute difference in thickness of about one percent between Facet 5 and its thickest neighboring facet creates a 2-fold symmetric corner state at the edges of the widest quantum well formed on Facet 5 for Geometry 1 and a single corner state at the corner between Facets 5 and Facet 6 (next thickest neighboring facet) for Geometry 2, respectively. Consequently, our theoretical calculations nicely predict that the formation of corner states with ideal 6-fold symmetry clearly requires a near-perfect hexagonal geometry and that even small variations of the hexagonal shape lead to a complete localization of the wavefunction at the corners connecting the two widest quantum wells. As the thickness variation parameter v, i.e. the thickest facet, increases, the sharp localization of the probability distribution at the corners shifts towards the center of the thickest side resulting in the delocalization of the excitons from the corners towards the center of the widest quantum well. For $v = 1\,\text{nm}$ corresponding to a relative thickness fluctuation of approximately 5 monolayers, the probability distribution of the excitons is fully localized in the widest quantum well side facet. Considering the nanowires studied here in scanning transmission electron microscopy, v ranges from about 0.9 nm up to 1.6 nm compared to the mean value of $\langle d \rangle = 5.5\,\text{nm}$ for a perfect hexagonal quantum well ring. Consequently, excitons do not anymore distribute over all six corners but can be readily considered to be fully localized on the widest facet of the radial quantum well. Moreover, our scanning transmission electron microscopy analysis shows that in realistic nanowire quantum well systems more pronounced deviations of the perfect hexagonal symmetry, e.g. deformation of the perfect hexagonal shape, occur and are expected to enhance the localization of the excitons on the widest quantum well facets. In this sense, the two chosen geometries can be considered as representative examples.

Secondly, the exciton energies are calculated as a function of v for both geometries and are plotted in Figure 2.13. As expected, the ground state exciton energies clearly shift red with increasing v, as it is known for regular, planar quantum well heterostructures [153]. Moreover, the nearly perfect overlap of the exciton energies obtained for the two geometries confirms that the ground state excitonic energy does not depend on the shape of the cross-section. Instead, it is defined solely by the width of the thickest side, if the widest side is sufficiently thicker than the second widest side. In the following, the results of these calculations are compared to our experimental data. The red shaded area in Figure 2.13 indicates the excitonic energy region of the quantum well emissions of the NW4, NW5 and NW6 ranging between 1.556 eV and 1.598 eV and the corresponding increase of quantum well thickness compared to the symmetric case. From this comparison, the thickness deviations of both quantum well segments are expected to be approximately 1.4 nm and 3.8 nm, respectively, exceeding those obtained from scanning transmission electron microscopy analysis which range from 0.9 nm to 1.6 nm. In comparison, the blue shaded area in Figure 2.13 highlights the exciton energy levels expected from the quantum well thicknesses obtained from our scanning transmission electron microscopy analysis which are expected to be approximately between 1.598 eV and 1.618 eV. Considering the approximations applied in the model, in particular, the infinite energy barriers, an overestimation of the exciton ground state energy with respect to the well thickness is expected. Therefore, the results of our calculations can be considered in good agreement with our experimental

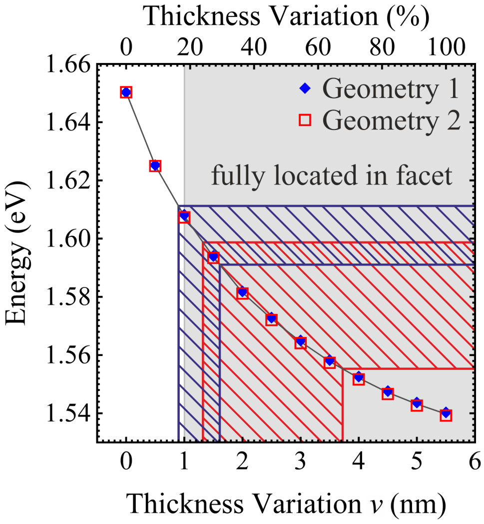

Figure 2.13: Excitonic transition energies obtained from the electron-hole model versus quantum well thickness variation parameter v. Gray area indicates quantum well thickness variation for the localization of the charge carriers within the thickest sidewall facet. The blue shaded area highlights the range of widths of the thickest side facet measured by scanning transmission electron microscopy and the corresponding range of calculated energies. The red shaded box associates the experimentally obtained emission energies of the radial quantum well with the calculated facet thicknesses.

findings. Moreover, the gray colored area indicates the quantum well thickness deviation at which the probability distribution of the excitons is fully localized in the widest quantum well side facet. Again, the complete overlap of the blue shaded and the gray colored area highlights the localization of the excitons on the widest quantum well facets.

2.6.3 Charge carrier dynamics

In order to probe the carrier dynamics and to identify the origin of the emission of the quantum wells, we performed temporally resolved photoluminescence of the core and the radial quantum wells of NW4 and NW5. Figure 2.14 (a) shows a selected spectrum of NW4 at the position along the nanowire indicated by a yellow box in Figure 2.10 (a). We observe a prominent emission peak centered at 1.517 eV from the almost phase-pure zincblende nanowire core featuring also a weak low-energy shoulder associated with a low density of twin plane defects. Moreover, it consists of a broad emission band at an energy of approximately 1.571 eV originating from the inhomogeneous radial quantum well. The temporally resolved photoluminescence of the core and the radial quantum well of NW4 are plotted in Figure 2.14 (b). Both, core and quantum well, exhibit the established mono-exponential decay of an isolated system. The characteristic decay time of the core of $\sim 0.7\,\mathrm{ns}$ is well consistent with literature data for free excitons in GaAs nanowires [85, 106, 108]. Moreover, the emission of the quantum well shows a slightly faster decay compared to the lifetime of the core with a characteristic decay time of about $\sim 0.5\,\mathrm{ns}$.

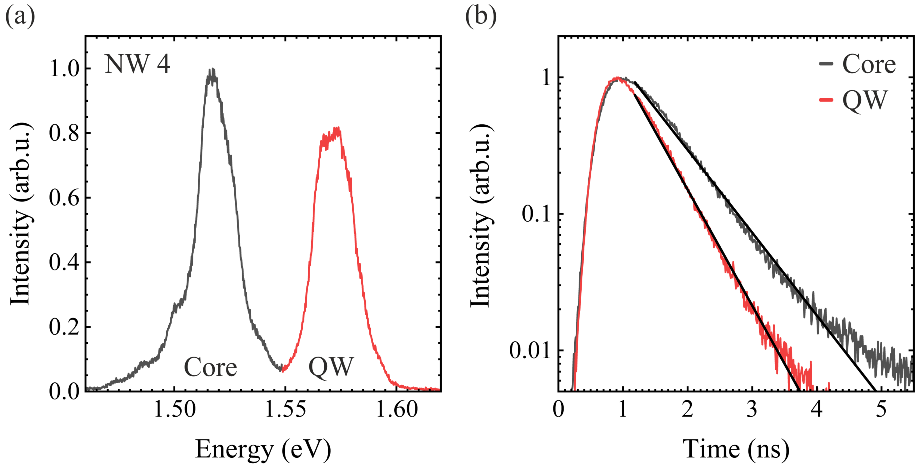

Figure 2.14: (a) Time-integrated photoluminescence spectrum of NW4 showing the emission peak of the core at an energy of 1.517 eV and the radial quantum well at an energy of approximately 1.571 eV. (b) Time evolution of photoluminescence intensity recorded for each peak of the spectrum of NW4. Both, core and quantum well, exhibit the established mono-exponential decay of an isolated system. The solid lines are guides to the eyes.

In Figure 2.15 (a), we present a spectrum of NW5 recorded at the position along the nanowire which is highlighted by a yellow box in Figure 2.10 (b). It consists of two overlapping emission bands of the radial quantum well at energies of approximately 1.561 eV (blue, referred as QW1) and 1.585 eV (orange, referred as QW2) as well as the emission of the zincblende core with peak centered at approximately 1.513 eV. This double peak structure of the radial quantum well originates from two spatially separated but sightly overlapped quantum well systems, which exhibit the maximum thickness at their respective axial position within the radial quantum well structure. The temporally resolved photoluminescence signals of the core and both quantum well emission signals are depicted in Figure 2.15 (b). The core exhibits again a clear mono-exponential decay with the characteristic decay time of ~ 0.7 ns. In strong contrast, we observe a clear bi-exponential decay for both quantum well emission signals. Clearly, we observe coupled emission dynamics of QW1 and QW2: while QW1 has a fast decay with a lifetime of $\tau_{\mathrm{QW1,fast}} = 0.4$ ns at short times and a slow decay time $\tau_{\mathrm{QW1,slow}} = 0.7$ ns at longer times, the decay time of QW2 decreases from $\tau_{\mathrm{QW2,slow}} = 0.6$ ns at short times to $\tau_{\mathrm{QW2,fast}} = 0.3$ ns at longer times. This anti-correlated behavior, which can be clearly seen by the cross-over of the two time-resolved photoluminescence curves in Figure 2.15 (b) can be explained by a charge carrier transfer between two interconnected quantum well systems. More precisely, it results from a carrier charge transfer from the higher energetic quantum well system QW2 towards the lower energetic QW1 as schematically illustrated in Figure 2.15 (c). Consequently, these anti-correlated recombination rates are an unambiguous fingerprint of coupled emission dynamics and, thus, direct evidence that QW1 and QW2 are in fact interconnected.

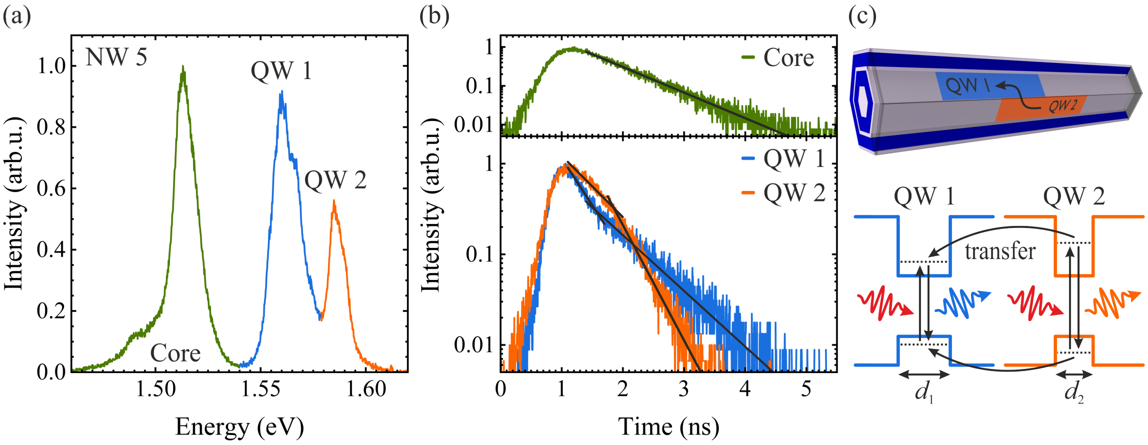

Figure 2.15: (a) Time-integrated photoluminescence spectrum of NW5 showing the core emission and a double peak structure of the radial quantum well (attributed to the two spatially separated but interconnected quantum well systems with the largest thickness). (b) Time evolution of photoluminescence intensity recorded for each peak of the photoluminescence spectrum of NW5. The solid lines are guides to the eyes, showing an anti-correlated time evolution for both quantum wells suggesting a dynamic charge exchange between coupled systems. (c) Schematic illustration of the charge carrier transfer form the higher energetic QW2 to the lower energetic QW1 within the tubular quantum well structure and bandprofile of the two spatially separated but interconnected quantum well segments of the radial heterostructure.

In the next chapters, these coupled carrier dynamics of QW1 and QW2 are studied, showing that this redistribution of charge carriers can be also triggered and even reversed on subnanosecond time scales by the acousto-electric effect. Moreover, these coupled charge carrier dynamics are exploited to isolate the temporal signature of gyrating electric fields of a surface acoustic wave.

2.7 Conclusion

In this chapter, we have provided an overview of the growth of self-catalyzed GaAs-AlGaAs nanowires heterostructures on a Si(111) substrate utilizing a molecular beam epitaxy system. In particular, for such grown nanowires, growth conditions and nucleation have a major impact on morphology, crystal structure and growth rate anisotropies which influence the optical and electrical properties of nanowire heterostructures. However, in nanowires and nanowire based heterostructures, these result in pronounced structural and compositional variations within ternary compounds and at interfaces of such heterostructures. Consequently, radial quantum well heterostructures often exhibit pronounced thickness fluctuations and, independent of the quantum well thickness, deviations from a perfect hexagonal cross-section. Here, we have investigated the structural, optical and electronic properties of a hexagonal quantum well system embedded in commonly grown GaAs/$Al_{0.3}Ga_{0.7}As$ core/shell nanowire heterostructures. The results presented here have multiple important implications for the realization of functional, high performance core-shell nanowire heterostructures with embedded quantum nanostructures. They show that small deviations of the perfect hexagonal cross-section of the radial quantum well result in a significant change of the optical and electronic properties. Moreover, small variations of the quantum well thickness on the sidewall facets strongly affect the localization of the charge carrier distribution. In particular, the commonly observed six-fold corner states-like symmetry of a perfect hexagonal shape is rapidly lifted and the localization of charge carriers fully occurs at the side facets. This, in turn, results in a change of the optical and electrical properties. Hence, moderate deformations from the perfect symmetric hexagonal geometry leads to clear spectral broadening and multi-peak structures of the photoluminescence spectrum of the radial quantum well system. Furthermore, these well width fluctuations induce the formation of spatially separated but interconnected quantum well systems clearly showing coupled carrier dynamics between local emission centers. In the following chapters, these coupled carrier dynamics can be also triggered and even reversed on subnanosecond time scales by the acousto-electric effect.

Thus, to create the often predicted highly symmetric quantum states, the perfection down to the monolayer accuracy is required and defines one great challenge for future experiments. Alternative routes may be derived from tailoring composition-driven faceting [122] with elegant growth modulation techniques developed for wafer-scale substrates, for instance the serpentine superlattice [153, 154] and pave the way towards one-dimensional quantum confined systems on the one-dimensional nanowire geometry.

Chapter 3

Surface acoustic waves

Surface acoustic waves being first treated in 1885 by Lord Rayleigh [41] are mechanical waves that are confined close to the surface of a solid and can propagate over large distances with only low dissipation. In addition, when propagating on piezoelectric materials, like GaAs and $LiNbO_3$, these mechanical waves are accompanied by a gyrating electric field [42] allowing to efficiently excite and detect surface acoustic waves on piezoelectric surfaces. This opens up the way for their implementation in various devices of today which provides wide-range of applications in phononic technologies of industrial relevance. In particular, the low propagation velocities and the possibility to efficiently excite surface acoustic waves by electrical signals on a piezoelectric substrate allow to easily convert electrical signals to short wavelength surface acoustic waves and vice versa and, thus, enable the realization of surface acoustic wave filters on a chip scale. These filters are nowadays used in telecommunication and data transport devices operating at frequencies ranging from about 10 MHz up to a few GHz.

Moreover, surface acoustic waves find applications in probing and controlling the elementary excitations in condensed matter by applying variable stress, strain and electric fields to nanostructures [40]. They strongly interact with any system which is located at or near to the surface of a crystal. In addition, the easy integration by standard semiconductor fabrication techniques enables the realization of various surface acoustic wave-semiconductor hybrid systems.

This chapter describes first the basic physical properties of surface acoustic waves and deduces the basic wave equations for a propagating surface acoustic wave. Afterwards, the most important mechanical and electrical characteristics of surface acoustic waves are discussed by means of the finite element method for the YZ-cut $LiNbO_3$ material system. Then, the excitation of surface acoustic waves on piezoelectric substrates by so called interdigital transducer and the fabrication of surface acoustic wave chips by different lithography methods are discussed. Finally, the interaction of semiconductor materials with surface acoustic waves is addressed giving insights in the modulation of the band structure and charge carriers dynamics within semiconductors.

A detailed description of the surface acoustic wave equations and the basic properties of surface acoustic waves can be found in literature [155–158].

3.1 Basic properties

Surface acoustic waves are theoretically characterized by the elastic behavior of solids. When propagating on a piezoelectric material, the mechanical wave induces an alternating electric field near the surface. For simplicity, we consider first the elastic behavior in non-piezoelectric, isotropic materials and then we introduce the piezoelectric effect.

3.1.1 Equations of motion of surface acoustic waves

In general, the elasticity of a material describes the internal forces within a homogeneous solid and the related displacement of an elementary region inside a solid from its equilibrium. Hereby, the stress tensor $\mathbf{T}$ expresses the resulting forces while the strain tensor $\mathbf{S}$ characterizes the displacements. For the theoretical description, we assume in the first step that a particle inside a solid is located at the equilibrium position of $\mathbf{x} = (x_1, x_2, x_3)$. Hence, the displacement by $\mathbf{u} = (u_1, u_2, u_3)$ from the equilibrium position results in a new position of the particle to $\mathbf{x} + \mathbf{u}$ and, consequently, in internal forces trying to restore this equilibrium state. As displacement and rotation of the material as a whole induce no internal forces, the deformation of a material can be defined by the strain tensor S_{ij}:

$$S_{ij}(x_1, x_2, x_3) = \frac{1}{2}\left(\frac{\partial u_i}{\partial x_j} + \frac{\partial u_j}{\partial x_i}\right), \quad i, j = 1, 2, 3. \tag{3.1}$$

As a consequence of this description, any displacement $(\partial u_i/\partial x_j = 0)$ and rotation $(\partial u_i/\partial x_j = -\partial u_j/\partial x_i)$ of the whole material result in no strain. Moreover, the diagonal elements of this tensor describe the strain occurring along the coordinate axes, while the off-diagonal elements represent the shear strain of a solid. Further, the strain tensor is symmetrical $(S_{ij} = S_{ji})$ reducing the strain tensor to six independent components.
The internal forces acting on an area and its direction within a solid are described with their strength by the stress tensor T_{ij} which is schematically depicted in Figure 3.1. For

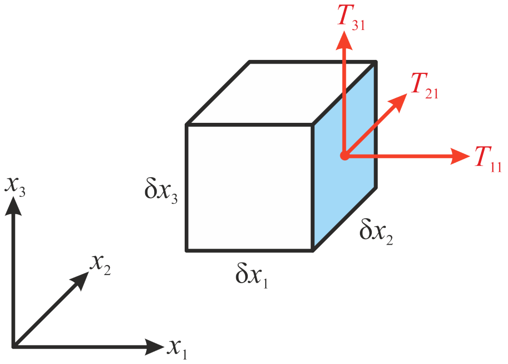

Figure 3.1: Forces on the center of one side of an infinitesimal volume element δV. T_{ij} describes the compressive and tensile forces (T_{11}) and shear forces (T_{21} and T_{31}) acting on an area and its direction. Figure adapted from [159].

an elastic material, stresses are according to Hooke's law proportional to strains providing the strains are sufficiently small:

$$T_{ij}(x_1, x_2, x_3) = c_{ijkl} S_{kl}, \quad i, j, k, l = 1, 2, 3. \tag{3.2}$$

The stiffness (elasticity) tensor c_{ijkl} is in general a fourth rank tensor with 81 components. As the stress tensor and strain tensor have the same symmetry, only 36 components of stiffness tensor are independent $(c_{ijkl} = c_{jikl}, c_{ijkl} = c_{ijlk})$. In addition, due to thermodynamic reasons, it can be shown that relation $c_{ijkl} = c_{klij}$ must apply for the stiffness tensor and the number of independent components can be further reduced to 21. Due to these symmetry properties, these tensors are symmetric in pairs of indices and can be written in the form of a 6×6 matrix as $c_{\alpha\beta}$ by following rules:

$$\begin{aligned} &\alpha = 1 \to ij = 11, \quad \alpha = 2 \to ij = 22, \quad \alpha = 3 \to ij = 33, \\ &\alpha = 4 \to ij = 23, \quad \alpha = 5 \to ij = 31, \quad \alpha = 6 \to ij = 12. \end{aligned} \tag{3.3}$$

Furthermore, depending on the crystal class, the number of independent components can be even further reduced as it would be the case for *3m* class to which Lithium Niobate ($LiNbO_3$) belongs.

For the dynamic deformation of a solid, stress and strain are functions of time and position and the displacement $u(x)$ can be described by Newton's law $F = m \cdot \ddot{u}$. Thus, the force per unit volume is equal to the density ρ multiplied by the acceleration. Following, the equations of motion are given by the wave equation:

$$\rho \frac{\partial^2 u_i}{\partial t^2} = \frac{\partial T_{ij}}{\partial x_j} \tag{3.4}$$

having solutions which are plane waves with transversal and longitudinal propagating modes. However, this wave equation is only valid for non-piezoelectric, anisotropic solids neglecting piezoelectric effect.

For piezoelectric materials, restoring electric forces have to be additionally taken into account. In general, piezoelectricity is only found in anisotropic solids which lack internal symmetry in their crystal structure leading to the coupling of elastic strains and stresses in a crystal to electric fields and displacements. Despite its weak impact on the elastic behavior, the effect of piezoelectricity plays a crucial role for the excitation of surface acoustic waves by electrical signals and, thus, can not be neglected in the theoretical analysis. The excitation of surface acoustic waves will be discussed in Section 3.3.

In piezoelectric materials, the stress at a certain point depends, in addition to the strain, also on the electric field $\mathcal{E}$ at this point. Hence, an external electric field induces mechanical displacements via the inverse piezoelectric effect and Hooke's law has to be extended for piezoelectric materials. It can be written as following:

$$T_{ij} = c_{ijkl} S_{kl} - e_{kij} \mathcal{E}_k. \tag{3.5}$$

Moreover, a mechanical displacement of a piezoelectric material results in a electric displacement field **D** which induces an electric field $\mathcal{E}$. Hence, the electric displacement field does not only depend on the electrical field but is also related to the strain:

$$D_i = \epsilon_{ij}\mathcal{E}_j + e_{ijk}S_{jk} \tag{3.6}$$

where ϵ_{ij} is the permittivity of the material and the piezoelectric tensor e_{ijk} relates the elasticity to the electric fields having the symmetry of $e_{ijk} = e_{ikj}$. Both correlations can be considered as a stiffening of the stress **T** by the electric field and an additional polarization of the electric displacement field **D** through the mechanical displacement **S**, respectively.

The equation of motion, Equation 3.4, is still valid in piezoelectric materials. Nevertheless, both, Newton's equation of motion and the Maxwell equations, have to be solved simultaneously due to the coupling of elastic and electric waves in piezoelectric materials. Thus, the solution are mixed elasto-electromagnetic waves. Since the speed of elastic waves is much slower than that of the speed of electromagnetic waves, the electrodynamic solutions of the equations can be neglected and the electric field can be derived from the gradient of the potential:

$$\mathcal{E}_i = -\frac{\partial \Phi}{\partial x_i}. \tag{3.7}$$

Applying this relation (Equation 3.7) in the definition of stress in a piezoelectric material (Equation 3.5) in combination with the equation of motion (Equation 3.4) and the definition of the strain tensor **S** (Equation 3.1), the equation of motion for an elastic piezoelectric material is given by:

$$\rho\frac{\partial^2 u_i}{\partial t^2} = e_{kij}\frac{\partial^2 \Phi}{\partial x_j \partial x_k} + c_{ijkl}\frac{\partial^2 u_k}{\partial x_j \partial x_l}. \tag{3.8}$$

By assuming the material to be an insulator, we can also conclude that there are no free charge carriers resulting in $\nabla\mathbf{D} = 0$. Hence, Equation 3.7 becomes:

$$e_{jkl}\frac{\partial^2 u_l}{\partial x_j \partial x_k} - \epsilon_{jk}\frac{\partial^2 \Phi}{\partial x_j \partial x_k} = 0. \tag{3.9}$$

Both Equations 3.8 and 3.9 provide four coupled differential equations relating the four quantities u_i and ϕ. Finally, the motion of wave in a piezoelectric material can be determined if proper boundary conditions are applied.

3.1.2 Boundary conditions of surface acoustic waves

For the mathematical description of a surface wave which propagates along a surface, the equations of motion have to fulfill the mechanical and electrical boundary conditions of a material with a free surface: therefore, we consider a crystal that is extended infinitely along the x_1 and x_3 and occupies the half-space $x_2 < 0$. As there can be no forces on the surface of the material, the stress components have to vanish:

$$T_{12} = T_{22} = T_{32} = 0 \,|_{x_2=0}. \tag{3.10}$$

In addition, for a wave propagating on surface, the displacements have to decay towards the lower end of the material:

$$u_i = 0 \,|_{x_2 \to -\infty}. \tag{3.11}$$

As piezoelectric materials are considered, electrical boundary conditions have to be satisfied in addition to mechanical boundary conditions. In general, the electric potential at the interface of the piezoelectric material and the medium of the upper half space has to be continuous:

$$\Phi_3 \,|_{x_2 \to 0,\, x_2<0} = \Phi_3 \,|_{x_2 \to 0,\, x_2>0}. \tag{3.12}$$

Further, similar to the displacement, the potential has to vanish at infinity in both half-spaces:

$$\Phi = 0 \,|_{x_2 \to \pm\infty}. \tag{3.13}$$

At last, for the boundary conditions of the electrical fields, two cases are usually considered. In the first case, the material of the upper half space ($x_3 > 0$) is a perfect dielectric (no free charges) resulting in the continuity of the normal component of the electrical displacement field D_2 and the tangential components of the electric field $E_{1,3}$. In the second case, the surface of the piezoelectric material is covered by a metal (with infinite conductivity). Hence, the electric potential Φ and the tangential fields ($E_{1,3}$ and $D_{1,3}$) are zero at the interface and the normal component of the electric displacement field D_2 is discontinuous. In addition, these electrical boundary conditions have impact on the phase velocity of a surface wave. For a surface wave, the phase velocity depends on the medium covering the surface through its permittivity ϵ_d. Thereby, three important cases can be distinguished:

(i) The surface is covered by a thin metallic film (short-circuit condition with $\epsilon_d = \epsilon_\infty$) resulting in a velocity v_∞

(ii) The surface is covered with a hypothetical medium with permittivity $\epsilon_d = 0$ (open-circuit condition) resulting in a velocity v_0

(iii) The surface is covered by vacuum ($\epsilon_d = \epsilon_0$) resulting in a velocity v_r which is between the two extremes v_∞ and v_0 so that $v_\infty < v_r < v_0$.

The velocity v_∞ is less than v_0 since the metal film on top of the surface partially suppresses the piezoelectricity of the underlying substrate. For materials with a high permittivity, such as $LiNbO_3$, the phase velocity of v_r is very similar to v_0. With both velocities v_∞

and v_0, the electromechanical coupling coefficient of a surface wave K_S can be defined by:

$$K_S = \frac{v_0^2 - v_\infty^2}{v_0^2 + \frac{\epsilon_d}{\epsilon_p} v_\infty^2} \tag{3.14}$$

with ϵ_p being the permittivity of the piezoelectric. The electromechanical coupling coefficient is related to the fraction of electrical energy which is transformed into mechanical energy at the surface. Consequently, it is a measure how efficiently the electric excitation signal can be coupled into a piezoelectric surface acoustic wave.

3.1.3 Method for numerically solving the equations of motion

Due to the complexity of Equation 3.6 and Equation 3.7, general solutions of the surface waves can not be derived analytically for anisotropic materials, but have to be calculated numerically. For solving, we first assume the propagation of the wave to be in the x_3-direction while the surface normal is assumed to be the x_2-direction. Hence, the solutions can be written as

$$\begin{aligned} u_i &= u_{i,0} e^{i(\omega t - k x_3)} e^{\chi k x_2}, \quad i = 1,2,3 \\ \Phi &= \Phi_0 e^{i(\omega t - k x_3)} e^{\chi k x_2}. \end{aligned} \tag{3.15}$$

As this wave depends only spatially on x_2 and x_3 ($\partial/\partial x_2 = \chi k$ and $\partial/\partial x_3 = -ik$), the derivatives in the x_1-direction disappear ($\partial/\partial x_1 = 0$). By plugging this approach into the equations of motion (Equations 3.8 and 3.9), the coupled differential equation system can be represented in following matrix representation:

$$\begin{pmatrix} \Gamma_{11} - \rho v^2 & \Gamma_{12} & \Gamma_{13} & \gamma_1 \\ \Gamma_{21} & \Gamma_{22} - \rho v^2 & \Gamma_{23} & \gamma_2 \\ \Gamma_{31} & \Gamma_{32} & \Gamma_{33} - \rho v^2 & \gamma_3 \\ \gamma_1 & \gamma_2 & \gamma_3 & -\epsilon \end{pmatrix} \begin{pmatrix} u_1 \\ u_2 \\ u_3 \\ u_4 \end{pmatrix} = 0. \tag{3.16}$$

with $v = \omega/k$ being the speed of the wave and the matrix elements being:

$$\begin{aligned} \Gamma_{il} &= c_{i33l} - c_{i22l}\chi^2 + i\chi(c_{i23l} + c_{i32l}) \\ \gamma_l &= e_{33l} - e_{22l}\chi^2 + i\chi(e_{23l} + e_{32l}) \\ \epsilon &= \epsilon_{33} - \epsilon_{22}\chi^2 + i\chi(\epsilon_{23} + \epsilon_{32}). \end{aligned} \tag{3.17}$$

The explicit values for Lithium Niobate can be obtained from the stiffness, piezo-electricity and permittivity tensors depicted in Appendix.

In general, the wave equation in matrix representation can be solved by setting the determinant of Equation 3.16 to zero. If the speed of the wave v is fixed, this results in eight solutions for the value χ which are in general complex. As u_i and Φ have to vanish for $x_2 \to -\infty$, only values with negative imaginary parts can be allowed. Consequently, there are four values of χ in general denoted by $\chi^{(n)}$, $n = 1, 2, 3, 4$ and the general solution results from the superposition of the four independent solutions for each value of $\chi^{(n)}$:

$$\begin{aligned} u_i &= \sum_{n=1}^{4} u_i^{(n)} = \left(\sum_{n=1}^{4} u_{i,0}^{(n)} e^{\chi^{(n)} k x_2} \right) e^{i(\omega t - k x_3)} \\ \Phi &= \sum_{n=1}^{4} \Phi^{(n)} = \left(\sum_{n=1}^{4} \Phi_0^{(n)} e^{\chi^{(n)} k x_2} \right) e^{i(\omega t - k x_3)} \end{aligned} \tag{3.18}$$

where $u_{i,0}^{(n)}$ and $\Phi_0^{(n)}$ are the displacement and the potential corresponding to $\chi^{(n)}$. In addition, the coefficients $u_{i,0}^{(n)}$ and $\Phi_0^{(n)}$ have to fulfill the boundary conditions. These conditions can be written again in matrix representation for which the determinant has to be zero. However, the determinant will only be zero if the correct value of the speed of the wave v is chosen. Consequently, the solution is found by iterating the entire procedure for different values of v until the boundary condition determinant vanishes. Finally, a solution can be found for the surface acoustic waves propagating with sound velocity v_{SAW}:

$$\omega = v_{\mathrm{SAW}} \cdot k \quad \leftrightarrow \quad f = \frac{v_{\mathrm{SAW}}}{\lambda}. \tag{3.19}$$

One possible solution is the so-called piezoelectric Rayleigh wave [41], named after Lord Rayleigh who first described it in 1885. These waves exhibit characteristically an elliptical motion and a polarization of the particles as well as a gyrating electric field which occur in the sagittal plane defined by the surface normal and the propagation direction. This wave is typically used when working with $LiNbO_3$ substrates clearly dominating over the shear and bulk waves. Its penetration depth is about one wavelength and the anisotropy of the crystal's sound velocity strongly depends on the crystal cut and the propagation direction. In addition, solutions of the wave equations can be obtained by finite element modeling (FEM) of the Rayleigh wave modes which is discussed in the following section.

3.2 Finite element modeling of surface acoustic waves

In this section, the most important mechanical and electrical characteristics of surface acoustic waves propagating on a $LiNbO_3$ crystal are discussed. Therefore, we consider a Y-cut $LiNbO_3$ crystal with the major propagation direction along the Z-axis, which is predominantly used in this work, and calculate the mode of the surface acoustic wave by finite element modeling.

In a first step, we define the geometry and assign it to the material and its corresponding values for density ρ, elasticity tensor c, piezoelectric tensor e and dielectric permittivity ϵ. Since the solution of the wave is periodic in space, the geometry can be reduced to one unit cell of the expected wave mode. The parameters used for the simulations presented in this work are summarized in Appendix B.1. In the next step, appropriate boundary conditions are defined. As the surface acoustic wave is periodic in propagation direction,

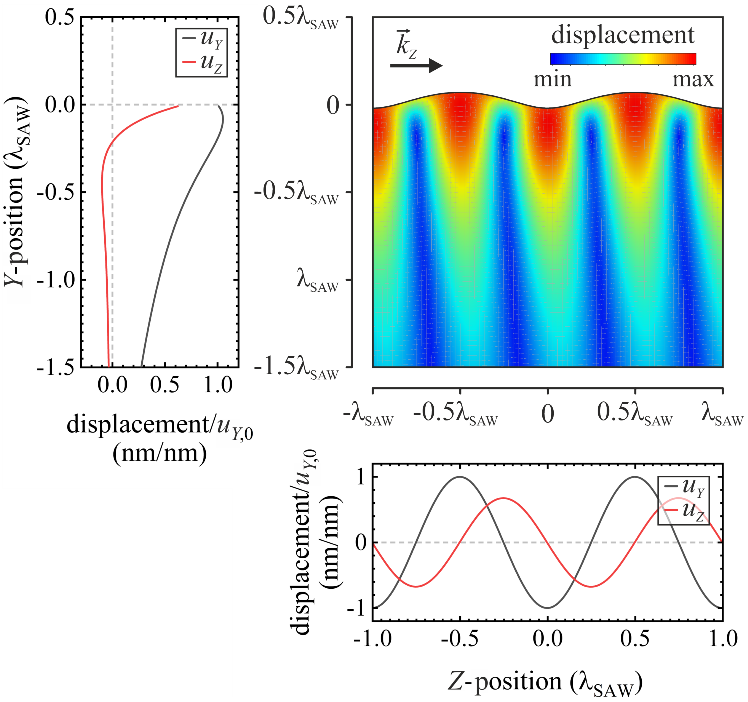

Figure 3.2: Calculated mechanical properties of a Rayleigh surface acoustic wave propagating along the Z-direction of a Y-cut $LiNbO_3$ crystal. Center panel: total displacement of a Rayleigh surface acoustic wave as color scale and displacement profile (u_Y, u_Z). The displacement is not to scale. Left panel: depth (Y)-dependence of displacement components of the vertical direction u_Y (black line) and the horizontal direction u_Z (red line). Lower panel: displacement components u_Y and u_Z along the surface of the $LiNbO_3$ crystal. All given values scale linearly with the surface acoustic wave amplitude and are normalized to $u_{Y,0} = 1\,\mathrm{nm}$.

the length of the unit cell is set to multiple integer of the surface acoustic wave wavelength and periodic boundary conditions at both ends are defined for the displacement u and the electric potential Φ. For the surface ($Y = 0$), a free boundary condition with no constrains and no charges is defined, while at the bottom of the unit cell the boundary is assumed to be mechanically fully constrained and have zero potential yet providing a sufficient height of the unit cell ($3 - 4 \cdot \lambda_{\mathrm{SAW}}$). As the motion of particles and the gyration of the electric field occur in the plane defined by the surface normal and the propagation direction, the material perpendicular to that plane can be considered to be infinite and, thus, again periodic boundary conditions can be applied. Finally, the geometry is divided in finite elements and the underlying piezoelectric equations of motion are numerically solved for each element by ensuring the coupling of all neighboring elements. For a Y-cut $LiNbO_3$ crystal with the major propagation direction along the Z-axis, the finite element modeling simulations yield a sound velocity of $v_{\mathrm{SAW}} = 3483\,\mathrm{m/s}$.

In Figure 3.2, the spatial mode profile of a Rayleigh surface acoustic wave propagating along the Z-direction of a Y-cut $LiNbO_3$ crystal is presented with the spatial dimensions given in units of the surface acoustic wave wavelength (λ_{SAW}). As all mechanical quantities scale linearly with the amplitude of the surface acoustic wave, all extracted properties are

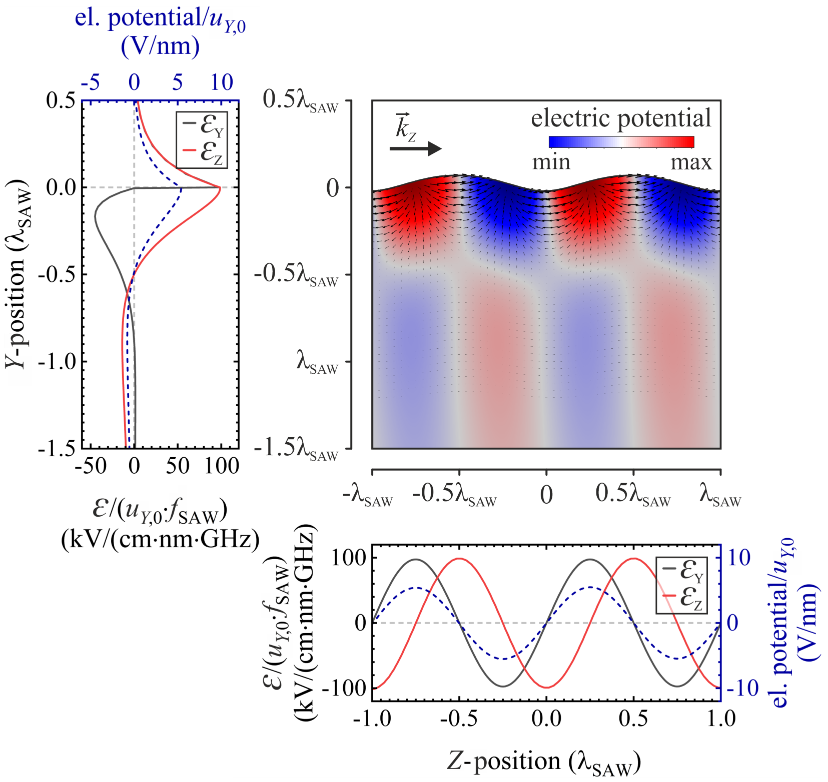

Figure 3.3: Calculated electrical properties of a Rayleigh surface acoustic wave propagating along the Z-direction of a Y-cut $LiNbO_3$ crystal. Centre panel: spatial profile of the electric potential (color coded) and the derived electric field (arrows) in the YZ-$LiNbO_3$ crystal. The displacement is not to scale. Left panel: depth (Y)-dependence of the resulting transverse $\mathcal{E}_Y$, (black line) and longitudinal $\mathcal{E}_Z$, (red line) electric field components as well as the electric potential Φ (blue dashed line). Lower panel: amplitude of $\mathcal{E}_Y$, $\mathcal{E}_Z$, and Φ along the surface of the $LiNbO_3$ crystal. All given values scale linearly with the surface acoustic wave amplitude and are normalized to $u_{Y,0} = 1\,\text{nm}$. Moreover, the electric field components $\mathcal{E}$ scale linearly with the surface acoustic wave frequency and are normalized to $f_{SAW} = 1\,\text{GHz}$.

normalized to the maximum vertical displacement at the surface of $u_{Y,0} = 1\,\text{nm}$. The center panel shows the spatial profile of total displacement of the $LiNbO_3$ crystal induced by a Rayleigh surface acoustic wave in false-color representation. In the lower panel, the dependence of the two displacement components u_Y and u_Z are evaluated along the surface ($Y = 0$) exhibiting the characteristic elliptical motion of the Rayleigh wave. Hence, both components show the expected sinusoidal dependence of both components which are shifted by the phase of $\pi/2$ and have different amplitudes. In the left panel, the depth dependence of the normalized longitudinal (u_Z) and transverse (u_Y) displacements are presented within the substrate exhibiting rapid decay into the substrate.

Moreover, in piezoelectric materials, such as $LiNbO_3$, the mechanical wave induces a piezoelectric potential. In Figure, 3.3, the electric properties of a Rayleigh surface acoustic wave propagation along the Z-direction of a Y-cut $LiNbO_3$ crystal is analyzed. The spatial profile of the electric potential (color coded) is presented in the center panel together with the derived gyrating electric field (arrows). Again, all extracted quantities scale linearly to the maximum vertical displacement at the surface and are normalized to $u_{Y,0} = 1\,\mathrm{nm}$. In addition, the electrical field components are normalized to $f_{\mathrm{SAW}} = 1\,\mathrm{GHz}$, since they are proportional to the spatial derivative of the electric potential and, thus, scale linearly to the surface acoustic wave frequency f_{SAW}. The lower panel shows dependence of the electric potential Φ and the electrical fields $\mathcal{E}_Y$ and $\mathcal{E}_Z$ along the surface of the substrate. Again, our results of the finite element modeling exhibit the characteristic $\pi/2$ phase shift between the longitudinal and the transverse electric field components of the surface acoustic wave on $\mathrm{LiNbO_3}$ which reflects the gyrating nature of the electric field in the plane defined by the surface normal and the propagation direction. Moreover, the decays of the longitudinal ($\mathcal{E}_Z$) and transverse ($\mathcal{E}_Y$) components of the electric field are depicted in the left panel, confirming again the tight confinement at the surface of a $\mathrm{LiNbO_3}$ substrate.

3.3 Excitation of surface acoustic waves

The excitation and detection of a surface acoustic wave on a piezoelectric substrate was first introduced by White and Voltmer in 1965 [160]. They utilized the inverse piezoelectric effect to excite and detect surface acoustic waves by an electric signal which induces the deformation of the underlying substrate. Therefore, small stripes of metal electrodes, so-called fingers, are deposited on the surface of a substrate and used to apply the electrical potential to the substrate. Their arrangement forms a so-called interdigital transducer (IDT) which consists of two sets of such interdigitating comb-shaped electrodes. Moreover, for the effective generation of surface acoustic waves, the crystal orientation of the substrate and the alignment of the interdigital transducer to this orientation are crucial. Nowadays, such interdigital transducers allow to perfectly address defined propagation directions on piezoelectric substrates due to high precision fabrication methods. The simplest configuration of such a structure is a Split-1 interdigital transducer which is depicted in Figure 3.4 (a). When a radio frequency (rf) signal is applied to the interdigital transducer structure, the high frequency alternating voltage induces a mechanical distortion of the piezoelectric crystal underneath. If the frequency f_{rf} hits the resonance condition of the interdigital transducer (Equation 3.20), the propagating deformations, which are excited by each electrode, interfere constructively with the waves created at all other fingers and result in a surface acoustic wave propagating in both directions from the interdigital transducer:

$$\lambda_{\mathrm{SAW}} = 4 \cdot p = \frac{v_{\mathrm{SAW}}}{f_{\mathrm{rf}}} \tag{3.20}$$

with λ_{SAW} and v_{SAW} being the wavelength and velocity of the surface acoustic wave and p being the pitch of the electrodes. In addition, it is also possible to excite certain higher harmonics of the resonance frequency. For a Split-1 interdigital transducer, only odd numbered harmonics can be launched as even harmonics are suppressed due to the symmetric arrangement of the fingers.

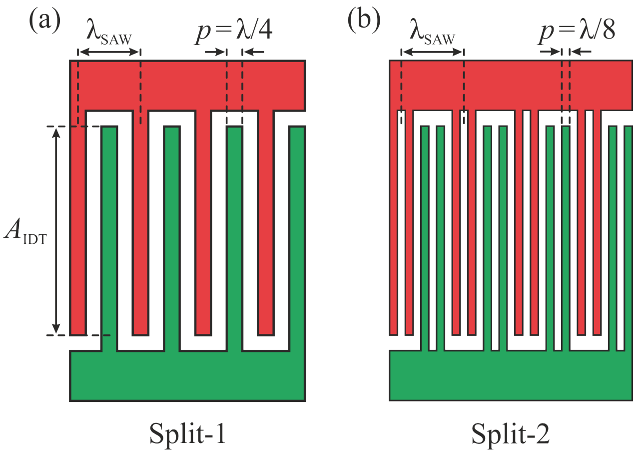

Figure 3.4: Schematic of an interdigital transducer geometry design in (a) Split-1 and (b) Split-2 configuration. The finger period determines the wavelength of the surface acoustic wave λ_{SAW}. The metallization ratio p/a is the fraction of the area covered by the electrodes with a finger width p. The overlapping area of the fingers is the transducer aperture A_{IDT}.

Other important geometrical parameters are the transducer aperture A_{IDT}, the transducer length as well as the metallization ratio p/a. The aperture is defined by the overlap between the fingers of the each comb-shaped electrode and determines the lateral expansion of the wavefront. The metallization ratio p/a is the fraction of the area covered by the electrodes with a finger width p. In this work, the metallization ratio is typically chosen to be $p/a = 0.5$ setting the width of the fingers equal to their distance. Note, the metallization ratio is important for the efficient excitation of higher harmonics.

Moreover, other configurations, such as a Split-2 interdigital transducer which is depicted in Figure 3.4 (b), allow the more efficient generation of higher odd harmonic frequencies and strongly reduce the reflectivity of these interdigital transducers. In this Split-2 configuration, a pair-wise arrangement of fingers of each comb-shaped electrode leads to a wavelength-to-finger width relation of $\lambda_{\mathrm{SAW}} = 8 \cdot p$. Additionally, more complex layouts, such as interdigital transducers with varying finger period (tapered, dispersive) and such as finger arrangements with an asymmetric ordering which are able to generate even harmonics can be realized. In this work, predominantly Split-2 interdigital transducers were used.

3.4 Sample design

In order to probe and manipulate semiconductor nanowires by surface acoustic waves, these waves have to be efficiently excited on a substrate with properly designed sample geometries. As the nanowires examined in this work can be transferred onto any suitable material, $LiNbO_3$ substrate is chosen which is one of the standard materials used for surface acoustic waves and fits the requirements for the high coupling of energy into the electromechanical wave. As already explained in the previous section, interdigital

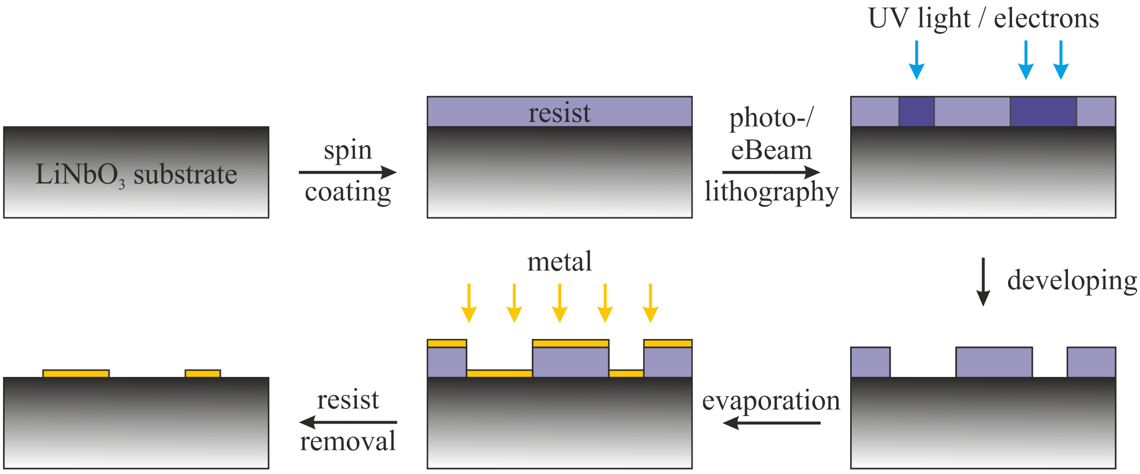

Figure 3.5: Schematic illustration of the fabrication process of a surface acoustic wave chip utilizing photo- or electron-beam lithography. The $LiNbO_3$ substrate is spin coated with a suitable resist which is illuminated with either an ultraviolet light through a chromium mask or an electron beam to pattern the resist at defined areas. The exposed resist is then removed within a developer solution. Afterwards, metal is evaporated on the substrate. After evaporation, a lift-off is performed removing the remaining resist and the metal structures at the exposed areas cover the substrate surface.

transducers have to be processed for the electrical excitation of surface acoustic waves on the surface of the substrate. The interdigital transducer structures themselves are fabricated by a standard lift-off process using a resist mask which is patterned by optical or electron beam lithography. The whole fabrication process is schematically illustrated in Figure 3.5. For both lithography processes, a positive resist is spin coated on the substrate and baked on a hot plate. Afterwards, the resist is exposed either by an ultraviolet (UV) light using a chromium mask or an electron beam using a focused beam of electrons which scans the substrate, to transfer the pattern into the resist at defined areas. Hereby, electron beam lithography has the advantage of the flexible designs varying from chip to chip and the fabrication of structures being much smaller than a few micrometers. The exposed resist is then removed within a developer solution. After a short cleaning step in a plasma cleaner, the substrates are inserted into an evaporation chamber, in which 5 nm of titanium as an adhesion agent, and 50 nm aluminum are deposited for the metal fingers and contacts. Finally, the rest of the resist is removed in a lift-off process and, thus, only the metal structures at the exposed areas remain at the substrate surface.

The fabricated interdigital transducers are oriented along the Z-direction of a Y-cut $LiNbO_3$ substrate and are arranged in a delay line configuration which is formed by two identical interdigital transducers located opposite to each other as shown in the scanning electron micrograph in Figure 3.6. Consequently, both interdigital transducers of this configuration can be characterized by measuring the transmission of such a delay line with one interdigital transducer acting as a transmitting and the other as a receiving transducer. Moreover, additional delay lines are aligned along the X-direction of the substrate allowing the excitation of surface acoustic waves perpendicular to the propagation

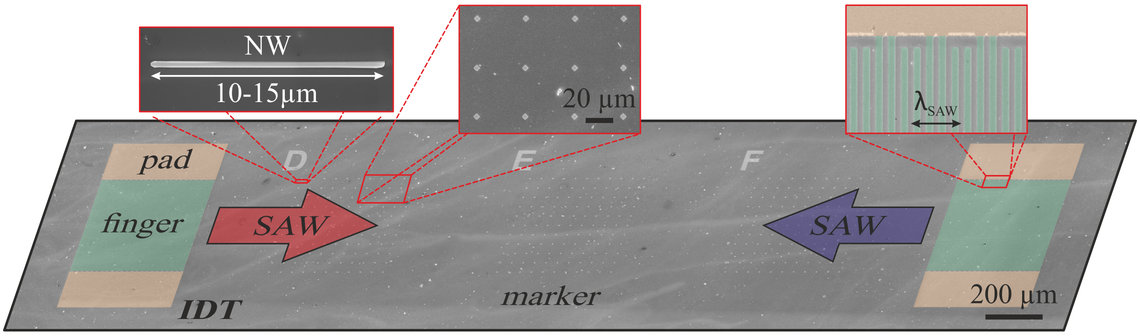

Figure 3.6: Scanning electron micrograph of a surface acoustic wave delay line along the Z-direction of a Y-cut $LiNbO_3$ substrate for single nanowire acousto-optoelectric spectroscopy. Fingers and contact pads of both interdigital transducers are colored in green and orange, respectively. Magnified images show the finger structure of a Split-2 interdigital transducer used for surface acoustic wave generation, the markers, used for orientation on the sample, and a single nanowire aligned with the surface acoustic wave's propagation direction, respectively.

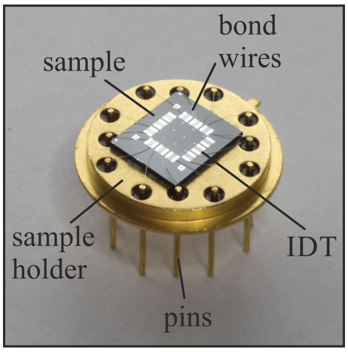

Figure 3.7: A sample with several delay lines is mounted on a sample holder with interdigital transducers wire-bonded to the pins. The chip carrier fits into the socket of the cryostat. Electrical connection is realized by high frequency wires outside to the radio frequency connectors of the cryostat.

direction predominantly used in this work. In addition, markers are fabricated on the sample to allow easy orientation and navigation on the sample.

For the acoustic measurements, the nanowires have to be transferred from the growth substrate to the surface acoustic wave chip with the lithographically defined interdigital transducers. Therefore, two different methods are used. With the so-called flip-chip method, nanowires are transferred from the growth substrate to the chip by bringing both under moderate pressure into contact and displacing them with respect to each other. This procedure breaks off the as-grown nanowires at their base and transfers nanowires onto the surface acoustic wave chip. In addition, nanowires can be directly transferred onto the surface acoustic wave chip by drop-casting of a nanowire solution obtained from sonication of an as-grown substrate piece in isopropyl alcohol. After transfer, we select well-isolated individual nanowires which are aligned with their [111] growth axis along the Z-propagating surface acoustic wave within ±5° as shown in Figure 3.6.

For the measurements, the sample is mounted to a chip carrier as shown in Figure 3.7 that can be integrated into the low temperature cryostat. To ensure good thermal contact, the substrate is glued to the chip carrier using a silver adhesive. Moreover, the interdigital transducers are connected to gold plated pins of chip holders by wire bonding. The chip carrier allows for individual contacting of up to eight interdigital transducers and can be used in the different setups to connect the electronics to the chip.

3.5 Interfacing semiconductor heterostructures with surface acoustic waves

The interaction of semiconductor heterostructures with a propagating surface acoustic wave is governed by the surface acoustic wave's piezoelectric and strain fields. Both, the mechanical and the electrical modulation, directly influence the charge carriers by the deformation potential and the acousto-electric coupling and, thus, have strong impact on the optical and electrical properties of semiconductors. Hence, the static and dynamic behavior of carriers in semiconductors have to be described under external influences, such as applied fields or optical excitation, that cause deviation from the thermal equilibrium conditions.

The contribution of the strain field on the control of semiconductor nanostructures is caused by the deformation potential of the mechanical wave. As mentioned above, the elliptical motion of the atoms induces dynamic stresses and strains, influencing the lattice constant of a crystal and, thus, the bandgap energy of a semiconductor. Thereby, a tensile strain increases the lattice constant, leading to a decrease of the bandgap energy. In contrast, a compressive strain decreases the lattice constant leading to an increase of the bandgap energy. As a consequence, this effect is directly correlated with the surface acoustic wave's mechanical amplitude and potential inducing a type-I band edge modulation.

Beside the mechanical wave, surface acoustic waves are also accompanied by piezoelectric fields which cause a type-II band edge modulation of the conduction and valance band within semiconductor nanostructures being periodic both in time and space (cf. Figure 3.8). This results in stability points for electrons in the conduction band and holes in the valance band which are separated by $\lambda_{\mathrm{SAW}}/2$ and propagate along with the wave. Moreover, the electric field can dissociate photo-generated excitons which, subsequently, leads to the spatial separation of electrons and holes and induces the spatio-temporal dynamics of such dissociated charge carriers. This gives rise to both, the suppression of the optical emission of the semiconductor nanostructures and the bipolar transport of electrons and holes with the propagating surface acoustic wave. It is to mention that for the experiments performed in this work, the contribution of the strain fields plays only a minor role, while acousto-electric modulation via electric fields significantly contributes to spatio-temporal charge carrier dynamics.

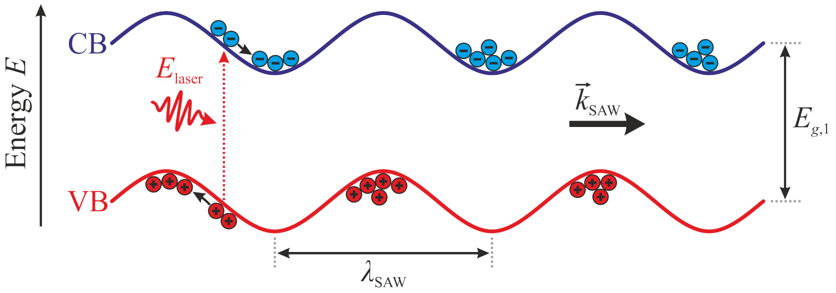

Figure 3.8: Type-II band modulation of a semiconductor induced by the piezoelectric potential of a surface acoustic wave. The conduction and valance band are modulated dynamically. The piezoelectric fields dissociate the excitons and induce a bipolar charge transport. Both charge carriers are spatially separated by λ_{SAW}.

The charge carrier dynamics in semiconductors are mainly driven by diffusion and drift currents and, thus, by the band edge modulation through the electric field of a the surface acoustic wave having a strong impact on the transport of charge carriers. This transport can set in for sufficiently large electric field strengths by inducing drift currents along the propagation direction of the surface acoustic wave. Thereby, the carrier transport in semiconductors is mainly limited by scattering processes, and occurs with a mean drift velocity v_{drift}. This velocity is related to the electric field and the mobility $\mu_{n,p}$ for electrons and holes (at low fields) and has to become comparable to the sound velocity in the medium for the transport of charge carriers along the surface acoustic wave's propagation direction by the electric field:

$$\mu_{n,p} \cdot \mathcal{E}_{\text{SAW}} = v_{n,p}^{\text{drift}} \geq v_{\text{SAW}}. \tag{3.21}$$

Otherwise the charge carriers show an oscillating behavior around the point of excitation without an efficient transport along this direction. Moreover, both types of charge carriers have to be considered separately since they can exhibit different mobilities, which are proportional to the inverse of the effective mass of electrons and holes. In general, for charged particles, the electric field results in a current $\mathbf{J}^{\text{drift}}$ for electrons and holes which is given by:

$$\begin{aligned} \mathbf{J}_n^{\text{drift}} &= en\mathbf{v}_n^{\text{drift}} = en\mu_n\boldsymbol{\mathcal{E}} \\ \mathbf{J}_p^{\text{drift}} &= ep\mathbf{v}_p^{\text{drift}} = ep\mu_p\boldsymbol{\mathcal{E}}. \end{aligned} \tag{3.22}$$

Moreover, a nonuniform charge carrier distribution, for example, due to the local injection, will lead to a process of diffusion by which the carriers migrate from the region of high concentration towards the region of low concentration. Again, this process depends on the mobility of each charge carrier and, thus, charge carriers with higher mobilities distribute faster along equal energy levels. This flow of carriers, is called the diffusion current $\mathbf{J}^{\text{diff}}$ and is given by:

$$\begin{aligned} \mathbf{J}_n^{\text{diff}} &= eD_n\boldsymbol{\nabla}n \\ \mathbf{J}_p^{\text{diff}} &= -eD_p\boldsymbol{\nabla}p. \end{aligned} \tag{3.23}$$

Here, $D_{n,p}$ is the material- and particle-dependent diffusion constant while n and p are spatially dependent carrier concentrations. The diffusion constants can be obtained from the Einstein relation $D_{n,p} = \mu_{n,p} \cdot k_\mathrm{B} \cdot T/e$ with the Boltzmann constant k_B and the elementary charge e. The total current can be obtained from the combination of the drift and diffusion current for the different types of charge carriers:

$$\mathbf{J}_{n,p} = \mathbf{J}_{n,p}^{\mathrm{drift}} + \mathbf{J}_{n,p}^{\mathrm{diff}}. \tag{3.24}$$

While the current-density equations are for steady state conditions, the surface acoustic wave induced charge carrier dynamics are time-dependent phenomena and, thus, the continuity equations have to be considered:

$$\begin{aligned} \frac{\partial n}{\partial t} &= \frac{1}{e}\nabla \mathbf{J}_n + G_n - R_n \\ \frac{\partial p}{\partial t} &= \frac{1}{e}\nabla \mathbf{J}_p + G_p - R_p. \end{aligned} \tag{3.25}$$

It follows that the net change of the carrier concentration is the difference between generation $G_{n,p}$ and recombination $R_{n,p}$ of each charge carrier, in addition to the spatial change for each charge carrier species. In our experiments, the initial generation of electrons and holes results exclusively from the excitation pulse of a laser. The recombination of both charge carriers first creates an exciton, which then decays with a certain probability, by emitting a photon or dissociating into an electron and a hole. As the exciton, as a neutral quasi-particle, is in a first approximation unaffected by electric fields, it only underlies the diffusion process.

The surface acoustic wave induced movement can be, thus, determined by the drift and diffusion equations coupled with the Poisson equation of electrons, holes and excitons. For simplicity, it is assumed that the charge carrier dynamics occur along the x-direction which is also realistic for the quasi one-dimensional nanostructures examined in this work. This reduces the problem to a one-dimensional calculation and, thus, the complexity of a computational implementation. Consequently, the coupled drift and diffusion equations for electrons, holes and excitons are given by:

$$\begin{aligned} \frac{\partial n}{\partial t} &= D_n \frac{\partial^2 n}{\partial x^2} + \mu_n \frac{\partial(\mathcal{E}_x \cdot n)}{\partial x} + G - R + T \\ \frac{\partial p}{\partial t} &= D_p \frac{\partial^2 p}{\partial x^2} + \mu_p \frac{\partial(\mathcal{E}_x \cdot p)}{\partial x} + G - R + T \\ \frac{\partial X}{\partial t} &= D_X \frac{\partial^2 X}{\partial x^2} + R - \frac{X}{\tau_X} - T \end{aligned} \tag{3.26}$$

with n, p and X being the density of electrons, holes and excitons and $\mathcal{E}_x$ being the electric field in x-direction. The generation rate G of the charge carriers is determined by an external laser pulse while the recombination rate R is for low charge carrier concentrations proportional to the overlap, i.e. product of electrons and holes with $R = c_X \cdot n \cdot p$ determining the generation rate of excitons and with c_X denoting the probability of an exciton creation [161]. The dissociation of excitons into electrons and holes is characterized by the ionization rate of excitons T via tunneling. The radiative decay of excitons occurs with the decay constant τ_X.

Consequently, the dynamics of the charge carriers are predominantly determined by two different contributions of the electric field $\boldsymbol{\mathcal{E}}(\mathbf{r}, t) = \boldsymbol{\mathcal{E}}_{\text{ind}}(\mathbf{r}, t) + \boldsymbol{\mathcal{E}}_{\text{SAW}}(\mathbf{r}, t)$ which can be distinguished by the external part arising form the surface acoustic wave, and an induced part resulting from the charge carrier distributions. For one-dimensional dynamics, only the longitudinal contribution of the surface acoustic wave's piezoelectric field $\mathcal{E}_{\text{SAW}}(x, t)$ has to be considered and, thus, charge carriers are influenced by the electric potential $\Phi_{\text{SAW}} = \Phi_{\text{SAW}}^{(0)} \sin(kx - \omega t + \phi)$. Thus, it is derived by:

$$\mathcal{E}_{\text{SAW}}(x, t) = -\nabla \Phi_{\text{SAW}} = -\mathcal{E}_0 \cos(kx - \omega t + \phi) \tag{3.27}$$

with $\mathcal{E}_0$ being the amplitude of the oscillating field, and k and ω being the wave vector and the frequency of the surface acoustic wave, respectively.
The second contribution $\boldsymbol{\mathcal{E}}_{\text{ind}}(\mathbf{r}, t)$ arises from the inhomogeneous distribution of electrons and holes and is given by using the Poisson equation for one-dimensional systems by:

$$\frac{\partial \mathcal{E}_{\text{ind}}(x, t)}{\partial x} = \frac{e(p(x, t) - n(x, t))}{\epsilon} \tag{3.28}$$

where ϵ is dielectric constant. Due to the comparatively small charge carrier densities and the high electric fields of the surface acoustic wave, this contribution have only minor influence.
This mathematical description is the basis of the calculation of the charge carrier dynamics in the examined semiconductor nanowires. In particular, the coupled differential Equations 3.26 are solved by finite element methods in an explicit way which was implemented by Florian Schülein in his PhD thesis [162].

Chapter 4

Acousto-optoelectric spectroscopy [1]

For our acousto-optoelectric investigations on semicondutor nanowires, the optical properties of excitons and free charge carriers are probed and manipulated under influence of piezoelectric surface acoustic waves. By utilizing the acousto-electric coupling between photo-excited charge carriers and the piezoelectric field of a surface acoustic wave, acousto-optoelectric spectroscopy gives direct insights into the charge carrier dynamics in these nanostructures [39, 43, 163–166]. These induced dynamics, in turn, strongly modulate the optical emission properties in the time domain and lead to characteristic fingerprints which can be detected in photoluminescence experiments [28, 45, 167, 168].
For acousto-optoelectric spectroscopy, a standard photoluminescence setup is used which is extended by electric devices for the generation and timing of the surface acoustic waves. This technique allows to analyze the energy-resolved and time-resolved behavior of the emission of the investigated nanostructures providing distinct insights into the properties and dynamics of various nanosystems. Here, this chapter addresses the basic implementation of this setup and, in particular, the electric excitation of a surface acoustic wave which drives the aforementioned dynamics of the photo-excited charge carriers in the nanostructure. Due to the complexity of its implementation, the correct timing of all components is crucial. Hence, the optical excitation, optical detection and excitation of the surface acoustic wave have to be accurately adjusted in time to enable the exact interaction of all devices.
In addition, this chapter describes the major key characteristics of acoustically driven charge carrier dynamics in near-pristine zincblende nanowires with low rational twin density which is discussed in more detail by Jörg Kinzel in his PhD thesis [169]. Finally, it addresses the observed coupled emission dynamics and redistribution of charge carriers on subnanosecond time scales within two interconnected quantum well systems of a nanowire heterostructure which is partly published in Nano Letters [13].

4.1 Experimental methods

The principle of acousto-optoelectric spectroscopy on semiconductor nanowires is schematically depicted in Figure 4.1. For our measurements, various nanowire heterostructures with a length usually ranging between $l_{\mathrm{NW}} = 10\,\mu\mathrm{m}$ and $15\,\mu\mathrm{m}$ are transferred onto a

---

[1] partly published and with permission from [13]. Copyright 2019 American Chemical Society.

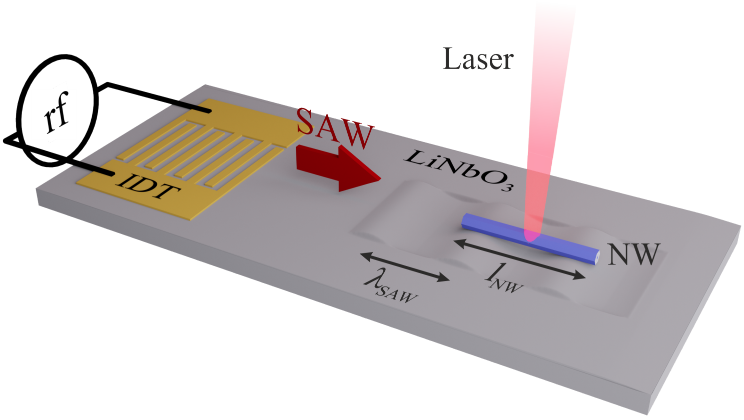

Figure 4.1: Schematic illustration of a typical surface acoustic wave chip used for the acousto-optoelectric spectroscopy on single nanowires (not to scale). It consists of an interdigital transducer which generates a surface acoustic wave. The surface acoustic wave propagates towards the nanowire being parallel aligned to the surface acoustic wave's propagation direction and induces a counterclockwise gyrating electric field that dissociates and accelerates electrons and holes within the nanowire structure and, thus, induces the spatio-temporal charge carrier dynamics.

YZ-cut $\mathrm{LiNbO_3}$ substrate with lithographically pre-patterned interdigital transducers. By applying a resonant radio frequency signal to the interdigital transducers, a Rayleigh-type surface acoustic wave is generated propagating with a phase velocity $c_{\mathrm{SAW}} = 3495\,\mathrm{m/s}$ along the surface of the $\mathrm{LiNbO_3}$ crystal. The design of the interdigital transducer corresponds to a wavelength of $\lambda_{\mathrm{SAW}} = 18\,\mathrm{\mu m}$ and, thus, to a resonance frequency of $f_{\mathrm{SAW}} = 194\,\mathrm{MHz}$ and an acoustic period $T_{\mathrm{SAW}} = 5.15\,\mathrm{ns}$. For our experiments, nanowires, which are aligned with their [111] growth direction parallel to the surface acoustic wave's propagation direction, are selected and studied by their optical properties. All experiments are performed at low temperature of $T = 8\,\mathrm{K}$ and, consequently, occur in the classical multiphonon regime since the thermal energy exceeds the energy of a single phonon ($k_{\mathrm{B}}T >> h/T_{\mathrm{SAW}}$). Moreover, electron-hole pairs inside the nanowires are excited by an above-bandgap diode laser at low optical powers allowing to study charge carrier dynamics in the limit of low carrier concentrations. When propagating on a piezoelectric substrate, the mechanical wave induces a gyrating electric field driving these dynamics of such photo-generated charge carriers. Since λ_{SAW} defines the length scale on which the surface acoustic wave induced charge carrier dynamics occur, comparable dimensions of the surface acoustic wave's wavelength and the nanowire length are mandatory [38]. Finally, the resulting emission of the nanowires is than analyzed by its time-integrated and time-resolved behavior.

The experimental configuration of the acousto-optoelectric spectroscopy setup is depicted in Figure 4.2. It can be divided in three main building blocks: optical excitation (red box), surface acoustic wave excitation (blue box) and optical detection (green box). The optical excitation of electron-hole pairs is realized by an above-bandgap laser (PicoQuant, LDH-

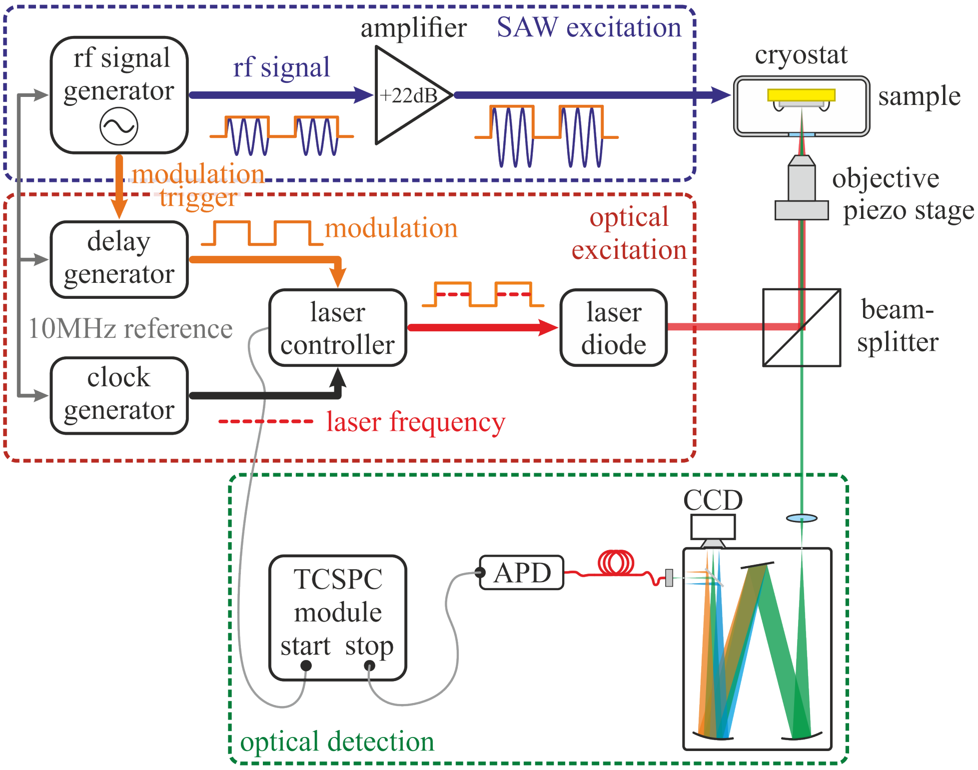

Figure 4.2: Experimental setup for acouto-optoelectric spectroscopy on semiconductor nanowires consisting of three main building blocks: optical excitation (red box), surface acoustic wave excitation (blue box) and optical detection (green box). Optical excitation of the nanowires is realized by a pulsed laser source with a repetition rate set by the clock signal. For modulated surface acoustic wave excitation, the gate signals of both, surface acoustic wave excitation and optical excitation, are synchronized by delaying both respective gate signals in time. For optical excitation at fixed times during the acoustic cycle, the repetition rate of the laser source is locked to the radio frequency generator and set to an integer fraction of f_{SAW}. A 10 MHz reference signal is applied to ensure time alignment of all building blocks. Optical excitation and detection is positioned and focused onto the sample in a liquid helium cryostat by a piezo stage and a microscope objective. The optical detection signal is spectrally filtered by a grating monochromator. For time-integrated detection, a multi-channel optical detector is used. For time correlated single photon counting, single photon events are detected by a time-resolved single-channel detector and correlated to a clock signal with a frequency applied to the laser source.

D-C-660) with a wavelength of $\lambda_{\text{Laser}} = 660\,\text{nm}$, a pulse width below $\tau_{\text{Laser}} < 90\,\text{ps}$ and a variable repetition rate up to 80 MHz. The laser diode is triggered externally by a laser controller (PicoQuant, PDL 800-D) allowing the adjustment of the optical output power (P_{Laser}), while the repetition rate f_{Laser} is provided by a clock generator (Stanford Research System, CG635). For the excitation of nanostructures, the laser beam is focused to a spot size of $d_{\text{Laser}} \approx 1.5\,\mu\text{m}$ by a x50 microscope objective which is mounted to a high-precision closed-loop piezo-system (Piezojena, NV40) that enables the recording of high-resolution intensity profiles over larger areas. For low temperature measurements, the samples are mounted onto a He-flow cryostat which is cooled down to temperatures of about 8 K. Finally, the optical excitation is separated from the optical detection by a beamsplitter.

For spectral analysis, the collected emission of the nanowires is spectrally dispersed by a Czerny-Turner grating monochromator with a focal length of 0.5 m (Andor, Shamrock 500i) and is then detected by a thermoelectrically cooled charge-coupled device (CCD) (Andor, iDus 416) allowing the detection of time-integrated but energy-resolved emission. In order to fully resolve the surface acoustic wave induced charge carrier dynamics, time-resolved studies have to be conducted. Therefore, the charge-coupled device has to be replaced by a single photon silicon avalanche photodetector (APD) which is connected by a multi mode fiber to the spectrograph that is used to spectrally filter the collected photoluminescence emission. This allows the detection of single photon events with a specific energy at a high time resolution $\tau_{\text{APD}} < 350\,\text{ps}$. These events are then correlated with a trigger signal from the laser controller by a time-correlated single photon counting (TCSPC) module measuring the time delay Δt between excitation and detection of a photon. By accessing many of these time stamps for many photons, this results in a histogram revealing the temporal decay characteristics of the system. In general, the decay times in this thesis are obtained directly from the raw data without further deconvolution of an instrument response function. Moreover, the hierarchy of the system's parameters is $\tau_{\text{Laser}} < \tau_{\text{APD}} < d_{\text{Laser}}/c_{\text{SAW}} \approx 430\,\text{ps}$. Thus, the resolution is determined mainly by the size of the laser spot in the setup.

For the excitation of surface acoustic waves, this standard photoluminescence setup is extended by the integration of the surface acoustic wave components. Due to the different speed of the optical, electronic and acoustic signals, the exact timing and, thus, the synchronization of each component are essential. For this purpose, the cryostat is additionally equipped with radio frequency connectors allowing to apply high-frequency signals to the surface acoustic wave chips. This radio frequency signal for the surface acoustic wave excitation is generated by a radio frequency signal generator (Stanford Research Systems, SG382) and amplified by a radio frequency amplifier (Mini-Circuits, ZHL-2010+) which allows to further increase the radio frequency amplitude, before being applied to the radio frequency connectors of the cryostat. To prevent unwanted thermal effects and interference of reflected surface acoustic wave beams at interdigital transducers or sample edges, the excitation of the wave is modulated in time. Consequently, the optical excitation needs to be modulated as well and both, optical and surface acoustic wave excitation, have to be synchronized. This can be realized by applying a gate signal, which is generated by a delay generator (Stanford Research Systems, DG645), to the gating input of the laser controller. Moreover, the delay generator is triggered by the radio frequency generator to emit the gate signal which is delayed in time to synchronize the arrival time of the laser pulses and the time when the surface acoustic wave reaches the nanowire. This temporal delay mainly compensates the different signal propagation times of the surface acoustic wave and laser excitation.

A key characteristic of acousto-optoelectric spectroscopy is that electron-hole pairs can be photo-generated at a well-defined time during the surface acoustic wave cycle to fully resolve the surface acoustic wave driven dynamics of a process. This, in particular, allows to correlate the recorded behavior of the dynamics to the gyrating electric field of the propagating surface acoustic wave. Therefore, both frequencies of surface acoustic wave and optical excitation have to be synchronized in addition to the temporal overlap of both excitations. Hereby, the frequency of the surface acoustic wave is reverenced to a multiple integer of the repetition frequency of the laser, $n \cdot f_{\text{Laser}} = f_{\text{SAW}}$, with n being integer [28, 39, 169–171]. Thus, the laser pulses have a fixed relationship to the phase of the surface acoustic wave and each laser pulse excites electron-hole pairs at the same time during an acoustic cycle. The time of excitation within an acoustic period can be varied by tuning the relative phase, i.e. temporal delay, between the optical and surface acoustic wave excitation. To ensured the exact time alignment of all instruments, each component has to be locked to the same clock reference signal of 10 MHz. For the following experiments, the surface acoustic wave frequency was set to $f_{\text{SAW}} = 194\,\text{MHz}$ while a laser frequency of $f_{\text{Laser}} = 19.4\,\text{MHz}$ was applied. Consequently, charge carriers are excited at every tenth surface acoustic wave cycle ensuring that the decay of the charge carriers takes place much faster than the optical excitation.

As mentioned above, the charge carriers within nanowires can be optically excited at a well-defined time during the acoustic cycle and their dynamics can be probed in the time domain. A full timing scheme of such phase-locked experiments conducted in this thesis is depicted in Figure 4.3 [42, 172]. The absolute time t is determined by the surface acoustic wave at the position of the excitation spot on the nanowires. Thereby, the vertical displacement component u_Y (blue curve) serves as a reference and we assign the local phase, at which the electric field vector $\boldsymbol{\mathcal{E}}$ (red arrow) is transverse, pointing downwards towards the substrate, to $t = 0$. As the absolute time t progresses, the displacement components oscillate with $u_Y \propto \sin(2\pi f_{\text{SAW}} t)$ and the induced electric field vector $\boldsymbol{\mathcal{E}}$ gyrates counterclockwise near to the surface of the YZ-cut LiNbO_3 crystal [42]. By setting the delay time τ between the laser and the surface acoustic wave excitation from 0 to T_{SAW}, charge carriers can be excited at a well-defined phase Φ of the acoustic cycle with $\tau = T_{\text{SAW}} \cdot \Phi/360°$. Consequently, the charge dynamics can be probed and manipulated at different surface acoustic wave phases in stroboscopic measurements. Without this phase lock relationship, the dynamics would be averaged over the whole surface acoustic wave period. In addition, for the temporal-resolved measurements, the time stamps of all detection events are recorded relatively to the laser excitation by the time Δt and presented in a histogram.

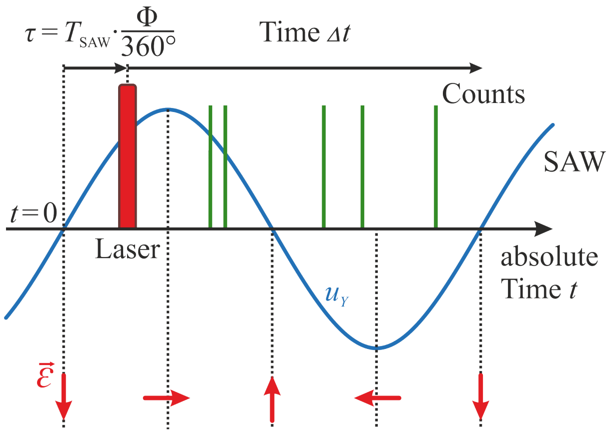

Figure 4.3: The transverse displacement component u_Y (blue) oscillates with an acoustic period of T_{SAW}. The local phase of the surface acoustic wave oscillation sets the absolute time t of the experiment. Pulsed laser excitation, marked in red, is delayed by $\tau = T_{\mathrm{SAW}} \cdot \Phi/360°$ injecting electrons and holes. As time progresses, the electric field vector gyrates counterclockwise as indicated in the lower part. The individual time-resolved detection events are registered relatively to the laser excitation.

In general, the orientation of electric field, i.e. the type-II band edge modulation, at the position of the laser spot at the time of the laser excitation programs the subsequent surface acoustic wave-driven carrier dynamics. In Figure 4.4, schematics of the relative orientation of a nanowire, the oscillating components of the surface acoustic wave-induced electric field and the type-II band edge modulation are shown for fixed surface acoustic wave phases defining the orientation of the electric field and nanowire axis. At the surface acoustic wave phase of $\Phi = 0°$, the electric field is orientated perpendicular to the surface towards the substrate and the resulting maximum of electric potential is located at the position of the nanowire creating an unstable point for electrons in the conduction band and a stable point for holes in the valence band, respectively. Thus, if the radio frequency power is sufficiently high, electrons are accelerated away from the unstable point of excitation dissociating in the direction of the adjacent stable minima. This leads to a spatial separation of electrons and holes along the axis of the nanowire strongly suppressing the radiative recombination. For $\Phi = 180°$, this situation is reversed with the electrons (holes) being now located at the stable (unstable) point of the conduction band. However, hole acceleration from the point of generation to their stable valance band maxima is weak compared to the electrons as their low mobility μ_p inhibits transport by the surface acoustic wave [28]. As a consequence, holes remain mostly stationary preventing the effective separation of electrons and holes and leading to a pronounced photoluminescence emission. In turn, the electric fields at $\Phi = 90°$ and 270° are aligned parallel and antiparallel to surface acoustic wave propagation direction inducing a steep slope in the band modulation. At these surface acoustic wave phases, electrons and holes experience large electric fields leading to an acceleration of the electrons and holes along the axis of nanowires in opposite directions and, consequently, dissociating the photo-excited electron-hole pairs.

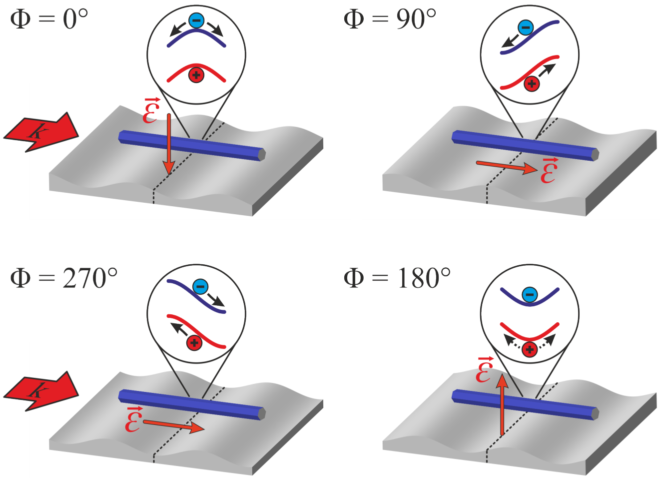

Figure 4.4: Schematics of relative orientation of a nanowire and the components of the surface acoustic wave-induced electric field at a fixed point relative to the surface acoustic wave and at different surface acoustic wave phases between laser and surface acoustic wave excitation. Electric field periodically gyrates at a fixed position (laser spot) along the nanowire with time. The insets show the carrier dynamics induced by the spatial type-II band edge modulation of the surface acoustic wave.

4.2 Charge carrier dynamics in zincblende GaAs nanowires

The acouto-optoelectric spectroscopy on GaAs nanowires has been studied in previous works demonstrating these spectroscopy technique to be a versatile tool to study and manipulate these systems [28, 38, 39, 46–49]. In particular, it reveals characteristic fingerprints of acoustically driven charge carrier dynamics which are demonstrated in the following for a GaAs-AlGaAs core-shell nanowire, referred to as NW7, with a predominant zincblende crystal phase with only very few individual twin defects [85].

In a first step, the surface acoustic wave induced quenching of the nanowire emission is probed. Therefore, a surface acoustic wave is applied without phase locking of wave and laser excitation, and the photoluminescence emission of the nanowire is spectrally resolved for increasing acoustic power. In Figure 4.5, the time-integrated photoluminescence emission spectra (left panel) are presented as a function of different acoustic powers (P_{rf}) applied to the interdigital transducer with a frequency of $f_{\mathrm{SAW}} = 194\,\mathrm{MHz}$. For no surface acoustic wave applied or low acoustic powers, a characteristic zincblende emission signal is detected at photon energy $E_{\mathrm{ZB}} = 1.522\,\mathrm{eV}$. As P_{rf} is increased, the overall photoluminescence emission is quenched due to the effective separation of electrons and holes. This quenching behavior is further analyzed by extracting the normalized integrated photoluminescence intensity (normalized to the maximum of the unperturbed emission at low $P_{\mathrm{rf}} < -15$ dBm) from these spectra. The obtained data is plotted in the right panel of Figure 4.5. At low surface acoustic wave powers, the emission signal is not reduced as the modulation of the conduction and valance band by the electric field is weak and radiative recombination of the excitons is unperturbed (cf. left inset). As the acoustic power and, thus, the electric field amplitude of the surface acoustic wave increases, the

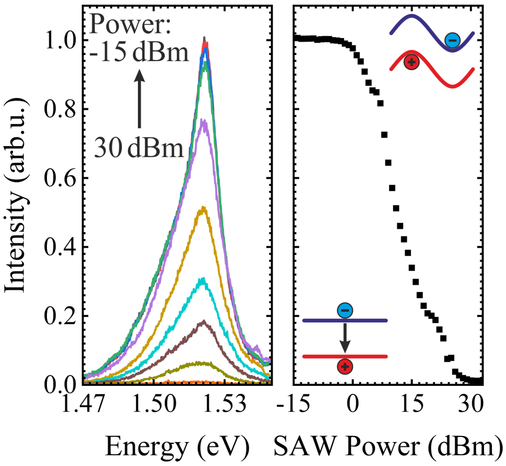

Figure 4.5: Emission spectra (left panel) at the center of a zincblende GaAs nanowires with few rotational twin defects modulated by a continuous surface acoustic wave for varying surface acoustic wave powers P_{rf} applied to an interdigital transducers. Spectra from top to bottom correspond to the increasing surface acoustic wave power in steps of $\Delta P_{\mathrm{rf}} = 5\,\mathrm{dBm}$. Right panel: Extracted normalized photoluminescence intensities of the free zincblende excitons as a function of surface acoustic wave power P_{rf}. The insets indicate the magnitude of the band edge modulation induced by the surface acoustic wave at low and high acoustic power. With increasing surface acoustic wave power density, the overall emission is quenched due to the efficient dissociation and acceleration of electrons and holes by the surface acoustic wave's piezoelectric field.

overall photoluminescence emission quenches above an acoustic power of $P_{\mathrm{rf}} > 0$ dBm and is almost completely suppressed for $P_{\mathrm{rf}} = 30$ dBm. This quenching behavior arises from the efficient separation of the photo-generated of electrons-holes pairs due to the surface acoustic wave induced type-II band edge modulation as depicted schematically in the right inset [28]. At the onset of the induced surface acoustic wave dynamics, the electric field is not sufficient for charge carrier transport and the electrons and holes are only oscillating over small travel distances. With increasing acoustic powers, the electric field drives the dynamics of the electrons and a transport of the electrons sets in while holes remain quasi-stationary due to their lower mobility. At high P_{rf}, the spatial band structure modulation separates electrons and holes to the stable points in the conduction band and valence band, respectively, and both charge carrier species are transported by the surface acoustic wave. Thus, the radiative recombination is strongly suppressed.

For phase-locked excitation condition, the laser pulse has a fixed relation to the radio frequency signal and a time-integrated emission spectrum or a time-resolved histogram is recorded for different surface acoustic wave phases. This allows to probe the surface acoustic wave driven carrier dynamics at distinct surface acoustic wave phases in a stroboscopic measurement. In time-integrated experiments, the local and dynamic modulation of the emission of a nanowire and the dynamic surface acoustic wave controlled injection into the different emission channels are analyzed. For a single emission channel, the surface acoustic wave induced type-II band modulation does not directly affect the energy of the

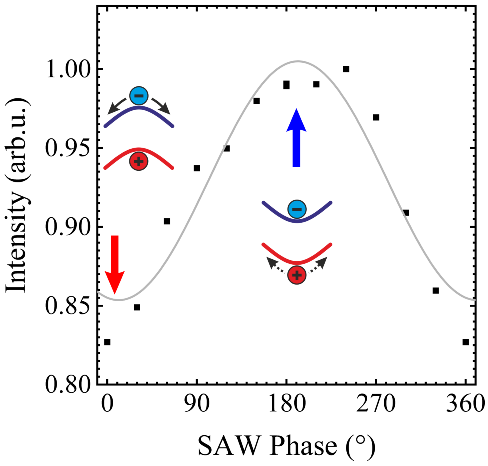

Figure 4.6: Phase-resolved integrated photoluminescence intensities of the free zincblende excitons as a function of the surface acoustic wave phase Φ. The phase between laser and surface acoustic wave programs the recombination dynamics of the charge carriers. The insets indicate the band edge modulation induced by the surface acoustic wave at photo-excitation. Gray line shows the regression of the photoluminescence intensity using the sine function.

emitted photon while the intensity of the emitted light is changed since the height of the bandgap is the same over the whole nanowire and only the absolute values of the bands are different at different positions. The dynamic modulation of the emission of NW7 is illustrated in Figure 4.6 showing the integrated intensity of the photoluminescence spectrum as a function of the surface acoustic wave phase. The intensity modulation corresponds to the sinusoidal modulation of the band structure and reflects the efficiency of separation of excitons. Depending on the band modulation at photo-excitation, the separation of electrons and holes is more efficient and, thus, the emission intensity varies with the phase of the surface acoustic wave. For $\Phi = 0°$ (left inset), electrons are generated at the unstable maximum of the conduction band, while holes are located at the stable maximum in the valence band. This leads to a fast dissociation of electrons away from the holes towards the adjacent minima strongly suppressing the radiative recombination, and thus, the emission signal. For $\Phi = 180°$ (right inset), this situation is reversed and electrons are generated at the stable minimum reducing the dissociation of electrons. Since the holes remain quasi-stationary due to their low mobility, this results in an increased recombination of the photo-excited electron and hole pairs at the position of generation and, thus, in a maximum of the photoluminescence signal.

The time-resolved analysis of the photons emitted from the recombination of excitons allows the more complete description and gives deep insights into the surface acoustic wave driven dynamics and recombination processes of electrons and holes. To this end, the time evolution of the photoluminescence emission of the nanowire is recorded under phase-locked optical excitation. The photoluminescence time-transients recorded from NW7 are presented in Figure 4.7 for no surface acoustic wave applied as well as for the optical generation of electrons and holes at the surface acoustic wave induced stable points

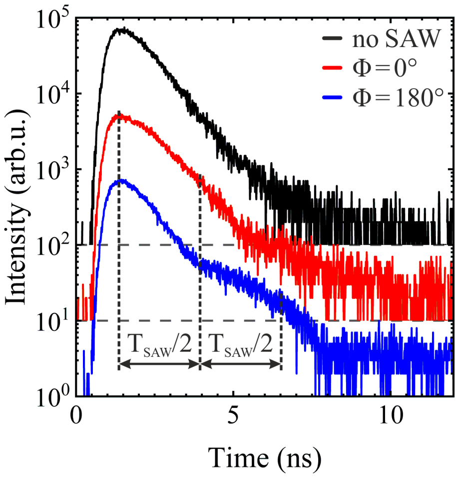

Figure 4.7: Time-resolved photoluminescence emission of a zincblende GaAs nanowire with few rotational twin defects for the phase-locked excitation condition. The unperturbed emission (black curve) reveals the established mono-exponential decay. The surface acoustic wave modulated emissions (red and blue curve) show clear fingerprints of acoustically driven charge carrier dynamics. The shift of the surface acoustic wave phase by 180° results in a $T_{\mathrm{SAW}}/2$ shifted intensity modulation.

in the conduction and valance band, respectively. The reference transient of the unperturbed nanowire emission exhibits the established clear mono-exponential decay of an isolated system with a decay time of $\sim 0.9\,\mathrm{ns}$ [85, 106, 108]. By applying a surface acoustic wave, the observed transients show clear modulations which differ for both characteristic excitation conditions. For generation of electrons at stable conduction band minimum ($\Phi = 180°$), an increased recombination rate of the nanowire emission is observed directly after photo-excitation due to the increased spatial overlap of electrons and holes induced by the piezoelectric potential of the surface acoustic wave. As time progresses, the electrons are separated from the quasi-stationary holes resulting in a reduction of the recombination rate. Here, it is important to note that the electric fields of the surface acoustic wave are not sufficient for transporting the electrons in propagation direction. Instead, electrons show sinusoidal trajectories about the excitation spot. Thus, an increased recombination rate is again observed an acoustic period later. For the reversed excitation condition, at which electrons are generated at an unstable point ($\Phi = 0°$), the strong quenching of the emission signal is delayed by $T_{\mathrm{SAW}}/2$ after photoexcitation due to the initial, efficient separation of electrons and holes. As again time progresses, the direct overlap of electrons and holes occurs at the point of excitation leading to an increased recombination rate. Thus, the modulations of both surface acoustic wave driven transients are shifted by $T_{\mathrm{SAW}}/2$ and exhibit characteristic fingerprints of acoustically driven charge carrier dynamics [28, 38, 169].

4.3 Triggering of the carrier redistribution in radial nanowire quantum wells

Acousto-optoelectric spectroscopy allows to resolve coupled emission dynamics and an exchange of the charge carriers on subnanosecond time scales within interconnected transition channels of nanowire heterostructures [13, 39, 48]. In the following, it is shown that the aforementioned redistribution of carriers in the asymmetric, radial quantum well of NW6 (cf. Section 2.5.2) can be triggered and even reversed on subnanosecond time scales by the acousto-electric effect. When propagating on a piezoelectric substrate, the mechanical wave induces an electric field gyrating in the sagittal plane accelerating charge carriers along the axis of the nanowire and around the circumference of the radial quantum well. Again, it can be considered that, for the selected power regime ($P_{\mathrm{rf}} = 3\,\mathrm{dBm}$), the electric field dissociates photo-excited excitons and induces the dynamics of such generated electrons, while holes remain quasi-stationary due to their lower mobility. Thus, in addition to the generation, radiative and non-radiative recombination processes of the excitons, two further processes contribute to the dynamics in our experiment. The surface acoustic wave-driven electron dynamics lead to (i) the injection of electrons to a region with stationary holes and (ii) the depletion of electrons from a region with a quasi-stationary hole distribution. These processes result in the formation and dissociation of excitons, respectively. These characteristic signatures of the surface acoustic wave-driven charge carrier dynamics can be resolved in characteristic, time-modulated photoluminescence transients under influence of surface acoustic waves. Thus, the injection of electrons results in an increase of the optical signal, giving rise to a reduction of the total decay rate. In contrast, the depletion causes an additional loss channel increasing the overall decay rate due to the spatial separation of electrons and holes.

In the left panel of Figure 4.8, the time-integrated photoluminescence emission spectrum of the radial quantum well of NW6 is depicted without a surface acoustic wave applied. This spectrum is recorded at the position of two neighboring emission centers of the quantum well that spatially overlap along the nanowire (indicated in Figure 2.10 (c)) and, hence, show two dominant emission peaks, labeled as $\mathrm{QW}_{6,1}$ and $\mathrm{QW}_{6,2}$, at energies of $E_{\mathrm{QW}_{6,1}} = 1.558\,\mathrm{eV}$ and $E_{\mathrm{QW}_{6,3}} = 1.573\,\mathrm{eV}$, respectively. The recorded surface acoustic wave-modulated, time-resolved photoluminescence transients for each emission peak are shown in the right panel of Figure 4.8. Both transients exhibit clear anti-correlations, which arise from surface acoustic wave-induced charge carrier dynamics: at the times indicated by the black arrows, the transient of the energetically lower emission feature ($\mathrm{QW}_{6,1}$) exhibits an increase of the total decay rate, while the total decay rate of the energetically higher emission signal ($\mathrm{QW}_{6,2}$) decreases, i.e. reemerges. This observation points towards a depletion of electron population of the energetically lower quantum well and an injection of these electrons into the energetically higher quantum well. Moreover, we observe the reversed process, a transfer from the energetically higher into the energetically lower quantum well region, at the times highlighted by the red arrow. Thus, the observed anti-correlations can be attributed to dynamically triggered electron transfer between two

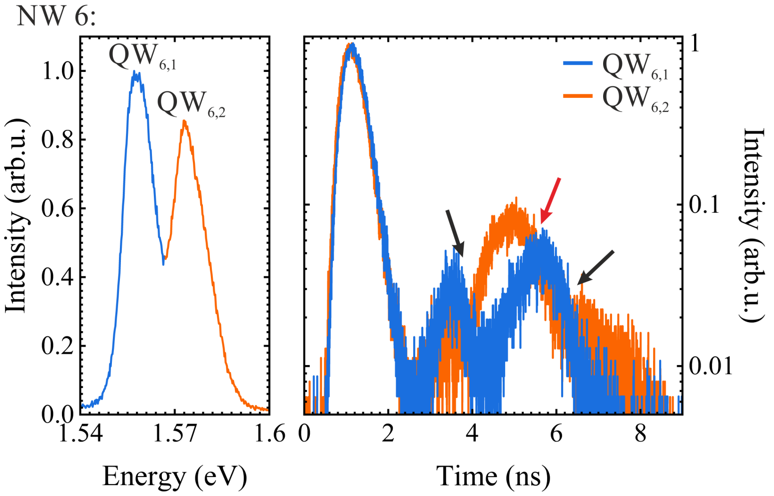

Figure 4.8: Representative time-integrated and corresponding time-resolved photoluminescence emission spectra of NW6 at the position with two different emission energies (blue, orange) of the two quantum well systems. The transients exhibit an anti-correlated behavior between both quantum well systems (indicated by black and red arrows). This can be attributed to a dynamically triggered electron transfer between two interconnected quantum wells due to the gyrating electric field of the surface acoustic wave (black arrow: electron transfer from blue transient, i.e., $QW_{6,1}$, to orange, i.e., $QW_{6,2}$; red arrow: electron transfer from orange transient to blue).

interconnected quantum wells of the radial quantum well system due to the oscillating electric field of the surface acoustic wave. Most importantly, this transfer is reversible and can be triggered on subnanosecond time scales [13].

Chapter 5

Electron cycloids driven by the transverse spin of a surface acoustic wave [1]

As Lord Rayleigh investigated the propagation of surface waves on elastic materials, he discovered that these waves exhibit a characteristic, counterclockwise elliptical particle motion in the sagittal plane [41]. This "rolling" motion corresponds to an angular momentum which is strikingly similar to spin-momentum locking. Spin-momentum locking is a universal wave phenomenon which was recently observed in various electromagnetic and electronic systems [173–185] and, thus, is a promising candidate for future applications in electronics and photonics. In particular, for these systems, the momentum of the waves, the decay direction as well as the spin form a locked triplet in which the spin is locked to the momentum and the directional transport of energy strongly depends on local polarization of evanescent waves.

In photonics, recent experiments demonstrated the phenomenon of spin-momentum locking by the scattering of surface plasmon polaritons in metasurfaces [174, 186], the coupling of cold atoms to optical fibers [175] and in the emission of quantum dots near topological photonic crystals [187–189]. Moreover, in 2D materials, it has been shown that the coupling between the valley-polarized excitons in tungsten disulfide and the transverse optical spin of plasmonic nanowire modes leads to the directional propagation of circularly polarized excitations [190]. In magnon modes of a spherical magnon resonator, the spin-orbit coupled nature of the whispering gallery modes for photons results in a magnon-induced nonreciprocity [191]. All this has raised the interest of observing spin-momentum locking and related phenomena in piezoelectric surface acoustic waves.

Surface acoustic waves, which are described by the motion of particles, are fundamentally different waves compared to photonic modes and fermionic states in electronic systems. Despite this fundamental difference, however, they show similar properties to spin-momentum locking which is a universal property arising from evanescent waves. Thus, there are remarkable parallels between electromagnetic, electronic and surface acoustic waves [192–194]. More precisely, Rayleigh surface acoustic waves consist of a transverse and longitudinal displacement of the particles in the plane normal to the surface of a medium and parallel to the propagation. In addition to that, the $\pi/2$-phase shift between both displace-

---

[1] mainly published and with permission from [42]. Copyright 2021 The Authors, Creative Commons Attribution-NonCommercial license (Published by Science Advances).

ment components reflects the characteristic elliptical rolling motion of such waves. This is, analogous to surface plasmon polariton, the manifestation of acoustic spin in Rayleigh surface acoustics; making such waves an archetypical example of spin-momentum locking of elastic waves. Despite the early postulation of the gyrating, elliptical motion of surface acoustic waves by Lord Rayleigh, the direct observation of this transverse spin angular momentum has remained an open challenge.

In this chapter, the full spin dynamics of the elastic waves and the electric field are presented by detecting ultrafast electron cycloids driven by the gyrating electric field which is induced by a surface acoustic wave propagating on the surface of a YZ-cut $\mathrm{LiNbO_3}$ crystal. First, the basic properties of spin-momentum locking, in particular in electromagnetic waves, is discussed. Afterwards, it is shown that both, the elliptical motion of particles and the gyrating electric field of surface acoustic waves, possess acoustic spin and spin-momentum locking properties by numerically solving the equations of motion for $\mathrm{LiNbO_3}$. The transverse spin of the electric field can be detected and probed by advanced ultafast nanophotonic techniques. Therefore, a unique nanowire sensor with a tubular quantum well is used which is presented in the next sections. It provides the direct signature of spin-momentum locking in acoustic waves through time-resolved motion of electron cycloids. Finally, it is shown that the entire gyrating vector field, within a sub-wavelength volume, is mapped through time-resolved detection of the longitudinal and transverse motion of electrons in the nanowire sensor.

The main results of this chapter were published in Science Advances under the title "Ultrafast electron cycloids driven by the transverse spin of a surface acoustic wave" [42]. The measurements were conducted by Lisa Janker. The theoretical calculations were performed in collaboration by Farhad Khosravi and Zubin Jacob at the University of Alberta, Canada and Purdue University, USA.

5.1 Spin-momentum locking

Spin-momentum locking is a universal wave phenomenon for which the momentum of the wave, the decay direction, and the spin form a triplet in which the spin is locked to the momentum. Further, it describes the origin of unidirectional, chiral, intrinsic properties of electromagnetic, electronic and acoustic systems and is known for more than a century to occur in propagating electromagnetic waves possessing both linear and angular momenta along the direction of propagation.

In paraxial beams, the propagation of light is predominantly along one direction and the electric fields are transverse because the light possesses essentially only two Cartesian components which are perpendicular to the propagation direction. These electromagnetic waves are circularly polarized plane waves propagating along the z-axis, $\boldsymbol{\mathcal{E}}(\mathbf{r}, t) = (\mathbf{x} + i\mathbf{y}) \exp(i(kz - \omega t))$, where the wave vector $\mathbf{k} = k\mathbf{z}$ is perpendicular to the electric field. For these waves, the electric field vector gyrates clockwise or anticlockwise in the transverse xy-plane around the propagation axis which can be associated with a spin

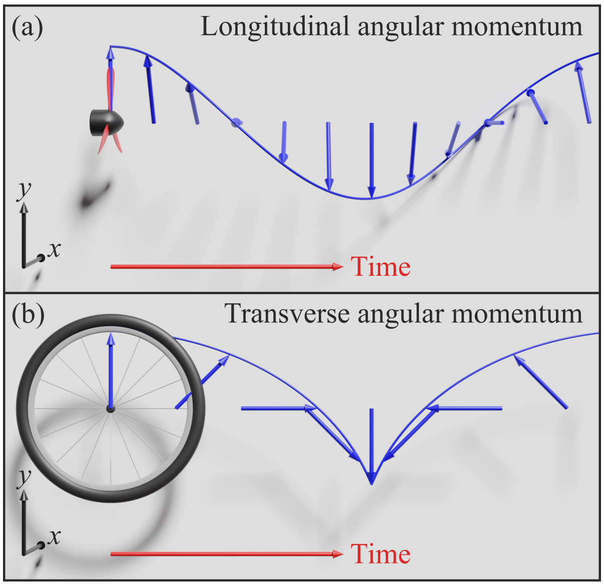

Figure 5.1: Illustration of longitudinal and transverse spin angular momentum. (a) Longitudinal spin angular momentum occurs, for example, in a paraxial beam of light. The electric field vector gyrates around the propagation direction, which is similar to the rotating movement of rotor blades. (b) Transverse spin angular momentum occurs, for example, for transversely gyrating electric field for the case of an evanescent light wave, being similar to the rotating movement of rolling bicycle wheel. Figure adapted from [176].

vector that is longitudinal to the propagation direction and, thus, results in a longitudinal spin angular momentum [176]. As a consequence, propagating electromagnetic waves carry both, momentum and longitudinal spin being defined by the wave vector and circular polarization, respectively. This behavior can be compared with the rotating movement of rotor blades as shown in Figure 5.1 (a).

In contrast, evanescent waves possess a spin which is transverse to the direction of the momentum and the direction of decay. Such plane waves are, e.g., propagating along the z-axis and exponentially decaying along the x-axis. Hence, the components of the wave vector can be described by $k_x = i(k_z^2 - k^2)^{1/2}$. In addition, the transverse x-component of the electric field can be written as $\mathcal{E}_x(\mathbf{r}, t) \propto \exp(-k_x x + ik_z z - i\omega t)$ and the longitudinal z-component as $\mathcal{E}_z(\mathbf{r}, t) \propto -i(k_x/k_z)\exp(-k_x x + ik_z z - i\omega t)$. As these transverse and longitudinal field components exhibit a $\pi/2$-phase shift, this phase difference results in an electric field vector gyrating in the sagittal xz-plane and, thus, implies the occurrence of a transversely spinning electric field. Consequently, evanescent electromagnetic waves carry momentum and transverse spin, resulting in a transversal spin angular momentum which is determined by the circular polarization being orthogonal to the wave vector [176]. Hereby, this behavior is very similar to the motion of the spinning spokes of a rolling wheel as depicted in Figure 5.1 (b). In particular, the fundamental behavior of the transverse spin angular momentum is the connection of propagation and spinning direction and, consequently, changing the propagation direction will lead to a change in spinning direction [176].

5.2 Transverse spin of a Rayleigh surface acoustic wave

Rayleigh surface acoustic waves exhibit many universal phenomena similar to evanescence waves in optics and electromagnetism. In particular, both have transverse and longitudinal components, with respect to the propagation direction on the surface of a material, with a phase difference of $\pi/2$ between these two components. Consequently, surface acoustic waves are expected to have a transverse spin angular momentum and, hence, spin-momentum locking properties of the displacement field as well as of the gyrating electric field.

To access the spin-momentum properties of a surface acoustic wave, we numerically solve the equations of motion for a surface acoustic wave propagating on the surface of one of the technologically most relevant piezoelectric substrates, $\mathrm{LiNbO_3}$ [156, 195], with the parameters taken from reference [196]. Therefore, a Rayleigh surface acoustic wave is considered, without any loss of generality, to propagate along the Z-direction of a Y-cut $\mathrm{LiNbO_3}$ crystal surface. As mentioned before, the solutions for Rayleigh surface acoustic waves are found by solving Equations 3.8 and 3.9 together with the boundary conditions for the stress components (Equation 3.10) and the electric displacement fields at the surface. The method for solving these equations in matrix representation is described in more detail in Section 3.1 and [197]. Using this approach, we can finally determine the displacement vector components u_i, electric field components E_i as well as the propagation velocity of the wave $v = \omega/k$.

Figure 5.2 (a) shows the calculated real space profile of the surface acoustic wave with the color-coded electric potential superimposed. Since the piezoelectric potential is varying in space and time, it induces a gyrating electric field, which is indicated by arrows in the wave profile. Figures 5.2 (b) and (c) show the displacements and the electric fields in the sagittal plane (YZ-plane) marked by dotted lines in Figure 5.2 (a). The displacement and electric field vectors illustrate the amount and the direction of the displacement and the electric field in the $\mathrm{LiNbO_3}$ crystal and in the vacuum on top of the crystal, respectively. Note that the wavelength of the surface acoustic wave is determined to be $\lambda_{\mathrm{SAW}} = 18\,\mu\mathrm{m}$.

Next, we demonstrate the transverse spin properties of the piezoelectric Rayleigh surface acoustic wave. The electromagnetic and acoustic spin are given by [198–200],

$$S_{\mathrm{E}} = \frac{1}{2\omega}\,\mathrm{Im}(\epsilon_0 \mathbf{E}^* \times \mathbf{E} + \mu_0 \mathbf{H}^* \times \mathbf{H}) \tag{5.1}$$

and [193, 201],

$$S_{\mathrm{A}} = \frac{1}{2\omega}\,\mathrm{Im}(\rho \mathbf{v}^* \times \mathbf{v}), \tag{5.2}$$

respectively. Here, E, H, ρ, and v are the electric field, magnetic field, mass density, and velocity vector which is equal to the time-derivative of the displacement vector, respectively. As an electrostatic approximation is assumed for solving the equations for the Rayleigh waves, only the electric field contributes to the electromagnetic spin S_{E} in our case. The results of the normalized acoustic and electromagnetic spins are analyzed in the side panels of Figures 5.2 (b) and (c) as a function of Y-coordinate for propagation along

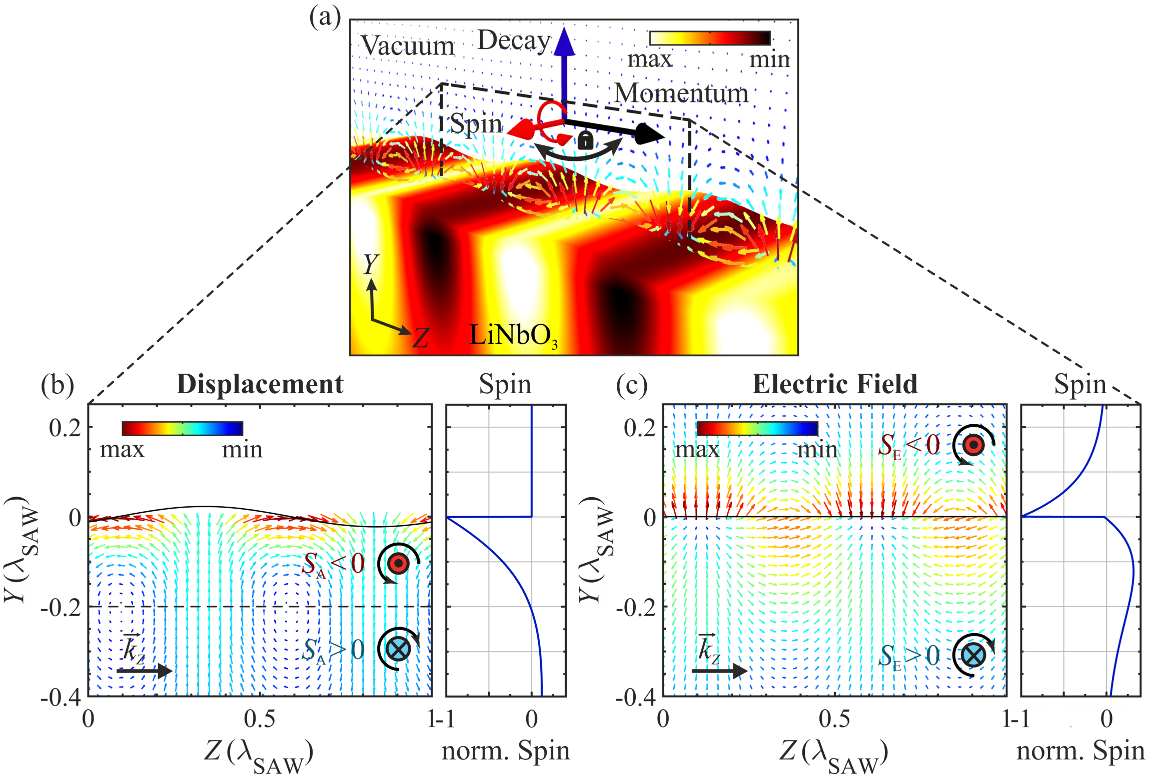

Figure 5.2: Spin-momentum locking of a Rayleigh-type surface acoustic wave. (a) Calculated real space profile of a Rayleigh surface acoustic wave propagating along the Z-direction on a Y-cut $LiNbO_3$ crystal. The color code is the piezoelectric potential and arrows show the calculated electric field in the halfspace above the solid. Momentum, decay and spin of the gyrating electric field generated by a Rayleigh-type surface acoustic wave form a right-handed triplet. The direction of the spin for both electric field and displacement are locked to the propagation direction. (b) Calculated displacement and (c) electric field (main panels) of the Rayleigh surface acoustic wave. The side panels show the normalized magnitude of the transverse spin normal to the surface ($Y = 0$) calculated from the mechanical motion and electric field as described in the main text. The mechanical spin shows a characteristic sign change at $\approx 0.2\lambda_{\text{SAW}}$ below the surface, i.e. from being counterclockwise to clockwise, while the electrical spin changes from counterclockwise to clockwise exactly at the surface.

the positive Z-direction ($k_Z > 0$), respectively. The acoustic spin within the material (Figure 5.2 (b)) is orientated out of the sagittal plane close to the surface and flips sign, i.e. is pointing in opposite direction, at about 0.2 wavelength away from the surface as shown by dashed line. This highlights that even though the direction of the acoustic spin is locked to the direction of momentum and the decay, it does not necessarily result in a conventional right-handed triplet with both, the momentum and decay, and, thus, is an universal property of Rayleigh-type surface acoustic waves. In contrast, the electromagnetic spin (Figure 5.2 (c)) is orientated out of plane on top of the surface. Hence, the momentum, decay and spin form a right-handed triplet as shown in Figure 5.2 (a). Inside the $LiNbO_3$ crystal, the electromagnetic spin flips together with the decay direction. Thus, the right-hand momentum, decay and spin triplet are maintained.

These results clearly demonstrate the spin-momentum locking properties for the electric field and the displacement of a surface acoustic wave. Thus, changing the direction of the propagation (changing the sign of k_Z) results in a flip of all spin components.

5.3 Ultrafast nanoscale sensing of the transverse spin

The direct observation of the transverse spin of a Rayleigh-type surface acoustic wave proved to be an outstanding challenge as it demands an ultrafast, nanoscale vector field sensor operating at frequencies in the megahertz to gigahertz regime. At this point, it should be mentioned, that former methods for measuring the acoustic spin of airborne sound occur at lower frequencies up to a few kilohertz and utilize macroscopic meta-atoms with dimensions in the millimeter to centimeter regime. These macroscopic dimensions and moderate frequencies usually do not require advanced detection techniques and allow to directly sense the local pressure field and, thus, the acoustic spin of airborne sound by macroscopic pressure sensors [201, 202]. However, these techniques are not suitable for detecting the spin of a radio frequency Rayleigh surface acoustic waves at several 100 MHz as the wavelength is reduced to a few micrometers due to the approximately one order of magnitude higher phase velocity.

For sensing the transverse spin of a Rayleigh surface acoustic wave, piezoelectric materials are used as a substrate since stress and strain in these materials induce a gyrating electric field on the surfaces [156, 195]. In particular, this allows to observe the spinning electric field of the Rayleigh surface acoustic wave, yet, it demands for an ultrafast sensor at the nanoscale specifically sensitive to electric fields. Therefore, a GaAs/(Al)GaAs multishell heterostructure nanowire is used as a spin sensor for the direct temporal observation of this spinning electric field since electrons inside this nanostructure couple strongly to the electrical spin of the surface acoustic wave [13, 39]. A single nanowire is transferred onto a conventional surface acoustic wave device with a design wavelength of $\lambda_{\mathrm{SAW}} = 18\,\mu\mathrm{m}$ of the interdigital transducer which corresponds to a precession period of the electric spin of $T_{\mathrm{SAW}} = 5.15\,\mathrm{ns}$. Experiments are performed at a temperature of $T = 8\,\mathrm{K}$.

To confirm the strong electrical coupling of the surface acoustic waves propagating on the surface of YZ-cut $\mathrm{LiNbO_3}$ substrate to the nanowire, we performed a time dependent finite element modeling simulation of the interaction between the acoustic and piezoelectric fields of the surface acoustic wave on the $\mathrm{LiNbO_3}$ crystal and a GaAs nanowire. Therefore, a nanowire with a length equal to λ_{SAW} is considered to sample all local phases of the surface acoustic wave in a single simulation run [39]. The results are presented in Figure 5.3. The spatial profile of the calculated structural deformation, the electric potential (color-coded) and the derived electric field (arrows) are shown for a GaAs nanowire on YZ-$\mathrm{LiNbO_3}$ hybrid device in Figure 5.3 (a). In particular, both, the mechanical wave and the electric components, clearly couple into the GaAs nanowire. The time dependent evolution of the electric field components is further investigated at the center in the nanowire in Figure 5.3 (b). These simulation results clearly demonstrate that the characteristic

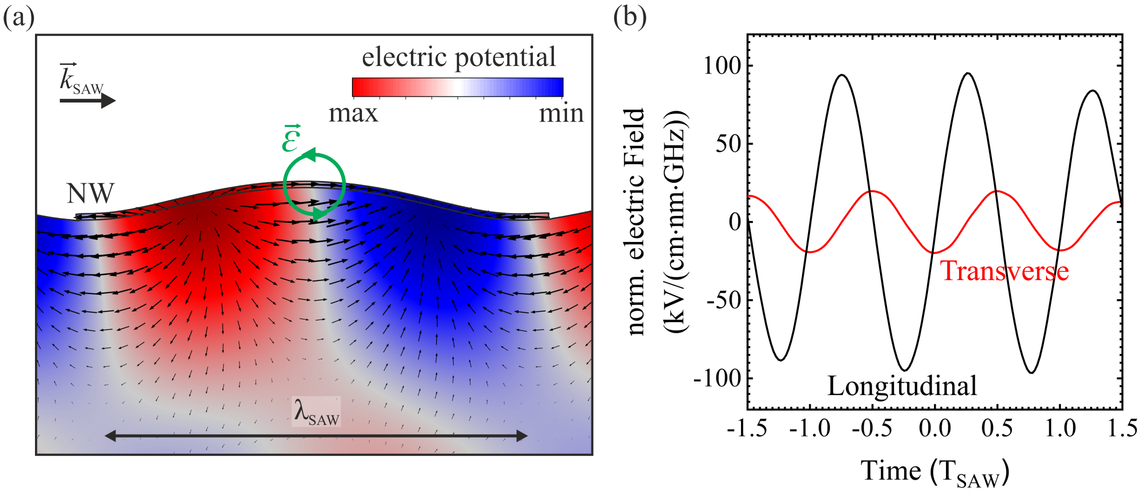

Figure 5.3: (a) FEM calculated electric potential (color code) and electric field (arrows) of the surface acoustic wave in the YZ-cut $\mathrm{LiNbO_3}$ substrate and the nanowire. (b) Longitudinal and transverse components of $\boldsymbol{\mathcal{E}}$ in the center of the nanowire showing the $\pi/2$-phase shift characteristic for Rayleigh surface acoustic waves. The piezoelectric field induces the spatial separation and transport of electron-hole pairs in the radial quantum well.

$\pi/2$-phase shift between the longitudinal (parallel to the propagation direction) and transverse (normal to the surface) components of the electric field, which reflects the elliptical character, is faithfully transferred into the nanowire. This gyrating electric fields, in turn, spatial dissociate and transport in the experiment the photo-generated electron-hole (e-h) pairs [28], i.e. excitons and lead to the colloidal movement of the charge carriers in the GaAs/(Al)GaAs multishell nanowire.

The nanowire sensor itself consists of a GaAs/(Al)GaAs multishell heterostructure, which is wrapped around a GaAs core with a length of about $l_{\mathrm{NW}} = 15\,\mu\mathrm{m}$. Note, the nanowire used here as a sensor is the same nanowire, referred to as NW5 in Section 2.6. The schematic in Figure 5.4 (a) illustrates the nanowire sensor with a nominally 5 nm GaAs (gray) radial quantum well which is embedded in higher bandgap $\mathrm{Al_{0.3}Ga_{0.7}As}$ barriers. This unique three-dimensional geometry is fundamental for experimentally sensing the transverse spin of the electric field of a surface acoustic wave. As already mentioned in Section 2.6, the condition for growth of this radial heterostructure results in thickness fluctuations and deviations from a perfect hexagonal cross-section, which is crucial for the ultrafast nanoscale sensing. For this particular nanowire, the thickness of the quantum well is locally increased compared to its nominal value resulting in two distinct quantum well segments on neighboring facets, which are spatially displaced along the nanowire with a small spatial overlap area. This arrangement is shown schematically in orange and blue in Figure 5.4 (a). In the following, we refer to these segments as QW1 (blue) and QW2 (orange), respectively. In particular, QW1 with a thickness d_1 is located on the upper facet while QW2 with a thickness $d_2 < d_1$, is located on the lower facet. Due to these large inhomogeneities, the charge carriers localize in both segments being the widest,

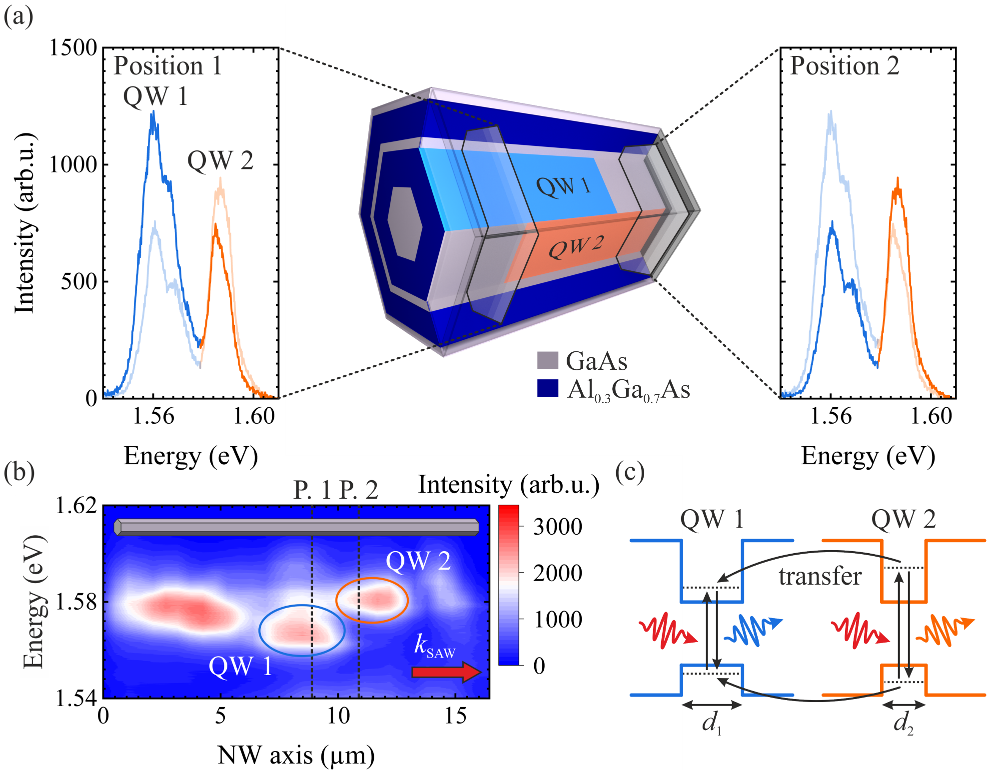

Figure 5.4: (a) Schematic of the tubular quantum well heterostructure wrapped around the core of NW5. QW1 (blue) and QW2 (orange) are offset by $d_{\mathrm{SAW}} \approx 2.0\,\mu\mathrm{m}$ along the axis of the nanowire and located on the upper and lower side facet, respectively. The photoluminescence spectra from two positions show that QW1 and QW2 can be distinguished by their characteristic emission energies. (b) Photoluminescence mapping of the tubular GaAs quantum well heterostructure wrapped around the core in axial direction exhibiting several different emission signals of the GaAs-quantum well including QW1 (blue circle) and QW2 (orange circle). Dotted lines mark the two positions of photoluminescence spectra in (a). The propagation direction of the surface acoustic wave is parallel aligned to the nanowire. (c) Bandprofile of the two spatially separated but interconnected quantum well segments of the radial heterostructure together with optical pumping (up arrows) and emission processes (down arrows) as well as charge carrier transfer between the quantum well segments.

respective side facets of the tubular quantum well. Thus, both segments exhibit different quantization energies allowing that they can be readily distinguished from their optical emission.

The right and left panel of Figure 5.4 (a) show low temperature photoluminescence spectra recorded at two different positions which are offset along the nanowire axis by $d_{\mathrm{axial}} = 2.0\,\mu\mathrm{m}$. The spectrum from the other position is plotted in light lines in each panel for comparison. The detected photoluminescence emission originates from recombination of excitons within each quantum well segment. At Position 1 (left), the emission of QW1 (blue) at an energy of about 1.562 eV dominates, while emission of QW2 (orange) at an energy of about 1.585 eV is comparably weak. At Position 2 (right), the opposite intensity distribution is found, with QW2 showing an increased intensity compared to

QW1. These configuration is further analyzed by the spectral map of the tubular quantum well recorded along the nanowire axis which is depicted in Figure 5.4 (b). It exhibits several different emission regions of the GaAs-quantum well including the two distinct quantum well segments, QW1 (marked by blue circle) and QW2 (marked by orange circle). Both regions of emission are spatially displaced along the nanowire by about 2.0 µm with a small spatial overlap. Moreover, the two positions of both photoluminescence spectra are highlighted by dotted lines. Note, for the acousto-optoelectric spectroscopy experiments, the laser spot was focused in between both positions at which both emission centers exhibit similar intensities. This leads to a distribution of quasi-stationary holes in both regions allowing electrons to recombine there whenever being injected. Since the separation of the recombination centers is sufficiently small, both emissions can be analyzed at the same time by using a ≥ 5 µm detection spot.

In addition, it was shown in Section 2.6 that these two quantum well segments, QW1 and QW2, exhibit unambiguous fingerprints of coupled emission dynamics. The anti-correlated recombination rates observed in the detected time transients of QW1 and QW2 show that a charge carrier transfer occurs between these two segments as schematically illustrated in the band diagram in Figure 5.4 (c). Thus, this is the direct evidence that QW1 and QW2 are interconnected.

Later, the dynamic transfer between QW1 and QW2 is used to isolate the temporal signature of the gyrating electric field. To determine if the electric field components are sufficient enough for electron transfer, we evaluate the piezoelectric potential difference between both quantum well segments. By extracting the normalized maximal values of the electric fields in the center of the nanowire from the results of the finite element modelling simulations in Figure 5.3 (b), we find that the longitudinal (E_Z) and transverse (E_Y) components of the electric field oscillate between $\pm E_{Z,\mathrm{max}} = \pm 95\,\frac{\mathrm{kV}}{\mathrm{cm}} \cdot \frac{u_{Y,0} \cdot f_{\mathrm{SAW}}}{\mathrm{nm} \cdot \mathrm{GHz}}$ and $\pm E_{Y,\mathrm{max}} = \pm 21\,\frac{\mathrm{kV}}{\mathrm{cm}} \cdot \frac{u_{Y,0} \cdot f_{\mathrm{SAW}}}{\mathrm{nm} \cdot \mathrm{GHz}}$ over one acoustic period, respectively. Since the wavelength of a Rayleigh wave ($\lambda_{\mathrm{SAW}} = 18$µm) is much larger than the separation between QW1 and QW2 ($d_{\mathrm{axial}} = 2.0$ µm) the electric field can be regarded as approximately the same for the region of both quantum well segments. The frequency applied to the interdigital transducer is $f_{\mathrm{SAW}} = 194$ MHz while typical amplitudes of the deformation in Y-directions are in the order of 500 pm. Consequently, this leads to a longitudinal electric field component of about $E_{Z,\mathrm{max}} = 9.2\,\frac{\mathrm{kV}}{\mathrm{cm}}$ and transverse component of about $E_{Y,\mathrm{max}} = 2.0\,\frac{\mathrm{kV}}{\mathrm{cm}}$. Note, the dimensions of the two segments within the tubular quantum well system are in axial direction $d_{\mathrm{axial}} = 2.0$ µm and in radial direction $d_{\mathrm{radial}} = 120$ nm. Thus, this results in a potential difference of $e \cdot \Phi_{Z,\mathrm{max}} = 1.8$ eV in longitudinal direction and $e \cdot \Phi_{Y,\mathrm{max}} = 24$ meV in transverse direction. Finally, the potential differences in our experiments are large enough to overcome the energy difference of about 23 meV between QW1 and QW2.

Taken together, the two interconnected segments QW1 and QW2 are offset with a small spatial overlap along the propagation direction of the surface acoustic wave, with QW1 being closer to the interdigital transducer launching the surface acoustic wave. Moreover, they are in their transverse direction normal to the $\mathrm{LiNbO_3}$ surface with QW2 being closer to the surface. This spatial offset as well as the distinguishable emission energies are essential for isolating the temporal signatures of electric transverse spin of the surface acoustic wave by utilizing these coupled charge carrier dynamics of QW1 and QW2.

5.4 Electron cycloids in radial nanowire quantum wells

By performing acousto-optoelectric spectroscopy, the cycloidal carrier dynamics driven by the gyrating electric fields of a surface aoustic wave are systematically studied in the aforementioned radial quantum well of the GaAs-$Al_{0.3}Ga_{0.7}As$ core-shell nanowire sensor. In particular, the surface acoustic wave-driven charge carrier dynamics between both quantum well systems can be resolved in characteristic time-modulated photoluminescence transients. Importantly, for the experimental selected power $P_{\mathrm{rf}} = -4\,\mathrm{dBm}$, the electric field dissociates photo-generated excitons and drives the dynamics of such generated electrons, while holes remain quasi-stationary as their low mobility inhibits transport by the surface acoustic wave. Thus, the experimental observation can be attributed to spatio-temporal dynamics of electrons [28], which are driven in cycloids in our nanowire sensor. These electron cycloids, in turn, enable us to gain direct insights in spin-momentum locking properties of acoustic waves which we present in the following.

In Figure 5.5 (a) and (b), the recorded time evolution of the emission of QW1 and QW2 is plotted as a function of the delay time τ between laser and surface acoustic wave excitation and the time after photoexcitation Δt (see Chapter 4) in false-color representation, respectively. As mentioned before, for $\tau = 0$, the electric field vector $\boldsymbol{\mathcal{E}}$ at photo-excitation is transverse, pointing downwards towards the substrate, and tuning τ will rotate $\boldsymbol{\mathcal{E}}$ counterclockwise at the photo excitation. As we tune the delay time τ over a full acoustic cycle, we firstly resolve a clear T_{SAW}-periodic intensity modulation of the emission of both

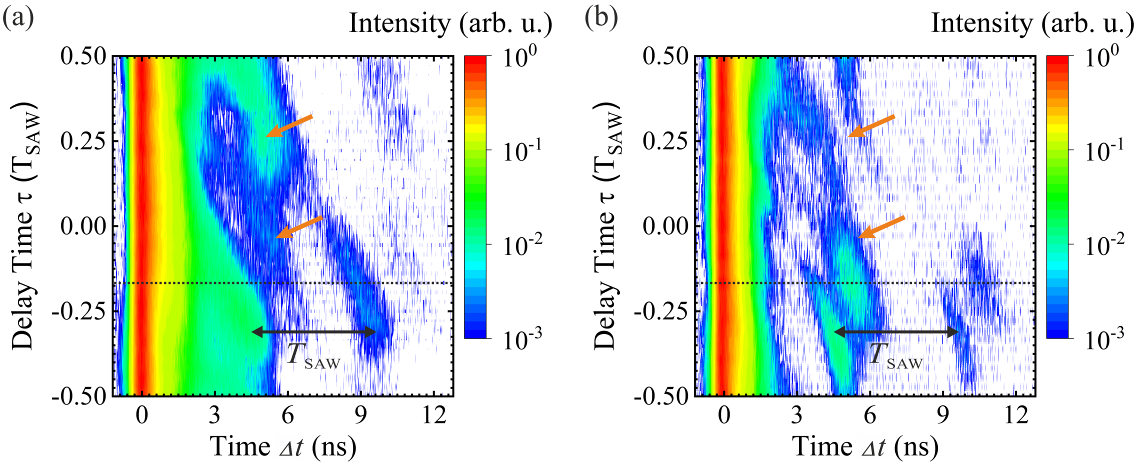

Figure 5.5: Stroboscopic overview photoluminescence spectra of (a) QW1 and (b) QW2 recorded over one acoustic cycle ($P_{\mathrm{rf}} = -4\,\mathrm{dBm}$) showing periodic oscillations and an anti-correlated behavior of both emissions (orange arrows).

quantum well systems in the experiment for each delay due to the periodical separation of electrons and holes along the nanowire axis. This effect arises from an acoustically-driven carrier transport along the nanowire axis due to the oscillating electric field parallel to the nanowire axis [28, 38]. Secondly, we observe pronounced anti-correlated intensity oscillations of both quantum well channels that are marked by orange arrows. These arise from a carrier transfer between the two facets of the radial quantum well, which is dynamically triggered by the surface acoustic wave's oscillating electric field perpendicular to the nanowire axis. This mechanism is analyzed for the selected delay time of $\tau = -T_{\mathrm{SAW}}/6$ indicated by the dotted lines [cf. Figure 5.5 (a) and (b)] in detail in Figure 5.6 (complete overview can be found in Appendix).

As a reminder, in our experiments to sense the electric spin of a surface acoustic wave, we define the absolute time t by the orientation of the electric field of the surface acoustic wave at the position of the laser spot on the system as shown in Figure 5.6 (a) and described in detail in Chapter 4. Hereby, the electric field vector $\boldsymbol{\mathcal{E}}$ (red arrow) is transverse at $t = 0$, pointing downwards towards the substrate, and characteristically gyrates counterclockwise at the position of QW1 and QW2 with a period of $T_{\mathrm{SAW}} = 5.15\,\mathrm{ns}$. This time-dependent electric field induces the charge carrier dynamics inside the three-dimensional quantum well structure of the nanowire via the acousto-electric effect. This allows us to observe the transverse spin of the surface acoustic wave by electron cycloids as illustrated schematically in the lower part of Figure 5.6 (a). In particular, the electric field accelerates electrons (black) counterclockwise inside the heterostructure between the regions of QW1 and QW2 as the absolute time t progresses. For instance, at $t = 0$ (Schematic I), electrons are accelerated upwards inside the heterostructure. Importantly, the negative charge of the electron does not affect the counterclockwise gyrating sense of electric transverse spin, which is fully preserved. However, the direction of the accelerating force (indicated by black arrows) exhibits an π phase shift which is illustrated in the sequence of the Schematics I to IV.

The experimental data confirming the cyclic motion of the electrons which are driven by the electric transverse spin, is depicted for the delay $\tau = -T_{\mathrm{SAW}}/6$ in Figure 5.6 (b) and (c). The raw photoluminescence time transients of QW1 (blue) and QW2 (orange) are plotted in Figure 5.6 (b) as a function of the absolute time t, which is the sum of the two independent time scales, the delay time τ and the time after photoexcitation Δt, such that $t = \tau + \Delta t$. In addition, the raw time transients are processed to calculate the degree of normalized emission intensity defined as $DoEI = (I_{\mathrm{QW1}} - I_{\mathrm{QW2}})/(I_{\mathrm{QW1}} + I_{\mathrm{QW2}})$ being a measure of the electron population of the two quantum well segments. For $DoEI = +1$ and $DoEI = -1$, emission occurs only from QW1 and QW2, respectively. The full set of both data is presented in the Appendix in which we tune τ over the full acoustic cycle. These data confirm the spin momentum locking properties of the surface acoustic wave.

At the delay time $\tau = -T_{\mathrm{SAW}}/6$, the laser generates charge carriers at the time $t = -0.8\,\mathrm{ns}$. As time progresses after excitation, the left-handed gyrating electric field rotates counterclockwise and accelerates electrons antiparallel to direction of the electric field. For $t = 0$, the electric field is orientated downwards along -Y-direction (Schematic I) accel-

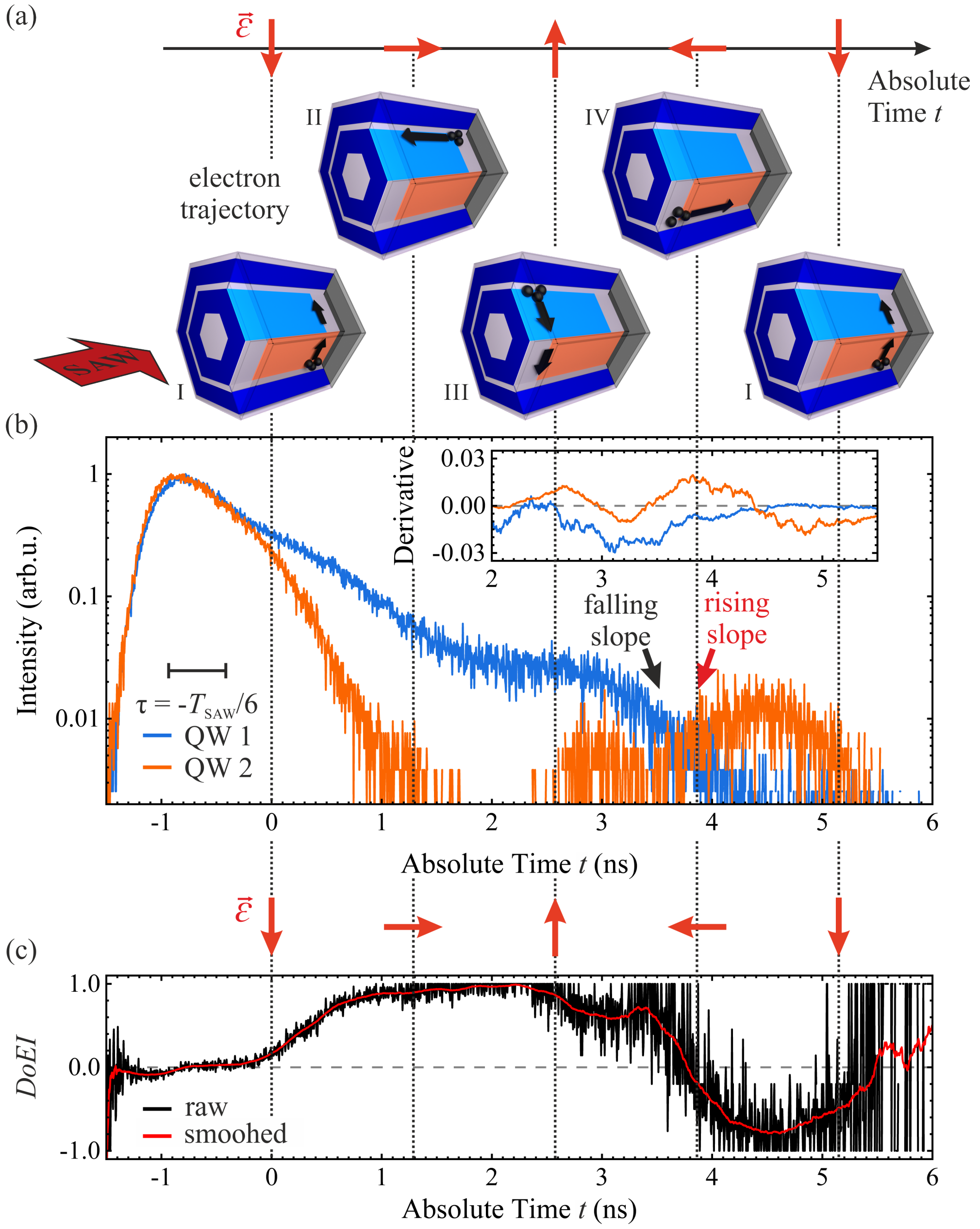

Figure 5.6: (a) The schematics show the motion of electrons (black) and the orientation of the electric field vector within the quantum well at distinct times during the acoustic cycle. The direction of this motion is exactly opposite to the orientation of the electric field vector $\boldsymbol{\mathcal{E}}$ and leads to cyclic, gyrating trajectories. The sense of this cycloid is set by the transverse spin. (b) Experimental observation of electron cycloids in the time-dependent photoluminescence of QW1 (blue) and QW2 (orange). The two transients exhibit clear anti-correlated rising and falling slopes (arrows) at characteristic times during the acoustic cycles shown in (a). These anti-correlations are direct evidence for the cyclic motion of the electrons inside the tubular quantum well. The inset shows the derivative of the transients illustrating the opposite slopes of the two signals in the selected time interval. A conservative estimate of the temporal resolution is given by the scale bar. (c) Degree of normalized emission intensity $DoEI = \frac{I_{QW1}-I_{QW2}}{I_{QW1}+I_{QW2}}$ derived from the data in (b). The black and red lines are raw and smooth data, respectively.

erating electrons in the opposite direction towards the upper facet of the nanowire. At this time, the raw time transients show an increased quenching of the emission intensity of QW2 while the decay rate of QW1 is reduced. This anti-correlated behavior is clearly observed as an increase of the *DoEI* to +1 (Figure 5.6 (c)), which is direct evidence of coupled depopulation of QW2 and population of QW1. Here, electrons are transferred from the lower, QW2, to the upper facet, QW1, of the radial quantum well due to the transverse component of the electric field as indicated in the Schematic I. As t progresses, the intensity of QW2 remains low while the intensity of QW1 decays very slowly resulting in a plateau of *DoEI*. Both observations arise from the combination of two effects which are induced by the electric field being orientated parallel to the wavevector of the surface acoustic wave $\boldsymbol{\mathcal{E}} \parallel \mathbf{k}$ and, thus, accelerating electrons in the opposite direction as shown in Schematic II. This results first in the electron depopulation of QW2 along the axial direction completely quenching the emission. Secondly, electrons are injected into the region of QW1 and, thus, remain in the emission region containing quasi-stationary holes. This induced motion does not open any additional loss channel. Therefore, it does not strongly affect the optical decay progress. The next distinct effect occurs during the acoustic cycle at $t = 2.7\,\mathrm{ns}$. At this time, $\boldsymbol{\mathcal{E}}$ is again transverse, yet, being orientated upwards. As a consequence, electrons are accelerated towards the substrate. This leads to a depopulation of QW1, which is located on the upper facet, and to an injection into QW2 on the lower facet. As the surface acoustic wave propagates further, the electric field vector rotates antiparallel and, thus, moves electrons along the axial direction towards QW2. In the raw time transients, the expected anti-correlated behavior is observed showing the quenching of the emission of QW1 while that of QW2 reappears as marked by arrows in Figure 5.6 (b). The inset depicts the derivative of the raw data illustrating the opposite slopes of both transients. In addition, the calculated *DoEI* initially decreased slowly, then rapidly drops and becomes negative. At $t = 4.4\,\mathrm{ns}$ the electrons have completed the full cycloid and the *DoEI* reaches its global minimum. Finally, at $t = T_{\mathrm{SAW}} = 5.15\,\mathrm{ns}$, the next surface acoustic wave cycle starts with the emission of QW2 quenching and *DoEI* increasing again. The local maxima of *DoEI* may arise from the weak but finite motion of the holes with a lower mobility compared to the electrons [28, 45]. Taken together, all observed anti-correlated intensity modulations of the time transients faithfully reproduce the cycloidal motion of electrons within the tubular quantum well driven by the transverse electrical spin of the surface acoustic wave.

Similar characteristic signatures are resolved for the two photoluminescence transients at all other delay times τ plotted in Figure 5.7 for τ ranging between 0 and $-T_{\mathrm{SAW}}/4$. Most notably, a clear anti-correlated behavior of the emission of the two quantum well systems is faithfully observed at times t with the electric field oriented perpendicular to the nanowire axis (Schematics I and III) for all τ. More precisely, at times at which the electric field points downwards, i.e. towards the substrate (dotted lines corresponding to Schematic I) all transients are anti-correlated. As explained above, this signature is a clear fingerprint of an electron transfer from QW2 to QW1. In addition, the expected reversed process, a transfer from QW1 to QW2, is observed at τ's shifted by $T_{\mathrm{SAW}}/2$.

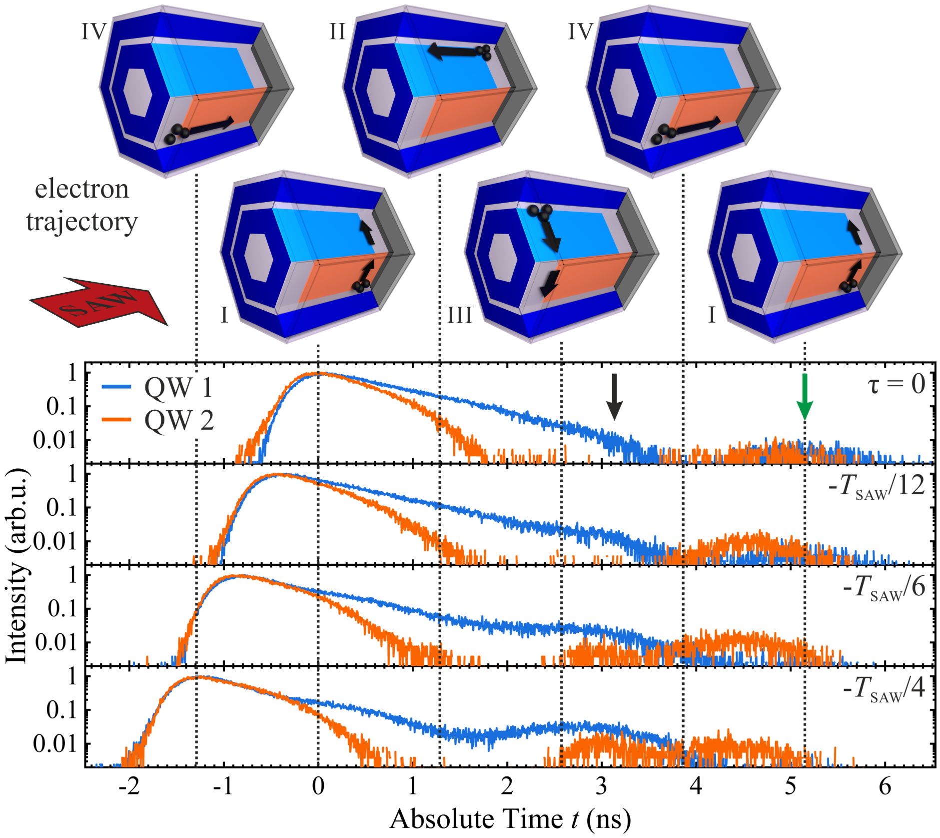

Figure 5.7: Representative time-resolved photoluminescence emission spectra of QW1 (blue) and QW2 (orange) for different delay times τ. The transients exhibit an oscillating behavior of the emission of both quantum wells due to an acoustically driven electron transport (black spheres and arrows) along the nanowire axis due to the oscillating electric field parallel to the nanowire axis (Schematic II and IV) as well as an anti-correlated behavior between both 2D systems. The latter can be attributed to a dynamically triggered electron transfer between the two quantum wells due to the oscillating electric field perpendicular to the nanowire axis (Schematic I and III). This induces an overall oscillating movement in radial direction around the radial quantum well and in axial direction along the nanowire. Black and green arrows indicate characteristic fingerprints due to the electric field orientation at the time of photoexcitation.

Remarkably, the data in Figure 5.7 also show that the electric field orientation at the time of photoexcitation leaves characteristic fingerprints in the photoluminescence dynamics. Hence, the measured intensity oscillations depend on the starting conditions, i.e. delay time τ and, thus, strongly influence the underlying temporal overlap of mobile electrons and quasi-stationary holes. When changing the delay time from $\tau = 0$ (upper transients) to $\tau = -T_{\mathrm{SAW}}/4$ (lower transients), the electric field at photoexcitation is rotated counterclockwise, from being perpendicular (pointing downwards) to being antiparallel to the propagation direction of the surface acoustic wave. Thus, the force component at photoexcitation which accelerates electrons into QW2 along the nanowire axis at photoexcitation ($\Delta t = 0$), increases as the delay time is tuned. Moreover, before the electrons are transferred from QW1 into QW2 (Schematic III), they are, at the time $t = T_{\mathrm{SAW}}/4$, accelerated antiparallel to the propagation direction of the surface acoustic wave (Schematic II). Thus, QW2 is depleted along the nanowire axis in direction away from QW2. As a consequence, for $\tau = 0$, the acceleration of electrons towards the substrate (Schematic III) does not result in a spatial overlap of mobile electrons and quasi-stationary holes due to this preceding depletion of QW2 along the nanowire axis at time $t \geq T_{\mathrm{SAW}}/4$. Thus, no reemergence of its emission signal is observed for $\tau = 0$. When tuning the delay time τ, the net force and acceleration of the electrons parallel to the propagation direction at $\Delta t = 0$ increases. Consequently, also the number of electrons injected into QW2 increases when they are transferred from QW1 into QW2. This results in an increase of the temporal signal of QW2 at $t > T_{\mathrm{SAW}}/2$ (black arrow in Figure 5.7) as τ is decreased from 0 to $-T_{\mathrm{SAW}}/4$. Moreover, we observe that both time transients exhibit again a clear anti-correlation showing the reemergence of the emission of QW1 and the suppression of the emission of QW2 (green arrow in Figure 5.7) as the next acoustic cycle starts at $t = T_{\mathrm{SAW}} = 5.15\,\mathrm{ns}$. Further, the reemerging emission intensity of QW1 is reduced as the delay time is tuned from $\tau = 0$ and $-T_{\mathrm{SAW}}/4$ resulting from the simultaneous depletion of QW2 and injection of electrons into QW1 (Schematic I) and the charge carrier distribution programmed at photo excitation.

5.5 Conclusion

In this chapter, we have presented the unique spin-momentum locking property of a surface acoustic wave propergating on the surface of YZ-cut $\mathrm{LiNbO_3}$ substrate. Spin-momentum locking itself is a universal wave phenomenon, in which the direction of spin is locked to the propagation direction of the surface acoustic wave, and the momentum of the wave, the decay direction and the spin form a locked triplet. By solving the equations of motion for surface acoustic waves, we have shown that both, acoustic wave and gyrating electric field, have transverse spin and spin-momentum locking properties. In particular, the acoustic spin within the material flips sign at about 0.2 wavelength away from the surface demonstrating that the spin-momentum locking properties of the acoustic wave do not necessarily result in a conventional right-handed triplet and, thus, are universal properties of Rayleigh-type surface acoustic waves. In contrast, the electromagnetic spin results in the conventional right-handed triplet which flips together with the decay direction. By probing the spin of the electric field, we can gain direct insights into the spin properties of surface acoustic waves. This, however, demands an ultrafast, nanoscale vector field sensor operating at frequencies in the megahertz to gigahertz regime which is realized by the three-dimensional nature of the tubular quantum well embedded in a nanowire heterostructure enabling us to faithfully detect electron cycloids driven by the transverse spin momentum of a surface acoustic wave. Here, the gyrating electric field vector induces a counterclockwise motion of electrons between two separated, but interconnect quantum well segments which are located on neighboring sidewall facets. Thus, the subnanosecond temporal resolution of our ultrafast sensor is able to detect the orientation and, consequently, the gyration of the electric field vector at frequencies $\geq 100\,\mathrm{MHz}$, which is important for phonon-based hybrid quantum technologies [203–209]. Moreover, these results demonstrate the importance of local interaction between nanophotonics and nanoacoustic structures in observing the angular momentum phenomenon of a surface acoustic wave which proved to be challenging. Finally, the nanowire-based method initiates for the direct detection of photonic skyrmions and, eventually, spatially resolved angular momentum detection of light and sound in quantum optical, photonic, and optomechanical systems [210–213].

Chapter 6

Sub-nanosecond acousto-electric carrier dynamics in polytypic nanowires [1]

III-V semiconductor nanowires are often characterized by the mixing of zincblende and wurtzite crystal phases which frequently occur along the nanowire axis [14, 52, 62, 63, 215]. In most materials, this crystal phase mixing leads to a static type-II modulation of the conduction and valence band edges which induces the localization of electrons and holes within different regions along the nanowire axis [72, 216] and, thus, results in new channels, e.g., for optical recombination and electrical transport. Hence, the free exciton transition occurring in the pure zincblende crystal phase as well as bound, indirect exciton transitions occurring at zincblende twinning defects and at the interface of extended wurtzite and zincblende segments were observed in such nanowires, respectively [16–24]. In addition to these optical properties, such stacking fault defects and crystal phase boundaries act as scattering centers which certainly affect carrier transport along the nanowires [25–28]. Therefore, the insight of charge carrier dynamics within different, interconnected channels of nanowires is crucial for the realization of future high performance nanoelectronic and nanophotonic devices [2, 4, 6, 30, 33].

Here, acousto-optoelectric spectroscopy gives direct insights into these charge carrier dynamics by utilizing the acousto-electric coupling between charge carriers and the piezoelectric field of surface acoustic waves [39, 43, 163–166] and comparing the underlying spatio-temporal dynamics to calculation [28, 45, 167]. To date, this versatile technique is limited to single transport channels which can be analyzed via its characteristic emission signal in the optical spectrum. To unravel coupled dynamics, this limitation can be overcome by high-order correlation techniques, which are widely applied in optics to study a broad variety of nanosystems [217–221].

In this chapter, the acousto-optoelectric spectroscopy technique, which is described in Chapter 4, is advanced to a multi-channel platform to directly and simultaneously observe the time-depended surface acoustic wave-modulated emission of up to three spectrally filtered transition channels. This, in particular, enables to directly obtain higher-order correlations revealing clear fingerprints of the underlying coupled carrier dynamics within polytypic GaAs-(Al)GaAs core-shell nanowires. In the first part, the implemented com-

---

[1] mainly published and with permission from [172] and [214]. Copyright 2021 American Physical Society and Copyright 2021 The Authors (Published by IOP Publishing Ltd).

bination of three-channel cross-correlation and acousto-optoelectric spectroscopy is presented. In the next part, the structural and optical properties of two different types of typically polytypic nanowires are discussed, which clearly differ in the crystal structure along their axes and, thus, exhibit three different transition channels. The third and forth part present the results on the time-resolved acousto-optoelectric spectroscopy and the resolved acoustically driven spatio-temporal carrier dynamics in the temporal modulation of each transition channel by corroborating our experiments with numerical simulations that model the carrier dynamics. Finally, we deduce the interplay as well as the charge carrier transfer between each transition channel by correlating these transition channels in a second-order photon correlation functions, and access the full information of the three transition channels by exploring the third-order intensity correlation function.

The main results of this chapter are published in Physical Review Applied and Nanotechnology under the titles "High-Dimensional Acousto-optoelectric Correlation Spectroscopy Reveals Coupled Carrier Dynamics in Polytypic Nanowires" [172] and "Sub-nanosecond acousto-electric carrier redistribution dynamics and transport in polytypic GaAs nanowires" [214], respectively. Transmission electron microscopy has been performed in collaboration with Maximilian Gnedel and Johannes Berlin.

6.1 Three-channel cross-correlation acousto-optoelectric spectroscopy

To unravel coupled dynamics of different transport and/or recombination channels in various nanostructures, we advance our acousto-optoelectric spectroscopy to a multi-channel photon correlation platform allowing us to monitor the time-dependent surface acoustic wave modulated emission of up to three spectrally isolated decay channels. To this end, this technique is implemented by combining phase-locked optical micro-photoluminescence spectroscopy and the simultaneous time-resolved detection of three-channels.

The experimental setup for three-channel cross-correlation acousto-optoelectric spectroscopy is depicted in Figure 6.1 (a). Therefore, two nominally identical interdigital transducers forming a delay line are used to generate two surface acoustic wave beams which propagate in opposite directions. These two directions are in the following referred to as $+k$- (left to right) and $-k$- (right to left) propagating surface acoustic waves. Again, interdigital transducers with a wavelength of $\lambda_{\mathrm{SAW}} = 18\,\mu\mathrm{m}$ and a corresponding acoustic period (frequency) of $T_{\mathrm{SAW}} = 5.08\,\mathrm{ns}$ ($f_{\mathrm{SAW}} = 197\,\mathrm{MHz}$) were fabricated on a commonly used, strong piezoelectric YZ-cut $\mathrm{LiNbO_3}$ substrate. For our experiment, polytypic GaAs-(Al)GaAs core-shell nanowires are transferred onto the active region of the surface acoustic wave-chip in between the two interdigital transducers. The surface acoustic wave chip itself is mounted in a low temperature ($T = 8\,\mathrm{K}$) micro-photoluminescence setup. The parts of the setup used for the optical and surface acoustic wave excitation remain unchanged as described in Chapter 4 while the optical detection is advanced by a simultaneous three-channel time-resolved detection. Hereby, the signal components of different emission bands

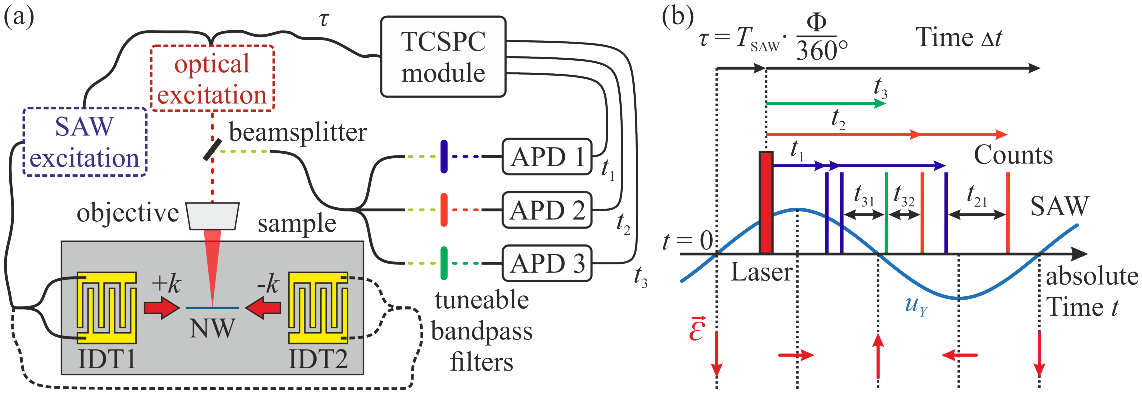

Figure 6.1: (a) Schematic of the three-channel cross-correlation acousto-optoelectric spectroscopy setup – phase-locked, micro-photoluminescence spectroscopy probes a single nanowire. The emission of different recombination channels is spectrally isolated and detected by single photon silicon avalanche photodetectors and recorded by multi-channel time-correlated single photon counting electronics. (b) Timing scheme – the local phase of the surface acoustic wave oscillation (blue) sets the absolute time t, of the experiment. Laser excitation (red bar) is delayed by $\tau = T_{\mathrm{SAW}} \cdot \Phi/360°$ and individual time stamps of subsequent detection events on each channel are registered relatively to the laser excitation.

are collected by the objective and analyzed either by time-integrated multi-channel detection using a cooled charge coupled device detector or after spectral filtering in the time-domain by single photon detectors and time-correlated single photon counting. For the multi-channel photon correlation experiments, the emission of the nanowire is split via a symmetric 1x3 fiber beam splitter and each of its three outputs is spectrally filtered by a tunable bandpass filter (FWHM bandwidth of 3.0 nm) to isolate the emission of individual emission bands. These signals are detected by three similar single-photon silicon avalanche photodetectors (APDs) with a time resolution <350 ps while the time-correlated single photon counting (TCSPC) is performed by a five-channel time tagger.

As stated above, the nanowire studied can be optically excited at a well-defined time during the acoustic cycle by referencing the frequency of the surface acoustic wave to a multiple integer of the repetition frequency of the laser, $n \cdot f_{\mathrm{Laser}} = f_{\mathrm{SAW}}$, with n being integer. The full timing scheme of the multi-channel photon correlation experiment is depicted in Figure 6.1 (b). The absolute time t is set by the surface acoustic wave at position of the laser spot on the nanowire studied. As the absolute time t progresses, the vertical displacement u_Y oscillates and the electric field vector $\boldsymbol{\mathcal{E}}$ [red arrows] gyrates counterclockwise close to the surface. The delay time τ between the laser and the surface acoustic wave can be adjusted to any value between $\tau = [0, T_{\mathrm{SAW}}]$. Individual time stamps of all detection events (t_i) are recorded relatively to the laser excitation by one of detectors (APD i) as shown in Figure 6.1 (b). Hence, this allows to perform a full analysis of the detection events on the three channels.

First, conventional single channel analysis on each channel i can be performed simultaneously by referencing the respective, registered events to the laser excitation. Most importantly, correlations between the three channels can be rigorously determined because we do not have to perform recordings for individual, single channels but all signals are recorded simultaneously for all channels in a single run. For multi-channel photon correlation experiments analyzing three channels, the time differences (relative to the laser pulse) t_{ij} are determined between detection events of channels i and j as illustrated in Figure 6.1 (b). Then, these time differences are used to calculate three second-order intensity correlations:

$$g_{ij}^{(2)}(t_{ij}) = \frac{\langle I_i(t) I_j(t + t_{ij}) \rangle}{\langle I_i(t) \rangle \langle I_j(t) \rangle} \tag{6.1}$$

and the third-order intensity correlations:

$$g_{1,2,3}^{(3)}(t_{21}, t_{3,1}) = \frac{\langle I_1(t) I_2(t + t_{21}) I_3(t + t_{31}) \rangle}{\langle I_1(t) \rangle \langle I_2(t) \rangle \langle I_3(t) \rangle}. \tag{6.2}$$

6.2 Structural and optical characterization

The nanowire structure studied in this chapter nominally consists of a GaAs core with a diameter of 60-80 nm and typical lengths $l_{\mathrm{NW}} > 10\,\mu\mathrm{m}$. It is overgrown by a 60 nm thick $\mathrm{Al_{0.3}Ga_{0.7}As}$ shell with 3 nm thick radial GaAs quantum well embedded in the center of the shell [85, 117]. For passivation, a GaAs capping layer of 10 nm was added to prevent oxidation. In particular, the as-grown nanowires crystallized in a predominately polytypic nature which is characterized by intermixing of zincblende and wurtzite crystal phase segments of random length along the nanowire axis. This leads to a static type-II modulation of the conduction and valence band edges and is known to result in different recombination channels which can be distinguished from their optical transition energies [17, 18, 20–23].

To determine the microstructural properties along the axis of such grown nanowires, we performed high-resolution transmission electron microscopy on representative nanowires. The transmission electron microscopy images of two representative nanowires acquired along their entire length are shown in Figure 6.2 (a) and Figure 6.3 (a) together with selected diffraction patterns which are taken in the upper and lower part of both nanowires. Both types of nanowires differ in the variation of their crystal structure along their axis. The crystal structure of nanowires, referred to as Type-1 (Figure 6.2 (a)), predominantly exhibits in the lower part a zincblende phase with occasional rotational twins separated by individual twin defects, which is clearly confirmed by the associated diffraction pattern showing in this region the characteristic zincblende reflections of individual zincblende twin defects (ZB-A and ZB-B sensitive reflections are marked by red and blue circles). Such twin defects can be understood as a monolayer thick insertion of the wurtzite material in a zincblende matrix [23, 24, 222, 223]. Towards the upper part of the nanowire the crystal structure becomes more disordered with a higher density of rotational twin defects. At the top of the nanowire, the crystal structure consists of a larger number of extended wurtzite segments within the zincblende phase. As a consequence, the diffraction pattern in the upper part shows characteristic wurtzite reflections (marked by green circles) and a streaky diffraction pattern confirming the high disorder in the crystal structure.

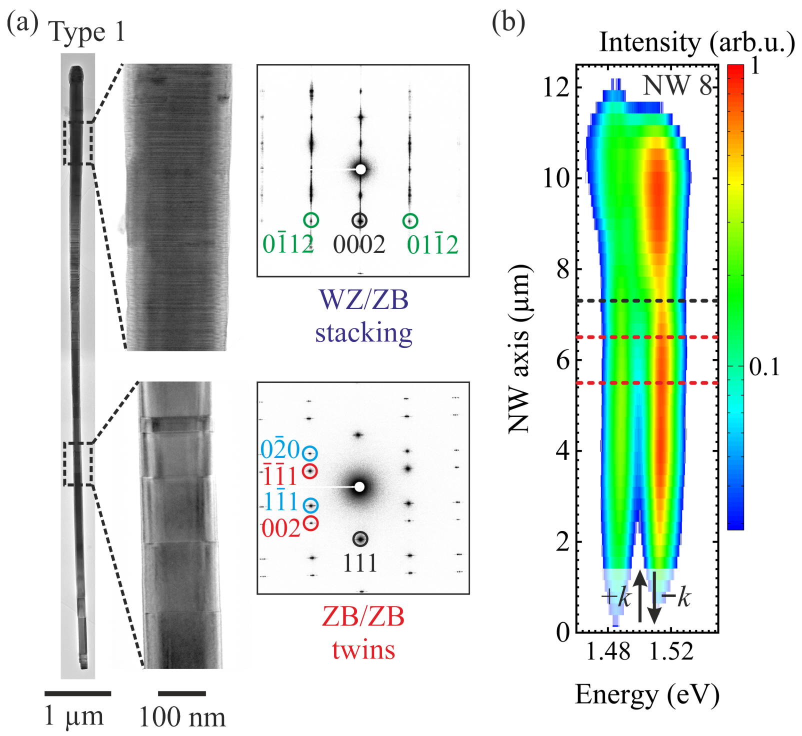

Figure 6.2: (a) Transmission electron microscopy images and corresponding diffraction patterns of a Type-1 GaAs-AlGaAs core-shell nanowire. The lower region of Type-1 nanowire exhibits a zincblende crystal structure with few twin defects. ZB-A and ZB-B sensitive reflections are marked by blue and red circles. The upper region contains also larger wurtzite phase segments and defects. Wurtzite sensitive reflections, as marked by green circles, are clearly visible in the diffraction pattern. (b) Spatial photoluminescence maps along a further nanowire, referred to as NW8, at low optical pump power densities ($2.8\,\mathrm{W/cm^2}$). NW8 is associated with a crystal structure of Type-1. The black dashed line marks the change of the crystal structure along the nanowire. The red dashed lines indicate the region of excitation along the nanowire for acousto-optoelectric spectroscopy.

In contrast, nanowires, referred to as Type-2 (Figure 6.3 (a)), consist of extended zincblende phase domains occurring along their axis and, thus, exhibit no extended wurtzite segments. Moreover, the density of rotational twin defects increases only slightly towards the upper region of the nanowire resulting there in a larger number of short zincblende segments, yet no wurtzite segments are observed. Thus, the diffraction patterns at the lower and the upper part of Type-2 nanowire show exclusively zincblende reflections. Consequently, nanowires of Type-2 are considered to exhibit a more homogenous crystal structure along their axes than nanowires of Type-1. These changes of crystal structure are known to have a pronounced influence on the optical properties of nanowires, which is confirmed by optical spectroscopy.

Next, we analyze the evolution of the photoluminescence spectra recorded along the axis of such nanowires. In Figure 6.2 (b) and Figure 6.3 (b), low temperature ($T = 8\,\mathrm{K}$) photoluminescence spectral maps are presented along the axis of two representative nanowires,

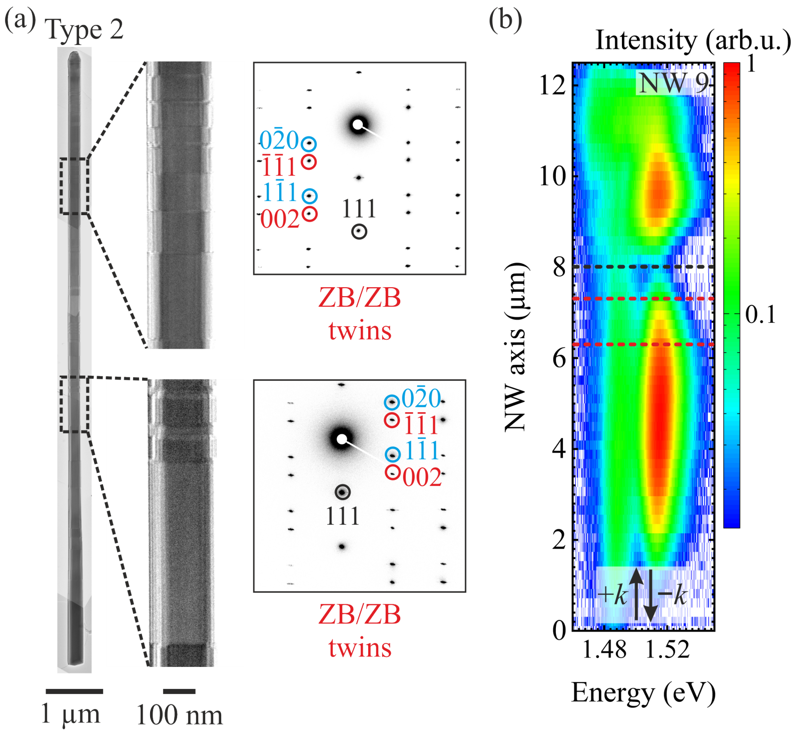

Figure 6.3: (a) Transmission electron microscopy images and corresponding diffraction patterns of a Type-2 GaAs-AlGaAs core-shell nanowire. Nanowires of Type-2 exhibit a zincblende crystal structure along the entire nanowire with the twin defect density slightly increasing towards the upper end. ZB-A and ZB-B sensitive reflections are marked by blue and red circles. (b) Spatial photoluminescence maps along a further nanowire, referred to as NW9, at low optical pump power densities ($8.5\,\mathrm{W/cm^2}$). NW9 is associated with a crystal structure of Type-2. The black dashed line indicates a change of the crystal structure along the nanowire. The red dashed lines highlight the region of excitation along the nanowire for acousto-optoelectric spectroscopy.

which are referred to as NW8 and NW9, respectively. The color-coded emission intensity is plotted as a function of axial position and photon energy. The emission spectra of both nanowires exhibit characteristic, position-dependent changes along their axis and a pronounced reduction of the emission intensity at approximately the same position along their axis marked by black dashed lines. This observation, in turn, indicates that a change of the microstructure occurs during growth of the nanowire core. In the following, the emission of both nanowires is analyzed in the regions highlighted by red boxes. Moreover, we performed acousto-optoelectric spectroscopy at same positions to assess the influence of polytypism on the spatio-temporal carrier dynamics within nanowire cores.

For both types of nanowires, different recombination channels can be distinguished which characteristically occur in polytypic GaAs nanowires. The photoluminescence spectra recorded near the center of NW8 and NW9 (right panels) and the corresponding different recombination channels (left panels) are shown in Figure 6.4 with the assignment being consistent to literature [111, 223]. The type-II band alignment within the polytypic nanowires results in the localization of electrons and holes in zincblende and wurtzite

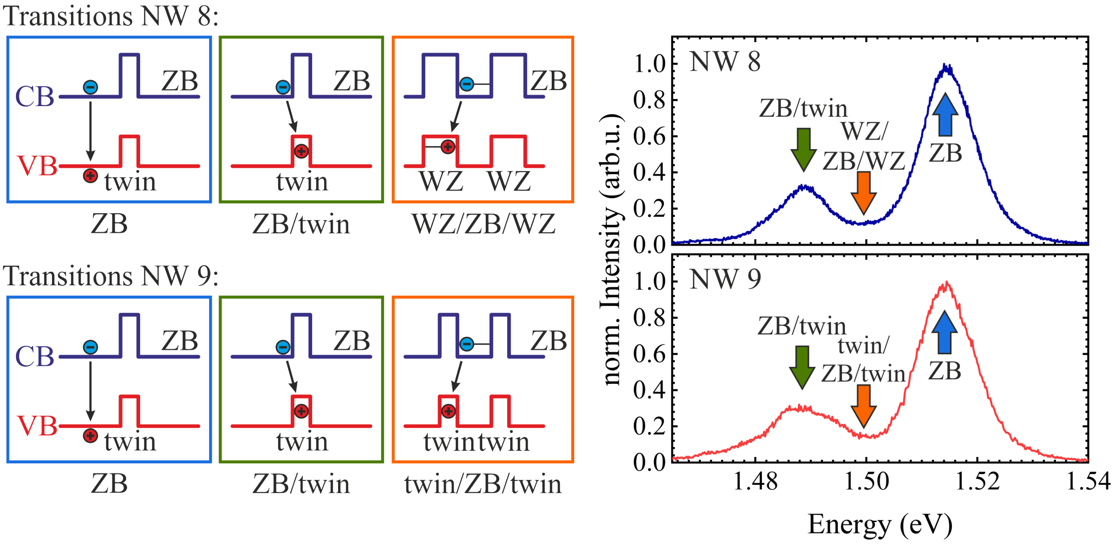

Figure 6.4: Left panels: Schematics of the emission processes occurring in each nanowire. Recombination of direct excitons in pure zincblende phase (ZB) and spatially indirect excitons localized at twin defects (ZB/twin) exist in both nanowires. In NW8, indirect exciton recombination occurs between quantum confined electrons in short zincblende segments and quantum confined holes in short wurtzite segments (WZ/ZB/WZ), whereas indirect excitons are present between quantum confined electrons and holes localized at twin defects (twin/ZB/twin) in NW9. Right panels Typical photoluminescence spectra observed at the center of NW8 and NW9, respectively. Arrows mark the different recombination transitions.

regions along their axes, respectively. In the presence or absence of quantum confinement, three dominant recombination channels exist for both nanowires, which are depicted schematically in Figure 6.4, respectively: (i) the emission of free excitons (ZB transition) which recombine spatially directly in extended zincblende phase regions (left panel, blue boxes), is observed at a photon energy $E_{\mathrm{ZB}} = 1.514\,\mathrm{eV}$, which is marked by blue arrows in the spectra of both nanowires. (ii) Spatially indirect recombination between quasi-free electrons in the extended zincblende crystal phase and quantum confined holes at rotational twin defects and in short wurtzite phase segments (left panel, green boxes). This recombination occurs predominantly in zincblende phase regions containing several twin defects, which can be also considered as a monolayer thick insertion of the wurtzite material in a zincblende matrix [23, 24, 222, 223], or short wurtzite segments. The emission of this recombination is observed at lower photon energies of $E_{\mathrm{ZB/twin}} = 1.488\,\mathrm{eV}$ as marked by green arrows in both spectra of both nanowires. In the following, this emission signal is referred to ZB/twin transitions. (iii) Spatially indirect recombination between quantum confined electrons in short zincblende regions and quantum confined holes (left panel, orange boxes). Here, both types of nanowires differ in their recombination channels. The position-dependent photoluminescence emission of NW8 presented in Figure 6.2 (b) shows that the emission slightly shifts from the main ZB emission peak towards lower energies and broadens in the upper part of the nanowire compared to the lower part at which photoluminescence emission peaks at 1.514 eV and 1.488 eV are observed. This behavior is directly linked to the change of the crystal structure along the nanowire from predominantly zincblende to a highly mixed phase containing extended wurtzite segments. The shifted emission is attributed to the indirect exciton recombination at the interface of short wurtzite and short zincblende segments in the highly mixed region of NW8. This emission signal is referred to WZ/ZB/ZB transitions and schematically illustrated in the orange box in the upper left panel of Figure 6.4. This WZ/ZB/WZ transition arises from the recombination of quantum confined electrons in short zincblende segments and quantum confined holes in short wurtzite segments in the highly mixed region of NW8. In particular for such thin segments, motional quantization contributes and the energy of electrons and holes shifts away from their respective band edges. This, in turn, leads to the observed shift of the emission energy [223] which is marked by the orange arrow in the spectrum. In contrast, no shift in energy of the position-dependent ZB emission of NW9 is observed along the nanowire axis. Thus, the emission occurring at an energy between that of the ZB- and ZB/twin transitions (marked by orange arrow) is attributed to indirect exciton transitions between quantum confined electrons and holes localized at twin defects (lower left panel, orange box). Again, as both electrons and holes are confined, this gives rise to a shift towards higher (lower) energies compared to the ZB/twin (ZB) emission peak. In the following, this transition is referred to as twin/ZB/twin recombination and marked by the orange arrow in the spectrum of NW9.

In order to probe the carrier dynamics of the different emission bands, we performed the temporally resolved photoluminescence of the three characteristic emission bands of each

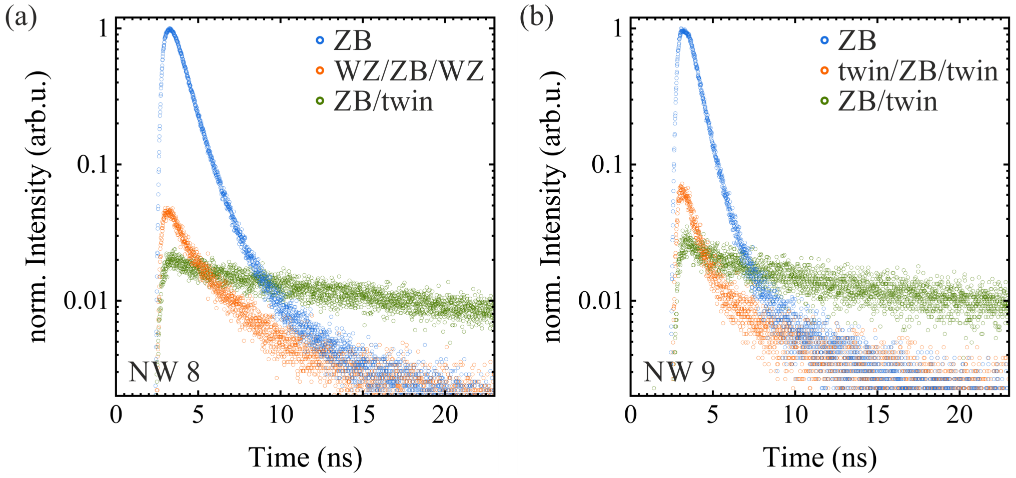

Figure 6.5: Corresponding time-resolved photoluminescence emission spectra of (a) NW8 and (b) NW9. (a) Time transients of NW8 show luminescence of the free ZB (blue) exciton peak at 1.514 eV and the indirect ZB/twin (green) excitons transitions at single twinning defects at 1.488 eV and indirect WZ/ZB/WZ (orange) exciton transitions at 1.499 eV. (b) Time-resolved luminescence of NW9 of the free ZB (blue) peak at 1.514 eV, the indirect ZB/twin (green) transitions at single twinning defects at 1.488 eV and indirect twin/ZB/twin (orange) exciton transitions at 1.499 eV. All transients clearly exhibit a bi-exponential nature of the decay with a fast decay at short times and a slow time constant at longer times. The respective fast and slow decay times are shown in Table 6.1.

	NW8			NW9		
	ZB	WZ/ZB/WZ	ZB/twin	ZB	twin/ZB/twin	ZB/twin
τ_{fast} (ns)	1.0	1.9	7.1	0.8	0.9	4.4
τ_{slow} (ns)	7.8	18.3	42.6	8.0	10.8	39.2

Table 6.1: Slow and fast decay times τ_{slow} and τ_{fast} of the free ZB (blue), the indirect ZB/twin (green) and indirect WZ/ZB/WZ (orange) exciton transitions of NW8 and of the free ZB (blue), the indirect ZB/twin (green) and indirect twin/ZB/twin (orange) exciton transitions of NW9, respectively.

nanowire. The corresponding detected transients of free ZB exciton (blue arrow), the indirect ZB/twin excitons transitions at single twinning defects (green arrow) and the indirect WZ/ZB/WZ or twin/ZB/twin transition (orange) of NW8 and NW9 are compared in Figure 6.5 (a) and (b) without a surface acoustic wave applied, respectively. For all transitions of both nanowires, we clearly observe a biexponential decay of the photoluminescence emission with fast and slow time constants which are summarized in Table 6.1. While the free ZB transition and the indirect ZB/twin transition of both nanowires show almost similar decay rates, the indirect WZ/ZB/WZ transition of NW8 and twin/ZB/twin transition of NW9 slightly differs. Here, both decays of the twin/ZB/twin transition of NW9 are faster. These differences may be due to the deeper penetration depth of the hole wavefunctions localized at the twin defects into the zincblende segments and vice versa resulting in an increased overlap of both wavefunctions and, thus, in faster decay rates. Furthermore, the observed decay dynamics are in good agreement with previous reports [18, 24, 224] confirming our assignment.

After analyzing the unperturbed nanowire emission, the charge carrier dynamics are determined by acousto-optoelectric spectroscopy. In particular, as the degree of polytypism varies along the nanowire axis, it is expected that the propagation direction of the surface acoustic wave has a pronounced impact on the resulting charge carrier dynamics.

6.3 Time-averaged surface acoustic wave spectroscopy

In a first step, the emission behavior of both polytypic GaAs nanowires is probed under time-averaged surface acoustic wave excitation. In Figure 6.6 (a), the time-integrated photoluminescence emission spectra of both nanowires are shown as a function of the applied acoustic power (P_{rf}) for $+k$- (left panels) and $-k$- (right panels) propagation direction of the surface acoustic waves. Both nanowires are aligned the same way, that the $+k$- and $-k$-directions are orientated towards and away from the highly polytypic regions, respectively, which is illustrated by the schematics on the top. As P_{rf} and, thus, the electric field amplitude of the surface acoustic wave increases, the overall photoluminescence emission quenches due to the efficient separation of electrons and holes by the electric field. Obviously, we observe that the quenching behavior of the ZB and ZB/twin emissions clearly differs for the NW8 when the propagation direction of the surface acoustic wave is re-

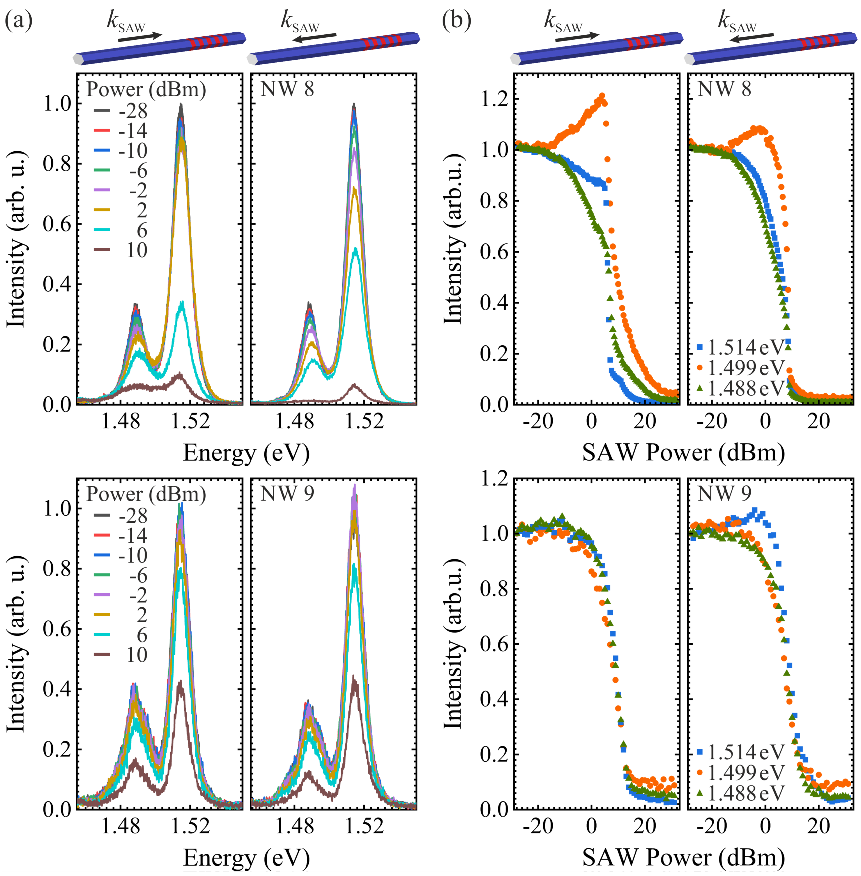

Figure 6.6: (a) Emission spectra at the center of both GaAs nanowires (NW8-top and NW9-bottom) modulated by a surface acoustic wave at a frequency $f_{\mathrm{SAW}} = 197\,\mathrm{MHz}$ for varying acoustic power P_{rf} applied to the interdigital transducers and for $+k$-propagating (left panels) and $-k$-propagating (right panels) surface acoustic wave. With increasing acoustic power, the overall emission is quenched due to the efficient dissociation and acceleration of electrons and holes by the piezoelectric field of the surface acoustic wave. (b) Extracted normalized photoluminescence intensities of the free excitons in pure zincblende crystal phase at 1.514 eV and the indirect excitons transitions at twin defects at 1.488 eV, and indirect excitons between confined electrons and confined holes at 1.499 eV as a function of acoustic power P_{rf}.

versed, while no pronounced difference is present for NW9. Moreover, the emission of the ZB/twin excitons of NW8 shifts towards higher energies for both propagation directions with increasing radio frequency power, whereas the indirect exciton energy of NW9 is not affected by the surface acoustic wave.

In the following, these quenching properties are further analyzed by extracting the normalized integrated photoluminescence intensity of all three emission bands from each spectrum (normalized to the unperturbed emission at low acoustic powers, $P_{\mathrm{rf}} < -28\,\mathrm{dBm}$). The extracted data are evaluated in Figure 6.6 (b) for the direct exciton transition in zincblende GaAs (blue) and the indirect ZB/twin exciton transition at twin defects (green) and the indirect exciton transition between confined electrons and confined holes (orange), respectively. Considering each transition individually, the integrated intensity of the ZB transition and the ZB/twin transition of both nanowires exhibit a continuous quenching behavior for both surface acoustic wave propagation directions. This quenching properties are similar to that known for several other III-V semiconductor nanosystems [28, 38, 43, 44, 50]. Note, the non-monotonic quenching behavior of the zincblende emission, i.e. the weak increase of the overall intensity at low acoustic powers, is well known in literature for 1D and 2D systems [47, 167]. It arises from an increase of the electron-hole overlap due to their dissimilar carrier mobilities [167]. In contrast to that, the indirect WZ/ZB/WZ exciton transition of NW8 (orange) shows a different evolution than the indirect twin/ZB/twin exciton transition of NW9. Most remarkably, the photoluminescence intensity of NW8 does not decrease monotonically, yet, it first reaches a pronounced maximum at low acoustic power levels (of about $0 \pm 4\,\mathrm{dBm}$) and then decreases afterwards until it is almost fully suppressed. Such a non-monotonic behavior has been previously found in systems with zero-dimensional trapping sites or quantum dots [225, 226] and, thus, suggests either an injection of electrons and holes into the region with a high wurtzite/zincblende density leading there to the formation of indirect excitons [226] or a suppression of the depletion of these excitons from this region [225]. Consequently, this behavior is expected to occur in Type-1 nanowires. In contrast, the photoluminescence emission between the ZB and ZB/twin channels of NW9 quenches monotonously and, hence, the feeding of higher energetic indirect transition channels, such as the WZ/ZB/WZ transition, is absent. Consequently, it is more likely to occur in nanowires of Type-2. In addition, such properties can be attributed to a more homogeneous distribution of trapping sites along the nanowire axis compared to NW8.

6.4 Single channel time-resolved charge carrier dynamics

In this section, the impact of polytypism varying along the nanowire axis on the acoustically driven charge carrier dynamics is investigated for NW8 and NW9. Thereby, to gain a detailed understanding of the underlying mechanisms, the surface acoustic wave-induced emission dynamics of the three characteristic transition bands of each nanowire are analyzed and compared to numerical calculations of the acoustically driven carrier dynamics for surface acoustic waves propagating in $+k$- and $-k$-direction. In particular, we assume two general, static band edge modulations with realistic parameters for the band edge discontinuities, which are induced due to the polytypic crystal structure, and realistic parameters for the transport mobilities of electrons and holes in our numerical calculations. The applied surface acoustic waves had a frequency of $f_{\mathrm{SAW}} = 197\,\mathrm{MHz}$ and a power level of $P_{\mathrm{rf}} = 7 \pm 3\,\mathrm{dBm}$. In following, we show that all three emission bands of each nanowire exhibit characteristic, T_{SAW}-periodic intensity modulations which depend on the surface acoustic wave phase Φ. This demonstrates that the orientation of the electric field at the position of the laser spot at the time of the laser excitation programs subsequent acoustically driven carrier dynamics [168]. Moreover, the modulations are not in phase but exhibit clear correlations and anti-correlations, which point towards coupled charge carrier dynamics. Because both types of nanowires differ in the their crystal structure, they show different behaviors when the surface acoustic propagation direction is changed. For the Type-1 nanowires, these modulations strongly depend on the propagation direction of the surface acoustic wave, while no pronounced directionality is found for Type-2 nanowires. Furthermore, we show that these key characteristics can be well reproduced in the numerical simulations by assuming two general band edge modulations and realistic parameters for the band edge discontinuities and transport mobilities of electrons and holes.

In this section, we first introduce the two band edge modulations used for modeling both nanowires in the numerical calculations. Afterwards, the dynamic modulations of Type-1 and Type-2 nanowires are analyzed and corroborated by numerical calculations of the acoustically driven spatio-temporal carrier dynamics.

6.4.1 Band edge modulation of Type-1 and Type-2 polytypic nanowires

To gain quantitative information on the charge carrier dynamics and the resulting emission properties, the surface acoustic wave-induced spatio-temporal charge carrier dynamics are calculated and compared to the surface acoustic wave-driven modulations of the three emission bands of each nanowire. In our numerical calculations, the spatio-temporal dynamics of the electron (n) and hole (p) concentrations are determined by solving the semiclassical drift and diffusion equations for a band edge modulation set by the electric potential of the surface acoustic wave and the static band edge modulation which is induced by the polytypic crystal structure along the nanowire axis. The corresponding, coupled differential equations for spatial and temporal evolution are derived in Section 3.5 for the one-dimensional model such as nanowires. For the detailed description of the model, we refer to references [28, 45, 167]. In addition, the product $n \cdot p$ is calculated as it is proportional to the optical recombination intensity observed in our experiment.

In our simulations, five electron-hole pairs are generated by a laser pulse with a duration of 50 ps in a Gaussian spot with a diameter of 1.5 µm and are accelerated by a surface acoustic wave with a frequency of $f_{\mathrm{SAW}} = 200$ MHz which corresponds to a wavelength of $\lambda_{\mathrm{SAW}} = 17.5$ µm. The length of the nanowire is set to λ_{SAW} with the generation spot in the center (Position $x = 0$). The exciton recombination rate is derived from the measured photoluminescence decay times and is specified to $\tau_{\mathrm{exciton}} = 1.0$ ns. Moreover, we consider only radiative processes within the nanowire at low temperatures (10 K) and non-radiative losses at the boundary of the simulation region. The simulations were performed over 90 acoustic cycles and three excitation pulses leading to a stable steady state solution.

For the realization of the band edge modulation which is induced by the polytypic crystal structure, an additional static potential has to be superimposed to the sinusoidal electric potential of the surface acoustic wave. Consequently, the charge carriers which are accelerated by the electric fields of the surface acoustic wave are influenced by this perturbation. In particular, we assume a basic geometry of a static type-II band modulation of an otherwise pure zincblende nanowire with separated embedded wurtzite-type and twin-type segments for our calculations. The band edge modulations of both ge-

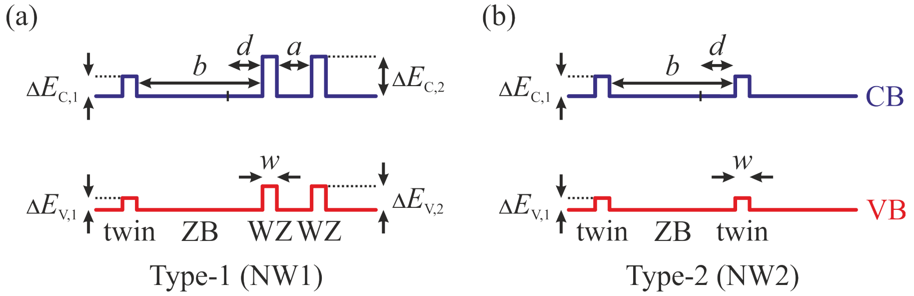

Figure 6.7: Schematic illustration of the polytypic band edge modulation used for the models for (a) Type-1 and (b) Type-2 nanowires. Both geometries are based on transmission electron microscopy analysis in Section 6.2. NW8 represents nanowires of Type-1, whereas NW9 is associated with Type-2. Type-1 nanowires consist of a single twin-type segment at the lower part and two separated wurtzite-type segments in the upper part of the nanowires. Type-2 nanowires are modeled by a single twin-type segment at the lower and upper part of the nanowires, respectively. The dimensions of the parameters are listed in Table 6.2.

$\Delta E_{C,1}$	$\Delta E_{V,1}$	$\Delta E_{C,2}$	$\Delta E_{V,2}$	w	b	d	a
7.5 meV	5.5 meV	15 meV	11 meV	200 nm	2.8 µm	800 nm	800 nm

Table 6.2: Dimensions of the static type-II band modulation used for the models for Type-1 and Type-2 nanowires as shown in Figure 6.7. Here, w, b and a are the width of each segment, the separation of the twin segment in lower part and the first segment of the upper part as well as the separation of the wurtzite-type segments in the upper part, respectively. d denotes the distance of the nearest segment to the generation spot. ΔE_C and ΔE_V are the corresponding effective band offsets in the conduction and valance band.

ometries, which represent basic versions of Type-1 (NW8) and Type-2 (NW9) nanowires found in our transmission electron microscopy analysis (cf. Figure 6.2 and Figure 6.3), are schematically depicted in Figure 6.7 (a) and (b), respectively. For both geometries, a single twin-type segment is introduced in the lower parts of each nanowire with effective band offsets $\Delta E_{C,1}$ and $\Delta E_{V,1}$ in the conduction and valance band. This represents the low rotational twin density in the lower parts of both types of nanowires. Most crucial, both geometries for each nanowire are different from each other in their band modulation in the upper part. For a Type-1 nanowire, two separated wurtzite-type segments are embedded within the pure zincblende phase with the effective band offsets of these wurtzite-type segments set to $\Delta E_{C,2}$ and $\Delta E_{V,2}$, which is twice the effective band offset of a twin-type segment. In contrast, a Type-2 nanowire consists of only one second twin-type barrier with effective band offsets $\Delta E_{C,1}$ and $\Delta E_{V,1}$ in the upper part of the band structure. Both models predominantly reflect the crystal structure along the axis of both nanowires, i.e. the highly disordered upper part of Type-1 nanowires as well as the more homogeneous crystal structure of Type-2 nanowire with occasionally rotational twins.

The corresponding dimensions of the static type-II band modulation used for the models for Type-1 and Type-2 nanowires are summarized in Table 6.2. In our calculations, all segments have a width of w. In addition, the twin segment in lower part of the nanowire and the first segment (lower wurtzite segment or upper twin segment) of the upper part are separated by a distance of b. The distance between both upper wurtzite segments of a Type-1 nanowire is set to a. Moreover, the nearest segment is located in a distance d to the generation spot at the center (Position $x = 0$). Thus, electron hole pairs are excited in both models in between the twin-type segment in the lower part and the first segment in the upper part.

The mobility of electrons and holes are set to $\mu_\mathrm{n} = 500\,\mathrm{cm}^2/(\mathrm{Vs})$ and $\mu_\mathrm{p} = 50\,\mathrm{cm}^2/(\mathrm{Vs})$, respectively [28]. Note, $\mu_\mathrm{p} = 0.1\mu_\mathrm{n}$ induces that holes remain quasi-stationary at the time of photoexcitation for the range of parameters considered in our calculations.

6.4.2 Charge carrier dynamics in Type-1 polytypic nanowires

In the first step, the acoustically driven dynamics of NW8 are analyzed for the surface acoustic wave propagating in $+k$-direction. The experimentally observed time transients of the three transitions (ZB: blue, ZB/twin: green, WZ/ZB/WZ: orange) are shown for different surface acoustic wave phases at the time of photoexcitation Φ and the $+k$-propagation direction in Figure 6.8. Clearly, all transients show expected characteristic surface acoustic wave induced modulations which depend on the studied recombination channel. These modulations are characteristic fingerprints of transport of electrons and holes along the nanowire axis which are driven by the oscillating electric field parallel to the axis [28, 38, 45].

For the surface acoustic wave phase $\Phi = 0°$ (lower panel), the ZB exciton transition (blue transient) exhibits a $T_\mathrm{SAW}/2$-periodic intensity modulation. As Φ is varied from $\Phi = 0°$ to $270°$ (from lower to upper panel), the temporal delay of the two recombination events (marked by two blue arrows) increases first and becomes maximum at $\Phi = 90°$. Afterwards, the temporal delay decreases, showing again a $T_\mathrm{SAW}/2$-periodic intensity oscillation at $\Phi = 180°$ and, finally, one broad event (marked by green arrow) with a T_SAW-periodic intensity modulation at $\Phi = 270°$.

The indirect ZB/twin transition at single twin defects at 1.488 eV (green transient) exhibits a T_SAW-periodic intensity modulation consisting of two pronounced recombination events marked by black and red arrows in Figure 6.8. Again, these transients clearly show a dependence on the phase Φ. After the initial decay at photoexcitation, the emission of the indirect ZB/twin transition reemerges at $t = 5T_\mathrm{SAW}/4$ (black arrow) for all surface acoustic wave phases and becomes more pronounced as the phase is tuned from $\Phi = 0°$ to $270°$. The second recombination event is observed at $t = 8.3\,\mathrm{ns}$ (red arrow) which is reduced in the emission intensity compared to the previous event for the phases $\Phi = 0°$ and $90°$. As the phase of the surface acoustic wave is tuned from $\Phi = 0°$ to $270°$, the overall emission intensity of both emission events increases with the emission intensity of the second event at $t = 8.3\,\mathrm{ns}$ exceeding that of the first event for the phases $\Phi = 180°$ and $270°$. Furthermore, this increased emission intensity at $t = 8.3\,\mathrm{ns}$ gradually decreases compared to the first event with each acoustic period until a steady state is reached at which both features have approximately the same intensity.

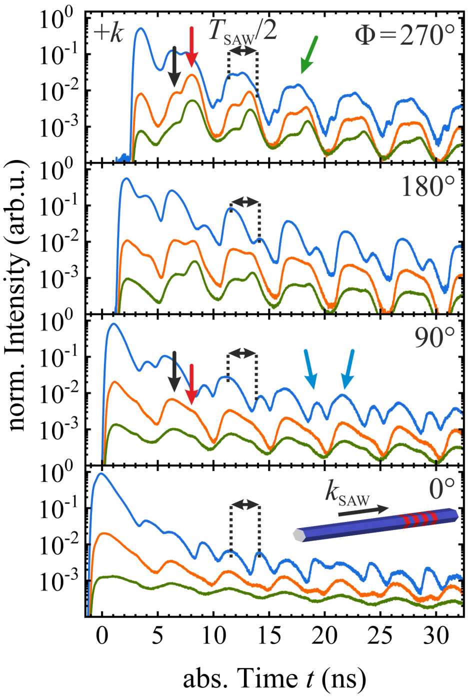

Figure 6.8: Time-resolved photoluminescence emission spectra of the free ZB (blue), the indirect ZB/twin (green) and the indirect WZ/ZB/WZ (orange) exciton transitions of NW8 for $+k$-propagating surface acoustic wave and different surface acoustic wave phases Φ. Traces are offset vertically for clarity. Blue and green arrows mark key characteristics of the intensity modulation of the free ZB transition. Red and black arrows indicate the distinct features of both indirect transients. All recombination events are marked by correspondingly colored, dashed ellipses in our calculations of $n \cdot p$ in Figure 6.9.

The emission of WZ/ZB/WZ transition (orange transient) exhibits an intensity modulation which is similar to the ZB/twin transition (green). This is expected as both are spatially indirect transitions and predominantly located in the same region of the nanowire. The observed slight differences may arise from the electron confinement in the short zincblende segments within the highly mixed WZ/ZB/WZ region which should result in electron levels located at higher energies in the zincblende crystal phase of such stacking fault. As a consequence, the electrons would be weakly bound leading to slightly different electron dynamics due to an increased electron activation from the stacking faults.

These key characteristics observed in the intensity modulations of each transient are well reproduced by our numerical modeling described in Section 6.4.1: in Figure 6.9, the spatio-temporal dynamics of the two carrier species as well as the product of the electron and hole distribution $n \cdot p$ are presented for the electric field at photo-excitation being orientated parallel and antiparallel to the propagation direction of the surface acoustic wave ($\Phi = 90°$ and $\Phi = 270°$). The spatio-temporal dynamics of both carrier species are plotted in false-color representation [n (orange), p (blue)] as a function of Δt (horizontal axis) and position (vertical axis) in Figure 6.9 (a) for $\Phi = 90°$ and $270°$. For both surface acoustic

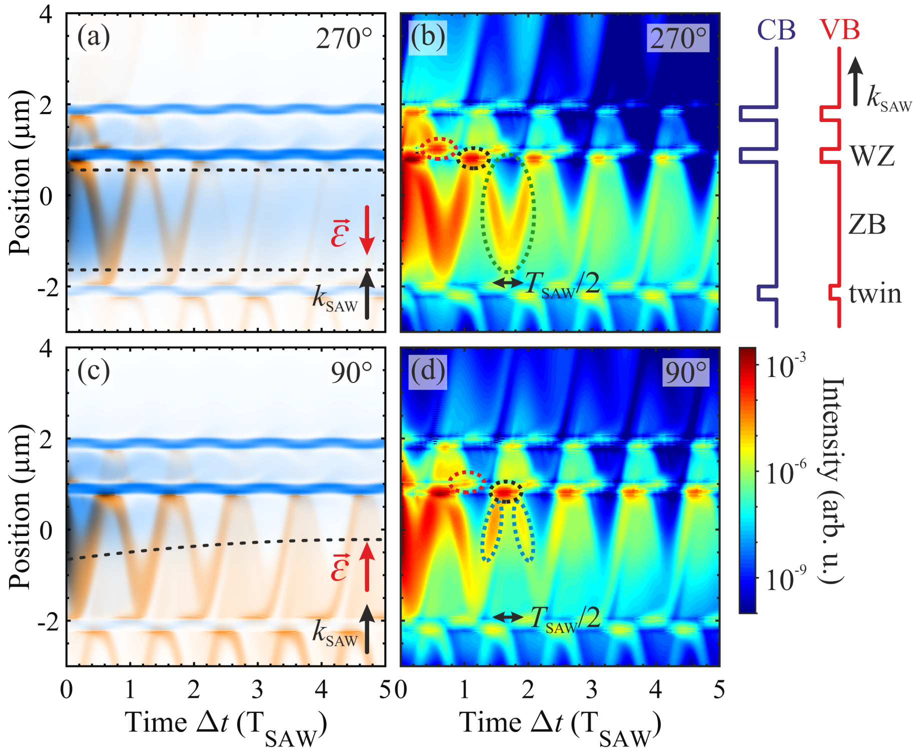

Figure 6.9: (a) Calculated electron (orange) and hole (blue) dynamics and (b) the product of electron and hole distribution of a Type-1 nanowire as a function of time and position for $+k$-propagating surface acoustic wave and surface acoustic wave phases $\Phi = 270^\circ$ and $\Phi = 90^\circ$. Charge carrier generation occurs at $x = 0$. Black dotted lines indicate the hole distribution in the zincblende part of the nanowire as a guide to the eye in (a). Right panel: Schematic of the corresponding band edge modulation of one twin and two wurtzite segments within a zincblende nanowire. Blue and green dotted ellipses in left panels of (b) highlight the change of the intensity modulation of the free zincblende transition (marked by blue and green arrows in Figure 6.8). Red and black dotted ellipses in (b) indicate the distinct features of indirect transients marked by corresponding arrows in Figure 6.8.

wave phases, holes (blue) are mostly localized inside the two wurtzite segments of the upper part of the nanowire and are located in the center zincblende part of the nanowire while only few holes are localized in the lower twin segment. Moreover, electrons (orange) are found in between the two upper wurtzite segments and in the overall lower zincblende region of the nanowire. As time progresses, electrons and holes are driven by the electric field of the surface acoustic wave, which results in sinusoidal trajectories. In general, these trajectories are smeared out in space and time for holes due to their lower mobility. In addition, most electrons in the lower zincblende region of the nanowire are periodically accelerated towards the upper wurtzite segments from which they are mainly reflected. As a fraction of the electrons can overcome these barriers, they can be transferred into the region between the two wurtzite-segments. Similar to our experimental data, the simulation results clearly reflect the initial transport of holes. The acceleration of hole concentration (blue) at photoexcitation occurs predominantly in the center part of the nanowire either away from ($\Phi = 270°$, upper panel of Figure 6.9 (a)) or towards ($\Phi = 90°$, lower panel of Figure 6.9 (a)) the lower wurtzite segment due to the orientation of the electric field. These distinct starting conditions lead either to an accumulation of holes near the region with the high stacking fault density or to their delocalization in the predominantly center zincblende region (apart from hole trapping in wurtzite segments). The hole distributions in the zincblende region are indicated by black dotted lines in Figure 6.9 as a guide to the eye.

Next, the product of the electron and hole distribution $n \cdot p$ is analyzed in Figure 6.9 (b). First, the modulation of the ZB exciton transition (blue transient) can be attributed to the charge carrier dynamics occurring in the center zincblende part of the nanowire. For $\Phi = 90°$ (parallel orientation), $n \cdot p$ exhibits two distinct maxima per acoustic cycle in the zincblende part which are marked by two blue dashed ellipses in the lower panel of Figure 6.9 (b). These maxima are located close to the interface between the center zincblende part and the lower wurtzite segment. As can be seen in the lower panel of Figure 6.9 (a), these maxima arise from the recombination of the oscillating electrons in the center zincblende region (orange) and the hole concentration (blue) which is accumulated in the center zincblende region near the lower wurtzite segment. In our experimental data in Figure 6.8, we can identify these recombination channels as two distinct peaks in the time-delayed emission signal, which are marked by blue arrows. In contrast, for $\Phi = 270°$ (antiparallel orientation), our calculations show an extended domain of large $n \cdot p$ marked by the green dashed ellipse in the upper panel of Figure 6.9 (b). Here, the oscillating electrons remain within the delocalized hole concentration as they are accelerated away from the lower wurtzite segment. Since $n \cdot p$ remains high over an extended time interval, the experimental data in Figure 6.8 show an extended, T_{SAW}-periodic plateau which is marked by the green arrow. Note, for the phases $\Phi = 0°$ and $\Phi = 180°$, the electric field is orientated perpendicular to the nanowire resulting in a reduced axial acceleration of holes in the zincblende phase at photoexcitation. Hence, holes in the center zincblende phase predominantly remain stationary at the point of generation for $\Phi = 0°$ or dissociate only partially from the point of generation for $\Phi = 180°$. Consequently, this results in a similar, yet not so efficiently transported hole distribution as obtained for the phase $\Phi = 90°$ and, thus again, in two recombination events per cycle which are also observed in our experimental data.

Second, the modulations of both indirect exciton transitions of NW8 (orange and green transients) are mostly governed by the charge carrier dynamics in the region with high stacking fault density which is modeled by the two upper wurtzite segments in our calculations. For both/all surface acoustic wave phases, $n \cdot p$ exhibits two distinct intensity maxima per acoustic cycle which are located at lower and upper interface of each wurtzite segment and are marked by red and black dashed ellipses in Figure 6.9 (b). Both maxima result from the recombination of holes trapped at wurtzite segments and electrons, which are accelerated in the respective directions towards the defects and are attributed to the two recombination events being highlighted by red and black arrows in the experimental data Figure in 6.8. Note, the quenching of the intensity modulation of the indirect exciton transitions each period is assigned to the acceleration of electrons towards the lower zincblende region of the nanowire, thus, partially removing the electrons from the region with the stacking faults. Moreover, the emission intensity clearly depends on the orientation of electric field at the time of laser excitation programming the electron concentration within the wurtzite segments. For $\Phi = 270°$ (upper panel in Figure 6.9 (a)), electrons are initially injected into the region with in the wurtzite segments leading to an increased electron concentration within the region of stacking faults compared to the phase $\Phi = 90°$ (lower panel in Figure 6.9 (a)). This gives rise to an increase of the intensity maxima of $n \cdot p$ which are located at the upper interfaces of the wurtzite segments (marked by red dashed ellipses) resulting from the acceleration of electrons towards the lower zincblende part of the nanowire. For $\Phi = 270°$, these intensity maxima are increased compared to the maxima of the following surface acoustic wave cycle which are located at the lower interfaces (black dashed ellipses), and which is clearly contrary to the case for $\Phi = 90°$. For $\Phi = 90°$, the intensity maxima at the upper interfaces are clearly reduced compared to the maxima of the next surface acoustic wave cycle located at the lower interfaces. This behavior is associated with the experimentally observed increase of the emission intensity at $t = 8.3\,\mathrm{ns}$ for $\Phi = 270°$ (red arrows in Figure 6.8). Note that $n \cdot p$ shows similar emission intensity at the lower twin segment for both phases which we assume to have a reduced impact on the modulation of both indirect exciton transitions of the NW8.

When changing the propagation direction to $-k$, the modulations of all transitions show marked differences compared to the previous case. The experimentally observed time transients of three transitions (ZB: blue, ZB/twin: green, WZ/ZB/WZ: orange) are depicted for different surface acoustic wave phases Φ and the $-k$-propagation direction in Figure 6.10. The ZB exciton transition still exhibits a T_{SAW}-periodic intensity modulation with two recombination events per surface acoustic wave cycle for which the temporal delay of the two recombination events varies in time as Φ is tuned. Yet, this temporal delay is reduced compared to the data observed for the $+k$-propagating surface acoustic waves. Moreover, both indirect exciton transitions exhibit a T_{SAW}-periodic modulation with two major recombination events varying in intensity (marked by black and red arrows). In contrast to $+k$-propagating surface acoustic waves, an increase of the intensity of the first recombination event compared to the second one is observed for the phase of $\Phi = 90°$ (black arrow). Moreover, for the phase of $\Phi = 90°$, the first event gradually decreases with each surface acoustic wave period (marked orange arrow) until a steady state is reached at which this event is lower in intensity compared to the following second event.

Again, these experimental observations are nicely reproduced by our numerical calculations for the surface acoustic wave propagating in $-k$-direction which is shown in Figure 6.11. The dynamics of n and p are analyzed in Figure 6.11 (a) for $\Phi = 90°$ and $270°$. Analogous to the $+k$-propagating surface acoustic wave, holes (blue) are predominantly localized inside the two upper wurtzite segments and in the center zincblende region of the nanowire near the two upper wurtzite segments while electrons (orange) oscillate in between the three segments for both surface acoustic wave phases. In particular, the electrons oscil-

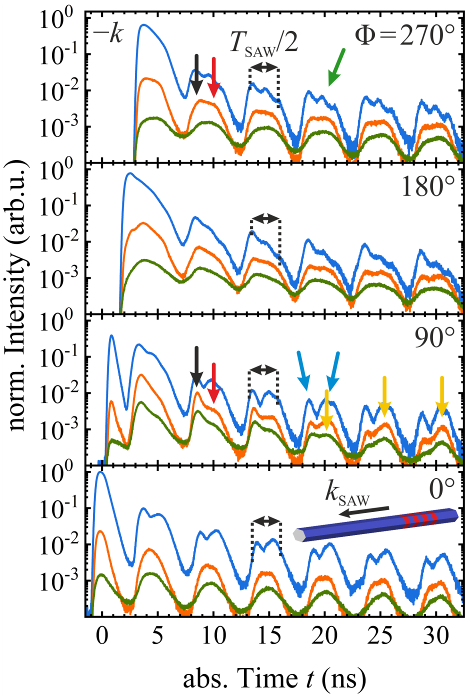

Figure 6.10: Time-resolved photoluminescence emission spectra of the free ZB (blue), the indirect ZB/twin (green) and the indirect WZ/ZB/WZ (orange) exciton transitions of NW8 for $-k$- propagating surface acoustic wave and different surface acoustic wave phases Φ. Traces are offset vertically for clarity. Blue and green arrows mark key characteristics of the intensity modulation of the free ZB transition. Red, black and orange arrows indicate the distinct features of both indirect transients. All recombination events are marked by correspondingly colored, dashed ellipses in our calculations of $n \cdot p$ in Figure 6.11.

lating in the lower part of the nanowire exhibit a net motion in the $-x$-direction and, thus, away from the quasi-stationary holes. However, some electrons are reflected by the lower twin barrier reducing the overall net motion and trapping oscillating electrons in the center region near both upper segments.

Also for the $-k$-propagating surface acoustic wave, the modulation of the ZB exciton transition (blue transient) results from precisely these charge carrier dynamics occurring in center zincblende part of the nanowire. For $\Phi = 90°$, $n \cdot p$ exhibits two recombination events per surface acoustic wave cycle in the center zincblende region, which are marked by two blue dashed ellipses in lower panel of Figure 6.11 (b). These maxima are located in between the lower twin segment and the lower wurtzite segment and arise from the recombination of the oscillating electrons in the center zincblende region (orange) and the hole concentration (blue) which are delocalized in the center zincblende region. Both maxima are identified in our experimental data in Figure 6.10 as two peaks in time-delayed emission signal, which are marked by blue arrows. For $\Phi = 270°$, our calculation of $n \cdot p$ shows a single recombination maximum per acoustic cycle near the lower wurtzite segment which is marked by the green dashed ellipse in upper panel of Figure 6.11 (b). Here, the oscillating electrons recombine within the hole concentration located near the lower wurtzite

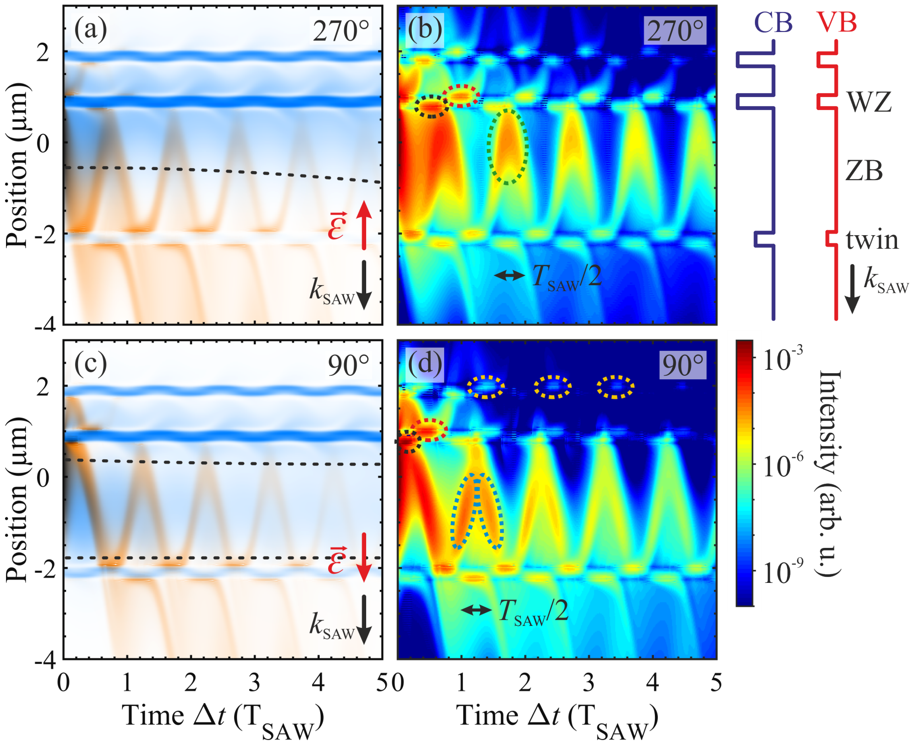

Figure 6.11: (a) Calculated electron (orange) and hole (blue) dynamics and (b) the product of electron and hole distribution of a Type-1 nanowire as a function of time and position for $-k$-propagating surface acoustic wave and surface acoustic wave phases $\Phi = 270°$ and $\Phi = 90°$. Charge carrier generation occurs at $x = 0$. Black dotted lines indicate the hole distribution in the zincblende part of the nanowire as a guide to the eye in (a). Right panel: Schematic of the corresponding band edge modulation of one twin and two wurtzite segments within a zincblende nanowire. Blue and green dotted ellipses in left panels of (b) highlight the change of the intensity modulation of the free zincblende transition (marked by blue and green arrows in Figure 6.10). Red, black and orange dotted ellipses in (b) indicate the distinct features of indirect transients marked by corresponding arrows in Figure 6.10.

segment as they are accelerated towards the upper region. Hence, the experimental data in Figure 6.10 show a T_{SAW}-periodic reemergence which is marked by the green arrow. The indirect exciton recombination occurs again at the upper and lower interfaces of each wurtzite segment, as shown by intensity maxima at both interfaces in our calculation of $n \cdot p$ (marked by black and red ellipses). Both maxima are associated to the two recombination events which are highlighted by red and black arrows in the experimental data shown in Figure 6.10. Similar to the $+k$-propagating surface acoustic wave, the intensity of each event depends on carrier concentration programmed at the photo-excitation. For $\Phi = 90°$, electrons are accelerated and injected into the stacking fault region shortly after photo-excitation. In our calculations of $n \cdot p$ (lower panel of Figure 6.11 (b)), a high density of electrons gives rise to an increased formation and recombination of indirect excitons (black dashed ellipse) when electrons are pushed to the barriers in the direction towards high stacking fault density. This effect increases also the electron concentration within the upper wurtzite segments and is assigned to the pronounced maximum in the experimental data marked black arrow in Figure 6.10. As time progresses, less electrons are injected into the highly polytypic regions per acoustic cycle as the population decays. Hence, at longer timescales, only electrons already trapped within the stacking faults contribute to the observed dynamics and our calculation of $n \cdot p$ shows a long persisting reemergence of the recombination at the upper interface of the upper wurtzite segment (marked by orange dashed ellipses in the lower panel of Figure 6.11 (b)). Similarly, the experimental data in Figure 6.10 exhibit a long persisting reemergence of the second event which is marked by orange arrows and assigned to this persisting recombination at the upper interface. For $\Phi = 270°$, the first recombination event in the experimental data (black arrow) is less pronounced since most electrons are transported away from the stacking fault region by the $-k$-propagating surface acoustic wave directly after photo excitation and the recombination events mainly result from electrons trapped within the stacking faults.

Taken together, our analyses unambiguously resolve signatures of coupled carrier dynamics triggering an exchange between different regions within NW8 (Type-1 nanowire). In particular, nanowires exhibiting a variation from a near-pristine zincblende crystal structure to a highly mixed crystal phase, show a clear dependence of the intensity modulations on the propagation direction of the acoustic wave and the studied recombination channel. In addition, the intensity modulations of the same recombination channel clearly change when the surface acoustic wave phase Φ is tuned demonstrating that the orientation of electric field at the position of the laser spot at the time of the laser excitation programs the subsequent surface acoustic wave-driven carrier dynamics [167, 168].

6.4.3 Charge carrier dynamics in Type-2 polytypic nanowires

Next, the acoustically driven dynamics of NW9 are analyzed for both surface acoustic wave propagation directions. The measured transients of the free ZB (blue), the indirect ZB/twin (green) and the indirect twin/ZB/twin (orange) exciton transitions are depicted in Figure 6.12 (a) and (b) for $+k$- and $-k$-propagating surface acoustic waves, respectively. Again, all transitions of NW9 exhibit characteristic intensity modulations, which are − in strong contrast to NW8 − almost identical for both propagation directions.

The ZB transition exhibits two distinct recombination events per acoustic period for all phases and is almost identical for both propagation directions. In general, the intensity of the first event of each cycle clearly exceeds the corresponding second event for all phases and the temporal delay between both events oscillates as the phase is tuned, being maximum at $\Phi = 90°$ (exhibiting a $T_{\mathrm{SAW}}/2$-periodic intensity modulation) and minimum at $\Phi = 270°$.

The ZB/twin transient features also two dominant recombination events (marked by red and black arrows) per acoustic cycle which are less pronounced compared to events of the ZB/twin transient of NW8. Moreover, the intensities of both events strongly depend on phase and only weakly on the propagation direction of the surface acoustic wave. For $+k$-propagating surface acoustic waves (Figure 6.12 (a)) and $\Phi = 90°$, the second event

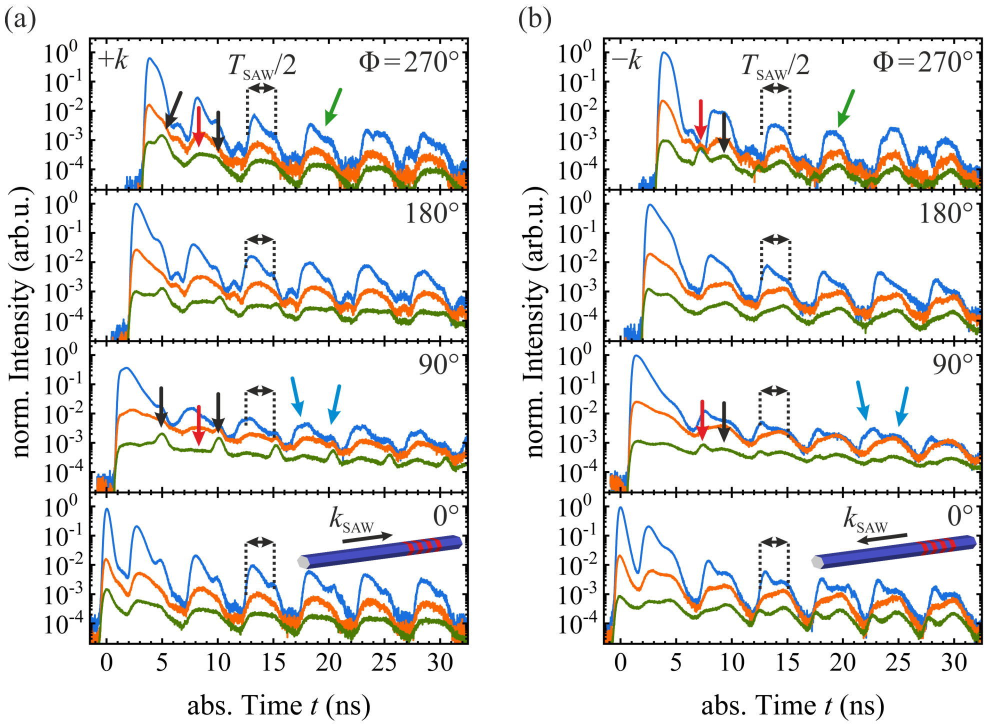

Figure 6.12: Time-resolved photoluminescence emission spectra of the free ZB (blue), the indirect ZB/twin (green) and the indirect twin/ZB/twin (orange) exciton transitions of NW9 for (a) $+k$- and (b) $-k$-propagating surface acoustic wave and for different surface acoustic wave phases Φ. Traces are offset vertically for clarity. Blue and green arrows mark key characteristics of the intensity modulation of the free ZB transition. Black and red arrows indicate the distinct features of both indirect transients. All recombination events are marked by correspondingly colored, dashed ellipses in our calculations of $n \cdot p$ in Figure 6.13 and 6.14, respectively.

(marked by black arrow) is slightly more pronounced and persists over long timescales. In contrast, the intensity of this second event strongly reduces with each period of the surface acoustic wave for $\Phi = 270°$. For $-k$-propagating surface acoustic waves (Figure 6.12 (b)), the first event (marked by red arrow) is slightly more pronounced and persists over long timescales for $\Phi = 90°$ and $\Phi = 270°$. The indirect twin/ZB/twin (orange) exciton transition exhibits similar, yet less pronounced intensity modulations as the ZB/twin exciton transition with both recombination events. Such behavior may be attributed to the reduced oscillatory motion of electrons within the shorter zincblende segments as well as to the reduced activation energy of electrons due to quantum confinement, or may also result from the increase of the density of short segments towards the upper end of the nanowire.

Again, the key characteristics of intensity modulations of NW9 are reproduced by numerical calculations and can be understood by considering the initial distributions of holes (blue) at the time of photoexcitation and the sinusoidal trajectories of the electrons (orange). The results are shown in Figure 6.13 and 6.14 for $+k$- and $-k$-propagating surface acoustic waves, respectively. For both surface acoustic wave directions and all phases

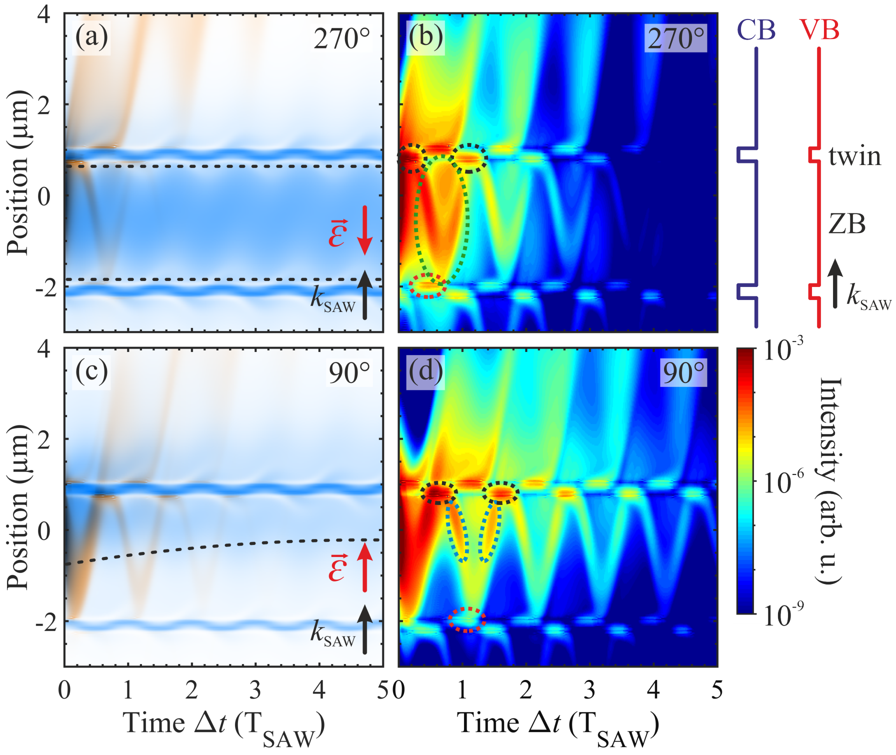

Figure 6.13: (a) Calculated electron (orange) and hole (blue) dynamics and (b) the product of electron and hole distribution of Type-2 nanowire as a function of time and position for $+k$-propagating surface acoustic wave and surface acoustic wave phases $\Phi = 270°$ and $\Phi = 90°$. Charge carrier generation occurs at $x = 0$. Black dotted lines indicate the hole distribution in the zincblende part of the nanowire as a guide to the eye in (a). Right panel: Schematic of the corresponding band edge modulation of two twin segments within a zincblende nanowire. Blue and green dotted ellipses in left panels of (b) highlight the change of the intensity modulation of the free zincblende transition (marked by blue and green arrows in Figure 6.12 (a)). Black, and red dotted ellipses in (b) indicate the distinct features of indirect transients marked by corresponding arrows in Figure 6.12 (a).

(Figure 6.13 (a) and Figure 6.14 (a)), holes are mainly found inside the two twin segments with a higher concentration in the upper twin segment and in the center zincblende region between both segments, while electrons mainly oscillate in between the two twin segments where they are retained. This behavior is in strong contrast to the results on Type-1 nanowires (NW8), showing a net directional transport of electrons for the surface acoustic wave propagating towards the zincblende region in the lower part of the nanowire. For Type-2 nanowires (NW9), both twin segments (in the lower and in the upper part of the nanowire) form barriers from which electrons are reflected giving rise to the cyclic motion which is mainly restricted to the center part of the nanowire and, thus, is almost independent on the propagation direction of the surface acoustic wave. As a consequence, the ZB transition shows almost identical modulations for $+k$- and $-k$-propagating surface acoustic waves. The observed differences of the ZB transients can be attributed to the initial conditions set by Φ.

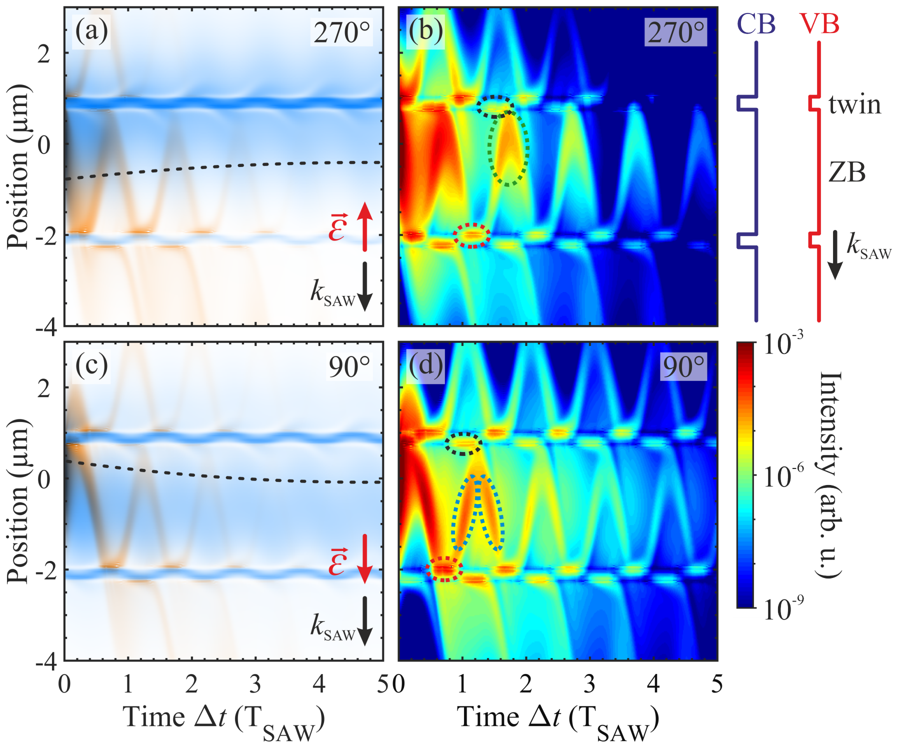

Figure 6.14: (a) Calculated electron (orange) and hole (blue) dynamics and (b) the product of electron and hole distribution of Type-2 nanowire as a function of time and position for $-k$-propagating surface acoustic wave and surface acoustic wave phases $\Phi = 270°$ and $\Phi = 90°$. Charge carrier generation occurs at $x = 0$. Black dotted lines indicate the hole distribution in the zincblende part of the nanowire as a guide to the eye in (a). Right panel: Schematic of the corresponding band edge modulation of two twin segments within a zincblende nanowire. Blue and green dotted ellipses in left panels of (b) highlight the change of the intensity modulation of the free zincblende transition (marked by blue and green arrows in Figure 6.12 (b)). Black, and red dotted ellipses in (b) indicate the distinct features of indirect transients marked by corresponding arrows in Figure 6.12 (b).

For $+k$-propagating surface acoustic waves, the propagation direction and the effective transport are orientated towards the upper twin segment. For $\Phi = 90°$, the initial transport of holes occurs towards the upper twin segment leading to the accumulation of the hole concentration in the center zincblende region near this upper segment (lower panel in Figure 6.13 (a)). As a consequence, the oscillating electrons recombine with quasi-stationary holes two times per acoustic cycle and our calculations show two distinct maxima in $n \cdot p$ per period in the zincblende part between both twin segments which are highlighted by two blue dashed ellipses in lower panel of Figure 6.13 (b). This behavior is attributed to the observed intensity modulation of the ZB transient in the experimental data (marked by two blue arrows in Figure 6.12 (a)). In contrast, for $\Phi = 270°$, the electric field at photo-excitation accelerates holes towards the lower twin segment resulting in the delocalization of the hole concentration between both twin defects (upper panel of Figure 6.13 (a)). Consequently, the electrons, oscillating in the zincblende region between the two twin segments, remain within the delocalized hole concentration and $n \cdot p$ exhibits a continuous domain of large intensity with an increased initial intensity (marked by the green dashed ellipse in the upper panel of Figure 6.13 (b)). In our experimental data in Figure 6.12 (a), this recombination can be identified as temporally reduced reemergence of the intensity of the ZB transient (marked by a green arrow) showing also an increased initial intensity in the time-delayed emission signal.

When reversing the surface acoustic wave propagation direction to $-k$-direction, the effective transport of charge carriers occurs towards the lower twin segment, and the dynamics of the oscillating electrons are reversed. For $\Phi = 90°$, the efficient transport of charge carriers in $-k$-direction gives rise to a holes distribution between the twin defects which is predominantly located near the lower twin segment (lower panel of Figure 6.14 (a)). Again, $n \cdot p$ shows two maxima per surface acoustic wave period near the interface of lower twin segments (highlighted by blue dashed ellipses in the lower panel of Figure 6.14 (b)). These events are again attributed to the two recombination events of the ZB exciton transition (highlighted by blue arrows in Figure 6.12 (b)). When changing the phase to $\Phi = 270°$ (upper panel in Figure 6.14 (a)), holes are accumulated near the upper twin segment which is located opposite to the propagation direction. As electrons are efficiently transported into $-k$-direction, this results in a reduced temporal overlap of electron and hole concentration and, hence, in a single recombination event in our calculation of $n \cdot p$ (marked by green dashed ellipse in the upper panel of Figure 6.14 (b)). Since $n \cdot p$ remains high over a distinct time interval, a T_{SAW}-periodic intensity modulation is observed in the ZB transient which is marked by the green arrow in Figure 6.12 (b).

The two dominant recombination events of the experimentally observed indirect ZB/twin exciton transition can be assigned to recombination of electrons and holes occurring at both interfaces of each segment. At each interface, $n \cdot p$ (Figure 6.13 (b) and Figure 6.14 (b)) exhibits one distinct maximum per surface acoustic wave cycle, which is highlighted by red and black dashed ellipses, respectively. Obviously, the recombination event occurring at the interface of the defect located in propagation direction is slightly more pronounced in our calculations of $n \cdot p$ compared to the corresponding second event of the same acoustic cycle (marked by black dashed ellipse in Figure 6.13 and red dashed ellipse in Figure 6.14). This behavior mainly results from the more efficient transport of electrons in the propagation direction of the surface acoustic wave and may lead to the weak dependence of the propagation direction on the experimentally observed indirect transients.

Taken together, NW9 (Type-2 nanowire) also shows clear characteristics of coupled carrier dynamics between the different emission bands which strongly depend on the orientation of electric field at photo-excitation. Moreover, no pronounced directionality is found for such nanowire with an extended near-pristine zincblende segment which is in strong contrast to nanowires of Type-1.

6.5 Higher-order time correlations

Higher-order correlation measurements allow to directly probe the temporal interdependencies between the different emission bands observed in the studied nanowires. In the following, we perform high-dimensional acousto-optoelectric correlation spectroscopy to resolve full correlations for the identification of interconnected activation and relaxation between the different emission bands which are driven by a surface acoustic wave. Thus, we are able to directly and simultaneously observe coupled carrier dynamics in polytypic nanowires.

6.5.1 Second-order time correlation of Type-1 and Type-2 nanowires

In the first step, we investigate the second-order intensity correlations between the three transitions of both dynamically driven nanowire systems, NW8 and NW9. To this end, the second-order correlation functions $g_{ij}^{(2)}(t_{ij})$ as defined by (Equation 6.1), are calculated between events of two transitions i,j for both propagation directions of surface acoustic waves with $i = 1, 2, 3$ corresponding to the ZB, ZB/twin and WZ/ZB/WZ (twin/ZB/twin) transitions of NW8 (NW9), respectively. Here, t_{21}, t_{31} and t_{32} are the time differences between the indirect ZB/twin–ZB, WZ/ZB/WZ–ZB and WZ/ZB/WZ–ZB/twin transitions for NW8 and the indirect ZB/twin–ZB, twin/ZB/twin–ZB and twin/ZB/twin–ZB/twin transitions for NW9.

The recorded $g_{ij}^{(2)}(t_{ij})$ data of the surface acoustic wave-driven, coupled carrier dynamics of NW8 are shown as a function of Φ in false-color representation in Figure 6.15 (a) and (b) for $+k$- and $-k$-propagation direction of the surface acoustic wave, respectively. The data is normalized to corresponding maximal intensity. In addition, the orientation of electric field $\boldsymbol{\mathcal{E}}$ at the time of photoexcitation with respect to the nanowire axis is depicted on the right. Obviously, the measured correlations between the two indirect transitions $g_{32}^{(2)}$ (WZ/ZB/WZ–ZB/twin, right panels) significantly differ from those obtained by correlation of each indirect transitions with the ZB emission $g_{i1}^{(2)}$ (left and center panels). As the phase Φ is varied, we resolve clear surface acoustic wave induced T_{SAW}-periodic and phase dependent modulations with characteristic fingerprints for both propagation directions in all $g_{ij}^{(2)}(t_{ij})$ data. These modulations in all $g_{ij}^{(2)}(t_{ij})$ data can be understood by considering the initial distributions of electrons and holes at the time of photoexcitation.

We begin our evaluation for the surface acoustic wave propagating in $+k$-direction (Figure 6.15 (a)) towards the highly disordered region at the upper region of NW8 consisting there of extended wurtzite and zincblende segments. First, the correlation between the two indirect transitions $g_{32}^{(2)}(t_{32})$ shows clear T_{SAW}-periodic intensity oscillations, $g_{32}^{(2)}(t_{32} = n \cdot T_{SAW})$, with n being integer. These oscillations confirm that the two indirect transitions are coupled and occur at the same time or at integer multiples of T_{SAW} for each surface acoustic wave phase. This is due to the fact that for both types of indirect transitions, holes are captured either within single twin plane defects or wurtzite segments which are predominantly located in the same region at the top of the nanowire.

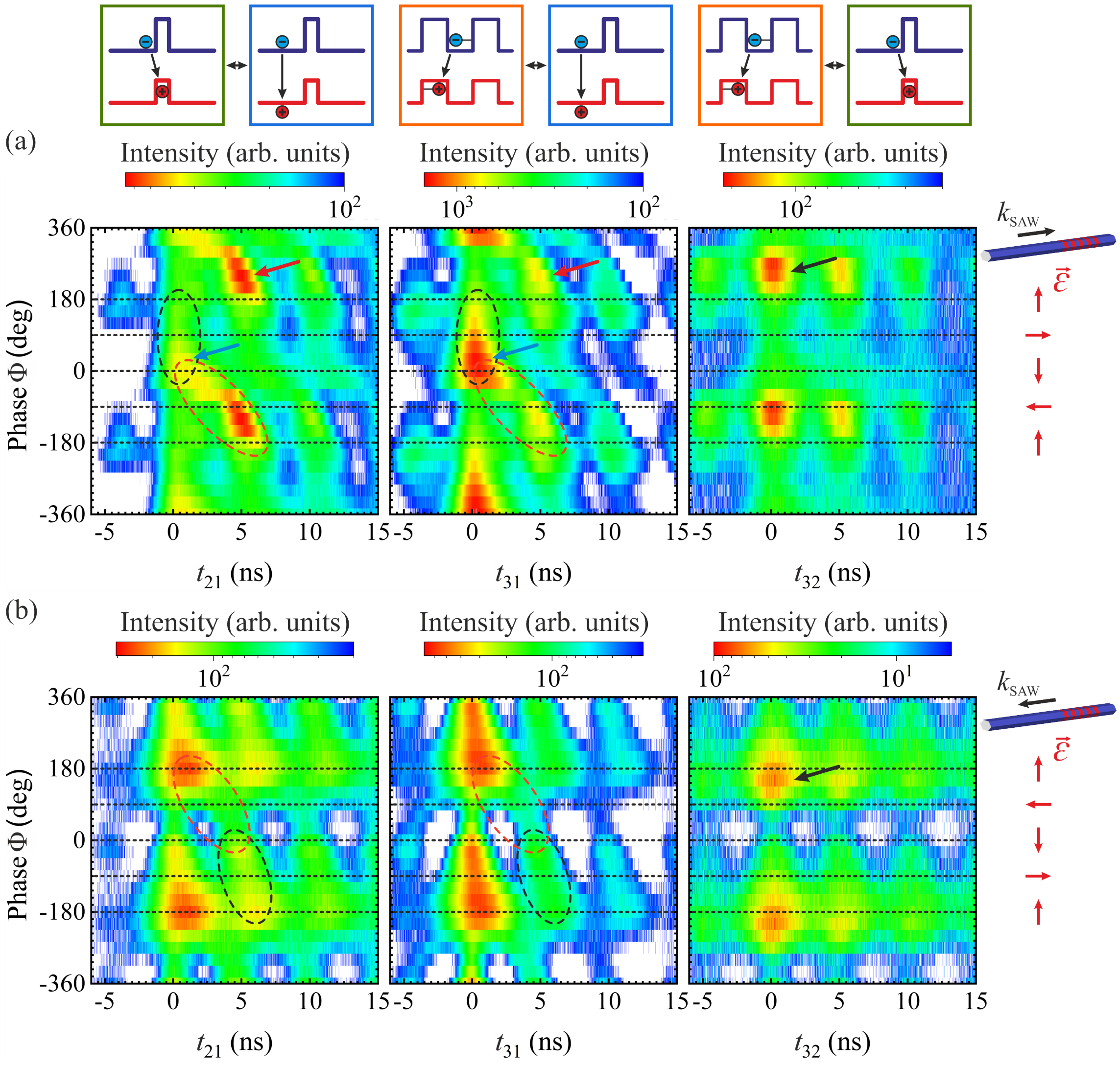

Figure 6.15: 2-channel correlation spectroscopy - $g^{(2)}_{i,j}(t_{ij})$ of the indirect ZB/twin exciton - ZB exciton ($i, j = 2, 1$, left panels), the indirect WZ/ZB/WZ exciton - ZB exciton ($i, j = 3, 1$, center panels) and indirect WZ/ZB/WZ exciton - ZB/twin exciton ($i, j = 3, 2$, right panels) as a function of the phase Φ for (a) $+k$- and (b) $-k$-propagation direction of the surface acoustic wave. The electric field orientation at photoexcitation is shown on the right. Characteristic correlation features are highlighted by arrows and ellipses.

Electrons, in contrast, are accelerated along the nanowire by the electric field and periodically shuffled back and forth to the region with high rotational twin density (ZB/twin) and the highly disordered wurtzite/zincblende region (WZ/ZB/WZ). As a result, holes contributing to each indirect transition recombine almost simultaneously with the oscillating electrons giving rise to the T_{SAW}-periodic intensity oscillations of $g_{32}^{(2)}(t_{32})$. Furthermore, the T_{SAW}-periodic oscillations exhibit a maximum intensity at $\Phi = 270°$ (marked by black arrow). At this phase, electrons are accelerated at the time of photoexcitation towards the highly mixed region and are captured within both types of stacking faults. As a consequence, this efficient capture probability increases the simultaneous recombination via both indirect transitions at the same time and, thus, favors an increase of $g_{32}^{(2)}(t_{32})$.
In contrast, both correlations $g_{i1}^{(2)}$ (left and center panel) show that both indirect transitions are temporally delayed to the ZB emission at distinct surface acoustic wave phases. As holes in the zincblende phase are more mobile, the distribution of the hole concentration within the pure zincblende region of the nanowire is determined by the orientation of the electric field at photoexcitation (cf. Section 6.4.2). For phases ranging between $\Phi = 0°$ and 180°, holes are accelerated towards the region with a high stacking fault density at the top of the nanowire by the axial component of the electric field at photoexcitation. Thus, the hole concentration within the zincblende part is accumulated near the region with the high stacking fault density as schematically depicted in the band diagram in Figure 6.16 (a). As the surface acoustic wave propagates, electrons are shuffled back and forth along the nanowire axis and recombine almost simultaneously with holes in the zincblende part near the highly disordered region or in the region with a high twin density (ZB/twin) and extended wurtzite segments (WZ/ZB/WZ), respectively. Hence, the correlations $g_{i1}^{(2)}$ (left and center panel) also show that each indirect and the direct transition occur at the

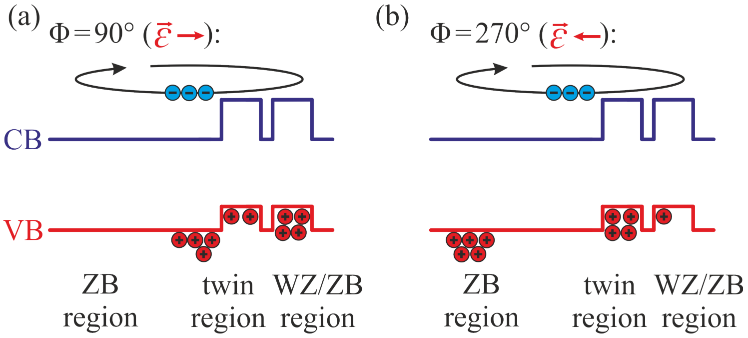

Figure 6.16: Schematic illustration of the hole distribution in NW8 programmed by the orientation of the electric field of a surface acoustic wave at the photo-excitation. (a) For $\Phi = 90°$, holes in the zincblende region are accumulated near the region with high stacking fault density. Moreover, the electric field orientation at photo-excitation gives rise to an increase of the hole density in the highly mixed wurtzite/zincblende region while the hole density is reduced at rotational twin defects. (b) For $\Phi = 270°$, the hole distribution in the zincblende region separated from the holes within the region with high stacking fault density and the hole density at rotational twin defects is increased compared to the hole density reduced in the highly mixed wurtzite/zincblende region.

same time or at integer multiples of T_{SAW}, marked by black dashed ellipses. For phases between $\Phi = 180°$ and $360°$, the electric field component parallel to the nanowire axis is pointing towards the pure zincblende region being maximum at $\Phi = 270°$. This results in an acceleration of the photogenerated holes towards the zincblende part of the nanowire. Consequently, holes in the zincblende part are separated from holes trapped within both types of stacking faults which is schematically shown in the band diagram in Figure 6.16 (b). Hence, for these phases, electrons oscillate back and forth between holes in the zincblende part and holes within the region with high stacking fault density. The electron dynamics lead to a temporal delayed emission of the direct and both indirect transitions. The magnitude of the electric field component parallel to the nanowire axis decreases for phases $\Phi > 270°$. Thus, the spatial separation of holes in the zincblende part and holes trapped within the region with high stacking fault density reduces. Consequently, the temporal delay between the direct and both indirect transitions reduces as well, which manifests itself in a clear shift of the $g_{i1}^{(2)}$ peaks marked by red dashed ellipses. Moreover, both correlations $g_{i1}^{(2)}$ exhibit a high intensity at $\Phi \approx 270°$ marked by red arrows. As discussed in the context of $g_{32}^{(2)}$, the electron density is increased within the stacking faults because at the time of photoexcitation the electric field is oriented in the opposite direction. This in turn results in an increased recombination rate of both indirect transitions. In addition, we first find that $g_{31}^{(2)}(t_{31})$ is maximum for Φ ranging between $0°$ and $180°$ and $t_{31} = 0$, (marked by blue arrows), In contrast, $g_{21}^{(2)}(t_{21})$ is maximum for Φ ranging between $180°$ and $360°$ and time differences of $0 < t_{21} < T_{\mathrm{SAW}}$, marked by red arrows. Both observations can be well understood by again considering the electric field component parallel to the nanowire axis: in the first case, holes are transferred along the nanowire from the region with high rotational twin density (ZB/twin) to the highly disordered region (WZ/ZB/WZ) when the electric field is orientated towards the highly mixed region at the time of photoexcitation. Hence, the hole density with the stacking faults is increased in the highly mixed region (WZ/ZB/WZ transitions) and lowered in region with high rotational twin density (ZB/twin transitions) as illustrated in the band diagram in Figure 6.16 (a). In the second case, the electric field is orientated towards the region with high rotational twin density. This gives rise to an increase of the hole density at rotational twin defects while the hole density is reduced in the highly wurtzite/zincblende mixed region (band diagram in Figure 6.16 (b)).

When reversing the direction to $-k$-propagation of the surface acoustic wave shown in Figure 6.15 (b), we find that the $g_{32}^{(2)}(t_{32})$ data in the right panel are strikingly similar to those for the $+k$-propagating surface acoustic waves in Figure 6.15 (a). This is expected because the underlying shuffling electron dynamics within the stacking fault region remain mostly unaffected and, thus, do the resulting correlations. In contrast, the $g_{21}^{(2)}$ and $g_{31}^{(2)}$ correlations shown in the left and center panels are reversed because the sense of the gyration of the electric field vector is reversed (cf. schematics on the right). For the phase between $\Phi = 180°$ and $360°$, the electric field points towards the stacking faults at the time of photoexcitation resulting in the accumulation of holes in the zincblende region near the region with the high stacking fault density. Thus, the indirect exciton transitions

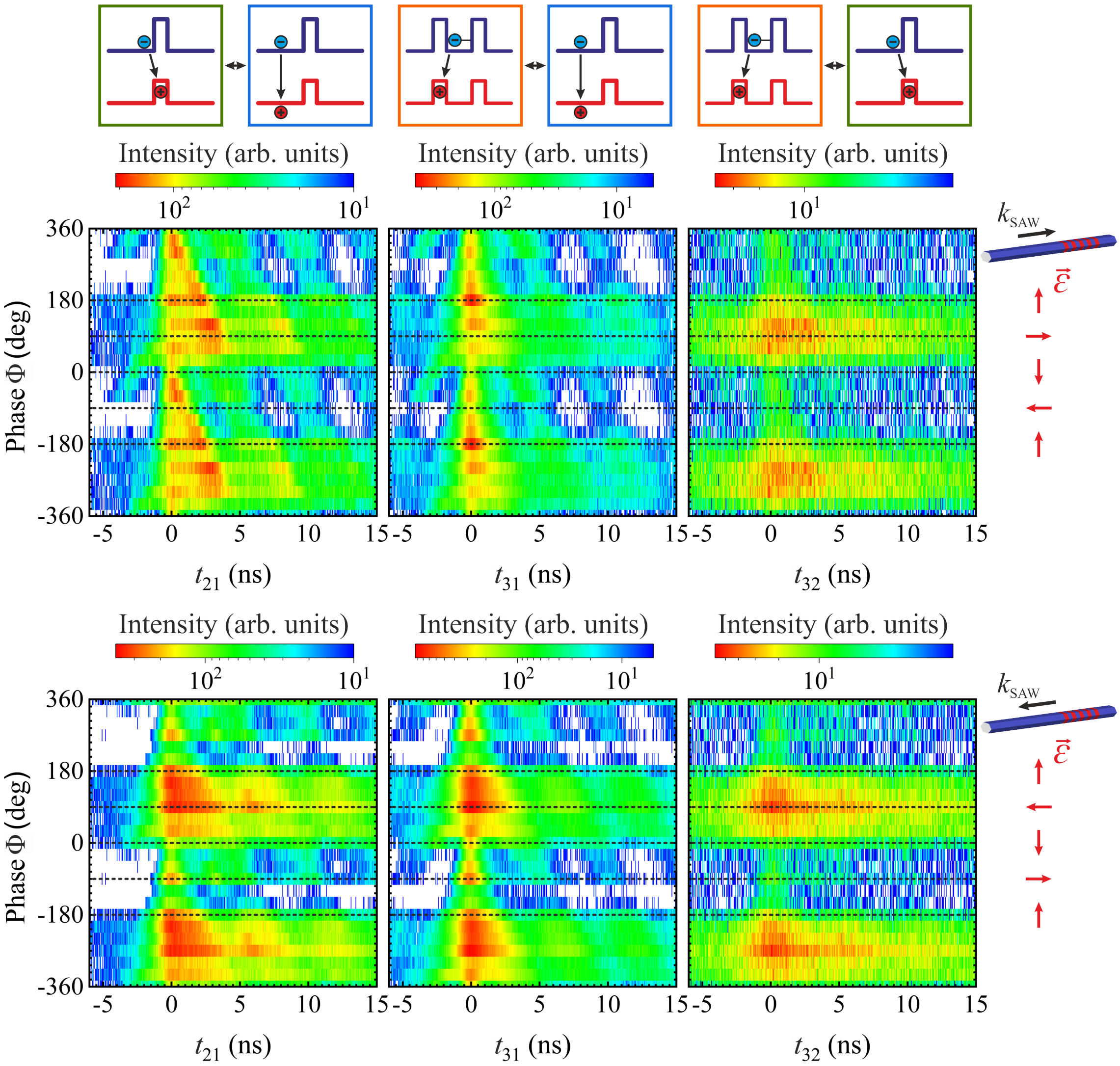

Figure 6.17: 2-channel correlation spectroscopy - $g^{(2)}_{i,j}(t_{ij})$ of the indirect ZB/twin exciton - ZB exciton ($i, j = 2, 1$, left panels), the indirect twin/ZB/twin exciton - ZB exciton ($i, j = 3, 1$, center panels) and indirect twin/ZB/twin exciton - ZB/twin exciton ($i, j = 3, 2$, right panels) as a function of the phase Φ for (a) $+k$- and (b) $-k$-propagation direction of the surface acoustic wave. The electric field orientation at photoexcitation is shown on the right.

and the free exciton transitions occur almost simultaneously (or at integer multiples of T_{SAW}) as marked by black dashed ellipses. Moreover, for phases from $\Phi = 0°$ to $180°$, the delay between recombination events in this setting shifts from T_{SAW} to 0 as marked by red dashed ellipses. This inverse behavior in contrast to the $+k$-propagation, since here the axial electric field component pointing to the left accelerates electrons in the opposite direction towards the highly mixed region. Moreover, slight differences of this inverse behavior result from the net transport of charge carriers which occurs away from the highly mixed region.

Next, we present analogous correlation data of the surface acoustic wave-driven, coupled carrier dynamics from NW9. The recorded correlations $g^{(2)}_{ij}(t_{ij})$ are presented as a function of Φ in false-color representation in Figure 6.17 (a) and (b) for $+k$- and $-k$-propagating of the surface acoustic wave, respectively. Again, all $g^{(2)}_{ij}(t_{ij})$ data show phase dependent modulations which are characteristic for Type-2 nanowires and can be understood by considering the initial distributions of electrons and holes at the time of photoexcitation. In strong contrast to NW8, they show almost identical modulation for both propagation directions and each individual decay channel. This is expected as Type-2 nanowires exhibit a more homogeneous distribution of trapping sites along the nanowire axis compared to Type-1 nanowires.

First, the correlations between both indirect transitions $g^{(2)}_{32}(t_{32})$ (right panels) show that both transitions occur predominately over all times for phases from $\Phi = 0°$ to $180°$ and both propagation directions decaying slowly for $t_{32} > 0$. For phases between $\Phi = 180°$ and $360°$, the correlations show a weak signal at $t_{32} = 0$ while almost no signal is observed for $t_{32} > 0$. This is expected as the homogeneous distribution of trapping sites results in equal distribution of long and short zincblende segments. Consequently, both, ZB/twin and twin/ZB/twin, excitons can recombine all over the nanowire axis and, thus, simultaneously and at all times of the surface acoustic wave cycle, respectively.

In addition, both correlations $g^{(2)}_{i1}$ (left and center panel) reveal that both indirect transitions occur predominantly simultaneously to the ZB emission. Similar to $g^{(2)}_{32}(t_{32})$, the correlation intensity of all $g^{(2)}_{i1}$ is high for the phases $\Phi = 0°$ to $180°$ and weak for phases between $\Phi = 180°$ and $360°$. This behavior arises from the more efficient exciton dissociation at the surface acoustic wave phase of $\Phi = 270°$ accelerating electrons in propagation direction of the surface acoustic wave at the photoexcitation. Moreover, all correlations $g^{(2)}_{i1}$ vary considerably, yet weakly pronounced with the surface acoustic wave phase showing it is sensitive to band edge modulation induced by the surface acoustic wave at the time of photoexcitation.

6.5.2 Third-order time correlation

Finally, we determine the third-order intensity correlations $g^{(3)}_{1,2,3}(t_{21}, t_{31})$ of all three transitions of NW8 as defined by (Equation 6.2). Here, t_{21} and t_{31} are the time differences between a detection of the first photon of the ZB transition and the detection of a photon of the indirect ZB/twin and WZ/ZB/WZ recombination, respectively. In the following,

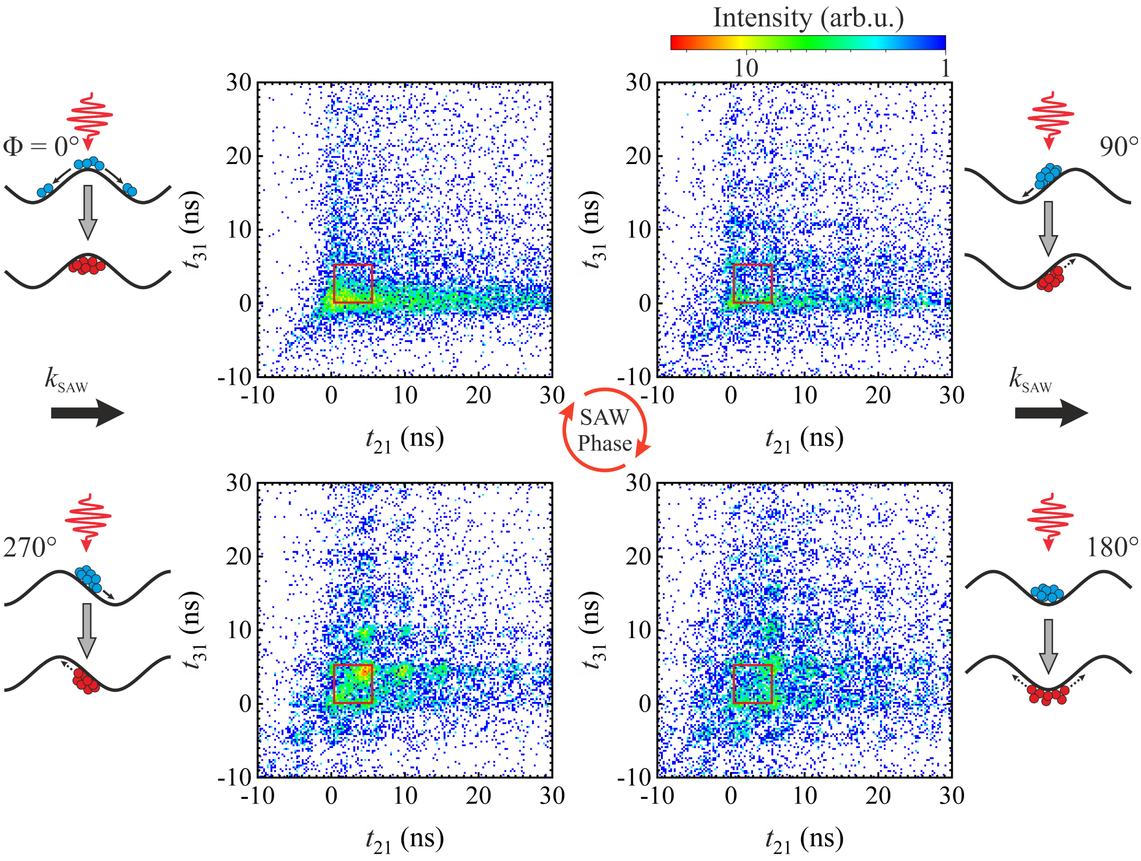

Figure 6.18: 3-channel correlation spectroscopy - $g^{(3)}_{1,2,3}(t_{21}, t_{31})$ of all three recombination channels for four characteristic values of Φ for a $+k$-propagating surface acoustic wave (color scale applies to all panels). The band edge modulation by the surface acoustic wave is shown as schematics. The red square marks T_{SAW} setting the period of the observed oscillations.

we restrict ourselves to one surface acoustic wave propagation direction, a $+k$-propagating surface acoustic wave to highlight our key findings. Note that for NW9 intensity of the third-order correlation is not sufficient enough to be significant.

In Figure 6.18, we plot the obtained $g^{(3)}_{1,2,3}$ color-coded as a function of t_{21} and t_{31} for four characteristic phases Φ of a $+k$-propagating surface acoustic wave. The respective excitation conditions are shown as schematics next to each data panel. All four data sets reveal T_{SAW}-periodic modulations in t_{21} and t_{31}. The red square marks T_{SAW} setting the period of the observed oscillations. The observation of these modulations is a distinct and characteristic fingerprint of a surface acoustic wave-induced charge carrier transport. Furthermore, the measured correlations strongly depend on Φ. At $\Phi = 0°$, holes are generated in a stable maximum of the valence band while electrons are generated in an unstable maximum of the conduction band. Consequently, electrons rapidly redistribute towards their adjacent stable minima along the nanowire axis while the less mobile holes remain predominantly at the point of photogeneration [28]. Thus, the three-photon correlations predominantly occur at $t_{21} = t_{31} = 0$. For $t_{31} = 0$, the signal decays slowly for $t_{21} > 0$. This is consistent with the two-photon correlation data in Figure 6.15 (a) where a strong signal is observed for $g_{31}^{(2)}(t_{31} = 0)$ because holes remain strongly localized in the region with high stacking fault density. In addition, no pronounced T_{SAW}-periodic oscillations are observed in the data being consistent with the symmetric distribution of electrons immediately after photogeneration. When tuning the phase to $\Phi = 180°$, the band edge modulation at the time of photoexcitation is reversed. Now, holes redistribute slowly in both directions while electrons are created at a stable minimum in the conduction band. Albeit being less efficient, the sketched symmetric spatial redistribution of holes leads to a pronounced T_{SAW}-periodic modulation in both t_{21} and t_{31} because this transfer is symmetric in both directions. Thus, holes are trapped in twin defects on the left and in wurtzite segments on the right. As electrons are shuffled back and forth to the region with high rotational twin density (ZB/twin) and region with extended wurtzite segments (WZ/ZB/WZ), recombination via the two channels is modulated with T_{SAW}. At $\Phi = 90°$ and $\Phi = 270°$, the axial electric field amplitude is maximum and oriented parallel or antiparallel to the wavevector of the surface acoustic wave, respectively. As a consequence, electrons are accelerated in opposite directions away from ($\Phi = 90°$) and towards ($\Phi = 270°$) the region with high stacking fault density. These different initial conditions have pronounced impact on the $g_{31}^{(2)}$ data. For $\Phi = 90°$, when electrons are first transported away from the WZ/ZB/WZ segments, three-photon coincidences are found at $t_{21} = t_{31} = 0$, analogous to the considerations made for $\Phi = 0°$. However, for $\Phi = 90°$, the motion of the electrons occurs only in one direction. This different initial condition preserves the timing precision of the surface acoustic wave-driven electron motion for $t_{21}, t_{31} > 0$. Therefore, the T_{SAW}-periodic modulation pattern is also preserved. For $\Phi = 270°$, electrons are accelerated towards the highly mixed region on the top of the nanowire. There, they are reflected by the energy barriers in the conduction band at the interface between zincblende and wurtzite GaAs. Thus, all indirect transitions are delayed by T_{SAW} compared to the predominant ZB-emission at $t = 0$. Hence, we expect that the maximum of three-photon coincidences occurs at $t_{21} = t_{31} = T_{\mathrm{SAW}}$, which is precisely observed in the experimental data.

6.6 Conclusion

In summary, we studied the coupled carrier dynamics in different types of polytypic GaAs nanowires in the limit of low carrier concentrations. The dynamics are driven by a $\approx 200\,\mathrm{MHz}$ piezoelectric surface acoustic wave and detected on the underlying timescales with sub-nanosecond time resolution. Therefore, we conducted a comprehensive study on exemplary polytypic GaAs nanowires employing structural characterization by transmission electron microscopy as well as optical and high-dimensional acousto-optoelectric correlation spectroscopy. To this end, we implemented a fully-fledged combination of three-channel cross-correlation and acousto-optoelectric spectroscopy allowing to simultaneously record the surface acoustic wave-induced modulations of up to three different emission channels. In particular, these data can be analyzed individually in a single channel analysis, but most importantly, as all channels are recorded simultaneously, second- and third-order correlations $g_{ij}^{(2)}(t_{ij})$ and $g_{1,2,3}^{(3)}(t_{21}, t_{31})$ can be faithfully determined from the data.

The analyses unambiguously resolve signatures of coupled carrier dynamics and carrier transport within the nanowire which are set by the distribution of wurtzite and twin defects. In our transmission electron microscopy analysis and scanning photoluminescence spectroscopy, we identify two families of nanowires with different degrees of polytypism. The first Type-1 exhibits two different regions along the nanowire axis, a near-pristine zincblende region and a highly disordered region consisting of extended wurtzite and zincblende segments. In contrast, the second Type-2 is pure zincblende with the twin defect density slightly increasing along the nanowire. Hence, both types of nanowires exhibit characteristic recombination channels which are assigned to different types of one spatially direct recombination (electrons and holes within the same crystal segment) and two spatially indirect recombination (electrons and holes localized in different segments). The surface acoustic wave induced suppression of the emission intensity as well as its dynamic temporal modulation show unambiguous fingerprints of the local bandedge variations induced by the crystal phase mixing. In particular, a Type-1 nanowire shows a clear dependence on the propagation direction of the acoustic wave and the studied recombination channel. In contrast, a Type-2 nanowire exhibits almost identical behaviors for both propagation directions and for each individual decay channel. The experimental findings are corroborated by numerical calculations of the surface acoustic wave-driven spatio-temporal carrier dynamics for two very general bandedge modulations of the two types of nanowires. These calculations, which assume either two wurtzite segments and one twin segment or two twin segments at different positions along the nanowire axis, reproduce the most important features found in our experimental observations by using realistic values of the electron and hole transport mobilities and barrier heights. They nicely confirm efficient trapping of holes in wurtzite and twin segments, which leads to long-time persistent storage. Electrons, in contrast, show pronounced dynamics in zincblende parts. Moreover, they show that carrier transport is efficient inside the individual segments. For Type-1 nanowires the presence of higher barriers in one direction leads to a net transport of electrons by a surface acoustic wave propagating towards the part of low stacking fault density. Consequently, the Type-1 nanowire shows a clear dependence of the intensity modulations on the surface acoustic wave propagation direction due to net transport in one direction. For Type-2 nanowires, the presence of lower barriers at both ends of the nanowire results in an oscillatory motion and no directionality is observed in this experiment. Moreover, we observe in our correlation measurements the correlated dynamics stemming from the surface acoustic wave-induced shuttling of electrons between the regions of the different emission bands. Finally, we showed that band edge modulation induced by the surface acoustic wave at the time of photoexcitation programs the subsequent correlated dynamics.

The results clearly show that holes are efficiently trapped in wurtzite segments and that already a low degree of crystal phase mixing may result in an efficient suppression of electron transport at low temperatures. Thus, long range (coherent) electrical transport in nanowires at low carrier concentrations require near-pristine nanowires with vanishing crystal phase mixing. Moreover, we point out that our method can be extended to other types of surface acoustic wave-modulated processes and different material systems [46, 168, 226–238].

Chapter 7

Conclusion and Outlook

Conclusion

In this thesis, we investigated the coupled charge carrier dynamics of type-I and type-II semiconductor nanowire heterostructures under the manipulation of piezoelectric surface acoustic waves. The surface acoustic waves dynamically modulate the optical properties of such nanowire structures via the acousto-electric coupling between the charge carriers and the electric field of the surface acoustic wave leading to characteristic fingerprints in the optical emission properties. These are analyzed by contact-free acousto-optoelectric spectroscopy which allows to detect the surface acoustic wave induced charge carrier dynamics in energy-resolved and time-resolved photoluminescence experiments. Thus, this technique provides distinct insights into the properties and dynamics of semiconductor nanowires with sub-nanosecond time resolution.

First, the structural, optical and electronic properties of a radial quantum well system embedded in a GaAs/$Al_{0.3}Ga_{0.7}As$ core/shell nanowire heterostructure are studied by their dynamic control with a surface acoustic wave. It was shown that small variations of a perfect hexagonal cross-section radial quantum well strongly affect the localization of the charge carrier distribution within the quantum well and, thus, lead to significant changes of the optical and electronic properties. Hence, moderate deformations result in the full localization of charge carriers at the thickest side facets clearly inducing spectral broadening or the formation of spatially separated but interconnected quantum well systems. Moreover, our observations directly prove the coupling and the carrier exchange between such two-dimensional emission channels in the same nanowire based quantum well heterostructure by the gyrating electric field of the surface acoustic wave. In particular, we observed the counterclockwise motion of electron cycloids between two separated, but interconnect quantum well segments being located on neighboring sidewall facets. In addition, by probing these electron cycloids, we gained direct insights into the spin properties of surface acoustic waves and were able to study the transverse spin momentum of the electric field of the surface acoustic wave. The observed spin-momentum locking itself is a universal wave phenomenon in which the direction of spin is locked to the propagation direction of the surface acoustic wave. Hereby, the momentum of the wave, the decay direction, and the spin form a locked triplet. By solving the equations of motion for surface acoustic waves, we showed that the acoustic spin flips within the material and, thus, forms a non-conventional triplet with the momentum of the wave and the decay direction. In contrast, the electromagnetic spin results in the conventional right-handed triplet which flips together with the decay direction.

In the second part of the thesis, the coupled carrier dynamics and carrier transport in different types of polytypic GaAs nanowires were investigated by employing structural characterization by transmission electron microscopy and optical and high-dimensional acousto-optoelectric correlation spectroscopy. In our transmission electron microscopy and scanning photoluminescence spectroscopy analysis, we identified two types of polytypic nanowires with different zincblende and wurtzite crystal phase mixing which induces distinct type-II band edge modulations and, thus, gives rise to three characteristic coupled recombination channels within each nanowire. Nanowires of the first type exhibit a change of the crystal structure from a near-pristine zincblende phase with occasional twin defects to a highly polytypic crystal structure with extended wurtzite and zincblende segments. In contrast, nanowires of the second type have a pure zincblende crystal structure with the twin defect density slightly increasing along the nanowire axis. Thus, the different crystal structures result in the formation of distinct, interconnected decay channels and, consequently, in pronounced differences in their surface acoustic wave-driven, spatio-temporal carrier dynamics for both types of nanowires. In particular, nanowires, which exhibit pronounced variations along their axis, show a clear dependence on the propagation direction of the surface acoustic wave, while no pronounced directionality is found for more homogeneous nanowires. Moreover, we reproduce the most important features in our experimental observations by numerical calculations of the surface acoustic wave-driven charge carrier dynamics using basic models of both types of nanowires. They show efficient trapping of holes in wurtzite and twin segments and pronounced electron dynamics in zincblende parts of the nanowire leading to the surface acoustic wave-triggered carrier exchange between different channels within each nanowire. In addition, we observed in our correlation measurements correlated charge carrier dynamics stemming from the surface acoustic wave-induced shuttling of electrons between the regions of the different emission bands. Finally, we show that band edge modulation induced by the surface acoustic wave at the time of photoexcitation programs the subsequent correlated dynamics.

Outlook

In this work, we investigated the charge carrier dynamics of type-I and type-II semiconductor nanowire heterostructures and correlated these with the structural and electronic properties which play a critical role in further predicting the electronic and optical properties of future nanowire heterostructure based devices. As these spatio-temporal charge carrier dynamics mainly depend on the transport mobility of both carrier species, our acousto-optoelectric spectroscopy provides a direct route to derive the transport mobilities of electrons and holes from a direct comparison between the experimentally observed and numerically calculated electron-hole interband recombination [28, 50]. In addition, surface acoustic wave based optical spectroscopy allows to dynamically tune and investigate the optical and electronic properties of nanostructures by the strain field of a surface acoustic wave [239]. Thus, this technique is ideally suited to study coherently strained (In)GaAs/(In,Ga)AlAs core/shell core-shell nanowires for which epitaxial strain is in-

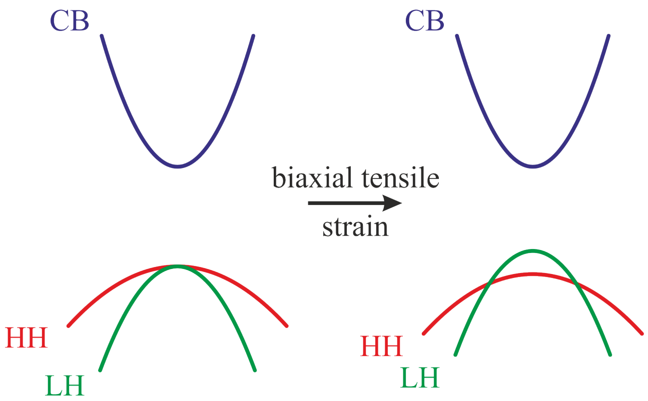

Figure 7.1: Schematic illustration of the effect of biaxial strain on the valance and conduction band states of III-V semiconductors. Under biaxial tensile strain, the light hole state is above the heavy hole state.

tentionally introduced along the radial {110} sidewall facets. Importantly, in strained (In)GaAs/(In,Ga)AlAs core/shell nanowires, biaxial strain can be controlled by the shell thickness and alloy compositions, which, in turn, affect the valence band properties.
Such strain engineering is particularly important for tuning the carrier dynamics of holes via changes of the valence band properties due to strain modification [240] allowing to increase the performance of e.g. planar double heterostructure lasers [241] or p-type field effect transistors [242]. In particular, biaxial tensile strain is known to induce a transition of the valence band ground state from heavy hole (HH) to light hole (LH) character in quantum confined heterostructures as schematically depicted in Figure 7.1. Thus, the light hole state is above the heavy hole state under biaxial tensile strain. This is expected to increase the hole mobility and/or lead to a modification of the density of states. Consequently, this transition can be directly verified by an enhancement of the hole mobility compared to unstrained nanowires in our acousto-optoelectric spectroscopy experiments.

To this end, we explored in a first acousto-optoelectric experiment the impact of strain on as-grown GaAs nanowire cores which are surrounded by lattice-mismatched (In,Ga)AlAs shells. A schematic of the cross-section of the as-grown nanowire core-multishell heterostructure is shown in Figure 7.2 (a). The nanowire structure consists of a GaAs core which is surrounded by a 5 nm AlAs shell which is followed by a 60 nm thick, quaternary $\mathrm{In_{0.3}Al_{0.3}Ga_{0.4}As}$ buffer layer being highly strained to the GaAs core. In addition, this structure is overgrown by an additional 10 nm thick $\mathrm{Al_{0.43}Ga_{0.57}As}$ shell and, finally, by a 5 nm thick GaAs capping layer for passivation.
A typical emission spectrum of an individual nanowire with no surface acoustic wave applied is shown in the limit of low carrier concentrations in Figure 7.2 (b). In this spectrum, we observe a photoluminescence signal centered at $E_{\mathrm{core}} = 1.296\,\mathrm{eV}$ which can be associated to carrier recombination in the highly tensile strained GaAs core of the nanowire [243]. At lower photon energies, the spectrum exhibits a pronounced emission band at an energy of $E_{\mathrm{shell}} = 1.489\,\mathrm{eV}$ which is associated to emission of the quaternary $\mathrm{In_{0.3}Al_{0.3}Ga_{0.4}As}$

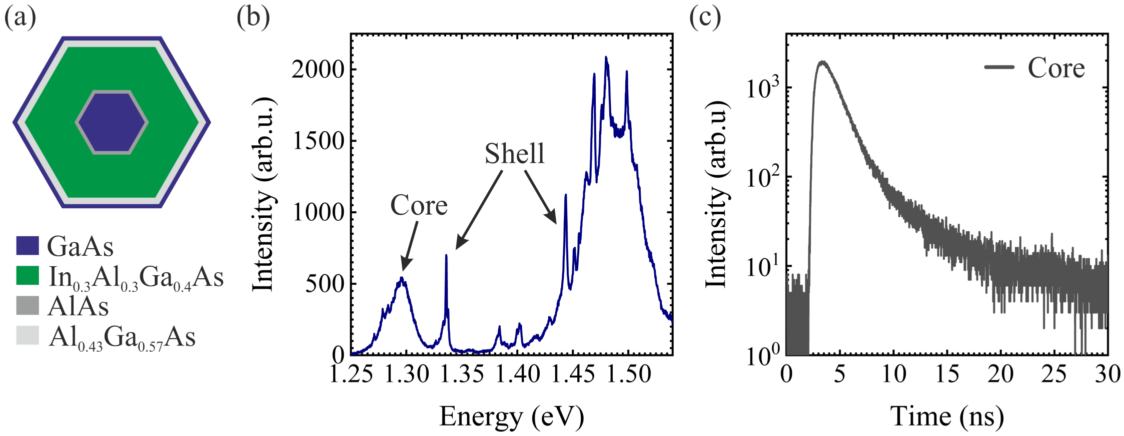

Figure 7.2: (a) Schematic of the nanowire cross-section consisting of GaAs core which is under tensile strain induced by a $In_{0.3}Al_{0.3}Ga_{0.4}As$ buffer layer. (b) Photoluminescence spectrum of a single, strained nanowire. The nanowire shows emission of the GaAs core and the $In_{0.3}Al_{0.3}Ga_{0.4}As$ buffer layer. (c) Corresponding time-resolved photoluminescence emission spectra of the nanowire core.

buffer layer. In addition, we find a series of single sharp lines at energies between 1.30 eV and 1.5 eV. These are attributed to the presence of quantum dot-like single-photon emitters [244], which may arise from randomly distributed alloy fluctuations and defects within the $In_{0.3}Al_{0.3}Ga_{0.4}As$ shell to local segregation effects [39, 48, 119, 121, 244]. To probe the carrier dynamics of the strained GaAs core, we performed the temporally resolved photoluminescence spectroscopy which is depicted in Figure 7.2 (c). Without a surface acoustic wave applied, the transient clearly shows a biexponential decay of the photoluminescence emission with a fast and a slow time constant $\tau_{\text{fast}} = 1.6\,\text{ns}$ and $\tau_{\text{slow}} = 4.9\,\text{ns}$, respectively. In particular, this recombination behavior points to radiative recombination of free excitons and indirect excitons localized at single twin defects [24]. The observed decay times are in good agreement with previous reports for unstrained GaAs nanowire cores [18, 24, 224].

Next, we present first results of the impact of biaxial tensile strain on the acoustically driven carrier dynamics within such a strained GaAs nanowire core. In our acousto-optoelectric spectroscopy measurements, we could identify two families of nanowires which differ in their acoustically driven carrier dynamics, yet show identical emission properties with no surface acoustic wave applied. In particular, while one type shows dynamics which are similar to unstrained GaAs nanowires [28], the second type of nanowires exhibits properties that have not been observed before in GaAs nanowires and which are presented in Figure 7.3. In Figure 7.3 (a), we plot the stroboscopic emission spectra of the tensile strained GaAs core for $P_{\text{rf}} = 13\,\text{dBm}$ and 27 dBm in false-color representation. At low acoustic powers, we observe a clear and pronounced modulation of the emission intensity as we tune the relative Phase Φ_{rel}. This behavior is well known from unstrained GaAs nanowires and arises from the electric field orientation at the moment of excitation [38]. Hence, depending on the electric field direction and strength, the exciton dissociation

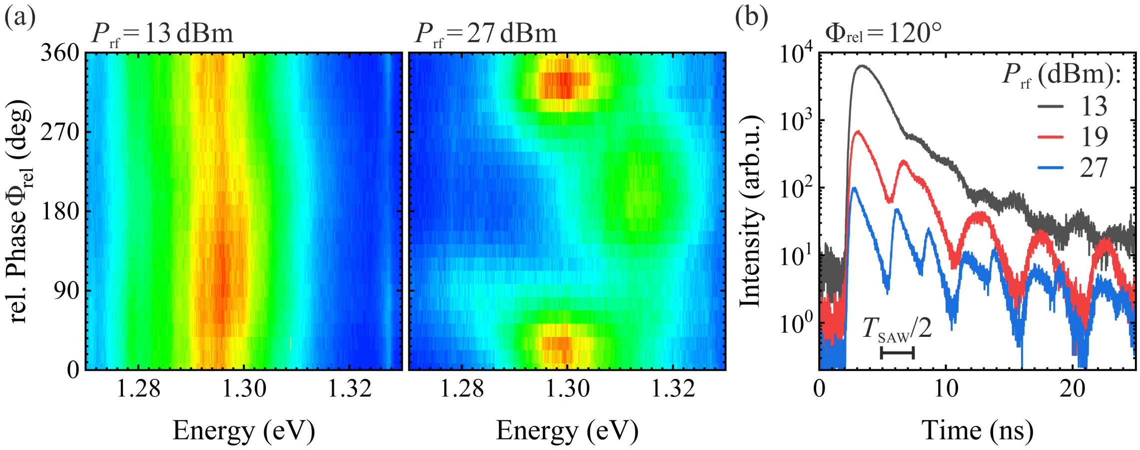

Figure 7.3: (a) Phase-resolved photoluminescence spectra recorded from a tensile strained GaAs nanowire core at different acoustic powers showing spectral intensity oscillations at low acoustic powers and modulation between two emission bands at high acoustic powers due to dynamic tuning by the surface acoustic wave. (b) Time-resolved photoluminescence emission of the strained GaAs core for increasing P_{rf} at a surface acoustic wave phase of $\Phi_{\mathrm{rel}} = 120°$. Traces are offset vertically for clarity. The transients at low and high acoustic powers exhibit a $T_{\mathrm{SAW}}/2$-periodic intensity modulation. At medium powers, the intensity modulation is T_{SAW}-periodic.

is more efficient and, thus, the emission intensity of recombination processes varies with the phase of the surface acoustic wave. Note, such a behavior is also observed at high acoustic powers in unstrained nanowires. For the tensile strained nanowires, however, we resolve at high acoustic powers both pronounced intensity and spectral modulations of the emission peak. In particular, two emission bands at energies of $E_{\mathrm{low}} = 1.299\,\mathrm{eV}$ and $E_{\mathrm{high}} = 1.314\,\mathrm{eV}$ are observed which are blueshifted compared to unperturbed emission at an energy of $E_{\mathrm{shell}} = 1.489\,\mathrm{eV}$ and, most importantly, occur at different phases Φ_{rel} of the acoustic cycle. First, this might indicate band mixing which is induced by the time-dependent coupling between the heavy- and light-hole states in the valence band due to the dynamical strain tuning by the surface acoustic wave [239]. Here, the transition energies vary at the positions of maximum tensile or compressive strain, respectively. Second, it might also result from the carrier injection by the electric field into different emission centers [46] arising from unintentional composition/strain inhomogeneities [245].

Moreover, the time-resolved photoluminescence emission of the strained GaAs core is shown in Figure 7.3 (b) for different P_{rf} and $\Phi_{\mathrm{rel}} = 120°$. Here, the transients of the strain GaAs core exhibit a $T_{\mathrm{SAW}}/2$-periodic intensity modulation at low and high acoustic powers while a T_{SAW}-periodic intensity modulation is observed at medium powers. This, in particular, is contrary to unstrained GaAs nanowires for which a T_{SAW}-periodic intensity modulation was observed as the acoustic power is varied. Hence, the observed T_{SAW}-periodic intensity at medium powers can be attributed to charge carrier dynamics occurring in polytypic nanowires [28]. In contrast, a $T_{\mathrm{SAW}}/2$-periodic intensity modulation is observed, for example, in perovskite nanowires exhibiting similar mobilities of electrons and holes [50]. This might indicate that also these strained nanowires have similar mobilities for electrons and holes which would result from the transition of the valence band ground state from heavy hole to light hole character due to tensile strain.

In conclusion, these tensile strained GaAs nanowires show first indications of a heavy-hole/light-hole ground state transition which have to be further investigated. Finally, strain engineering effects can be transferred to embedded quantum well nanowire heterostructures and 1D-confined, ultra thin nanowire structures allowing to enhance the performance of future nanowire-based nanoelectronic and nanophotonic devices.

Appendix A

Samples

A.1 List of sample names

The following table lists the sample numbers for the samples investigated in this thesis for possible future studies and for easier relocation.

Nanowire Name	Sample Name	Growth ♯
radial quantum well heterostructure		
NW1-NW3	TEM analysis	02-28-11.1
NW4-NW7	JKB156	02-28-11.1
polytypism		
Type-1/Type-2	TEM analysis	02-08-13.1
NW8-NW9	MS1	02-08-13.1
tensile strained		
-	MS2	Epi-994
NW10	MS3	Epi-1008
compressive strained		
-	MS4	Epi-733
-	MS4	Epi-734

Table A.1: List of sample names investigated in the course of this thesis.

A.2 List of growth parameters

The following table lists the sample numbers and the growth conditions for the samples shown in this thesis.

Growth ♯	Substrate	Layer	As BEP (10^{-5} mbar)	Ga flux (Å/s)	Al flux (Å/s)	In flux (Å/s)	Temp. (°C)
02-28-11.1	Si(111)	120 min GaAs core	0.5	0.25	-	-	627
	thermal	30 nm AlGaAs shell	3.7	0.25	0.107	-	492
		5 nm GaAs QW	3.7	0.25	-	-	492
		70 nm AlGaAs shell	3.7	0.25	0.107	-	492
		5 nm GaAs cap	3.7	0.25	-	-	492
02-08-13.1	Si(111)	150 min GaAs core	0.19	0.25	-	-	610
	thermal	30 nm AlGaAs shell	3.5	1.7	0.73	-	490
	with NIL	3 nm GaAs QW	3.5	1.7	-	-	490
		30 nm AlGaAs shell	3.5	1.7	0.73	-	490
		10 nm GaAs cap	3.5	1.7	-	-	490
Epi-994	Si(111)	43 min GaAs core	0.4	0.75	-	-	660
	eSAE	60nm InAlGaAs buffer	4.5	0.4	0.3	0.3	420
		2nm GaAs interlayer	4.5	0.765	-	-	420
		8nm InGaAs QW	4.5	0.765	-	0.135	420
		10 nm GaAs cap	4.5	0.765	-	-	420
Epi-1008	SOI	30 min GaAs core	0.5	1.0	-	-	650
	eSAE	5nm AlAs barrier	4.5	-	0.3	-	420
		60nm InAlGaAs buffer	4.5	0.4	0.3	0.3	420
		10 nm AlGaAs barrier	4.5	0.4	0.3	-	420
		5 nm GaAs cap	4.5	0.4	-	-	420
Epi-733	Si(111)	120 min GaAs core	0.3	0.494	-	-	650
	thermal	35nm AlGaAs shell	3.5	0.63	0.27	-	420
		8 nm GaAs QW	3.5	0.63	-	-	420
		35 nm AlGaAs shell	3.5	0.63	0.27	-	420
		5 nm GaAs cap	3.5	0.63	-	-	420
Epi-734	Si(111)	120 min GaAs core	0.3	0.494	-	-	650
	thermal	35nm AlGaAs shell	3.5	0.63	0.27	-	420
		8 nm InGaAs QW	3.5	0.63	-	0.094	420
		35 nm AlGaAs shell	3.5	0.63	0.27	-	420
		5 nm GaAs cap	3.5	0.63	-	-	420

Table A.2: List of the growth parameters of the nanowires investigated in the course of this thesis.

Appendix B

Parameters for the numerical simulations

B.1 Parameters for the numerical simulation of surface acoustic waves on LiNbO$_3$

The following table lists the basic constants of YZ-LiNbO$_3$.

$\rho\,(\mathrm{kg/m^3})$	4700
$c_{\alpha\beta}\,(10^{10}\mathrm{N/m^2})$	$\begin{pmatrix} 20.3 & 5.3 & 7.5 & 0.9 & 0 & 0 \\ 5.3 & 20.3 & 7.5 & -0.9 & 0 & 0 \\ 7.5 & 7.5 & 24.5 & 0 & 0 & 0 \\ 0.9 & -0.9 & 0 & 6.0 & 0 & 0 \\ 0 & 0 & 0 & 0 & 6.0 & 0.9 \\ 0 & 0 & 0 & 0 & 0.9 & 7.5 \end{pmatrix}$
$e_{\alpha\beta}\,(\mathrm{C/m^2})$	$\begin{pmatrix} 0 & 0 & 0 & 0 & 3.7 & -2.5 \\ -2.5 & 2.5 & 0 & 3.7 & 0 & 0 \\ 0.2 & 0.2 & 1.3 & 0 & 0 & 0 \end{pmatrix}$
$\epsilon_{\alpha\beta}\,(\epsilon_0)$	$\begin{pmatrix} 43.6 & 0 & 0 \\ 0 & 43.6 & 0 \\ 0 & 0 & 29.1 \end{pmatrix}$

Table B.1: List of the density ρ, the elasticity tensor c, the piezoelectric tensor e and the dielectric permittivity ϵ for YZ-LiNbO$_3$.

B.2 Parameters for the numerical simulation of charge carrier dynamics

The following table lists the parameters used for the numerical simulation of the surface acoustic wave-driven charge carrier dynamics in polytypic nanowires.

Sound velocity	3500 m/s
SAW frequency	200 Mhz
Permittivity GaAs	$12.5\cdot\epsilon_0$
Temperature	10 K
Mobilities:	
Electrons	500 cm^2/Vs
Holes	50 cm^2/Vs
Exciton binding energy	5 meV
Exciton radius	10 nm
Exciton generation rate	100 cm^2/s
Direct recombination rate	0.01 cm^2/s
Exciton lifetime	1000 ps
Exciton diffusion constant	2.2 cm^2/s
Spot width	1.5 μm
Number of photons	5
Pulse width	50 ps
Repetition time of laser	$30\cdot T_{\mathrm{SAW}}$
Simulation width	$90\cdot T_{\mathrm{SAW}}$

Table B.2: Complementary list of the parameters used for the numerical simulation of the surface acoustic wave-driven charge carrier dynamics in polytypic nanowires in the course of this thesis.

Appendix C

Additional Data

C.1 Full data set of the electron cycloids in radial nanowire quantum wells

In the main part of this thesis, we present and discuss in context of Section 5.4 the experimental observation of ultrafast electron cycloids for selected delays between the excitation laser pulse and the surface acoustic wave oscillation, $\tau = -T_{\mathrm{SAW}}/6$ to 0. Albeit the observed time transients exhibit unambiguous fingerprints of the cycloidal motion of electrons driven by the surface acoustic wave's transverse spin momentum, a pronounced overall decay is superimposed on these signals. In Figure C.1, we present the full set of raw data from QW1 (red) and QW2 (blue) in which the delay τ is tuned over the full acoustic cycle. Moreover, the derivatives of the complete data as well as the degree of normalized emission intensity defined as $DoEI = (I_{\mathrm{QW1}} - I_{\mathrm{QW2}})/(I_{\mathrm{QW1}} + I_{\mathrm{QW2}})$ are shown in Figure C.2 and Figure C.3. Both are directly derived from the smoothed raw data. Thus, we are able to inject electrons in the system at all characteristic times during the cycle and observed the subsequent electron dynamics at all characteristic times (cf. schematics in the upper part) with high count rates. The data presented here is published in Science Advances under the title "Ultrafast electron cycloids driven by the transverse spin of a surface acoustic wave" [42].

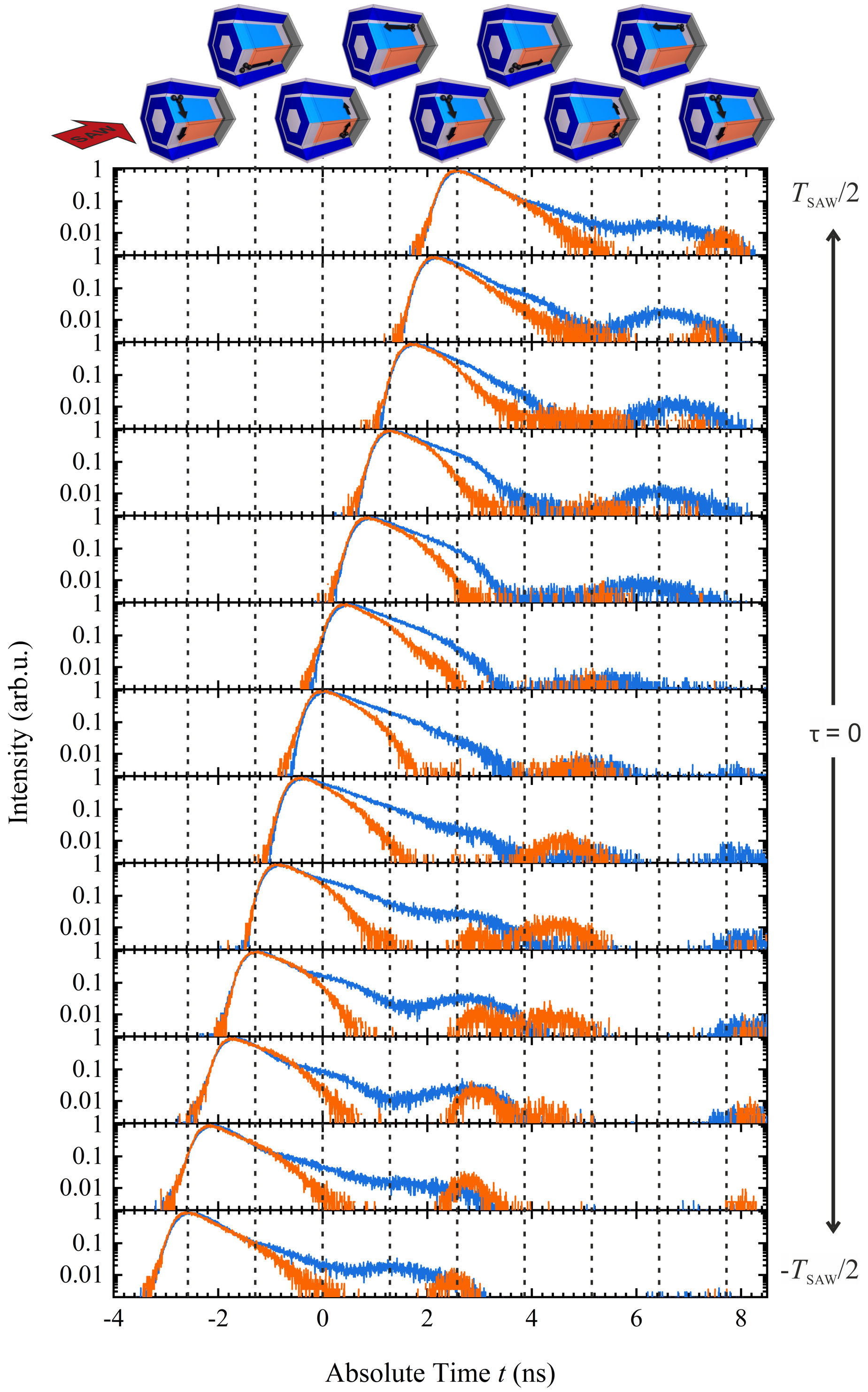

Figure C.1: Time dependent photoluminescence of QW1 (blue) and QW2 (red) as a function of absolute time t for the delay between the laser pulse and acoustic cycle τ. The schematics in the upper parts show the motion of electrons in the tubular quantum well at distinct times during the acoustic cycle.

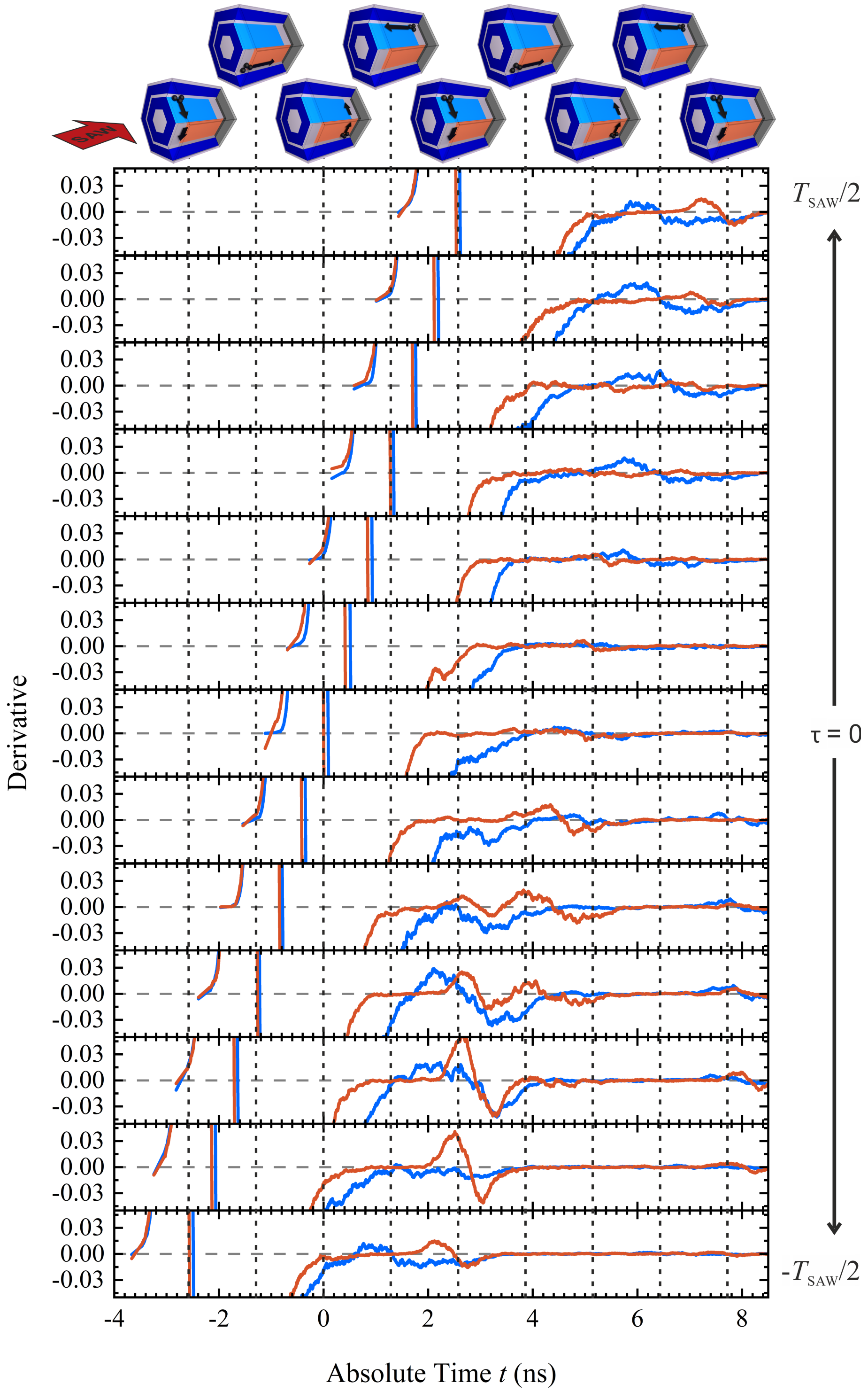

Figure C.2: Derivatives of the time dependent photoluminescence of QW1 (blue) and QW2 (red) as a function of absolute time t for the delay τ between the laser pulse and acoustic cycle. The schematics in the upper parts show the motion of electrons in the tubular quantum well at distinct times during the acoustic cycle.

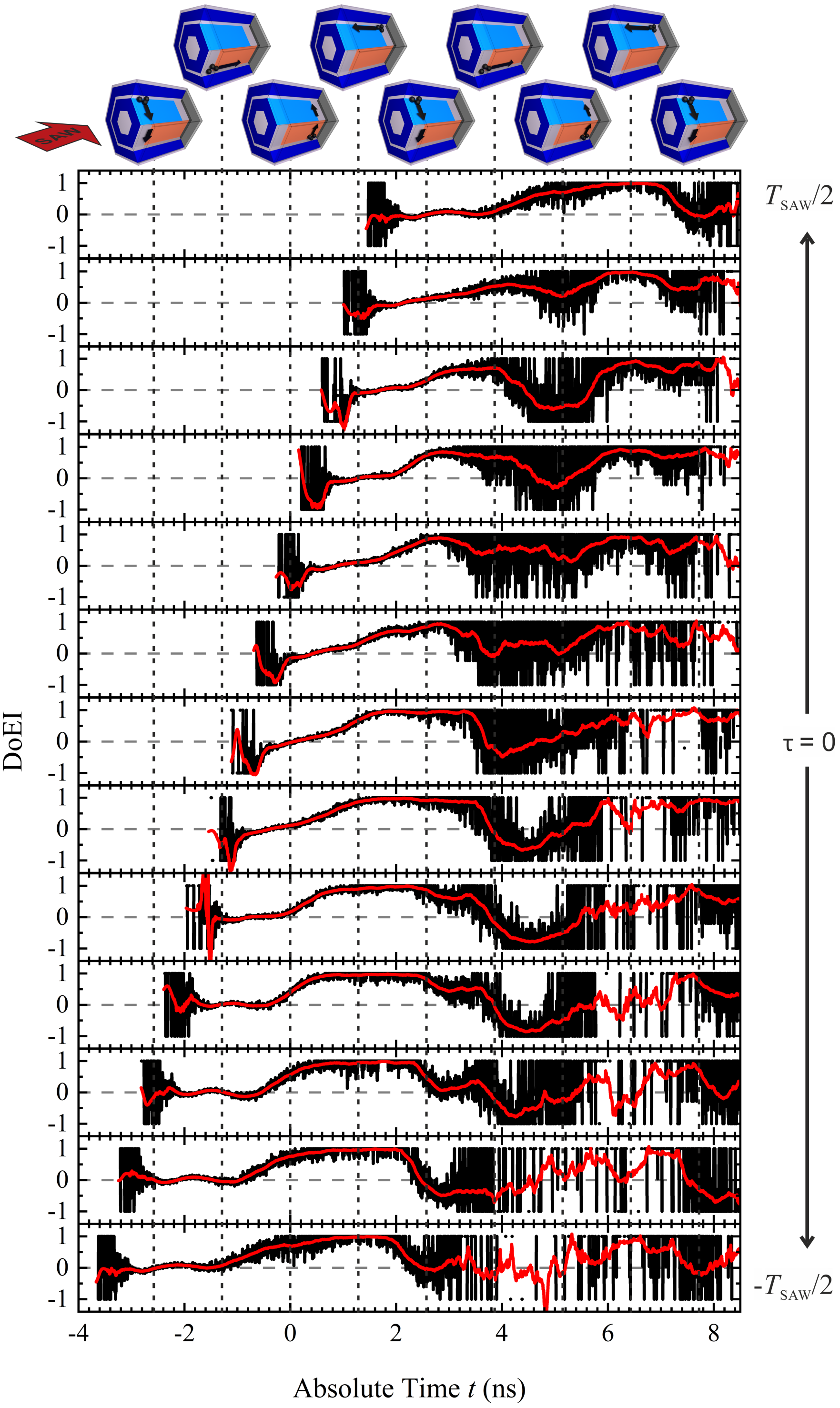

Figure C.3: Degree of normalized emission intensity $DoEI = (I_{\mathrm{QW1}} - I_{\mathrm{QW2}})/(I_{\mathrm{QW1}} + I_{\mathrm{QW2}})$ derived from the time dependent photoluminescence of QW1 and QW2 as a function of absolute time t for the delay τ between the laser pulse and acoustic cycle. The schematics in the upper parts show the motion of electrons in the tubular quantum well at distinct times during the acoustic cycle. The black and red lines are raw and smooth data, respectively.

C.2 Full data set of the single channel time-resolved charge carrier dynamics in polytypic nanowires

In context of Section 6.4, we present and discuss the time-resolved charge carrier dynamics in polytypic nanowires for selected surface acoustic wave phases Φ by performing single channel acousto-optoelectric sprectroscopy. The full sets of the acousto-optoelctric spectroscopy data of each transition of NW8 and NW9 are presented in Figure C.4 and Figure C.5 for $+k$- and $-k$-propagating surface acoustic waves. The corresponding recombination channels are shown as insets. The recorded intensity (normalized to corresponding maximal intensity) is plotted in false-color representation as a function of the phase Φ (vertical axis) and the time after photoexcitation Δt (horizontal axis). On the right, the electric field orientation is shown for different Φ marked by the horizontal dotted black lines in the data panels. As we tune the phase over two full acoustic cycles, we resolve clear surface acoustic wave induced intensity modulations for all three transitions of each nanowire and both directions of the surface acoustic wave. These modulations are characteristic fingerprints of transport of electrons and holes along the nanowire axis which are driven by the oscillating electric field parallel to the nanowire axis. While NW8 shows a clear dependence on the propagation direction of the acoustic wave and the studied recombination channel, NW9 exhibits almost identical behaviors for both propagation directions and for each individual decay channel.

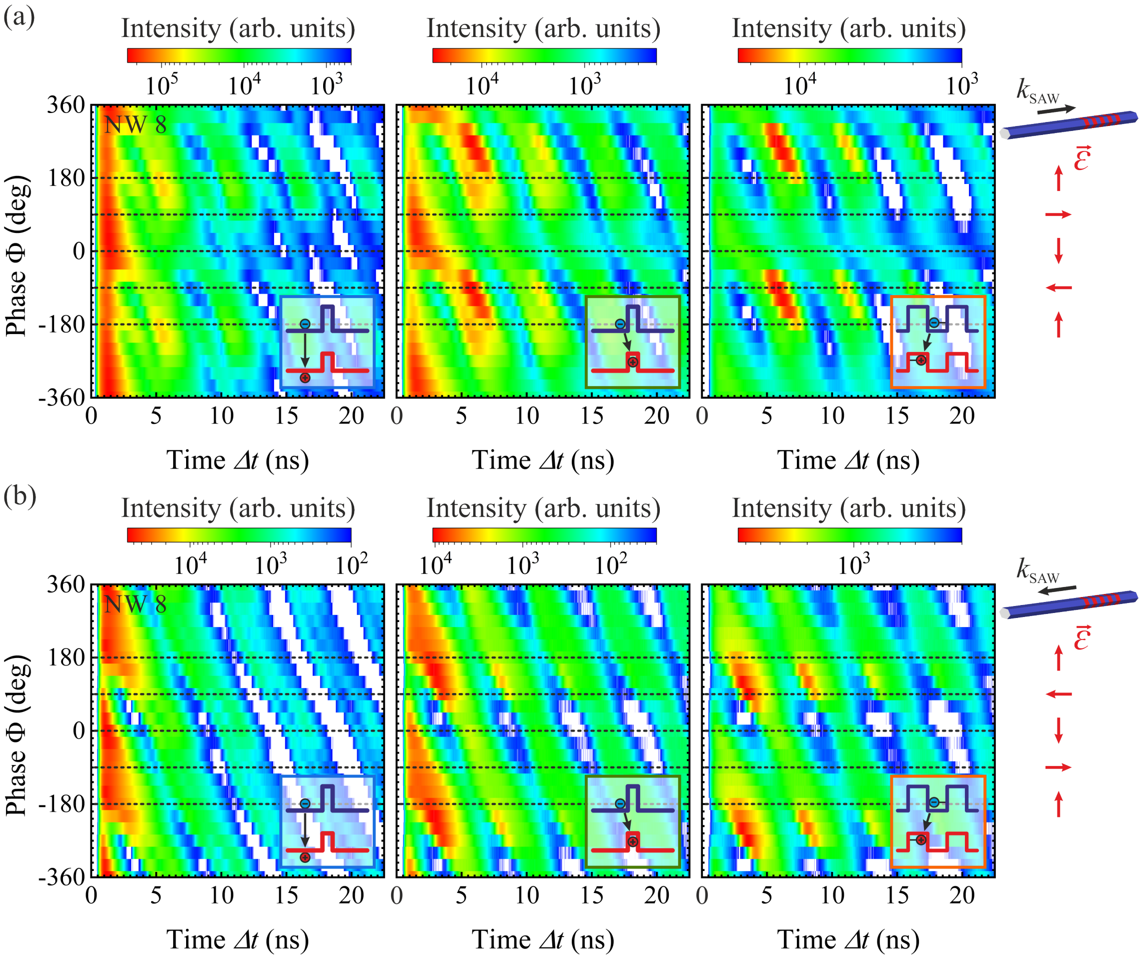

Figure C.4: Stroboscopic photoluminescence spectra of the ZB (left panels), the indirect ZB/twin (center panels) and indirect WZ/ZB/WZ (right panels) exciton transitions at the center of the NW8 for (a) $+k$- and (b) $-k$-propagating surface acoustic waves and phases of $\Phi = [-360°, 360°]$. The electric field orientation at photoexcitation is shown for different phases Φ on the right. The recorded transients show surface acoustic wave induced oscillations and exhibit clear dependencies on the propagation directions of the surface acoustic waves.

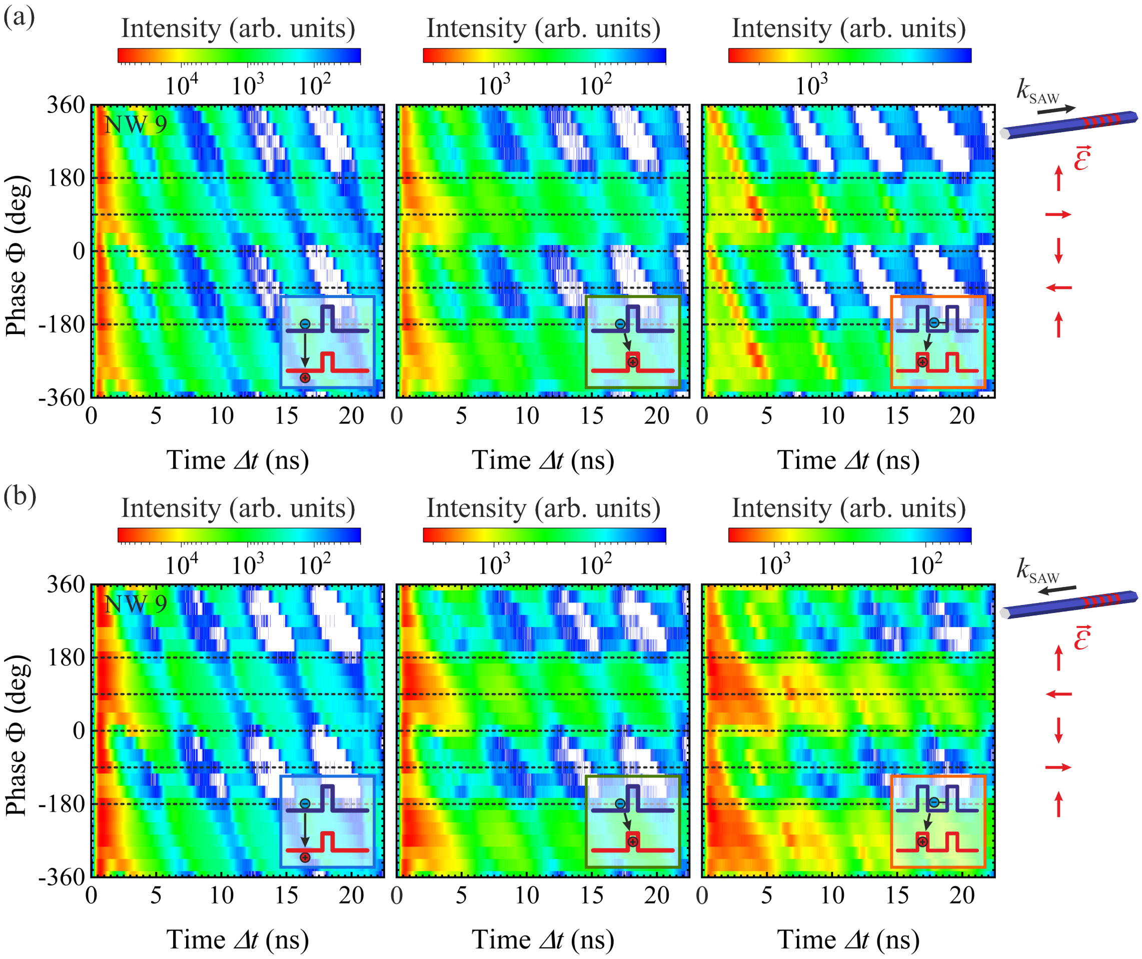

Figure C.5: Stroboscopic photoluminescence spectra of the ZB (left panels), the indirect ZB/twin (center panels) and indirect twin/ZB/twin (right panels) exciton transitions at the center of the NW9 for (a) $+k$- and (b) $-k$-propagating surface acoustic waves and phases of $\Phi = [-360°, 360°]$. The electric field orientation at photoexcitation is shown for different phases Φ on the right. The recorded transients show surface acoustic wave induced oscillations and exhibit no directionality on the propagation directions of the surface acoustic waves.

List of acronyms

APD	single photon silicon avalanche photodetector
CB	conduction band
CCD	charge coupled device
FEM	finite element method
FWHM	full width half maximum
HH	heavy hole
IDT	interdigital transducer
LH	light hole
ML	monolayer
NW	nanowire
PL	photoluminescence
QW	quantum well
rf	radio frequency
SAW	surface acoustic wave
SO	split-off
STEM-HAADF	scanning transmission electron microscopy in high-angle annular dark field mode
TCSPC	time-correlated single photon counting
UV	ultraviolet
VB	valence band
WZ	wurtzite
ZB	zincblende

Bibliography

1. G. E. Moore: Cramming more components onto integrated circuits. *Electronics* **38**(8) (1965), 114–117 (cit. on p. 1).

2. J. Appenzeller, J. Knoch, M. T. Bjork, H. Riel, H. Schmid, and W. Riess: Toward Nanowire Electronics. *IEEE Trans. Electron Devices* **55**(11) (2008), 2827–2845. DOI: 10.1109/TED.2008.2008011 (cit. on pp. 1, 77).

3. K. Tomioka, J. Motohisa, S. Hara, K. Hiruma, and T. Fukui: GaAs/AlGaAs core multishell nanowire-based light-emitting diodes on Si. *Nano Lett.* **10**(5) (2010), 1639–1644. DOI: 10.1021/nl9041774 (cit. on pp. 1, 18).

4. K. Tomioka, M. Yoshimura, and T. Fukui: A III–V nanowire channel on silicon for high-performance vertical transistors. *Nature* **488**(7410) (2012), 189–192. DOI: 10.1038/nature11293 (cit. on pp. 1, 2, 18, 77).

5. P. Krogstrup, H. I. Jørgensen, M. Heiss, O. Demichel, J. V. Holm, M. Aagesen, J. Nygard, and A. Fontcuberta i Morral: Single-nanowire solar cells beyond the Shockley-Queisser limit. *Nat. Photonics* **7**(4) (2013), 306–310. DOI: 10.1038/nphoton.2013.32 (cit. on pp. 1, 2, 18).

6. B. Mayer, D. Rudolph, J. Schnell, S. Morkötter, J. Winnerl, J. Treu, K. Müller, G. Bracher, G. Abstreiter, G. Koblmüller, and J. J. Finley: Lasing from individual GaAs-AlGaAs core-shell nanowires up to room temperature. *Nat. Commun.* **4**(1) (2013), 2931. DOI: 10.1038/ncomms3931 (cit. on pp. 1, 2, 18, 77).

7. F. Capasso: Band-Gap Engineering: From Physics and Materials to New Semiconductor Devices. *Science* **235**(4785) (1987), 172–176. DOI: 10.1126/science.235.4785.172 (cit. on pp. 1, 10).

8. M. S. Gudiksen, L. J. Lauhon, J. Wang, D. C. Smith, and C. M. Lieber: Growth of nanowire superlattice structures for nanoscale photonics and electronics. *Nature* **415**(6872) (2002), 617–620. DOI: 10.1038/415617a (cit. on pp. 1, 5).

9. L. J. Lauhon, M. S. Gudiksen, D. Wang, and C. M. Lieber: Epitaxial core–shell and core–multishell nanowire heterostructures. *Nature* **420**(6911) (2002), 57–61. DOI: 10.1038/nature01141 (cit. on pp. 1, 5, 11, 17).

10. F. Qian, S. Gradečak, Y. Li, C.-Y. Wen, and C. M. Lieber: Core/Multishell Nanowire Heterostructures as Multicolor, High-Efficiency Light-Emitting Diodes. *Nano Lett.* **5**(11) (2005), 2287–2291. DOI: 10.1021/nl051689e (cit. on pp. 1, 5, 11).

11. M. A. Verheijen, G. Immink, T. de Smet, M. T. Borgström, and E. P. A. M. Bakkers: Growth Kinetics of Heterostructured GaP-GaAs Nanowires. *J. Am. Chem. Soc.* **128**(4) (2006), 1353–1359. DOI: 10.1021/ja057157h (cit. on pp. 1, 5).

12. M. Paladugu, J. Zou, Y.-N. Guo, X. Zhang, Y. Kim, H. J. Joyce, Q. Gao, H. H. Tan, and C. Jagadish: Nature of heterointerfaces in GaAs/InAs and InAs/GaAs axial nanowire heterostructures. *Appl. Phys. Lett.* **93**(10) (2008), 101911. DOI: 10.1063/1.2978959 (cit. on pp. 1, 5).

13. M. M. Sonner, A. Sitek, L. Janker, D. Rudolph, D. Ruhstorfer, M. Döblinger, A. Manolescu, G. Abstreiter, J. J. Finley, A. Wixforth, G. Koblmüller, and H. J. Krenner: Breakdown of Corner States and Carrier Localization by Monolayer Fluctuations in Radial Nanowire Quantum Wells. *Nano Lett.* **19**(5) (2019), 3336–3343. DOI: 10.1021/acs.nanolett.9b01028 (cit. on pp. 1, 18, 19, 49, 59, 60, 66).

14. M. Koguchi, H. Kakibayashi, M. Yazawa, K. Hiruma, and T. Katsuyama: Crystal Structure Change of GaAs and InAs Whiskers from Zinc-Blende to Wurtzite Type. *Jpn. J. Appl. Phys.* **31**(Part 1, No. 7) (1992), 2061–2065. DOI: 10.1143/JJAP.31.2061 (cit. on pp. 1, 77).

15. K. Hiruma, M. Yazawa, T. Katsuyama, K. Ogawa, K. Haraguchi, M. Koguchi, and H. Kakibayashi: Growth and optical properties of nanometer-scale GaAs and InAs whiskers. *J. Appl. Phys.* **77**(2) (1995), 447–462. DOI: 10.1063/1.359026 (cit. on pp. 1, 5).

16. M. Mattila, T. Hakkarainen, M. Mulot, and H. Lipsanen: Crystal-structure-dependent photoluminescence from InP nanowires. *Nanotechnology* **17**(6) (2006), 1580–1583. DOI: 10.1088/0957-4484/17/6/008 (cit. on pp. 2, 77).

17. J. Bao, D. C. Bell, F. Capasso, J. B. Wagner, T. Mårtensson, J. Trägårdh, and L. Samuelson: Optical Properties of Rotationally Twinned InP Nanowire Heterostructures. *Nano Lett.* **8**(3) (2008), 836–841. DOI: 10.1021/nl072921e (cit. on pp. 2, 77, 80).

18. D. Spirkoska, J. Arbiol, A. Gustafsson, S. Conesa-Boj, F. Glas, I. Zardo, M. Heigoldt, M. H. Gass, A. L. Bleloch, S. Estrade, M. Kaniber, J. Rossler, F. Peiro, J. R. Morante, G. Abstreiter, L. Samuelson, and A. Fontcuberta i Morral: Structural and optical properties of high quality zinc-blende/wurtzite GaAs nanowire heterostructures. *Phys. Rev. B* **80**(24) (2009), 245325. DOI: 10.1103/PhysRevB.80.245325 (cit. on pp. 2, 6, 11, 15, 77, 80, 85, 116).

19. N. Akopian, G. Patriarche, L. Liu, J.-C. Harmand, and V. Zwiller: Crystal Phase Quantum Dots. *Nano Lett.* **10**(4) (2010), 1198–1201. DOI: 10.1021/nl903534n (cit. on pp. 2, 77).

20. M. Heiss, S. Conesa-Boj, J. Ren, H.-H. Tseng, A. Gali, A. Rudolph, E. Uccelli, F. Peiró, J. R. Morante, D. Schuh, E. Reiger, E. Kaxiras, J. Arbiol, and A. Fontcuberta i Morral: Direct correlation of crystal structure and optical properties in wurtzite/zinc-blende GaAs nanowire heterostructures. *Phys. Rev. B* **83**(4) (2011), 045303. DOI: 10.1103/PhysRevB.83.045303 (cit. on pp. 2, 8, 11, 77, 80).

21. U. Jahn, J. Lähnemann, C. Pfüller, O. Brandt, S. Breuer, B. Jenichen, M. Ramsteiner, L. Geelhaar, and H. Riechert: Luminescence of GaAs nanowires consisting of wurtzite and zinc-blende segments. *Phys. Rev. B* **85**(4) (2012), 045323. DOI: 10.1103/PhysRevB.85.045323 (cit. on pp. 2, 8, 11, 77, 80).

22. A. M. Graham, P. Corfdir, M. Heiss, S. Conesa-Boj, E. Uccelli, A. Fontcuberta i Morral, and R. T. Phillips: Exciton localization mechanisms in wurtzite/zinc-blende GaAs nanowires. *Phys. Rev. B* **87**(12) (2013), 125304. DOI: 10.1103/PhysRevB.87.125304 (cit. on pp. 2, 77, 80).

23. A. V. Senichev, V. G. Talalaev, I. V. Shtrom, H. Blumtritt, G. E. Cirlin, J. Schilling, C. Lienau, and P. Werner: Nanospectroscopic Imaging of Twinning Superlattices in an Individual GaAs-AlGaAs Core–Shell Nanowire. *ACS Photonics* **1**(11) (2014), 1099–1106. DOI: 10.1021/ph5002022 (cit. on pp. 2, 77, 80, 83).

24. D. Rudolph, L. Schweickert, S. Morkötter, L. Hanschke, S. Hertenberger, M. Bichler, G. Koblmüller, G. Abstreiter, and J. J. Finley: Probing the trapping and thermal activation dynamics of excitons at single twin defects in GaAs–AlGaAs core–shell nanowires. *New J. Phys.* **15**(11) (2013), 113032. DOI: 10.1088/1367-2630/15/11/113032 (cit. on pp. 2, 77, 80, 83, 85, 116).

25. M. D. Schroer and J. R. Petta: Correlating the Nanostructure and Electronic Properties of InAs Nanowires. *Nano Lett.* **10**(5) (2010), 1618–1622. DOI: 10.1021/nl904053j (cit. on pp. 2, 77).

26. C. Thelander, P. Caroff, S. Plissard, A. W. Dey, and K. A. Dick: Effects of Crystal Phase Mixing on the Electrical Properties of InAs Nanowires. *Nano Lett.* **11**(6) (2011), 2424–2429. DOI: 10.1021/nl2008339 (cit. on pp. 2, 77).

27. S. Morkötter, N. Jeon, D. Rudolph, B. Loitsch, D. Spirkoska, E. Hoffmann, M. Döblinger, S. Matich, J. J. Finley, L. J. Lauhon, G. Abstreiter, and G. Koblmüller: Demonstration of Confined Electron Gas and Steep-Slope Behavior in Delta-Doped GaAs-AlGaAs Core–Shell Nanowire Transistors. *Nano Lett.* **15**(5) (2015), 3295–3302. DOI: 10.1021/acs.nanolett.5b00518 (cit. on pp. 2, 18, 77).

28. J. B. Kinzel, F. J. R. Schülein, M. Weiß, L. Janker, D. D. Bühler, M. Heigl, D. Rudolph, S. Morkötter, M. Döblinger, Max Bichler, G. Abstreiter, J. J. Finley, A. Wixforth, G. Koblmüller, and H. J. Krenner: The Native Material Limit of Electron

and Hole Mobilities in Semiconductor Nanowires. *ACS Nano* **10**(5) (2016), 4942–4953. DOI: 10.1021/acsnano.5b07639 (cit. on pp. 2, 3, 49, 53–56, 58, 67, 70, 71, 73, 77, 87, 88, 90, 108, 114, 116, 117).

29. J. Becker, S. Morkötter, J. Treu, M. Sonner, M. Speckbacher, M. Döblinger, G. Abstreiter, J. J. Finley, and G. Koblmüller: Carrier trapping and activation at short-period wurtzite/zinc-blende stacking sequences in polytypic InAs nanowires. *Phys. Rev. B* **97**(11) (2018), 115306. DOI: 10.1103/PhysRevB.97.115306 (cit. on p. 2).

30. R. Chen, T.-T. D. Tran, K. W. Ng, W. S. Ko, L. C. Chuang, F. G. Sedgwick, and C. Chang-Hasnain: Nanolasers grown on silicon. *Nat. Photonics* **5**(3) (2011), 170–175. DOI: 10.1038/nphoton.2010.315 (cit. on pp. 2, 77).

31. D. Saxena, S. Mokkapati, P. Parkinson, N. Jiang, Q. Gao, H. H. Tan, and C. Jagadish: Optically pumped room-temperature GaAs nanowire lasers. *Nat. Photonics* **7**(12) (2013), 963–968. DOI: Doi10.1038/Nphoton.2013.303 (cit. on pp. 2, 18).

32. J. Miao, W. Hu, N. Guo, Z. Lu, X. Zou, L. Liao, S. Shi, P. Chen, Z. Fan, J. C. Ho, T.-X. Li, X. S. Chen, and W. Lu: Single InAs Nanowire Room-Temperature Near-Infrared Photodetectors. *ACS Nano* **8**(4) (2014), 3628–3635. DOI: 10.1021/nn500201g (cit. on p. 2).

33. M. Yao, N. Huang, S. Cong, C.-Y. Chi, M. A. Seyedi, Y.-T. Lin, Y. Cao, M. L. Povinelli, P. D. Dapkus, and C. Zhou: GaAs Nanowire Array Solar Cells with Axial p–i–n Junctions. *Nano Lett.* **14**(6) (2014), 3293–3303. DOI: 10.1021/nl500704r (cit. on pp. 2, 77).

34. O. Hayden, R. Agarwal, and C. M. Lieber: Nanoscale avalanche photodiodes for highly sensitive and spatially resolved photon detection. *Nat. Mater.* **5**(5) (2006), 352–356. DOI: 10.1038/nmat1635 (cit. on p. 2).

35. J. Treu, T. Stettner, M. Watzinger, S. Morkötter, M. Döblinger, S. Matich, K. Saller, M. Bichler, G. Abstreiter, J. J. Finley, J. Stangl, and G. Koblmüller: Lattice-Matched InGaAs–InAlAs Core–Shell Nanowires with Improved Luminescence and Photoresponse Properties. *Nano Lett.* **15**(5) (2015), 3533–3540. DOI: 10.1021/acs.nanolett.5b00979 (cit. on p. 2).

36. M. T. Björk, H. Schmid, C. D. Bessire, K. E. Moselund, H. Ghoneim, S. Karg, E. Lörtscher, and H. Riel: Si–InAs heterojunction Esaki tunnel diodes with high current densities. *Appl. Phys. Lett.* **97**(16) (2010), 163501. DOI: 10.1063/1.3499365 (cit. on p. 2).

37. T. Yang, S. Hertenberger, S. Morkötter, G. Abstreiter, and G. Koblmüller: Size, composition, and doping effects on In(Ga)As nanowire/Si tunnel diodes probed by conductive atomic force microscopy. *Appl. Phys. Lett.* **101**(23) (2012), 233102. DOI: 10.1063/1.4768001 (cit. on p. 2).

38. J. B. Kinzel, D. Rudolph, M. Bichler, G. Abstreiter, J. J. Finley, G. Koblmüller, A. Wixforth, and H. J. Krenner: Directional and Dynamic Modulation of the Optical Emission of an Individual GaAs Nanowire Using Surface Acoustic Waves. *Nano Lett.* **11**(4) (2011), 1512–1517. DOI: 10.1021/nl1042775 (cit. on pp. 2, 50, 55, 58, 71, 87, 90, 116).

39. M. Weiß, J. B. Kinzel, F. J. R. Schülein, M. Heigl, D. Rudolph, S. Morkötter, M. Döblinger, M. Bichler, G. Abstreiter, J. J. Finley, G. Koblmüller, A. Wixforth, and H. J. Krenner: Dynamic Acoustic Control of Individual Optically Active Quantum Dot-like Emission Centers in Heterostructure Nanowires. *Nano Lett.* **14**(5) (2014), 2256–2264. DOI: 10.1021/nl4040434 (cit. on pp. 2, 3, 19, 49, 53, 55, 59, 66, 77, 116).

40. P. Delsing, A. N. Cleland, M. J. A. Schuetz, J. Knörzer, G. Giedke, J. I. Cirac, K. Srinivasan, M. Wu, K. C. Balram, C. Bäuerle, T. Meunier, C. J. B. Ford, P. V. Santos, E. Cerda-Méndez, H. Wang, H. J. Krenner, E. D. S. Nysten, M. Weiß, G. R. Nash, L. Thevenard, C. Gourdon, P. Rovillain, M. Marangolo, J.-Y. Duquesne, G. Fischerauer, W. Ruile, A. Reiner, B. Paschke, D. Denysenko, D. Volkmer, A. Wixforth, H. Bruus, M. Wiklund, J. Reboud, J. M. Cooper, Y. Fu, M. S. Brugger, F. Rehfeldt, and C. Westerhausen: The 2019 surface acoustic waves roadmap. *J. Phys. D. Appl. Phys.* **52**(35) (2019), 353001. DOI: 10.1088/1361-6463/ab1b04 (cit. on pp. 2, 31).

41. Lord Rayleigh: On Waves Propagated along the Plane Surface of an Elastic Solid. *Proc. London Math. Soc.* **s1-17**(1) (1885), 4–11. DOI: 10.1112/plms/s1-17.1.4 (cit. on pp. 2, 31, 37, 61).

42. M. M. Sonner, F. Khosravi, L. Janker, D. Rudolph, G. Koblmüller, Z. Jacob, and H. J. Krenner: Ultrafast electron cycloids driven by the transverse spin of a surface acoustic wave. *Sci. Adv.* **7**(31) (2021), eabf7414. DOI: 10.1126/sciadv.abf7414 (cit. on pp. 2, 31, 53, 61, 62, 123).

43. C. Rocke, S. Zimmermann, A. Wixforth, J. P. Kotthaus, G. Böhm, and G. Weimann: Acoustically Driven Storage of Light in a Quantum Well. *Phys. Rev. Lett.* **78**(21) (1997), 4099–4102. DOI: 10.1103/PhysRevLett.78.4099 (cit. on pp. 2, 49, 77, 87).

44. P. V. Santos, M. Ramsteiner, and F. Jungnickel: Spatially resolved photoluminescence in GaAs surface acoustic wave structures. *Appl. Phys. Lett.* **72**(17) (1998), 2099–2101. DOI: 10.1063/1.121288 (cit. on pp. 2, 87).

45. A. García-Cristóbal, A. Cantarero, F. Alsina, and P. V. Santos: Spatiotemporal carrier dynamics in quantum wells under surface acoustic waves. *Phys. Rev. B* **69**(20) (2004), 205301. DOI: 10.1103/PhysRevB.69.205301 (cit. on pp. 2, 49, 73, 77, 88, 90).

46. A. Hernández-Mínguez, M. Möller, S. Breuer, C. Pfüller, C. Somaschini, S. Lazić, O. Brandt, A. García-Cristóbal, M. M. de Lima, A. Cantarero, L. Geelhaar, H. Riechert, and P. V. Santos: Acoustically Driven Photon Antibunching in Nanowires. *Nano Lett.* **12**(1) (2012), 252–258. DOI: 10.1021/nl203461m (cit. on pp. 2, 55, 111, 117).

47. S. Büyükköse, A. Hernández-Mínguez, B. Vratzov, C. Somaschini, L. Geelhaar, H. Riechert, W. G. van der Wiel, and P. V. Santos: High-frequency acoustic charge transport in GaAs nanowires. *Nanotechnology* **25**(13) (2014), 135204. DOI: 10.1088/0957-4484/25/13/135204 (cit. on pp. 2, 55, 87).

48. M. Weiß, F. J. R. Schülein, J. B. Kinzel, M. Heigl, D. Rudolph, M. Bichler, G. Abstreiter, J. J. Finley, A. Wixforth, G. Koblmüller, and H. J. Krenner: Radio frequency occupancy state control of a single nanowire quantum dot. *J. Phys. D. Appl. Phys.* **47**(39) (2014), 394011. DOI: 10.1088/0022-3727/47/39/394011 (cit. on pp. 3, 19, 55, 59, 116).

49. S. Lazić, E. Chernysheva, Ž. Gačević, H. P. van der Meulen, E. Calleja, and J. M. Calleja Pardo: Dynamic control of the optical emission from GaN/InGaN nanowire quantum dots by surface acoustic waves. *AIP Adv.* **5**(9) (2015), 097217. DOI: 10.1063/1.4932147 (cit. on pp. 3, 55).

50. L. Janker, Y. Tong, L. Polavarapu, J. Feldmann, A. S. Urban, and H. J. Krenner: Real-Time Electron and Hole Transport Dynamics in Halide Perovskite Nanowires. *Nano Lett.* **19**(12) (2019), 8701–8707. DOI: 10.1021/acs.nanolett.9b03396 (cit. on pp. 3, 87, 114, 118).

51. R. S. Wagner and W. C. Ellis: VAPOR-LIQUID-SOLID MECHANISM OF SINGLE CRYSTAL GROWTH. *Appl. Phys. Lett.* **4**(5) (1964), 89–90. DOI: 10.1063/1.1753975 (cit. on p. 5).

52. K. Hiruma, M. Yazawa, K. Haraguchi, K. Ogawa, T. Katsuyama, M. Koguchi, and H. Kakibayashi: GaAs free-standing quantum-size wires. *J. Appl. Phys.* **74**(5) (1993), 3162–3171. DOI: 10.1063/1.354585 (cit. on pp. 5, 77).

53. H. G. Grimmeiss: Deep Level Impurities in Semiconductors. *Annu. Rev. Mater. Sci.* **7**(1) (1977), 341–376. DOI: 10.1146/annurev.ms.07.080177.002013 (cit. on p. 5).

54. S. D. Brotherton and J. E. Lowther: Electron and Hole Capture at Au and Pt Centers in Silicon. *Phys. Rev. Lett.* **44**(25) (1980), 1711. DOI: 10.1103/PhysRevLett.44.1711 (cit. on p. 5).

55. J. E. Allen, E. R. Hemesath, D. E. Perea, J. L. Lensch-Falk, Z. Y. Li, F. Yin, M. H. Gass, P. Wang, A. L. Bleloch, R. E. Palmer, and L. J. Lauhon: High-resolution detection of Au catalyst atoms in Si nanowires. *Nat. Nanotechnol.* **3**(3) (2008), 168–173. DOI: 10.1038/nnano.2008.5 (cit. on p. 5).

56. S. Breuer, C. Pfüller, T. Flissikowski, O. Brandt, H. T. Grahn, L. Geelhaar, and H. Riechert: Suitability of Au- and Self-Assisted GaAs Nanowires for Optoelectronic Applications. *Nano Lett.* **11**(3) (2011), 1276–1279. DOI: 10.1021/nl104316t (cit. on p. 5).

57. C. Colombo, D. Spirkoska, M. Frimmer, G. Abstreiter, and A. Fontcuberta i Morral: Ga-assisted catalyst-free growth mechanism of GaAs nanowires by molecular beam epitaxy. *Phys. Rev. B* **77**(15) (2008), 155326. DOI: 10.1103/PhysRevB.77.155326 (cit. on pp. 5, 14, 15).

58. A. Fontcuberta i Morral, C. Colombo, G. Abstreiter, J. Arbiol, and J. R. Morante: Nucleation mechanism of gallium-assisted molecular beam epitaxy growth of gallium arsenide nanowires. *Appl. Phys. Lett.* **92**(6) (2008), 063112. DOI: 10.1063/1.2837191 (cit. on p. 5).

59. F. Jabeen, V. Grillo, S. Rubini, and F. Martelli: Self-catalyzed growth of GaAs nanowires on cleaved Si by molecular beam epitaxy. *Nanotechnology* **19**(27) (2008), 275711. DOI: 10.1088/0957-4484/19/27/275711 (cit. on p. 5).

60. S. Plissard, K. A. Dick, G. Larrieu, S. Godey, A. Addad, X. Wallart, and P. Caroff: Gold-free growth of GaAs nanowires on silicon: arrays and polytypism. *Nanotechnology* **21**(38) (2010), 385602. DOI: 10.1088/0957-4484/21/38/385602 (cit. on pp. 5, 15).

61. D. Rudolph, S. Hertenberger, S. Bolte, W. Paosangthong, D. Spirkoska, M. Döblinger, M. Bichler, J. J. Finley, G. Abstreiter, and G. Koblmüller: Direct Observation of a Noncatalytic Growth Regime for GaAs Nanowires. *Nano Lett.* **11**(9) (2011), 3848–3854. DOI: 10.1021/nl2019382 (cit. on pp. 5, 14, 15).

62. H. J. Joyce, J. Wong-Leung, Q. Gao, H. H. Tan, and C. Jagadish: Phase Perfection in Zinc Blende and Wurtzite III-V Nanowires Using Basic Growth Parameters. *Nano Lett.* **10**(3) (2010), 908–915. DOI: 10.1021/nl903688v (cit. on pp. 6, 77).

63. P. Caroff, K. A. Dick, J. Johansson, M. E. Messing, K. Deppert, and L. Samuelson: Controlled polytypic and twin-plane superlattices in III–V nanowires. *Nat. Nanotechnol.* **4**(1) (2009), 50–55. DOI: 10.1038/nnano.2008.359 (cit. on pp. 6, 7, 77).

64. V. G. Dubrovskii: *Nucleation Theory and Growth of Nanostructures.* NanoScience and Technology. Berlin, Heidelberg: Springer Berlin Heidelberg, 2014, pp. 499–571. DOI: 10.1007/978-3-642-39660-1 (cit. on p. 7).

65. F. Glas, J.-C. Harmand, and G. Patriarche: Why Does Wurtzite Form in Nanowires of III-V Zinc Blende Semiconductors? *Phys. Rev. Lett.* **99**(14) (2007), 146101. DOI: 10.1103/PhysRevLett.99.146101 (cit. on pp. 7, 15).

66. V. G. Dubrovskii, N. V. Sibirev, J. C. Harmand, and F. Glas: Growth kinetics and crystal structure of semiconductor nanowires. *Phys. Rev. B* **78**(23) (2008), 235301. DOI: 10.1103/PhysRevB.78.235301 (cit. on pp. 7, 15).

67. P. Krogstrup, H. I. Jørgensen, E. Johnson, M. H. Madsen, C. B. Sørensen, A. Fontcuberta i Morral, M. Aagesen, J. Nygård, and F. Glas: Advances in the theory of III–V nanowire growth dynamics. *J. Phys. D. Appl. Phys.* **46**(31) (2013), 313001. DOI: 10.1088/0022-3727/46/31/313001 (cit. on pp. 7, 15).

68. D. Jacobsson, F. Panciera, J. Tersoff, M. C. Reuter, S. Lehmann, S. Hofmann, K. A. Dick, and F. M. Ross: Interface dynamics and crystal phase switching in GaAs nanowires. *Nature* **531**(7594) (2016), 317–322. DOI: 10.1038/nature17148 (cit. on pp. 7, 15).

69. A. De and C. E. Pryor: Predicted band structures of III-V semiconductors in the wurtzite phase. *Phys. Rev. B* **81**(15) (2010), 155210. DOI: 10.1103/PhysRevB.81.155210 (cit. on pp. 7, 8, 11).

70. L. C. Lew Yan Voon, M. Willatzen, M. Cardona, and N. E. Christensen: Terms linear in k in the band structure of wurtzite-type semiconductors. *Phys. Rev. B* **53**(16) (1996), 10703–10714. DOI: 10.1103/PhysRevB.53.10703 (cit. on pp. 7, 8).

71. S. L. Chuang and C. S. Chang: k·p method for strained wurtzite semiconductors. *Phys. Rev. B* **54**(4) (1996), 2491–2504. DOI: 10.1103/PhysRevB.54.2491 (cit. on pp. 7, 8).

72. M. Murayama and T. Nakayama: Chemical trend of band offsets at wurtzite/zinc-blende heterocrystalline semiconductor interfaces. *Phys. Rev. B* **49**(7) (1994), 4710–4724. DOI: 10.1103/PhysRevB.49.4710 (cit. on pp. 8, 11, 77).

73. Z. Zanolli, F. Fuchs, J. Furthmüller, U. von Barth, and F. Bechstedt: Model GW band structure of InAs and GaAs in the wurtzite phase. *Phys. Rev. B* **75**(24) (2007), 245121. DOI: 10.1103/PhysRevB.75.245121 (cit. on pp. 8, 11).

74. J.-M. Jancu, K. Gauthron, L. Largeau, G. Patriarche, J.-C. Harmand, and P. Voisin: Type II heterostructures formed by zinc-blende inclusions in InP and GaAs wurtzite nanowires. *Appl. Phys. Lett.* **97**(4) (2010), 041910. DOI: 10.1063/1.3473779 (cit. on pp. 8, 11).

75. T. B. Hoang, A. F. Moses, H. L. Zhou, D. L. Dheeraj, B. O. Fimland, and H. Weman: Observation of free exciton photoluminescence emission from single wurtzite GaAs nanowires. *Appl. Phys. Lett.* **94**(13) (2009), 133105. DOI: 10.1063/1.3104853 (cit. on pp. 8, 11).

76. T. B. Hoang, A. F. Moses, L. Ahtapodov, H. Zhou, D. L. Dheeraj, A. T. J. van Helvoort, B.-O. Fimland, and H. Weman: Engineering Parallel and Perpendicular Polarized Photoluminescence from a Single Semiconductor Nanowire by Crystal Phase Control. *Nano Lett.* **10**(8) (2010), 2927–2933. DOI: 10.1021/nl101087e (cit. on pp. 8, 11).

77. S.-G. Ihn, M.-Y. Ryu, and J.-I. Song: Optical properties of undoped, Be-doped, and Si-doped wurtzite-rich GaAs nanowires grown on Si substrates by molecular beam epitaxy. *Solid State Commun.* **150**(15) (2010), 729–733. DOI: 10.1016/j.ssc.2010.01.037 (cit. on pp. 8, 11).

78. M. Moewe, L. C. Chuang, S. Crankshaw, C. Chase, and C. Chang-Hasnain: Atomically sharp catalyst-free wurtzite GaAs/AlGaAs nanoneedles grown on silicon. *Appl. Phys. Lett.* **93**(2) (2008), 023116. DOI: 10.1063/1.2949315 (cit. on pp. 8, 11).

79. B. Ketterer, M. Heiss, M. J. Livrozet, A. Rudolph, E. Reiger, and A. Fontcuberta i Morral: Determination of the band gap and the split-off band in wurtzite GaAs using Raman and photoluminescence excitation spectroscopy. *Phys. Rev. B* **83**(12) (2011), 125307. DOI: 10.1103/PhysRevB.83.125307 (cit. on pp. 8, 11).

80. B. Ketterer, M. Heiss, E. Uccelli, J. Arbiol, and A. Fontcuberta i Morral: Untangling the Electronic Band Structure of Wurtzite GaAs Nanowires by Resonant Raman Spectroscopy. *ACS Nano* **5**(9) (2011), 7585–7592. DOI: 10.1021/nn202585j (cit. on pp. 8, 11).

81. L. Ahtapodov, J. Todorovic, P. Olk, T. Mjåland, P. Slåttnes, D. L. Dheeraj, A. T. J. van Helvoort, B.-O. Fimland, and H. Weman: A Story Told by a Single Nanowire: Optical Properties of Wurtzite GaAs. *Nano Lett.* **12**(12) (2012), 6090–6095. DOI: 10.1021/nl3025714 (cit. on pp. 8, 11).

82. M. Fox: *Optical Properties of Solids.* Oxford: Oxford University Press, 2001 (cit. on p. 9).

83. M. Fox: *Quantum Optics: An Introduction.* Oxford and New York: Oxford University Press, 2006 (cit. on p. 9).

84. S. B. Nam, D. C. Reynolds, C. W. Litton, R. J. Almassy, T. C. Collins, and C. M. Wolfe: Free-exciton energy spectrum in GaAs. *Phys. Rev. B* **13**(2) (1976), 761–767. DOI: 10.1103/PhysRevB.13.761 (cit. on p. 10).

85. D. Rudolph, S. Funk, M. Döblinger, S. Morkötter, S. Hertenberger, L. Schweickert, J. Becker, S. Matich, M. Bichler, D. Spirkoska, I. Zardo, J. J. Finley, G. Abstreiter, and G. Koblmüller: Spontaneous Alloy Composition Ordering in GaAs-AlGaAs Core–Shell Nanowires. *Nano Lett.* **13**(4) (2013), 1522–1527. DOI: 10.1021/nl3046816 (cit. on pp. 14, 17–19, 21, 28, 55, 58, 80).

86. D. Rudolph: Growth of GaAs-based nanowires on silicon for optical applications. Doctoral Thesis. Technische Universität München, 2014 (cit. on p. 14).

87. B. Loitsch: GaAs based nanowires on silicon - growth and quantum confinement phenomena. Doctoral Thesis. Technische Universität München, 2017 (cit. on pp. 14, 18).

88. P. Krogstrup, R. Popovitz-Biro, E. Johnson, M. H. Madsen, J. Nygård, and H. Shtrikman: Structural Phase Control in Self-Catalyzed Growth of GaAs Nanowires on Silicon (111). *Nano Lett.* **10**(11) (2010), 4475–4482. DOI: 10.1021/nl102308k (cit. on p. 15).

89. F. Bastiman, H. Küpers, C. Somaschini, and L. Geelhaar: Growth map for Ga-assisted growth of GaAs nanowires on Si(111) substrates by molecular beam epitaxy. *Nanotechnology* **27**(9) (2016), 095601. DOI: 10.1088/0957-4484/27/9/095601 (cit. on p. 15).

90. S. Hertenberger, D. Rudolph, M. Bichler, J. J. Finley, G. Abstreiter, and G. Koblmüller: Growth kinetics in position-controlled and catalyst-free InAs nanowire arrays on Si(111) grown by selective area molecular beam epitaxy. *J. Appl. Phys.* **108**(11) (2010), 114316. DOI: 10.1063/1.3525610 (cit. on pp. 15, 16, 20).

91. D. Rudolph, L. Schweickert, S. Morkötter, B. Loitsch, S. Hertenberger, J. Becker, M. Bichler, G. Abstreiter, J. J. Finley, and G. Koblmüller: Effect of interwire

separation on growth kinetics and properties of site-selective GaAs nanowires. *Appl. Phys. Lett.* **105**(3) (2014), 033111. DOI: 10.1063/1.4891427 (cit. on pp. 15, 16, 20).

92. E. P. A. M. Bakkers, J. A. van Dam, S. De Franceschi, L. P. Kouwenhoven, M. Kaiser, M. Verheijen, H. Wondergem, and P. van der Sluis: Epitaxial growth of InP nanowires on germanium. *Nat. Mater.* **3**(11) (2004), 769–773. DOI: 10.1038/nmat1235 (cit. on p. 16).

93. A. L. Roest, M. A. Verheijen, O. Wunnicke, S. Serafin, H. Wondergem, and E. P. A. M. Bakkers: Position-controlled epitaxial III–V nanowires on silicon. *Nanotechnology* **17**(11) (2006), S271–S275. DOI: 10.1088/0957-4484/17/11/S07 (cit. on p. 16).

94. E. P. A. M. Bakkers, M. T. Borgström, and M. A. Verheijen: Epitaxial Growth of III-V Nanowires on Group IV Substrates. *MRS Bull.* **32**(2) (2007), 117–122. DOI: 10.1557/mrs2007.43 (cit. on p. 16).

95. M. Heiß, A. Gustafsson, S. Conesa-Boj, F. Peiró, J. R. Morante, G. Abstreiter, J. Arbiol, L. Samuelson, and A. Fontcuberta i Morral: Catalyst-free nanowires with axial $\mathrm{In}_x\mathrm{Ga}_{1-x}\mathrm{As}$/GaAs heterostructures. *Nanotechnology* **20**(7) (2009), 075603. DOI: 10.1088/0957-4484/20/7/075603 (cit. on p. 17).

96. S. Hertenberger, D. Rudolph, S. Bolte, M. Döblinger, M. Bichler, D. Spirkoska, J. J. Finley, G. Abstreiter, and G. Koblmüller: Absence of vapor-liquid-solid growth during molecular beam epitaxy of self-induced InAs nanowires on Si. *Appl. Phys. Lett.* **98**(12) (2011), 123114. DOI: 10.1063/1.3567496 (cit. on p. 17).

97. S. Hertenberger, S. Funk, K. Vizbaras, A. Yadav, D. Rudolph, J. Becker, S. Bolte, M. Döblinger, M. Bichler, G. Scarpa, P. Lugli, I. Zardo, J. J. Finley, M.-C. Amann, G. Abstreiter, and G. Koblmüller: High compositional homogeneity in In-rich InGaAs nanowire arrays on nanoimprinted SiO_2/Si (111). *Appl. Phys. Lett.* **101**(4) (2012), 043116. DOI: 10.1063/1.4738769 (cit. on p. 17).

98. J. Treu, M. Speckbacher, K. Saller, S. Morkötter, M. Döblinger, X. Xu, H. Riedl, G. Abstreiter, J. J. Finley, and G. Koblmüller: Widely tunable alloy composition and crystal structure in catalyst-free InGaAs nanowire arrays grown by selective area molecular beam epitaxy. *Appl. Phys. Lett.* **108**(5) (2016), 053110. DOI: 10.1063/1.4941407 (cit. on p. 17).

99. M. Sonner, J. Treu, K. Saller, H. Riedl, J. J. Finley, and G. Koblmüller: Carrier concentration dependent photoluminescence properties of Si-doped InAs nanowires. *Appl. Phys. Lett.* **112**(9) (2018), 091904. DOI: 10.1063/1.5019350 (cit. on p. 17).

100. J. Becker, M. O. Hill, M. Sonner, J. Treu, M. Döblinger, A. Hirler, H. Riedl, J. J. Finley, L. Lauhon, and G. Koblmüller: Correlated Chemical and Electrically Active Dopant Analysis in Catalyst-Free Si-Doped InAs Nanowires. *ACS Nano* **12**(2) (2018), 1603–1610. DOI: 10.1021/acsnano.7b08197 (cit. on p. 17).

101. G. Koblmüller, S. Hertenberger, K. Vizbaras, M. Bichler, F. Bao, J.-P. Zhang, and G. Abstreiter: Self-induced growth of vertical free-standing InAs nanowires on Si(111) by molecular beam epitaxy. *Nanotechnology* **21**(36) (2010), 365602. DOI: 10.1088/0957-4484/21/36/365602 (cit. on p. 17).

102. G. Koblmüller and G. Abstreiter: Growth and properties of InGaAs nanowires on silicon. *Phys. status solidi - Rapid Res. Lett.* **8**(1) (2014), 11–30. DOI: 10.1002/pssr.201308207 (cit. on p. 17).

103. T. Suzuki and M. Ogawa: Degradation of photoluminescence intensity caused by excitation-enhanced oxidation of GaAs surfaces. *Appl. Phys. Lett.* **31**(7) (1977), 473–475. DOI: 10.1063/1.89745 (cit. on p. 17).

104. W. E. Spicer, I. Lindau, P. Skeath, and C. Y. Su: Unified defect model and beyond. *J. Vac. Sci. Technol.* **17**(5) (1980), 1019–1027. DOI: 10.1116/1.570583 (cit. on p. 17).

105. D. E. Aspnes: Recombination at semiconductor surfaces and interfaces. *Surf. Sci.* **132**(1-3) (1983), 406–421. DOI: 10.1016/0039-6028(83)90550-2 (cit. on p. 17).

106. S. Perera, M. A. Fickenscher, H. E. Jackson, L. M. Smith, J. M. Yarrison-Rice, H. J. Joyce, Q. Gao, H. H. Tan, C. Jagadish, X. Zhang, and J. Zou: Nearly intrinsic exciton lifetimes in single twin-free GaAs/AlGaAs core-shell nanowire heterostructures. *Appl. Phys. Lett.* **93**(5) (2008), 053110. DOI: 10.1063/1.2967877 (cit. on pp. 18, 28, 58).

107. K. Tomioka, Y. Kobayashi, J. Motohisa, S. Hara, and T. Fukui: Selective-area growth of vertically aligned GaAs and GaAs/AlGaAs core–shell nanowires on Si(111) substrate. *Nanotechnology* **20**(14) (2009), 145302. DOI: 10.1088/0957-4484/20/14/145302 (cit. on p. 18).

108. O. Demichel, M. Heiss, J. Bleuse, H. Mariette, and A. Fontcuberta i Morral: Impact of surfaces on the optical properties of GaAs nanowires. *Appl. Phys. Lett.* **97**(20) (2010), 201907. DOI: 10.1063/1.3519980 (cit. on pp. 18, 28, 58).

109. B. Loitsch, D. Rudolph, S. Morkötter, M. Döblinger, G. Grimaldi, L. Hanschke, S. Matich, E. Parzinger, U. Wurstbauer, G. Abstreiter, J. J. Finley, and G. Koblmüller: Tunable Quantum Confinement in Ultrathin, Optically Active Semi-

conductor Nanowires Via Reverse-Reaction Growth. *Adv. Mater.* **27**(13) (2015), 2195–2202. DOI: 10.1002/adma.201404900 (cit. on p. 18).

110. B. Loitsch, J. Winnerl, G. Grimaldi, J. Wierzbowski, D. Rudolph, S. Morkötter, M. Döblinger, G. Abstreiter, G. Koblmüller, and J. J. Finley: Crystal Phase Quantum Dots in the Ultrathin Core of GaAs–AlGaAs Core–Shell Nanowires. *Nano Lett.* **15**(11) (2015), 7544–7551. DOI: 10.1021/acs.nanolett.5b03273 (cit. on p. 18).

111. B. Loitsch, M. Müller, J. Winnerl, P. Veit, D. Rudolph, G. Abstreiter, J. J. Finley, F. Bertram, J. Christen, and G. Koblmüller: Microscopic nature of crystal phase quantum dots in ultrathin GaAs nanowires by nanoscale luminescence characterization. *New J. Phys.* **18**(6) (2016), 063009. DOI: 10.1088/1367-2630/18/6/063009 (cit. on pp. 18, 82).

112. F. Qian, Y. Li, S. Gradečak, H.-G. Park, Y. Dong, Y. Ding, Z. L. Wang, and C. M. Lieber: Multi-quantum-well nanowire heterostructures for wavelength-controlled lasers. *Nat. Mater.* **7**(9) (2008), 701–706. DOI: 10.1038/nmat2253 (cit. on p. 18).

113. M. Fickenscher, T. Shi, H. E. Jackson, L. M. Smith, J. M. Yarrison-Rice, C. Zheng, P. Miller, J. Etheridge, B. M. Wong, Q. Gao, S. Deshpande, H. H. Tan, and C. Jagadish: Optical, Structural, and Numerical Investigations of GaAs/AlGaAs Core–Multishell Nanowire Quantum Well Tubes. *Nano Lett.* **13**(3) (2013), 1016–1022. DOI: 10.1021/nl304182j (cit. on pp. 18, 19, 26).

114. E. Dimakis, U. Jahn, M. Ramsteiner, A. Tahraoui, J. Grandal, X. Kong, O. Marquardt, A. Trampert, H. Riechert, and L. Geelhaar: Coaxial Multishell (In,Ga)As/GaAs Nanowires for Near-Infrared Emission on Si Substrates. *Nano Lett.* **14**(5) (2014), 2604–2609. DOI: 10.1021/nl500428v (cit. on pp. 18, 20).

115. T. Stettner, P. Zimmermann, B. Loitsch, M. Döblinger, A. Regler, B. Mayer, J. Winnerl, S. Matich, H. Riedl, M. Kaniber, G. Abstreiter, G. Koblmüller, and J. J. Finley: Coaxial GaAs-AlGaAs core-multishell nanowire lasers with epitaxial gain control. *Appl. Phys. Lett.* **108**(1) (2016), 011108. DOI: 10.1063/1.4939549 (cit. on pp. 18, 19).

116. T. Stettner, A. Thurn, M. Döblinger, M. O. Hill, J. Bissinger, P. Schmiedeke, S. Matich, T. Kostenbader, D. Ruhstorfer, H. Riedl, M. Kaniber, L. J. Lauhon, J. J. Finley, and G. Koblmüller: Tuning Lasing Emission toward Long Wavelengths in GaAs-(In,Al)GaAs Core–Multishell Nanowires. *Nano Lett.* **18**(10) (2018), 6292–6300. DOI: 10.1021/acs.nanolett.8b02503 (cit. on p. 18).

117. N. Erhard, S. Zenger, S. Morkötter, D. Rudolph, M. Weiss, H. J. Krenner, H. Karl, G. Abstreiter, J. J. Finley, G. Koblmüller, and A. W. Holleitner: Ultrafast Photodetection in the Quantum Wells of Single AlGaAs/GaAs-Based Nanowires.

Nano Lett. **15**(10) (2015), 6869–6874. DOI: 10.1021/acs.nanolett.5b02766 (cit. on pp. 18, 80).

118. D. M. Irber, J. Seidl, D. J. Carrad, J. Becker, N. Jeon, B. Loitsch, J. Winnerl, S. Matich, M. Döblinger, Y. Tang, S. Morkötter, G. Abstreiter, J. J. Finley, M. Grayson, L. J. Lauhon, and G. Koblmüller: Quantum Transport and Sub-Band Structure of Modulation-Doped GaAs/AlAs Core–Superlattice Nanowires. *Nano Lett.* **17**(8) (2017), 4886–4893. DOI: 10.1021/acs.nanolett.7b01732 (cit. on pp. 18, 19).

119. M. Heiss, Y. Fontana, A. Gustafsson, G. Wüst, C. Magen, D. D. O'Regan, J. W. Luo, B. Ketterer, S. Conesa-Boj, A. V. Kuhlmann, J. Houel, E. Russo-Averchi, J. R. Morante, M. Cantoni, N. Marzari, J. Arbiol, A. Zunger, R. J. Warburton, and A. Fontcuberta I Morral: Self-assembled quantum dots in a nanowire system for quantum photonics. *Nat. Mater.* **12**(5) (2013), 439–444. DOI: 10.1038/nmat3557 (cit. on pp. 19, 116).

120. L. Mancini, Y. Fontana, S. Conesa-Boj, I. Blum, F. Vurpillot, L. Francaviglia, E. Russo-Averchi, M. Heiss, J. Arbiol, A. Fontcuberta i Morral, and L. Rigutti: Three-dimensional nanoscale study of Al segregation and quantum dot formation in GaAs/AlGaAs core-shell nanowires. *Appl. Phys. Lett.* **105**(24) (2014), 243106. DOI: 10.1063/1.4904952 (cit. on p. 19).

121. N. Jeon, B. Loitsch, S. Morkoetter, G. Abstreiter, J. Finley, H. J. Krenner, G. Koblmueller, and L. J. Lauhon: Alloy Fluctuations Act as Quantum Dot-like Emitters in GaAs-AlGaAs Core–Shell Nanowires. *ACS Nano* **9**(8) (2015), 8335–8343. DOI: 10.1021/acsnano.5b04070 (cit. on pp. 19, 116).

122. N. Jeon, D. Ruhstorfer, M. Döblinger, S. Matich, B. Loitsch, G. Koblmüller, and L. Lauhon: Connecting Composition-Driven Faceting with Facet-Driven Composition Modulation in GaAs–AlGaAs Core–Shell Nanowires. *Nano Lett.* **18**(8) (2018), 5179–5185. DOI: 10.1021/acs.nanolett.8b02104 (cit. on pp. 19, 30).

123. C. Zheng, J. Wong-Leung, Q. Gao, H. H. Tan, C. Jagadish, and J. Etheridge: Polarity-Driven 3-Fold Symmetry of GaAs/AlGaAs Core Multishell Nanowires. *Nano Lett.* **13**(8) (2013), 3742–3748. DOI: 10.1021/nl401680k (cit. on p. 19).

124. S. Funk, M. Royo, I. Zardo, D. Rudolph, S. Morkötter, B. Mayer, J. Becker, A. Bechtold, S. Matich, M. Döblinger, M. Bichler, G. Koblmüller, J. J. Finley, A. Bertoni, G. Goldoni, and G. Abstreiter: High Mobility One- and Two-Dimensional Electron Systems in Nanowire-Based Quantum Heterostructures. *Nano Lett.* **13**(12) (2013), 6189–6196. DOI: 10.1021/nl403561w (cit. on pp. 19, 26).

125. C. L. Davies, P. Parkinson, N. Jiang, J. L. Boland, S. Conesa-Boj, H. H. Tan, C. Jagadish, L. M. Herz, and M. B. Johnston: Low ensemble disorder in quantum well tube nanowires. *Nanoscale* **7**(48) (2015), 20531–20538. DOI: 10.1039/C5NR06996C (cit. on pp. 19, 26).

126. T. Shi, H. E. Jackson, L. M. Smith, N. Jiang, Q. Gao, H. H. Tan, C. Jagadish, C. Zheng, and J. Etheridge: Emergence of Localized States in Narrow GaAs/AlGaAs Nanowire Quantum Well Tubes. *Nano Lett.* **15**(3) (2015), 1876–1882. DOI: 10.1021/nl5046878 (cit. on p. 19).

127. T. Shi, H. E. Jackson, L. M. Smith, N. Jiang, H. H. Tan, and C. Jagadish: Thermal Delocalization of Excitons in GaAs/AlGaAs Quantum Well Tube Nanowires. *Nano Lett.* **16**(2) (2016), 1392–1397. DOI: 10.1021/acs.nanolett.5b04864 (cit. on p. 19).

128. E. Uccelli, J. Arbiol, J. R. Morante, and A. Fontcuberta i Morral: InAs Quantum Dot Arrays Decorating the Facets of GaAs Nanowires. *ACS Nano* **4**(10) (2010), 5985–5993. DOI: 10.1021/nn101604k (cit. on p. 19).

129. J. Jadczak, P. Plochocka, A. Mitioglu, I. Breslavetz, M. Royo, A. Bertoni, G. Goldoni, T. Smolenski, P. Kossacki, A. Kretinin, H. Shtrikman, and D. K. Maude: Unintentional High-Density p-Type Modulation Doping of a GaAs/AlAs Core–Multishell Nanowire. *Nano Lett.* **14**(5) (2014), 2807–2814. DOI: 10.1021/nl500818k (cit. on pp. 19, 26).

130. A. Sitek, M. Ţolea, M. Niţă, L. Serra, V. Gudmundsson, and A. Manolescu: In-gap corner states in core-shell polygonal quantum rings. *Sci. Rep.* **7**(1) (2017), 40197. DOI: 10.1038/srep40197 (cit. on pp. 19, 23, 26).

131. A. Sitek, M. Urbaneja Torres, K. Torfason, V. Gudmundsson, A. Bertoni, and A. Manolescu: Excitons in Core–Shell Nanowires with Polygonal Cross Sections. *Nano Lett.* **18**(4) (2018), 2581–2589. DOI: 10.1021/acs.nanolett.8b00309 (cit. on pp. 19, 23, 24, 26).

132. A. Ballester, J. Planelles, and A. Bertoni: Multi-particle states of semiconductor hexagonal rings: Artificial benzene. *J. Appl. Phys.* **112**(10) (2012), 104317. DOI: 10.1063/1.4766444 (cit. on pp. 19, 26).

133. A. Sitek, L. Serra, V. Gudmundsson, and A. Manolescu: Electron localization and optical absorption of polygonal quantum rings. *Phys. Rev. B* **91**(23) (2015), 235429. DOI: 10.1103/PhysRevB.91.235429 (cit. on pp. 19, 23).

134. A. Sitek, G. Thorgilsson, V. Gudmundsson, and A. Manolescu: Multi-domain electromagnetic absorption of triangular quantum rings. *Nanotechnology* **27**(22) (2016), 225202. DOI: 10.1088/0957-4484/27/22/225202 (cit. on pp. 19, 23).

135. M. A. Herman, D. Bimberg, and J. Christen: Heterointerfaces in quantum wells and epitaxial growth processes: Evaluation by luminescence techniques. *J. Appl. Phys.* **70**(2) (1991), R1–R52. DOI: 10.1063/1.349613 (cit. on pp. 19, 23).

136. T. Ruf, J. Spitzer, V. F. Sapega, V. I. Belitsky, M. Cardona, and K. Ploog: Interface roughness and homogeneous linewidths in quantum wells and superlattices studied by resonant acoustic-phonon Raman scattering. *Phys. Rev. B* **50**(3) (1994), 1792–1806. DOI: 10.1103/PhysRevB.50.1792 (cit. on p. 19).

137. K. L. Campman, H. Schmidt, A. Imamoglu, and A. C. Gossard: Interface roughness and alloy-disorder scattering contributions to intersubband transition linewidths. *Appl. Phys. Lett.* **69**(17) (1996), 2554–2556. DOI: 10.1063/1.117737 (cit. on p. 19).

138. H. Sakaki, T. Noda, K. Hirakawa, M. Tanaka, and T. Matsusue: Interface roughness scattering in GaAs/AlAs quantum wells. *Appl. Phys. Lett.* **51**(23) (1987), 1934–1936. DOI: 10.1063/1.98305 (cit. on p. 19).

139. T. Mårtensson, C. P. T. Svensson, B. A. Wacaser, M. W. Larsson, W. Seifert, K. Deppert, A. Gustafsson, L. R. Wallenberg, and L. Samuelson: Epitaxial III-V Nanowires on Silicon. *Nano Lett.* **4**(10) (2004), 1987–1990. DOI: 10.1021/nl0487267 (cit. on p. 20).

140. H. J. Joyce, Q. Gao, H. H. Tan, C. Jagadish, Y. Kim, X. Zhang, Y. Guo, and J. Zou: Twin-Free Uniform Epitaxial GaAs Nanowires Grown by a Two-Temperature Process. *Nano Lett.* **7**(4) (2007), 921–926. DOI: 10.1021/nl062755v (cit. on p. 20).

141. E. Russo-Averchi, M. Heiss, L. Michelet, P. Krogstrup, J. Nygard, C. Magen, J. R. Morante, E. Uccelli, J. Arbiol, and A. Fontcuberta i Morral: Suppression of three dimensional twinning for a 100% yield of vertical GaAs nanowires on silicon. *Nanoscale* **4**(5) (2012), 1486. DOI: 10.1039/c2nr11799a (cit. on p. 20).

142. N. V. Sibirev, M. Tchernycheva, M. A. Timofeeva, J.-C. Harmand, G. E. Cirlin, and V. G. Dubrovskii: Influence of shadow effect on the growth and shape of InAs nanowires. *J. Appl. Phys.* **111**(10) (2012), 104317. DOI: 10.1063/1.4718434 (cit. on p. 20).

143. V. G. Dubrovskii, T. Xu, A. Díaz Álvarez, S. R. Plissard, P. Caroff, F. Glas, and B. Grandidier: Self-Equilibration of the Diameter of Ga-Catalyzed GaAs Nanowires. *Nano Lett.* **15**(8) (2015), 5580–5584. DOI: 10.1021/acs.nanolett.5b02226 (cit. on p. 20).

144. C. Pöpsel, J. Becker, N. Jeon, M. Döblinger, T. Stettner, Y. T. Gottschalk, B. Loitsch, S. Matich, M. Altzschner, A. W. Holleitner, J. J. Finley, L. J. Lauhon, and G. Koblmüller: He-Ion Microscopy as a High-Resolution Probe for Complex

Quantum Heterostructures in Core–Shell Nanowires. *Nano Lett.* **18**(6) (2018), 3911–3919. DOI: 10.1021/acs.nanolett.8b01282 (cit. on p. 20).

145. W. I. Wang: Instabilities of (110) III–V compounds grown by molecular beam epitaxy. *J. Vac. Sci. Technol. B* **1**(3) (1983), 630. DOI: 10.1116/1.582567 (cit. on p. 22).

146. D. Bimberg, D. Mars, J. N. Miller, and D. Oertel: Structural changes of the interface, enhanced interface incorporation of acceptors, and luminescence efficiency degradation in GaAs quantum wells grown by molecular beam epitaxy upon growth interruption. *J. Vac. Sci. Technol. B* **4**(4) (1986), 1014. DOI: 10.1116/1.583572 (cit. on p. 23).

147. D. Bimberg, J. Christen, T. Fukunaga, H. Nakashima, D. E. Mars, and J. N. Miller: Cathodoluminescence atomic scale images of monolayer islands at GaAs/GaAlAs interfaces. *J. Vac. Sci. Technol. B* **5**(4) (1987), 1191. DOI: 10.1116/1.583710 (cit. on p. 23).

148. A. S. Brown, J. A. Henige, and M. J. Delaney: Photoluminescence broadening mechanisms in high quality GaInAs-AlInAs quantum well structures. *Appl. Phys. Lett.* **52**(14) (1988), 1142–1143. DOI: 10.1063/1.99185 (cit. on p. 23).

149. K. Brunner, G. Abstreiter, G. Böhm, G. Tränkle, and G. Weimann: Sharp-line photoluminescence of excitons localized at GaAs/AlGaAs quantum well inhomogeneities. *Appl. Phys. Lett.* **64**(24) (1994), 3320–3322. DOI: 10.1063/1.111265 (cit. on p. 23).

150. K. Leosson, J. R. Jensen, W. Langbein, and J. M. Hvam: Exciton localization and interface roughness in growth-interrupted GaAs/AlAs quantum wells. *Phys. Rev. B* **61**(15) (2000), 10322–10329. DOI: 10.1103/PhysRevB.61.10322 (cit. on p. 23).

151. M. Yoshita, N. Kondo, H. Sakaki, M. Baba, and H. Akiyama: Large terrace formation and modulated electronic states in (110) GaAs quantum wells. *Phys. Rev. B* **63**(7) (2001), 075305. DOI: 10.1103/PhysRevB.63.075305 (cit. on p. 23).

152. G. Ferrari, G. Goldoni, A. Bertoni, G. Cuoghi, and E. Molinari: Magnetic States in Prismatic Core Multishell Nanowires. *Nano Lett.* **9**(4) (2009), 1631–1635. DOI: 10.1021/nl803942p (cit. on p. 26).

153. R. C. Miller, D. A. Kleinman, and A. C. Gossard: Energy-gap discontinuities and effective masses for GaAs-Al$_x$Ga$_{1-x}$As quantum wells. *Phys. Rev. B* **29**(12) (1984), 7085–7087. DOI: 10.1103/PhysRevB.29.7085 (cit. on pp. 26, 30).

154. M. S. Miller, H. Weman, C. E. Pryor, M. Krishnamurthy, P. M. Petroff, H. Kroemer, and J. L. Merz: Serpentine superlattice quantum-wire arrays of (Al,Ga)As grown

on vicinal GaAs substrates. *Phys. Rev. Lett.* **68**(23) (1992), 3464–3467. DOI: 10.1103/PhysRevLett.68.3464 (cit. on p. 30).

155. D. P. Morgan: *Surface Acoustic Wave Filters: With Applications to Electronic Communications and Signal Processing.* Elsevier Science Publishers, 1991 (cit. on p. 31).

156. D. Royer and E. Dieulesaint: *Elastic Waves in Solids I: Free and Guided Propagation.* Springer-Verlag Berlin Heidelberg, 2000 (cit. on pp. 31, 64, 66).

157. D. Royer and E. Dieulesaint: *Elastic Waves in Solids II: Generation, Acousto-optic Interaction, Applications.* Springer-Verlag Berlin Heidelberg, 2000 (cit. on p. 31).

158. M. Weiß: Quantum Dot Optomechanics with Surface Acoustic Waves. Doctoral Thesis. Universität Augsburg, 2020 (cit. on p. 31).

159. L. Janker: Acousto-Electrically Driven Charge Carrier Dynamics in Metal Halide Perovskites: From Fundamental Studies to Sensor Applications. Doctoral Thesis. Universität Augsburg, 2020 (cit. on p. 32).

160. R. M. White and F. W. Voltmer: DIRECT PIEZOELECTRIC COUPLING TO SURFACE ELASTIC WAVES. *Appl. Phys. Lett.* **7**(12) (1965), 314–316. DOI: 10.1063/1.1754276 (cit. on p. 40).

161. J. Singh: *Electronic and Optoelectronic Properties of Semiconductor Structures.* New York: Cambridge University Press, 2003, pp. 68–70. DOI: 10.1017/CBO9780511805745 (cit. on p. 47).

162. F. J. R. Schülein: Dynamische Kontrolle optisch aktiver Halbleiter-Quantenpunkte mittels akustischer Oberflächenwellen. Doctoral Thesis. Universität Augsburg, 2014 (cit. on p. 47).

163. F. Alsina, P. V. Santos, R. Hey, A. García-Cristóbal, and A. Cantarero: Dynamic carrier distribution in quantum wells modulated by surface acoustic waves. *Phys. Rev. B* **64**(4) (2001), 041304. DOI: 10.1103/PhysRevB.64.041304 (cit. on pp. 49, 77).

164. A. Richter, G. Behme, M. Süptitz, C. Lienau, T. Elsaesser, M. Ramsteiner, R. Nötzel, and K. H. Ploog: Real-Space Transfer and Trapping of Carriers into Single GaAs Quantum Wires Studied by Near-Field Optical Spectroscopy. *Phys. Rev. Lett.* **79**(11) (1997), 2145–2148. DOI: 10.1103/PhysRevLett.79.2145 (cit. on pp. 49, 77).

165. F. Alsina, P. V. Santos, H.-P. Schönherr, W. Seidel, K. H. Ploog, and R. Nötzel: Surface-acoustic-wave-induced carrier transport in quantum wires. *Phys. Rev. B* **66**(16) (2002), 165330. DOI: 10.1103/PhysRevB.66.165330 (cit. on pp. 49, 77).

166. J. R. Gell, M. B. Ward, R. J. Young, R. M. Stevenson, P. Atkinson, D. Anderson, G. A. C. Jones, D. A. Ritchie, and A. J. Shields: Modulation of single quantum dot energy levels by a surface-acoustic-wave. *Appl. Phys. Lett.* **93**(8) (2008), 081115. DOI: 10.1063/1.2976135 (cit. on pp. 49, 77).

167. F. J. R. Schülein, J. Pustiowski, K. Müller, M. Bichler, G. Koblmüller, J. J. Finley, A. Wixforth, and H. J. Krenner: Surface acoustic wave controlled charge dynamics in a thin InGaAs quantum well. *JETP Lett.* **95**(11) (2012), 575–580. DOI: 10.1134/S0021364012110082 (cit. on pp. 49, 77, 87, 88, 97).

168. F. J. R. Schülein, K. Müller, M. Bichler, G. Koblmüller, J. J. Finley, A. Wixforth, and H. J. Krenner: Acoustically regulated carrier injection into a single optically active quantum dot. *Phys. Rev. B* **88**(8) (2013), 085307. DOI: 10.1103/PhysRevB.88.085307 (cit. on pp. 49, 87, 97, 111).

169. J. B. Kinzel: Akusto-elektrisch getriebene Modulation der Ladungsträgerdynamik in GaAs-Nanodrähten. Doctoral Thesis. Universität Augsburg, 2014 (cit. on pp. 49, 53, 58).

170. D. A. Fuhrmann, S. M. Thon, H. Kim, D. Bouwmeester, P. M. Petroff, A. Wixforth, and H. J. Krenner: Dynamic modulation of photonic crystal nanocavities using gigahertz acoustic phonons. *Nat. Photonics* **5**(10) (2011), 605–609. DOI: 10.1038/nphoton.2011.208. arXiv: 1205.1346 (cit. on p. 53).

171. S. Völk, F. Knall, F. J. R. Schülein, T. A. Truong, H. Kim, P. M. Petroff, A. Wixforth, and H. J. Krenner: Direct observation of dynamic surface acoustic wave controlled carrier injection into single quantum posts using phase-resolved optical spectroscopy. *Appl. Phys. Lett.* **98**(2) (2011), 023109. DOI: 10.1063/1.3541881. arXiv: 1011.1898 (cit. on p. 53).

172. M. M. Sonner, D. Rudolph, G. Koblmüller, and H. J. Krenner: High-Dimensional Acousto-optoelectric Correlation Spectroscopy Reveals Coupled Carrier Dynamics in Polytypic Nanowires. *Phys. Rev. Appl.* **16**(3) (2021), 034010. DOI: 10.1103/PhysRevApplied.16.034010 (cit. on pp. 53, 77, 78).

173. P. Lodahl, S. Mahmoodian, S. Stobbe, A. Rauschenbeutel, P. Schneeweiss, J. Volz, H. Pichler, and P. Zoller: Chiral quantum optics. *Nature* **541**(7638) (2017), 473–480. DOI: 10.1038/nature21037 (cit. on p. 61).

174. F. J. Rodríguez-Fortuño, G. Marino, P. Ginzburg, D. O'Connor, A. Martínez, G. A. Wurtz, and A. V. Zayats: Near-Field Interference for the Unidirectional Excitation of Electromagnetic Guided Modes. *Science* **340**(6130) (2013), 328–330. DOI: 10.1126/science.1233739 (cit. on p. 61).

175. J. Petersen, J. Volz, and A. Rauschenbeutel: Chiral nanophotonic waveguide interface based on spin-orbit interaction of light. *Science* **346**(6205) (2014), 67–71. DOI: 10.1126/science.1257671 (cit. on p. 61).

176. A. Aiello, P. Banzer, M. Neugebauer, and G. Leuchs: From transverse angular momentum to photonic wheels. *Nat. Photonics* **9**(12) (2015), 789–795. DOI: 10.1038/nphoton.2015.203 (cit. on pp. 61, 63).

177. K. Y. Bliokh and F. Nori: Transverse spin of a surface polariton. *Phys. Rev. A* **85**(6) (2012), 061801. DOI: 10.1103/PhysRevA.85.061801 (cit. on p. 61).

178. K. Y. Bliokh, A. Y. Bekshaev, and F. Nori: Extraordinary momentum and spin in evanescent waves. *Nat. Commun.* **5**(1) (2014), 3300. DOI: 10.1038/ncomms4300 (cit. on p. 61).

179. K. Y. Bliokh, D. Smirnova, and F. Nori: Quantum spin Hall effect of light. *Science* **348**(6242) (2015), 1448–1451. DOI: 10.1126/science.aaa9519 (cit. on p. 61).

180. T. Van Mechelen and Z. Jacob: Universal spin-momentum locking of evanescent waves. *Optica* **3**(2) (2016), 118. DOI: 10.1364/OPTICA.3.000118 (cit. on p. 61).

181. F. Khosravi, C. L. Cortes, and Z. Jacob: Spin photonics in 3D whispering gallery mode resonators. *Opt. Express* **27**(11) (2019), 15846. DOI: 10.1364/OE.27.015846 (cit. on p. 61).

182. L. Peng, L. Duan, K. Wang, F. Gao, L. Zhang, G. Wang, Y. Yang, H. Chen, and S. Zhang: Transverse photon spin of bulk electromagnetic waves in bianisotropic media. *Nat. Photonics* **13**(12) (2019), 878–882. DOI: 10.1038/s41566-019-0521-4 (cit. on p. 61).

183. C. H. Li, O. M. J. van 't Erve, J. T. Robinson, Y. Liu, L. Li, and B. T. Jonker: Electrical detection of charge-current-induced spin polarization due to spin-momentum locking in Bi_2Se_3. *Nat. Nanotechnol.* **9**(3) (2014), 218–224. DOI: 10.1038/nnano.2014.16 (cit. on p. 61).

184. S. Wu, V. Fatemi, Q. D. Gibson, K. Watanabe, T. Taniguchi, R. J. Cava, and P. Jarillo-Herrero: Observation of the quantum spin Hall effect up to 100 kelvin in a monolayer crystal. *Science* **359**(6371) (2018), 76–79. DOI: 10.1126/science.aan6003 (cit. on p. 61).

185. Y. Shi, J. Kahn, B. Niu, Z. Fei, B. Sun, X. Cai, B. A. Francisco, D. Wu, Z.-X. Shen, X. Xu, D. H. Cobden, and Y.-T. Cui: Imaging quantum spin Hall edges in monolayer WTe_2. *Sci. Adv.* **5**(2) (2019), eaat8799. DOI: 10.1126/sciadv.aat8799 (cit. on p. 61).

186. J. Lin, J. P. B. Mueller, Q. Wang, G. Yuan, N. Antoniou, X.-C. Yuan, and F. Capasso: Polarization-Controlled Tunable Directional Coupling of Surface Plasmon Polaritons. *Science* **340**(6130) (2013), 331–334. DOI: 10.1126/science.1233746 (cit. on p. 61).

187. I. Söllner, S. Mahmoodian, S. L. Hansen, L. Midolo, A. Javadi, G. Kiršanskė, T. Pregnolato, H. El-Ella, E. H. Lee, J. D. Song, S. Stobbe, and P. Lodahl: Deterministic photon–emitter coupling in chiral photonic circuits. *Nat. Nanotechnol.* **10**(9) (2015), 775–778. DOI: 10.1038/nnano.2015.159 (cit. on p. 61).

188. S. Barik, A. Karasahin, C. Flower, T. Cai, H. Miyake, W. DeGottardi, M. Hafezi, and E. Waks: A topological quantum optics interface. *Science* **359**(6376) (2018), 666–668. DOI: 10.1126/science.aaq0327 (cit. on p. 61).

189. T. Ozawa, H. M. Price, A. Amo, N. Goldman, M. Hafezi, L. Lu, M. C. Rechtsman, D. Schuster, J. Simon, O. Zilberberg, and I. Carusotto: Topological photonics. *Rev. Mod. Phys.* **91**(1) (2019), 015006. DOI: 10.1103/RevModPhys.91.015006 (cit. on p. 61).

190. S.-H. Gong, F. Alpeggiani, B. Sciacca, E. C. Garnett, and L. Kuipers: Nanoscale chiral valley-photon interface through optical spin-orbit coupling. *Science* **359**(6374) (2018), 443–447. DOI: 10.1126/science.aan8010 (cit. on p. 61).

191. A. Osada, R. Hisatomi, A. Noguchi, Y. Tabuchi, R. Yamazaki, K. Usami, M. Sadgrove, R. Yalla, M. Nomura, and Y. Nakamura: Cavity Optomagnonics with Spin-Orbit Coupled Photons. *Phys. Rev. Lett.* **116**(22) (2016), 223601. DOI: 10.1103/PhysRevLett.116.223601 (cit. on p. 61).

192. Y. Long, J. Ren, and H. Chen: Intrinsic spin of elastic waves. *Proc. Natl. Acad. Sci.* **115**(40) (2018), 9951–9955. DOI: 10.1073/pnas.1808534115 (cit. on p. 61).

193. K. Y. Bliokh and F. Nori: Spin and orbital angular momenta of acoustic beams. *Phys. Rev. B* **99**(17) (2019), 174310. DOI: 10.1103/PhysRevB.99.174310 (cit. on pp. 61, 64).

194. L. Burns, K. Y. Bliokh, F. Nori, and J. Dressel: Acoustic versus electromagnetic field theory: scalar, vector, spinor representations and the emergence of acoustic spin. *New J. Phys.* **22**(5) (2020), 053050. DOI: 10.1088/1367-2630/ab7f91 (cit. on p. 61).

195. K. A. Ingebrigtsen: Surface Waves in Piezoelectrics. *J. Appl. Phys.* **40**(7) (1969), 2681–2686. DOI: 10.1063/1.1658060 (cit. on pp. 64, 66).

196. G. Gautschi: *Piezoelectric Sensorics.* Berlin, Heidelberg: Springer Berlin Heidelberg, 2002. DOI: 10.1007/978-3-662-04732-3 (cit. on p. 64).

197. F. Khosravi: Unified Spin Electrodynamics of Dirac and Maxwell Fields. Doctoral Thesis. University of Alberta, 2020 (cit. on p. 64).

198. S. M. Barnett and L. Allen: Orbital angular momentum and nonparaxial light beams. *Opt. Commun.* **110**(5-6) (1994), 670–678. DOI: 10.1016/0030-4018(94)90269-0 (cit. on p. 64).

199. M. F. Picardi, A. V. Zayats, and F. J. Rodríguez-Fortuño: Janus and Huygens Dipoles: Near-Field Directionality Beyond Spin-Momentum Locking. *Phys. Rev. Lett.* **120**(11) (2018), 117402. DOI: 10.1103/PhysRevLett.120.117402 (cit. on p. 64).

200. M. F. Picardi, K. Y. Bliokh, F. J. Rodríguez-Fortuño, F. Alpeggiani, and F. Nori: Angular momenta, helicity, and other properties of dielectric-fiber and metallic-wire modes. *Optica* **5**(8) (2018), 1016. DOI: 10.1364/OPTICA.5.001016 (cit. on p. 64).

201. C. Shi, R. Zhao, Y. Long, S. Yang, Y. Wang, H. Chen, J. Ren, and X. Zhang: Observation of acoustic spin. *Natl. Sci. Rev.* **6**(4) (2019), 707–712. DOI: 10.1093/nsr/nwz059 (cit. on pp. 64, 66).

202. Y. Long, D. Zhang, C. Yang, J. Ge, H. Chen, and J. Ren: Realization of acoustic spin transport in metasurface waveguides. *Nat. Commun.* **11**(1) (2020), 4716. DOI: 10.1038/s41467-020-18599-y (cit. on p. 66).

203. M. J. A. Schuetz, E. M. Kessler, G. Giedke, L. M. K. Vandersypen, M. D. Lukin, and J. I. Cirac: Universal Quantum Transducers Based on Surface Acoustic Waves. *Phys. Rev. X* **5**(3) (2015), 031031. DOI: 10.1103/PhysRevX.5.031031 (cit. on p. 76).

204. M. V. Gustafsson, T. Aref, A. F. Kockum, M. K. Ekström, G. Johansson, and P. Delsing: Propagating phonons coupled to an artificial atom. *Science* **346**(6206) (2014), 207–211. DOI: 10.1126/science.1257219 (cit. on p. 76).

205. S. J. Whiteley, G. Wolfowicz, C. P. Anderson, A. Bourassa, H. Ma, M. Ye, G. Koolstra, K. J. Satzinger, M. V. Holt, F. J. Heremans, A. N. Cleland, D. I. Schuster, G. Galli, and D. D. Awschalom: Spin–phonon interactions in silicon carbide addressed by Gaussian acoustics. *Nat. Phys.* **15**(5) (2019), 490–495. DOI: 10.1038/s41567-019-0420-0 (cit. on p. 76).

206. A. Bienfait, K. J. Satzinger, Y. P. Zhong, H.-S. Chang, M.-H. Chou, C. R. Conner, É. Dumur, J. Grebel, G. A. Peairs, R. G. Povey, and A. N. Cleland: Phonon-mediated quantum state transfer and remote qubit entanglement. *Science* **364**(6438) (2019), 368–371. DOI: 10.1126/science.aaw8415 (cit. on p. 76).

207. M. Weiß, D. Wigger, M. Nägele, K. Müller, J. J. Finley, T. Kuhn, P. Machnikowski, and H. J. Krenner: Optomechanical wave mixing by a single quantum dot. *Optica* **8**(3) (2021), 291. DOI: 10.1364/OPTICA.412201 (cit. on p. 76).

208. D. A. Golter, T. Oo, M. Amezcua, K. A. Stewart, and H. Wang: Optomechanical Quantum Control of a Nitrogen-Vacancy Center in Diamond. *Phys. Rev. Lett.* **116**(14) (2016), 143602. DOI: 10.1103/PhysRevLett.116.143602 (cit. on p. 76).

209. E. A. Cerda-Méndez, D. N. Krizhanovskii, M. Wouters, R. Bradley, K. Biermann, K. Guda, R. Hey, P. V. Santos, D. Sarkar, and M. S. Skolnick: Polariton Condensation in Dynamic Acoustic Lattices. *Phys. Rev. Lett.* **105**(11) (2010), 116402. DOI: 10.1103/PhysRevLett.105.116402 (cit. on p. 76).

210. V. Peano, C. Brendel, M. Schmidt, and F. Marquardt: Topological Phases of Sound and Light. *Phys. Rev. X* **5**(3) (2015), 031011. DOI: 10.1103/PhysRevX.5.031011 (cit. on p. 76).

211. T. Van Mechelen and Z. Jacob: Photonic Dirac monopoles and skyrmions: spin-1 quantization [Invited]. *Opt. Mater. Express* **9**(1) (2019), 95. DOI: 10.1364/OME.9.000095 (cit. on p. 76).

212. C. Brendel, V. Peano, O. Painter, and F. Marquardt: Snowflake phononic topological insulator at the nanoscale. *Phys. Rev. B* **97**(2) (2018), 020102. DOI: 10.1103/PhysRevB.97.020102 (cit. on p. 76).

213. M. Forsch, R. Stockill, A. Wallucks, I. Marinković, C. Gärtner, R. A. Norte, F. van Otten, A. Fiore, K. Srinivasan, and S. Gröblacher: Microwave-to-optics conversion using a mechanical oscillator in its quantum ground state. *Nat. Phys.* **16**(1) (2020), 69–74. DOI: 10.1038/s41567-019-0673-7 (cit. on p. 76).

214. M. M. Sonner, M. Gnedel, J. C. Berlin, D. Rudolph, G. Koblmüller, and H. J. Krenner: Sub-nanosecond acousto-electric carrier redistribution dynamics and transport in polytypic GaAs nanowires. *Nanotechnology* **32**(50) (2021), 505209. DOI: 10.1088/1361-6528/ac2ac2 (cit. on pp. 77, 78).

215. B. J. Ohlsson, M. T. Björk, M. H. Magnusson, K. Deppert, L. Samuelson, and L. R. Wallenberg: Size-, shape-, and position-controlled GaAs nano-whiskers. *Appl. Phys. Lett.* **79**(20) (2001), 3335–3337. DOI: 10.1063/1.1418446 (cit. on p. 77).

216. N. Vainorius, D. Jacobsson, S. Lehmann, A. Gustafsson, K. A. Dick, L. Samuelson, and M.-E. Pistol: Observation of type-II recombination in single wurtzite/zinc-blende GaAs heterojunction nanowires. *Phys. Rev. B* **89**(16) (2014), 165423. DOI: 10.1103/PhysRevB.89.165423 (cit. on p. 77).

217. D. Magde, E. Elson, and W. W. Webb: Thermodynamic Fluctuations in a Reacting System—Measurement by Fluorescence Correlation Spectroscopy. *Phys. Rev. Lett.* **29**(11) (1972), 705–708. DOI: 10.1103/PhysRevLett.29.705 (cit. on p. 77).

218. J. Ries and P. Schwille: Fluorescence correlation spectroscopy. *BioEssays* **34**(5) (2012), 361–368. DOI: 10.1002/bies.201100111 (cit. on p. 77).

219. M. Aßmann, F. Veit, M. Bayer, M. van der Poel, and J. M. Hvam: Higher-Order Photon Bunching in a Semiconductor Microcavity. *Science* **325**(5938) (2009), 297–300. DOI: 10.1126/science.1174488 (cit. on p. 77).

220. J. Wiersig, C. Gies, F. Jahnke, M. Aßmann, T. Berstermann, M. Bayer, C. Kistner, S. Reitzenstein, C. Schneider, S. Höfling, A. Forchel, C. Kruse, J. Kalden, and D. Hommel: Direct observation of correlations between individual photon emission events of a microcavity laser. *Nature* **460**(7252) (2009), 245–249. DOI: 10.1038/nature08126 (cit. on p. 77).

221. E. R. Schmidgall, I. Schwartz, L. Gantz, D. Cogan, S. Raindel, and D. Gershoni: Deterministic generation of a quantum-dot-confined triexciton and its radiative decay via three-photon cascade. *Phys. Rev. B* **90**(24) (2014), 241411. DOI: 10.1103/PhysRevB.90.241411 (cit. on p. 77).

222. R. E. Algra, M. A. Verheijen, M. T. Borgström, L.-F. Feiner, G. Immink, W. J. P. van Enckevort, E. Vlieg, and E. P. A. M. Bakkers: Twinning superlattices in indium phosphide nanowires. *Nature* **456**(7220) (2008), 369–372. DOI: 10.1038/nature07570 (cit. on pp. 80, 83).

223. A. Senichev, P. Corfdir, O. Brandt, M. Ramsteiner, S. Breuer, J. Schilling, L. Geelhaar, and P. Werner: Electronic properties of wurtzite GaAs: A correlated structural, optical, and theoretical analysis of the same polytypic GaAs nanowire. *Nano Res.* **11**(9) (2018), 4708–4721. DOI: 10.1007/s12274-018-2053-5 (cit. on pp. 80, 82–84).

224. K. Pemasiri, M. Montazeri, R. Gass, L. M. Smith, H. E. Jackson, J. Yarrison-Rice, S. Paiman, Q. Gao, H. H. Tan, C. Jagadish, X. Zhang, and J. Zou: Carrier Dynamics and Quantum Confinement in type II ZB-WZ InP Nanowire Homostructures. *Nano Lett.* **9**(2) (2009), 648–654. DOI: 10.1021/nl802997p (cit. on pp. 85, 116).

225. S. Völk, F. J. R. Schülein, F. Knall, D. Reuter, A. D. Wieck, T. A. Truong, H. Kim, P. M. Petroff, A. Wixforth, and H. J. Krenner: Enhanced Sequential Carrier Capture into Individual Quantum Dots and Quantum Posts Controlled by Surface Acoustic Waves. *Nano Lett.* **10**(9) (2010), 3399–3407. DOI: 10.1021/nl1013053 (cit. on p. 87).

226. S. Völk, F. Knall, F. J. R. Schülein, T. A. Truong, H. Kim, P. M. Petroff, A. Wixforth, and H. J. Krenner: Surface acoustic wave mediated carrier injection into individual quantum post nano emitters. *Nanotechnology* **23**(28) (2012), 285201. DOI: 10.1088/0957-4484/23/28/285201 (cit. on pp. 87, 111).

227. O. D. D. Couto, Jr., S. Lazić, F. Iikawa, J. A. H. Stotz, U. Jahn, R. Hey, and P. V. Santos: Photon anti-bunching in acoustically pumped quantum dots. *Nat. Photonics* **3**(11) (2009), 645–648. DOI: 10.1038/nphoton.2009.191 (cit. on p. 111).

228. S. Lazić, E. Chernysheva, A. Hernández-Mínguez, P. V. Santos, and H. P. van der Meulen: Acoustically regulated optical emission dynamics from quantum dot-like emission centers in GaN/InGaN nanowire heterostructures. *J. Phys. D. Appl. Phys.* **51**(10) (2018), 104001. DOI: 10.1088/1361-6463/aaa8d5 (cit. on p. 111).

229. A. Crespo-Poveda, A. Hernández-Mínguez, B. Gargallo, K. Biermann, A. Tahraoui, P. V. Santos, P. Muñoz, A. Cantarero, and M. M. de Lima: Acoustically driven arrayed waveguide grating. *Opt. Express* **23**(16) (2015), 21213. DOI: 10.1364/OE.23.021213 (cit. on p. 111).

230. S. Kapfinger, T. Reichert, S. Lichtmannecker, K. Müller, J. J. Finley, A. Wixforth, M. Kaniber, and H. J. Krenner: Dynamic acousto-optic control of a strongly coupled photonic molecule. en. *Nat. Commun.* **6**(1) (2015), 8540. DOI: 10.1038/ncomms9540 (cit. on p. 111).

231. A. Vogele, M. M. Sonner, B. Mayer, X. Yuan, M. Weiß, E. D. S. Nysten, S. F. Covre da Silva, A. Rastelli, and H. J. Krenner: Quantum Dot Optomechanics in Suspended Nanophononic Strings. *Adv. Quantum Technol.* **3**(2) (2020), 1900102. DOI: 10.1002/qute.201900102 (cit. on p. 111).

232. S. Lazić, A. Espinha, S. Pinilla Yanguas, C. Gibaja, F. Zamora, P. Ares, M. Chhowalla, W. S. Paz, J. J. Palacios Burgos, A. Hernández-Mínguez, P. V. Santos, and H. P. van der Meulen: Dynamically tuned non-classical light emission from atomic defects in hexagonal boron nitride. *Commun. Phys.* **2**(1) (2019), 113. DOI: 10.1038/s42005-019-0217-6 (cit. on p. 111).

233. P. Rivera, J. R. Schaibley, A. M. Jones, J. S. Ross, S. Wu, G. Aivazian, P. Klement, K. Seyler, G. Clark, N. J. Ghimire, J. Yan, D. G. Mandrus, W. Yao, and X. Xu: Observation of long-lived interlayer excitons in monolayer $MoSe_2$–WSe_2

heterostructures. *Nat. Commun.* **6**(1) (2015), 6242. DOI: 10.1038/ncomms7242 (cit. on p. 111).

234. T. Yang, B.i Zheng, Z. Wang, T. Xu, C. Pan, J. Zou, X. Zhang, Z. Qi, H. Liu, Y. Feng, W. Hu, F. Miao, L. Sun, X. Duan, and A. Pan: Van der Waals epitaxial growth and optoelectronics of large-scale WSe_2/SnS_2 vertical bilayer p–n junctions. *Nat. Commun.* **8**(1) (2017), 1906. DOI: 10.1038/s41467-017-02093-z (cit. on p. 111).

235. D.-H. Kang, S. R. Pae, J. Shim, G. Yoo, J. Jeon, J. W. Leem, J. S. Yu, S. Lee, B. Shin, and J.-H. Park: An Ultrahigh-Performance Photodetector based on a Perovskite-Transition-Metal-Dichalcogenide Hybrid Structure. *Adv. Mater.* **28**(35) (2016), 7799–7806. DOI: 10.1002/adma.201600992 (cit. on p. 111).

236. C. Hu, D. Dong, X. Yang, K. Qiao, D. Yang, H. Deng, S. Yuan, J. Khan, Y. Lan, H. Song, and J. Tang: Synergistic Effect of Hybrid PbS Quantum Dots/2D-WSe_2 Toward High Performance and Broadband Phototransistors. *Adv. Funct. Mater.* **27**(2) (2017), 1603605. DOI: 10.1002/adfm.201603605 (cit. on p. 111).

237. J. Sun, Y. Choi, Y. J. Choi, S. Kim, J.-H. Park, S. Lee, and J. H. Cho: 2D–Organic Hybrid Heterostructures for Optoelectronic Applications. *Adv. Mater.* **31**(34) (2019), 1803831. DOI: 10.1002/adma.201803831 (cit. on p. 111).

238. M. J. A. Schuetz, J. Knörzer, G. Giedke, L. M. K. Vandersypen, M. D. Lukin, and J. I. Cirac: Acoustic Traps and Lattices for Electrons in Semiconductors. *Phys. Rev. X* **7**(4) (2017), 041019. DOI: 10.1103/PhysRevX.7.041019 (cit. on p. 111).

239. P. V. Santos, F. Alsina, J. A. H. Stotz, R. Hey, S. Eshlaghi, and A. D. Wieck: Band mixing and ambipolar transport by surface acoustic waves in GaAs quantum wells. *Phys. Rev. B* **69**(15) (2004), 155318. DOI: 10.1103/PhysRevB.69.155318 (cit. on pp. 114, 117).

240. E. Yablonovitch and E. O. Kane: Band structure engineering of semiconductor lasers for optical communications. *J. Light. Technol.* **6**(8) (1988), 1292–1299. DOI: 10.1109/50.4133 (cit. on p. 115).

241. C. E. Zah, R. Bhat, K. W. Cheung, N. C. Andreadakis, F. J. Favire, S. G. Menocal, E. Yablonovitch, D. M. Hwang, M. Koza, T. J. Gmitter, and T. P. Lee: Low-threshold ($\leq$ 92 A/cm^2) 1.6 μm strained-layer single quantum well laser diodes optically pumped by a 0.8 μm laser diode. *Appl. Phys. Lett.* **57**(16) (1990), 1608–1609. DOI: 10.1063/1.103362 (cit. on p. 115).

242. P. P. Ruden, M. Shur, D. K. Arch, R. R. Daniels, D. E. Grider, and T. E. Nohava: Quantum-well p-channel AlGaAs/InGaAs/GaAs heterostructure insulated-

gate field-effect transistors. *IEEE Trans. Electron Devices* **36**(11) (1989), 2371–2379. DOI: 10.1109/16.43656 (cit. on p. 115).

243. P. Schmiedeke, A. Thurn, S. Matich, M. Döblinger, J. J. Finley, and G. Koblmüller: Low-threshold strain-compensated InGaAs/(In,Al)GaAs multi-quantum well nanowire lasers emitting near 1.3 μm at room temperature. *Appl. Phys. Lett.* **118**(22) (2021), 221103. DOI: 10.1063/5.0048807 (cit. on p. 115).

244. L. Francaviglia, G. Tütüncüoglu, S. Martí-Sánchez, E. Di Russo, S. Escobar Steinvall, J. Segura Ruiz, H. Potts, M. Friedl, L. Rigutti, J. Arbiol, and A. Fontcuberta i Morral: Segregation scheme of indium in AlGaInAs nanowire shells. *Phys. Rev. Mater.* **3**(2) (2019), 023001. DOI: 10.1103/PhysRevMaterials.3.023001 (cit. on p. 116).

245. L. Balaghi, G. Bussone, R. Grifone, R. Hübner, J. Grenzer, M. Ghorbani-Asl, A. V. Krasheninnikov, H. Schneider, M. Helm, and E. Dimakis: Widely tunable GaAs bandgap via strain engineering in core/shell nanowires with large lattice mismatch. *Nat. Commun.* **10**(1) (2019), 2793. DOI: 10.1038/s41467-019-10654-7 (cit. on p. 117).

List of Publications

Published papers

- **"Correlated chemical and electrically active dopant analysis in catalyst-free Si-doped InAs nanowires"**
  J. Becker, M. O. Hill, M. Sonner, J. Treu, M. Döblinger, A. Hirler, H. Riedl, J. J. Finley, L. J. Lauhon, G. Koblmüller
  ACS Nano 12(2) (2018), 1603–1610, doi: 10.1021/acsnano.7b08197

- **"Carrier concentration dependent photoluminescence properties of Si-doped InAs nanowires"**
  M. Sonner, J. Treu, K. Saller, H. Riedl, J. J. Finley, G. Koblmüller
  Appl. Phys. Lett. 112 (2018), 091904, doi: 10.1063/1.5019350

- **"Carrier trapping and activation at short-period wurtzite/zinc-blende stacking sequences in polytypic InAs nanowires"**
  J. Becker, S. Morkötter, J. Treu, M. Sonner, M. Speckbacher, M. Döblinger, G. Abstreiter, J. J. Finley, and G. Koblmüller
  Phys. Rev. B 97 (2018), 115306, doi: 10.1103/PhysRevB.97.115306

- **"Breakdown of Corner States and Carrier Localization by Monolayer Fluctuations in Radial Nanowire Quantum Wells"**
  M. M. Sonner, A. Sitek, L. Janker, D. Rudolph, D. Ruhstorfer, M. Döblinger, A. Manolescu, G. Abstreiter, J. J. Finley, A. Wixforth, G. Koblmüller, H. J. Krenner
  Nano Lett. 19(5) (2019), 3336–3343, doi: 10.1021/acs.nanolett.9b01028

- **"Quantum Dot Optomechanics in Suspended Nanophononic Strings"**
  A. Vogele, M. M. Sonner, B. Mayer, X. Yuan, M. Weiß, E. D. S. Nysten, S. F. C. da Silva, A. Rastelli, H. J. Krenner
  Adv. Quantum Technol. 3(2) (2020), 1900102, doi: 10.1002/qute.201900102

- **"Ultrafast electron cycloids driven by the transverse spin of a surface acoustic wave"**
  M. M. Sonner, F. Khosravi, L. Janker, D. Rudolph, G. Koblmüller, Z. Jacob, H. J. Krenner
  Science Advances 7(31) (2021), eabf7414, doi: 10.1126/sciadv.abf7414

- **"High-dimensional acousto-optoelectric correlation spectroscopy reveals coupled carrier dynamics in polytypic nanowires"**
  M. M. Sonner, D. Rudolph, G. Koblmüller, H. J. Krenner
  Phys. Rev. Applied 16 (2021), 034010, doi: 10.1103/PhysRevApplied.16.034010

- **"Sub-nanosecond acousto-electric carrier redistribution dynamics and transport in polytypic GaAs nanowires"**
  M. M. Sonner, M. Gnedel, J. C. Berlin, D. Rudolph, G. Koblmueller, H. J. Krenner
  Nanotechnology 32(50) (2021), 505209, doi: 10.1088/1361-6528/ac2ac2

Danksagung

Zu guter Letzt möchte ich mich bei allen bedanken, die mich in den letzten Jahren unterstützt haben. Besonders danken möchte ich dafür folgenden Personen:

Hubert Krenner für die Betreuung und Ermöglichung dieser Arbeit, die Unterstützung durch die Jahre hindurch, für zahlreiche Ideen, die mir weitergeholfen haben, die netten Abende bei am Glasl Bier und seine griabige Art und Weise.

Gregor Koblmüller für die Faszination für Nanodrähte seit mehr als sieben Jahren, die Bereitstellung von Nanowire Proben, die hilfreichen Diskussionen und das konstruktive Feedback, sowie die Bereiterklärung zum Zweitprüfer.

Achim Wixforth und **Ferdinand Haider** für die tolle Atmosphäre am Lehrstuhl und die Unterstützung bei sämtlichen Fragen, Anliegen und Denkanstößen.

Lisa Janker und **Matthias Weiß** für die Einführung in die akusto-optoelektrische Spektroskopie und die Unterstützung bei technischen Fragen, sowie der restlichen Hoobgroup **Sebastian Hammer**, **Michelle Lienhart**, **Emeline Nysten**, **Tobias Petzak** und **Maximilian Wolf** für die tolle Zusammenarbeit, die fantastische Zeit, den Spaß, die etlichen Biere und vieles mehr.

Ein besonderer Dank geht an **Anja Vogele**, **Benjamin Mayer** und **Jonas Steffen**, die ich betreuen durfte und mit denen es mir eine Freude war, zusammenzuarbeiten. Ich hoffe sehr, dass sie so viel lernen konnten, wie ich in dieser Zeit, und wünsche ihnen alles Gute für ihre weitere (wissenschaftliche) Karriere.

Daniel Rudolph, **Bernhard Loitsch**, **Daniel Ruhstorfer** und **Paul Schmiedeke** für das Wachstum meiner Nanodraht Proben sowie die hilfreichen Diskussionen, welche zu neuen Ideen und Untersuchungen führten.

Anna Sitek, **Andrei Manolescu**, **Zubin Jacob** und **Farhad Khosravi** für die produktiven Kooperationen, und besonders, für die Entwicklung der theoretischen Modelle bzgl. der Ladungsträgerlokalisierung in radialen Quantentöpfen und des Spin von akustischen Oberflächenwellen, was wiederum maßgeblich zum Verständnis unserer Ergebnisse beigetragen hat.

Maximilian Gnedel, **Johannes Berlin** und **Markus Döblinger** für die Aufnahme von TEM Bildern und die Analyse dieser Daten.

Alexander Hupfer für die Hilfe bei etlichen Computerproblemen, bei technischen Problemen im Labor und Reinraum sowie bei vielen anderen kleinen und großen Problemen.

Andreas Hörner, **Sidonie Lieber**, **Olga Ustinov**, **Andreas Spörhase**, **Rudolf Herrmann**, **Adrian Mainka** und **Martina Mindt** für die Aufrechterhaltung des laufenden Forschungsbetriebes, für ihre großartige technische Unterstützung, für die Hilfe bei gefährlichen Chemikalien und die Lösung vieler Probleme.

Funda Cevic für ihre Unterstützung in administrativen, bürokratischen und organisatorischen Belangen.

Andrej Kamenac für den herzlichen Empfang am Lehrstuhl und die zahlreichen Diskussionen. **Roland Marstatt** für die genialen Eishockey Abende. **Matthias Küß** für die super Zeit auf unseren Konferenzen. **Nicolas Färber**, **Maximilian Gnedel**, **Anna Jötten**, **Abril Murillo-Sánchez**, **Alexander Reiner**, **Lukas Schnitzler**, **Sixuan Wang** und **Joshua Winkeljann** dafür, dass ihr so tolle Bürokollegen im 305 wart. **Manuel Brugger**, **Sascha Buchegger**, **Andreas Hefele**, **Sebastian Pentz** und **Tobias Stegmüller** als langjährige Kollegen. Euch allen, für die insgesamt konstruktive Arbeitsatmosphäre, die Kaffeepausen, die lustigen Gespräche und die tolle Zeit, die meine Zeit am EP1 so angenehm und unvergesslich gemacht haben.

Dem gesamten **Lehrstuhl EP1** für das tolle Arbeitsklima, viel Spaß, die genialen Partys und Lehrstuhlseminare sowie all die anderen Aktivitäten. Ich hab es genossen.

Meine **Freind** von dahoam und wo anders her, die imma für a Bier zu ham san.

Meiner **Familie** und meiner Freundin **Theresa** für ihre durchgehende Unterstützung und Liebe.

***

Diese Arbeit wurde finanziell unterstützt von der Nanosystems Initiative Munich (NIM) und der Deutsche Forschungsgemeinschaft (DFG).